UNIVERSITAT POLITÈCNICA DE CATALUNYA
BARCELONATECH
Escola Superior d'Enginyeries Industrial, Aeroespacial i Audiovisual de Terrassa

Structural study of a wind sensor for Mars under vibrations induced during launch

Document:
Annex

Author:
Alicia Lluzar Frias

Director - Co-director:
Juan Carlos Cante Teran - David Roca Cazorla

Degree:
Degree in Aerospace Technologies Engineering

Convocation:
Spring, 2022.

BACHELOR FINAL THESIS

Polytechnic University of Catalonia

Superior School of Industrial,
Aerospace and
Audiovisual Engineering of Terrassa

Structural department

Bachelor's degree thesis
Degree in Aerospace Technologies
Engineering

Bachelor Final Thesis

Submitted to

Structural department

In partial fulfillment of the requirements for the

Degree in Aerospace Technologies Engineering

By

Alicia Lluzar Frías

Structural study of a wind sensor for Mars under vibrations induced during launch

Director

Juan Carlos Cante Teran

Co-director

David Roca Cazorla

Contents

List of Figures

List of Tables

Appendix A

Tests

A.1 Fourier Transform

Fourier Transform is a powerful tool when it comes to a vibration analysis. It is widely used to transform a time domain signal into the frequency domain.

Fourier Transform takes name after Jean-Baptiste Joseph Fourier, a French mathematician who explained in his book *The Analytical Theory of Heat* that arbitrary functions could be written in terms of a sum of sines and cosines [18]. Then, after his first discovery, he also found out a second discovery that consisted in determining the amplitude of an individual sine or cosine wave with the use of an integral.

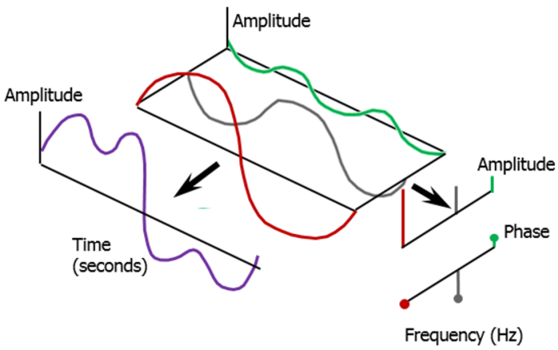

Figure A.1: Fourier Transform schematic representation [1].

As illustrated in figure A.1, with the use of the Fourier Transform a time domain signal can be discomposed into a sum of sinusoids each of which has an specific amplitude, phase and frequency. The ultimate goal of the Fourier Transform is to break down complex time signal into easily understood frequency components [18] with no data loss when moving form time domain to the frequency domain and vice versa. The equation that defines the transformation from time to frequency domain is the following:

$$F(j\omega) = \int_{-\infty}^{\infty} f(t)e^{-j\omega t}dt \tag{A.1}$$

where $F(j\omega)$ is the output of the Fourier Transform in the frequency domain and $f(t)$ is the input function in time domain. Moreover, the output of the Fourier Transform is a series of complex numbers of the form $Z = a + jb$ where a corresponds to the real part whereas b to the imaginary part. Complex numbers have an amplitude and a phase associated that can be computed using the following equations:

$$\|Z\| = \sqrt{a^2 + b^2} \qquad \theta = \tan\frac{a}{b} \tag{A.2}$$

Furthermore, there are two types of Fourier Transforms commonly used: the Discrete Fourier Transform (DFT) and the Fast Fourier Transform (FFT).

A.1.1 Discrete Fourier Transform (DFT)

The Discrete Fourier Transform [3] is a type of Fourier Transform that can be performed on a time signal composed by an arbitrary number of data points (N) separated by sample times (T). Considering that $f(t)$ is a continuous signal, N are the samples taken and that each sample can be seen as an impulse having an area equal to $f[k]$, equation A.1 can be written as:

$$F(j\omega) = \int_0^{(N-1)T} f(t)e^{-j\omega t}dt \tag{A.3}$$

$$= f[0]e^{-j0} + f[1]e^{-j\omega T} + ... + f[k]e^{-j\omega kT} + ... + f[N-1]e^{-j\omega(N-1)T} \tag{A.4}$$

However, as DFT is an approximation of the Fourier Transform since it is built with a finite set of frequencies, it could end up having some errors such as aliasing and leakage. Aliasing happens when the samples are not sufficiently close spaced to represent high-frequency components. Nevertheless, the error can be minimised by increasing the sample rate or by pre-filtering the signal.

Moreover, another crucial issue when analysing a vibration signal is leakage [2] and it occurs when a signal starts to leak into the surrounding frequencies so the Fourier Transform that appears do not line up well with the analysis frequency. This error can be minimised by taking more data points and applying a technique called windowing. The three most common windows used are triangle, Hanning window and Hamming window and they are compared in figures A.2 and A.3.

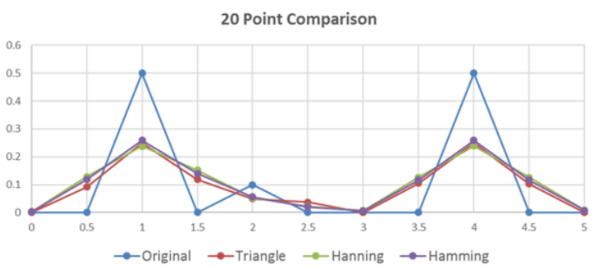

FIGURE A.2: Comparison between the original signal, the triangle window, the Hanning window and the Hamming window results when using 20 data points [2].

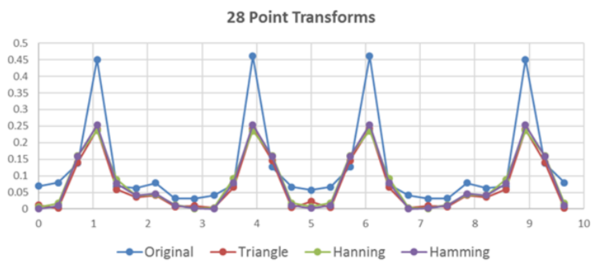

FIGURE A.3: Comparison between the original signal, the triangle window, the Hanning window and the Hamming window results when using 28 data points [2].

A.1.2 Fast Fourier Transform (FFT)

The Fast Fourier Transform is an algorithm that computes the discrete Fourier Transform of a sequence or its inverse [19]. By far the most commonly used FFT is the Cooley-Tukey algorithm discovered by James W. Cooley and John W. Tukey which is explained in their 1965 paper called *An algorithm for the machine calculation of complex Fourier series.* The paper discussed an algorithm for computing the DFT using a divide and conquer approach and, even though prior to them a similar technique was being used, their work was slightly different by showing how special advantage is gained when chosing N to be a power of two, $N = 2^m$ [20].

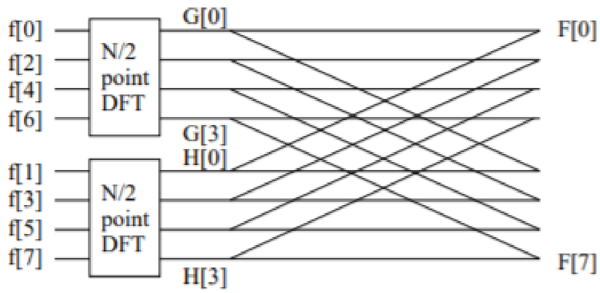

FIGURE A.4: FFT flow graph [3].

A.2 Quasi-static Structural Analysis

Launch phase is the most demanding on the whole space mission. Satellites are exposed to mechanical aggression in the form of sine vibration, acoustic pressure, shock and static acceleration during this phase. When doing a simulation or running a test, those external static and dynamic loads can be reduced into an equivalent quasi-static load.

A static load [21] is a steady-state external load typically associated with static equilibrium in which there is no acceleration. In contrast, a dynamic load varies with time and is associated with vibration. Furthermore, limit loads for a small satellite are typically defined either as quasi-static loads or as load factors, which are multiples of weight on Earth (gravity). For that reason, a quasi-static load and load factors are often expressed in terms of g units.

The main purpose of quasi-static load test is to simulate the launching phase caused by static and dynamic accelerations. Under that conditions, the satellite must be designed and produced to withstand these loads. Moreover, there are three methods commonly used in order to perform these simulations [21]:

- **Whiffle Tree Tests**. The whiffle tree test consists in reproducing the vibrations an accelerations induced by a launcher adaptor to the satellite by fitting the evaluated model into a testing adaptor which reproduces the static loads using weights, hydraulic jacks or similar components. In this kind of test, loads may be applied in three steps: static load, yield load and qualification load.

- **Centrifugal Tests**. A centrifugal test consists in reproducing an static acceleration environment by means of applying a centrifugal force acceleration to the evaluated model. In order to generate this centrifugal force acceleration it is used the rotatory motion of a cantilever arm [22].

- **Acceleration Tests**. An acceleration test consists in reproducing a vibration using an electrodynamics shaker [21]. A head expander is used in order to perform axial vibration test and, in contrast, a slip table is used in lateral vibration tests. Furthermore, those tests are performed using sine vibrations. For this method to work, the connection between the satellite and the shaker should represent the launcher adaptor as much as possible. So, considering the case of a sensor, the connection between the shaker and the sensor should be as realistic as possible.

A.2.1 Sine vibration test

Sine vibration testing produces an acceleration in a sine waveform. This acceleration is characterised by an amplitude level and a frequency both of which can be constant or vary during a range of time. Depending on the frequency, it can be considered two types of tests [23]:

- **Sine Dwell Test**. When the frequency of the vibration is kept constant and the amplitude of the acceleration or the amplitude of the displacement can be kept constant or can vary in order to change the energy level of the test.

- **Sine Sweep Test**. When the frequency of the vibration changes throughout the test. In this case, a product is subjected to an increment or decreased frequency sine vibration in order to detect the natural frequencies of critical elements of the product or unit load that is being tested.

Furthermore, both variations should have frequencies considerably lower than the first structural mode of the evaluated model.

A.2.2 Sine-burst test

A sine-burst test consist in applying an acceleration in a sine waveform modulating its amplitude. It can be divided into three regions depending on its amplitude. First, the amplitude increases, then it is kept constant to finally decrease until a null value.

The sinusoidal frequency is selected to be significantly lower than the fundamental vibration frequency of the test model in order to minimize dynamic response or amplification of the acceleration. That means that the model is being tested with a near-uniform acceleration. A sine-burst test is conducted over short duration in order to avoid unnecessary fatigue damage to the structural materials [4]. Figure A.5 is an example of the excitation applied considering a maximum acceleration of 12g.

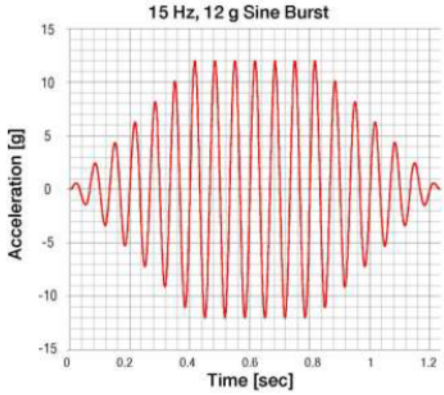

FIGURE A.5: Example Input Acceleration for a Sine-Burst Test [4].

A.3 Random Vibrations Analysis

Random vibration analysis plays an important role when it comes to secure the subsystems behaviour and stability during the launching phase of a spacial mission. Random vibration analysis is also more realistic than sinusoidal one because it evaluates the object in a range of frequencies including resonance.

In order to get a in-depth understanding in how to evaluate the response of an object submitted to a random vibration, this section will include an explanation of the difference between the spectrum and the autopower and the physical meaning of Power Spectral Density and Root-Mean-Square Acceleration.

A.3.1 Spectrum and Autopower

There are several types of spectral functions that can be computed using Fourier Transforms such as spectrum and autopower [1]. Although both types produce results of amplitude in front of frequency, the spectrum function takes into account the phase of the signal whereas the autopower eliminates the phase as shown in figure A.6.

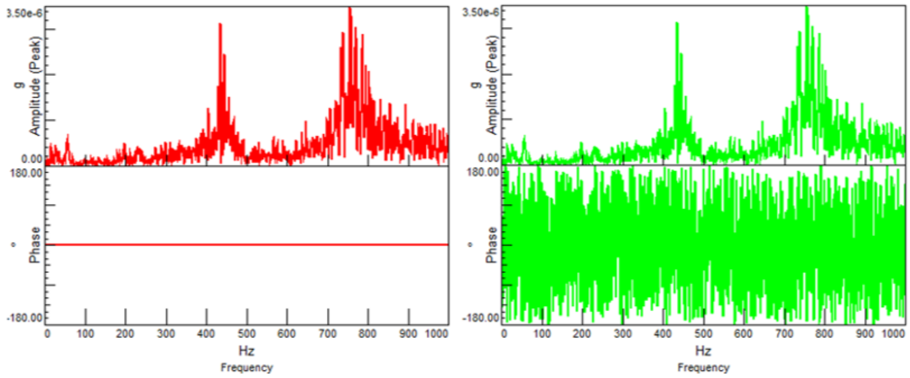

FIGURE A.6: Example of an autopower function (left) and a spectrum function (right) [1].

In order to understand how important phase is when processing spectral data, the Fourier Transform must be study for both cases. The mathematical difference between the spectrum and autopower in terms of the Fourier Transform is that, on the one hand, spectrum is a complex function with amplitude and phase that can be expressed as an imaginary number (a+bi) in front of frequency. On the other hand, in order to eliminate the phase, autopower multiplies the complex conjugate of the spectrum to obtain the Fourier Transform without phase [1].

$$\textit{Spectrum} \qquad G_{xx} = (a + bi) \tag{A.5}$$

$$\textit{Autopower} \qquad G_{xx} = S_x^* S_x = (a + bi)(a - bi) \tag{A.6}$$

By doing so, the autopower function has different units with respect to the spectrum function, it leaves the units squared (g^2 or power units). Furthermore, depending on the units of the autopower it can be commonly differentiate two types of functions [5]:

- **Autopower Linear functions**. It indicates that a square root has been performed after the complex conjugate multiplication. This kind of function has the same Fourier Transform peak amplitude as the spectrum.
- **Autopower Power functions**. It indicates that the results are presented after performing the complex conjugate multiplication, without doing the square root. This kind of function has the square Fourier Transform peak amplitude as the spectrum.

Moreover, one advantage of the autopower functions is that, when it comes to obtain an average of the signal it never turns out to be zero, whereas this result can be obtained when doing the average of a spectrum function [1]. Figures A.7 and A.8 shows a simple example of this fact.

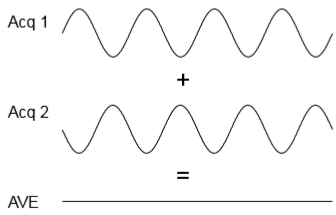

FIGURE A.7: Spectrum average [5].

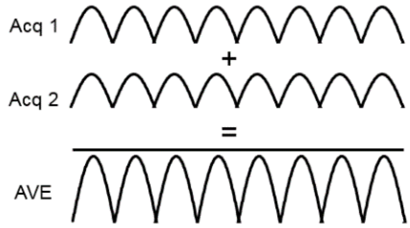

FIGURE A.8: Autopower average [5].

To conclude with, spectrum functions are widely used when the phase is required. However, when it comes to averaging or to get the correct amplitude of a signal, autopower turns to be the most useful and precise tool.

A.3.2 Power Spectral Density (PSD)

Power Spectral Density (PSD) [6] is the measure of the signal's power in front of the frequency. It is typically used to characterise random vibration signals because, as it normalises the amplitude of the signal with the spectral resolution employed, it permits comparing easily different vibrations independently of their resolution.

Imagine capturing different autopower spectrum using three different types of spectral resolution: 1Hz, 4Hz and 8Hz respectively. The resulting plots obtained will share the same shape although having different amplitude levels. The reason why it happens is because, as the frequency resolution gets finer (starting with 8Hz, then 4Hz and finally 1Hz), more data points are being used to measure the signal. Moreover, while the amplitude obtained for individual resolution frequencies appears to be different, the total sum of the data across the frequency range (RMS) is identical [6]. This phenomenon is shown in figure A.9.

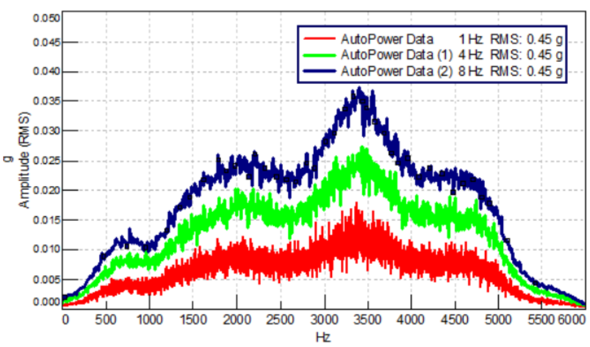

FIGURE A.9: Comparison of the autopower linear functions measured using three different spectral frequency resolutions [6].

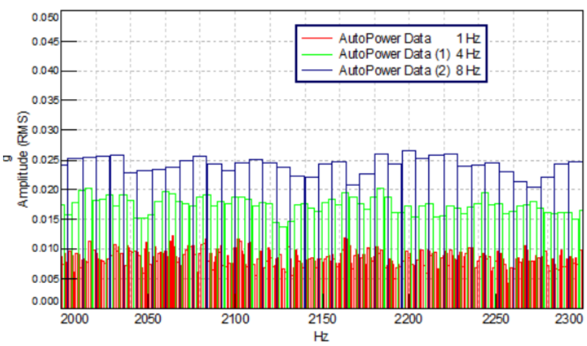

FIGURE A.10: Data block representation of the three autopower linear functions [6].

Furthermore, the spectral lines are key to get a better understanding about the origin of the different amplitudes. Spectral lines are discrete points in the frequency domain used to digitize the spectrum. Using block outlines as in figure A.10, the difference in the three measurements is more obvious. For a spectral resolution of 8Hz, as the number of discretisations is lower, there are less spectral lines. Moreover, the same amount of data has to be distributed in the different spectral lines resulting in storing more data per line which leads to a higher amplitude. The opposite happens with the 1Hz spectral resolution function which stores less data per spectral line due to its finer discretisation.

The apparent difference in the three autopower spectrum is solved by the implementation of the Power Spectral Density function. PSD is the responsible to normalise the amplitudes of each autopower function by the frequency resolution as shown in figure A.11. The term normalising means dividing the amplitude of each spectral line by the frequency resolution [6].

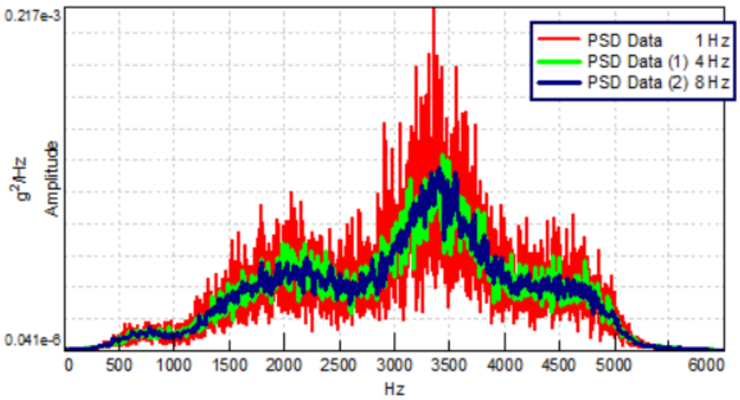

FIGURE A.11: Power Spectral Density function of the three autopower spectrum measured [6].

A.3.2.1 Equation of PSD using two sine waves

The frequency content of a random variable x(t) is represented by the power spectral density $W_x(f)$, defined as the mean-square response of an ideal narrow-band filter to x(t), divided by the bandwidth Δf of the filter in the limit as $\Delta f \longrightarrow 0$ at frequency [24]. Following this definition, the power spectral density can be computed as the following:

$$W_x(f) = lim_{\Delta f \longrightarrow 0} \frac{\bar{x^2}_{\Delta f}}{\Delta f} \tag{A.7}$$

$$\bar{x^2} = \int_0^\infty W_x(f)\ df \tag{A.8}$$

Moreover, the power spectral density can also be computed using Fourier series over a finite period of time (T) [24]. First, considering that the Fourier series is

$$x(t) = \bar{x} + \sum_{n=1}^{\infty} A_n \cos(2\pi f_n t) + \sum_{n=1}^{\infty} B_n \sin(2\pi f_n t) \tag{A.9}$$

where $f_n = n/T$ and the coefficients of the Fourier series are obtained from the equations below.

$$A_n = \frac{2}{T}\int_0^T x(t)\cos(2\pi f_n t)\ dt \tag{A.10}$$

$$B_n = \frac{2}{T}\int_0^T x(t)\sin(2\pi f_n t)\ dt \tag{A.11}$$

The power spectral density can be computed as the following.

$$\begin{aligned}\bar{x^2} = \frac{1}{T}\int_0^T &\left[\bar{x} + \sum_{n=1}^{\infty}\left(A_n\cos(2\pi f_n t) + B_n \sin(2\pi f_n t)\right)\right]\cdot \\ &\cdot\left[\bar{x} + \sum_{m=1}^{\infty}\left(A_m\cos(2\pi f_m t) + B_m \sin(2\pi f_m t)\right)\right]\ dt\end{aligned} \tag{A.12}$$

$$\bar{x^2} = \frac{1}{T}\int_0^T \left[(\bar{x})^2 + \sum_{n=1}^{\infty}\left(A_n^2\cos^2(2\pi f_n t) + B_n^2 \sin^2(2\pi f_n t)\right)\right]\ dt \tag{A.13}$$

$$\bar{x^2} = (\bar{x})^2 + \sum_{n=1}^{\infty}\frac{1}{2}\left[A_n^2 + B_n^2\right] \tag{A.14}$$

Then, using equation A.8 and considering that $\Delta f = 1/T$, the power spectral density RMS can be approximated by [24]

$$W_x(f_n) \approx \frac{T}{2}\left[A_n^2 + B_n^2\right] \tag{A.15}$$

A.3.3 Root-Mean-Square Acceleration (G_{RMS})

The Root-Mean-Square Acceleration [25] is the square root of the are under the PSD curve. However, in order to understand its physical meaning, G_{RMS} can be seen as the average of the square of the acceleration over time. Also, by the use of the mean square, the G_{RMS} is always positive.

Furthermore, if the acceleration measured is a pure sinusoid as in a steady-state vibration the Root-Mean-Square Acceleration would be $1/\sqrt{2}$ times the peak value.

In contrast, if a Gaussian random time history is considered, the root-mean square acceleration will be associated with the statistical properties of the function. Those statistical properties have been extracted from reference [25] and are the following:

- *68.3% of the time, the acceleration time history would have peaks that would not exceed the ± 1 sigma accelerations.*
- *95.4% of the time, the acceleration time history would have peaks that would not exceed the ± 2 sigma accelerations.*
- *99.7% of the time, the acceleration time history would have peaks that would not exceed the ± 3 sigma accelerations.*

Finally, table A.1 presents a summary of the different amplitudes and the G_{RMS} value for each autopower type considering a sine signal.

TABLE A.1: Summary of the autopower types and the amplitude modes and outputs where A is the value of the amplitude of a sinusoide [5].

Autopower Type	**Amplitude Mode**	**Amplitude Output**
Power	Peak	A^2
Power	Peak-to-peak	$4A^2$
Power	RMS	$A^2/2$
Linear	Peak	A
Linear	Peak-to-peak	$2A$
Linear	RMS	$A/\sqrt{2}$
PSD	Peak	$A^2/\Delta f$
PSD	Peak-to-peak	$4A^2/\Delta f$
PSD	RMS	$A^2/(2\Delta f)$

Appendix B

Mathematical formulation

B.1 Thin plate and flat shell theories

A plate is defined as a flat solid whose thickness is much smaller than its other dimensions and, in contrast, a shell is an extension of a plate to a nonplanar surface. The non-coplanarity introduces axial (membrane) forces in addition to flexural (bending and shear) forces, thus providing a higher overall structural strength.

The most commonly used thin plate and flat shell theories are three: the Kirchhoff thin plate theory proposed in 1850, the Reissner-Mindlin plate theory proposed in 1945 by Reissner and in 1951 by Mindlin and, finally, the Reissner-Mindlin flat shell theory. The three theories share almost the same assumptions and just differ in a few aspects.

The hypothesis of Kirchhoff thin plate theory extracted from reference [7] are the following:

1. *The points along a normal to the middle plane have the same vertical displacement (the thickness does not change during deformation).*
2. *The normal stress $\sigma_{z'}$ is negligible (plane stress assumption).*
3. *A straight line normal to the undeformed middle plane remains straight to the deformed middle plane.*
4. *In the points belonging to the middle plane (z = 0) $\bar{u}_{x'} = \bar{u}_{y'} = 0$. In other words, the points on the middle plane only move vertically.*
5. *A straight line normal to the undeformed middle plane remains normal to the deformed middle plane.*

Moreover, Kirchhoff thin plate theory is restricted to thin plates whose relation between thickness and an average edge is smaller than 0.1. This problem can be overcome by using the Reissner-Mindlin plate theory.

Reissner-Mindlin plate theory shares all the assumptions of Kirchhoff plate theory except for hypothesis number 5, a straight line normal to the undeformed middle plane remains straight but not necessarily orthogonal to the middle plane after deformation as shown in figure B.1. In this case, the hypothesis for Reissner-Mindlin plate theory extracted from reference [7] are:

1. *The points along a normal to the middle plane have the same vertical displacement (the thickness does not change during deformation).*
2. *The normal stress $\sigma_{z'}$ is negligible (plane stress assumption).*

3. *A straight line normal to the undeformed middle plane remains straight to the deformed middle plane.*

4. *In the points belonging to the middle plane (z = 0)* $\bar{u}_{x'} = \bar{u}_{y'} = 0$. *In other words, the points on the middle plane only move vertically.*

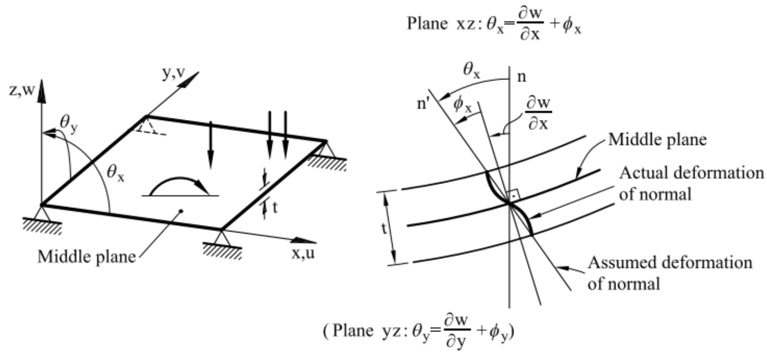

FIGURE B.1: Reissner-Mindlin plate theory [7].

Finally, flat shell elements are a direct extension of the Reissner-Mindlin plate theory, however, as a point on the middle plane do not move only vertically, assumption 4 is incorrect in this theory. In other words, Reissner-Mindlin flat shell theory's hypothesis are [7]:

1. *The points along a normal to the middle plane have the same vertical displacement (the thickness does not change during deformation).*

2. *The normal stress* $\sigma_{z'}$ *is negligible (plane stress assumption).*

3. *A straight line normal to the undeformed middle plane remains straight to the deformed middle plane.*

B.2 Reissner-Mindlin flat shell theory

Due to the curvature of the middle surface of an arbitrary shaped shell, the governing equations result to be quite complex, however, Reissner-Mindlin flat shell theory describes a way of overcoming this complexity by considering that the shell is composed by a number of folded plates. This theory has been extracted from references [7] and [8].

B.2.1 Local displacements

In order to obtain the local displacements field a rectangular shell will be considered and the middle plane of the flat shell will be taken as the reference surface for the kinematic description

[7]. This base will be formed by a vector normal to the middle plane (z'), and two arbitrary orthogonal directions contained in it (x' and y') as shown in figure B.2.

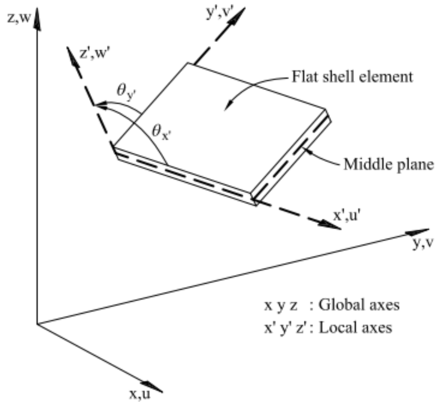

FIGURE B.2: Local and global axes of a rectangular flat shell [7].

Then, considering the assumptions previously made about the Reissner-Mindlin flat shell theory and with the help of figure B.3 which shows the local displacements of a flat shell, the displacements of a point A can be expressed as [7]:

$$u_{x'} = \bar{u}_{x'} + z'\theta_{y'} \tag{B.1}$$

$$u_{y'} = \bar{u}_{y'} + z'\theta_{x'} \tag{B.2}$$

$$u_{z'} = \bar{u}_{z'} \tag{B.3}$$

where $\bar{u}_{x'}$, $\bar{u}_{y'}$ and $\bar{u}_{z'}$ are the displacements of point O over the middle plane. Finally, the local displacements expressed in a vector form are [8]:

$$\{\mathbf{u}'\} = \begin{Bmatrix} u_{x'} \\ u_{y'} \\ u_{z'} \end{Bmatrix} = \begin{bmatrix} 1 & 0 & 0 & 0 & z' & 0 \\ 0 & 1 & 0 & -z' & 0 & 0 \\ 0 & 0 & 1 & 0 & 0 & 0 \end{bmatrix} \begin{Bmatrix} \bar{u}_{x'} \\ \bar{u}_{y'} \\ \bar{u}_{z'} \\ \theta_{x'} \\ \theta_{y'} \\ \theta_{z'} \end{Bmatrix} = [\mathbf{D}(z')]\{\bar{\mathbf{u}}'(x', y')\} \tag{B.4}$$

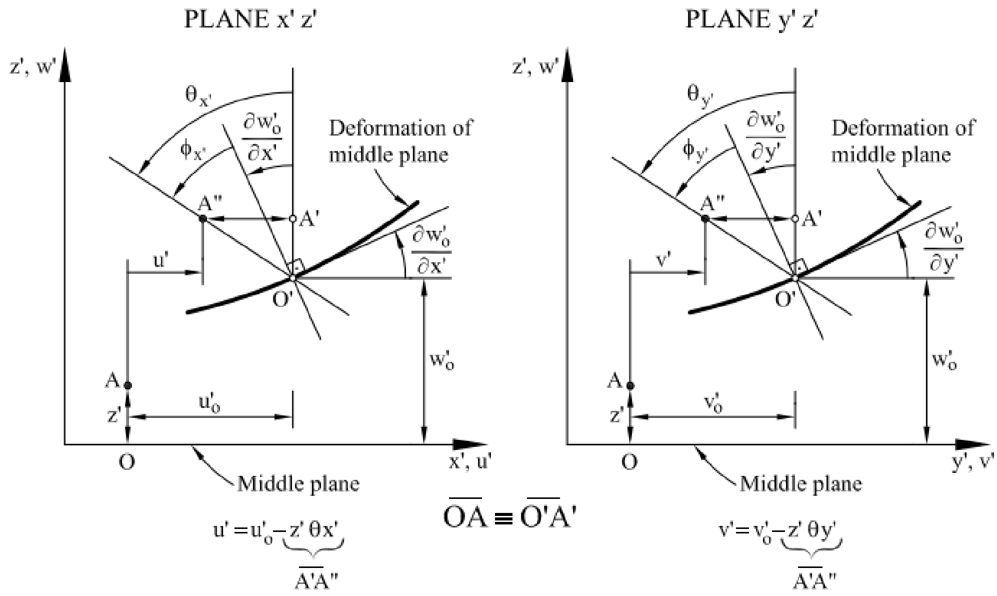

FIGURE B.3: Local displacements in a flat shell element. Reissner-Mindlin plate theory [7].

B.2.2 Local strain

Due to the plane stress assumption ($\sigma_{z'}$), the normal strain $\varepsilon_{z'}$ does not play any role in the internal work [7]. The local strain field for a flat shell element is the following:

$$\varepsilon_{x'x'} = \frac{\partial u_{x'}}{\partial x'} = \frac{\partial \bar{u}_{x'}}{\partial x'} + z'\frac{\partial \theta_{y'}}{\partial x'} \tag{B.5}$$

$$\varepsilon_{y'y'} = \frac{\partial u_{y'}}{\partial y'} = \frac{\partial \bar{u}_{y'}}{\partial y'} + z'\frac{\partial \theta_{x'}}{\partial y'} \tag{B.6}$$

$$\varepsilon_{z'z'} = \frac{\partial u_{z'}}{\partial z'} = 0 \tag{B.7}$$

$$\gamma_{x'y'} = \frac{\partial u_{y'}}{\partial x'} + \frac{\partial u_{x'}}{\partial y'} = \frac{\partial \bar{u}_{y'}}{\partial x'} + \frac{\partial \bar{u}_{x'}}{\partial y'} + z'\left(\frac{\partial \theta_{y'}}{\partial y'} - \frac{\partial \theta_{x'}}{\partial x'}\right) \tag{B.8}$$

$$\gamma_{x'z'} = \frac{\partial u_{z'}}{\partial x'} + \frac{\partial u_{x'}}{\partial z'} = \frac{\partial \bar{u}_{z'}}{\partial x'} + \theta_{y'} \tag{B.9}$$

$$\gamma_{y'z'} = \frac{\partial u_{z'}}{\partial y'} + \frac{\partial u_{y'}}{\partial z'} = \frac{\partial \bar{u}_{z'}}{\partial y'} - \theta_{x'} \tag{B.10}$$

Finally, the local strains expressed in a vector form are [8]:

$$\{\boldsymbol{\varepsilon}'\} = \begin{Bmatrix} \varepsilon_{x'x'} \\ \varepsilon_{y'y'} \\ \gamma_{x'y'} \\ \gamma_{x'z'} \\ \gamma_{y'z'} \\ \theta_{z'} \end{Bmatrix} = \begin{bmatrix} 1 & 0 & 0 & 0 & 0 & 0 & z & 0 & 0 \\ 0 & 1 & 0 & 0 & 0 & 0 & 0 & -z & 0 \\ 0 & 0 & 1 & 0 & 0 & 0 & 0 & 0 & z \\ 0 & 0 & 0 & 1 & 0 & 0 & 0 & 0 & 0 \\ 0 & 0 & 0 & 0 & 1 & 0 & 0 & 0 & 0 \\ 0 & 0 & 0 & 0 & 0 & 1 & 0 & 0 & 0 \end{bmatrix} \begin{Bmatrix} \bar{u}_{x',x'} \\ \bar{u}_{y',y'} \\ \bar{u}_{x',y'} + \bar{u}_{y',x'} \\ \bar{u}_{z',x'} + \theta_{y'} \\ \bar{u}_{z',y'} - \theta_{x'} \\ \theta_{z'} \\ \theta_{y',x'} \\ \theta_{x',y'} \\ \theta_{y',y'} - \theta_{x',x'} \end{Bmatrix} = [\mathbf{S}(z')]\{\bar{\boldsymbol{\varepsilon}}'(x',y')\} \tag{B.11}$$

in which $\theta_{z'}$ is a fictitious strain component.

B.2.3 Local stress

In order to introduce the plane stress condition ($\sigma_{z'} = 0$), the stress-strain relationship is expressed in the local coordinates [7]. After eliminating $\varepsilon_{z'}$, the relation between the local stresses and the local strains in the vector form can be defined as the following.

$$\{\boldsymbol{\sigma}'\} = \begin{Bmatrix} \sigma_{x'x'} \\ \sigma_{y'y'} \\ \tau_{x'y'} \\ \tau_{x'z'} \\ \tau_{y'z'} \\ \sigma_t^* \end{Bmatrix} = \begin{bmatrix} C_{11} & C_{12} & 0 & 0 & 0 & 0 \\ C_{21} & C_{22} & 0 & 0 & 0 & 0 \\ 0 & 0 & C_{33} & 0 & 0 & 0 \\ 0 & 0 & 0 & C_{44} & 0 & 0 \\ 0 & 0 & 0 & 0 & C_{55} & 0 \\ 0 & 0 & 0 & 0 & 0 & C_t^* \end{bmatrix} \begin{Bmatrix} \varepsilon_{x'x'} \\ \varepsilon_{y'y'} \\ \gamma_{x'y'} \\ \gamma_{x'z'} \\ \gamma_{y'z'} \\ \theta_{z'} \end{Bmatrix} = [\mathbf{C}']\{\boldsymbol{\varepsilon}'\} \tag{B.12}$$

in which the constitutive matrices are [8]

$$[\mathbf{C}'_p] = \begin{bmatrix} C_{11} & C_{12} & 0 \\ C_{21} & C_{22} & 0 \\ 0 & 0 & C_{33} \end{bmatrix} = \frac{E}{1-\nu^2} \begin{bmatrix} 1 & \nu & 0 \\ \nu & 1 & 0 \\ 0 & 0 & \frac{1-\nu}{2} \end{bmatrix} \tag{B.13}$$

$$[\mathbf{C}'_s] = k_s \begin{bmatrix} C_{44} & 0 \\ 0 & C_{55} \end{bmatrix} = k_s G \begin{bmatrix} 1 & 0 \\ 0 & 1 \end{bmatrix} = k_s \cdot \frac{E}{2(1+\nu)} \begin{bmatrix} 1 & 0 \\ 0 & 1 \end{bmatrix} \tag{B.14}$$

where E is the Young's modulus, ν the Poisson's ratio, G the shear modulus and $k_s = 5/6$ and is a shear correction factor as shown in figure B.4.

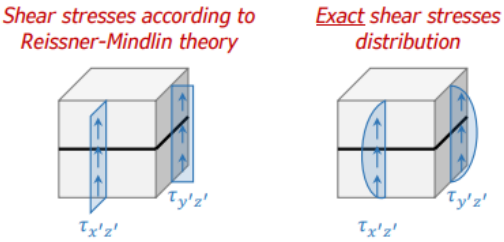

FIGURE B.4: Transverse shear stress distribution across the shell thickness [8].

B.2.4 Internal forces between plates

Then, the resultant internal force vector obtained as an integration of the stress vector at a point of the shell middle plane is

$$\{\hat{\mathbf{f}}'_{int}\} = \begin{Bmatrix} f_{x'} \\ f_{y'} \\ q_{x'y'} \\ q_{x'z'} \\ q_{y'z'} \\ m^*_{z'} \\ m_{y'} \\ m_{x'} \\ m_{x'y'} \end{Bmatrix} = \int_{-h/2}^{h/2} \begin{Bmatrix} \sigma_{x'x'} \\ \sigma_{y'y'} \\ \tau_{x'y'} \\ \tau_{x'z'} \\ \tau_{y'z'} \\ \sigma^*_t \\ z'\sigma_{x'x'} \\ -z'\sigma_{y'y'} \\ z'\tau_{x'y'} \end{Bmatrix} dz' = \int_{-h/2}^{h/2} \begin{bmatrix} 1 & 0 & 0 & 0 & 0 & 0 \\ 0 & 1 & 0 & 0 & 0 & 0 \\ 0 & 0 & 1 & 0 & 0 & 0 \\ 0 & 0 & 0 & 1 & 0 & 0 \\ 0 & 0 & 0 & 0 & 1 & 0 \\ 0 & 0 & 0 & 0 & 0 & 1 \\ z' & 0 & 0 & 0 & 0 & 0 \\ 0 & -z' & 0 & 0 & 0 & 0 \\ 0 & 0 & z' & 0 & 0 & 0 \end{bmatrix} \begin{Bmatrix} \sigma_{x'x'} \\ \sigma_{y'y'} \\ \tau_{x'y'} \\ \tau_{x'z'} \\ \tau_{y'z'} \\ \sigma^*_t \end{Bmatrix} dz' \tag{B.15}$$

$$\{\hat{\mathbf{f}}'_{int}\} = \int_{-h/2}^{h/2} [\mathbf{S}(z')]^T \{\boldsymbol{\sigma}'\} dz' \tag{B.16}$$

in which h corresponds to the shell thickness. Moreover, the resultant stresses have units of moment or force per unit width of the shell surface. Figures B.7 and B.6 present the sign convention for the descomposed internal forces due to plane stresses and shear stresses respectively.

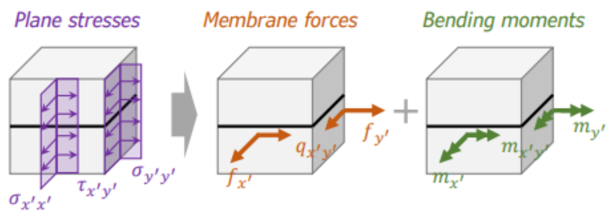

FIGURE B.5: Sign convention for the descomposed internal forces due to plane stresses [8].

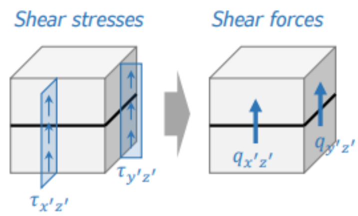

FIGURE B.6: Sign convention for the descomposed internal forces due to shear stresses [8].

B.2.5 Equilibrium equation

The equilibrium equation of a flat shell presented in the strong form is

$$\{\dot{\mathbf{p}}'\} = [\boldsymbol{\nabla}_{x'}] \cdot \{\boldsymbol{\sigma}'\} + \rho\{\mathbf{b}'\} + \{\mathbf{q}'\} \tag{B.17}$$

where $\{\dot{\mathbf{p}}'\}' = \rho\{\dot{\mathbf{u}}'\}$ is the linear momentum, ρ is the density, $\{\boldsymbol{\sigma}'\}$ is the local stress, $\{\mathbf{b}'\}$ are external body forces and $\{\mathbf{q}'\}$ are volume forces [8]. The boundary conditions of the problem are the prescribed displacements $\mathbf{u}'_p$ and the external traction forces $\mathbf{t}'$.

$$\mathbf{u}'_p = \mathbf{u}'|_{x'\epsilon\Gamma_u} \qquad\qquad \mathbf{t}' = \boldsymbol{\sigma}' \cdot \hat{\mathbf{n}}|_{x'\epsilon\Gamma_\sigma} \tag{B.18}$$

Furthermore, the principle of virtual work expressed as the weak form of the problem for all $\mathbf{u}'_p = 0$ is

$$\underbrace{\int_\Omega \{\delta\boldsymbol{\varepsilon}'\}^T\{\boldsymbol{\sigma}'\}d\Omega}_{Stiffness\ term} + \underbrace{\int_\Omega \{\delta\mathbf{u}'\}^T\rho\{\ddot{\mathbf{u}}'\}d\Omega}_{Inertial\ term} = \underbrace{\int_\Omega \{\delta\mathbf{u}'\}^T\left(\rho\{\mathbf{b}'\} + \{\mathbf{q}'\}\right)d\Omega}_{External\ body\ and\ volume\ forces} + \underbrace{\int_{\Gamma_\sigma} \{\delta\mathbf{u}'\}^T\{\mathbf{t}'\}d\Gamma_\sigma}_{External\ surface\ forces} \tag{B.19}$$

Focusing on each term of the previous equation and considering an isotropic material and the algebraic equations B.4, B.11 and B.12 previously obtained, the following expressions can be derived.

- **Stiffness term**

$$\int_\Omega \{\delta\varepsilon'\}^T\{\boldsymbol{\sigma}'\}d\Omega = \int_\Omega \{\delta\varepsilon'\}^T[\mathbf{C}']\{\delta\varepsilon'\}d\Omega = \int_S \{\delta\bar{\varepsilon}'\}^T \left(\int_{-h/2}^{h/2} [\mathbf{S}]^T[\mathbf{C}'][\mathbf{S}]dz'\right)\{\delta\bar{\varepsilon}'\}dS \tag{B.20}$$

$$[\bar{\mathbf{C}}'] = \int_{-h/2}^{h/2} [\mathbf{S}]^T [\mathbf{C}'] [\mathbf{S}] dz' \tag{B.21}$$

$$[\bar{\mathbf{C}}'] = h \begin{bmatrix} C_{11} & C_{12} & 0 & 0 & 0 & 0 & z_0' C_{11} & -z_0' C_{12} & 0 \\ C_{21} & C_{22} & 0 & 0 & 0 & 0 & z_0' C_{21} & -z_0' C_{22} & 0 \\ 0 & 0 & C_{33} & 0 & 0 & 0 & 0 & 0 & z_0' C_{33} \\ 0 & 0 & 0 & C_{44} & 0 & 0 & 0 & 0 & 0 \\ 0 & 0 & 0 & 0 & C_{55} & 0 & 0 & 0 & 0 \\ 0 & 0 & 0 & 0 & 0 & C_t^* & 0 & 0 & 0 \\ z_0' C_{11} & z_0' C_{12} & 0 & 0 & 0 & 0 & r_h'^2 C_{11} & r_h'^2 C_{12} & 0 \\ -z_0' C_{21} & -z_0' C_{22} & 0 & 0 & 0 & 0 & r_h'^2 C_{21} & r_h'^2 C_{22} & 0 \\ 0 & 0 & z_0' C_{33} & 0 & 0 & 0 & 0 & 0 & r_h'^2 C_{33} \end{bmatrix} \tag{B.22}$$

where the constants presented in the previous expression are equal to

$$C_{11} = C_{22} = \frac{E}{1-\nu^2} \qquad r_h'^2 = \frac{1}{h} \int_{-h/2}^{h/2} z'^2 dz' = \frac{h^2}{12} \tag{B.23}$$

$$C_{12} = C_{21} = \frac{E\nu}{1-\nu^2} \qquad z_0' = \frac{1}{h} \int_{-h/2}^{h/2} z' dz' = 0 \tag{B.24}$$

$$C_{33} = C_{44} = C_{55} = C_t^* = \frac{E}{2(1+\nu)} = G \tag{B.25}$$

As the center of mass is located on the origin of the local reference frame, z_0' is null and the bending and membrane stresses and strains are uncoupled. That leads to a simplification of equation B.22.

$$[\bar{\mathbf{C}}'] = h \begin{bmatrix} C_{11} & C_{12} & 0 & 0 & 0 & 0 & 0 & 0 & 0 \\ C_{21} & C_{22} & 0 & 0 & 0 & 0 & 0 & 0 & 0 \\ 0 & 0 & C_{33} & 0 & 0 & 0 & 0 & 0 & 0 \\ 0 & 0 & 0 & C_{44} & 0 & 0 & 0 & 0 & 0 \\ 0 & 0 & 0 & 0 & C_{55} & 0 & 0 & 0 & 0 \\ 0 & 0 & 0 & 0 & 0 & C_t^* & 0 & 0 & 0 \\ 0 & 0 & 0 & 0 & 0 & 0 & r_h'^2 C_{11} & r_h'^2 C_{12} & 0 \\ 0 & 0 & 0 & 0 & 0 & 0 & r_h'^2 C_{21} & r_h'^2 C_{22} & 0 \\ 0 & 0 & 0 & 0 & 0 & 0 & 0 & 0 & r_h'^2 C_{33} \end{bmatrix} \tag{B.26}$$

Finally, equation B.20 can be expressed as

$$\int_\Omega \{\delta\boldsymbol{\varepsilon}'\}^T\{\boldsymbol{\sigma}'\}d\Omega = \int_S \{\delta\bar{\boldsymbol{\varepsilon}}'\}^T[\bar{\mathbf{C}}'][\{\delta\bar{\boldsymbol{\varepsilon}}'\}dS \tag{B.27}$$

- **Inertial term**

$$\int_\Omega \{\delta\mathbf{u}'\}^T\rho\{\ddot{\mathbf{u}}'\}d\Omega = \int_\Omega \{\delta\bar{\mathbf{u}}'\}^T[\mathbf{D}]^T\rho[\mathbf{D}]\{\ddot{\mathbf{u}}'\}d\Omega = \int_S \{\delta\bar{\mathbf{u}}'\}^T\left(\int_{-h/2}^{h/2}[\mathbf{D}]^T\rho[\mathbf{D}]dz'\right)\{\ddot{\mathbf{u}}'\}dS \tag{B.28}$$

For isotropic material where the density is constant over the thickness, the integrate in thickness direction can be expressed as

$$[\bar{\boldsymbol{\rho}}'] = \int_{-h/2}^{h/2}[\mathbf{D}]^T\rho[\mathbf{D}]dz' = \rho h\begin{bmatrix} 1 & 0 & 0 & 0 & -z_0' & 0 \\ 0 & 1 & 0 & -z_0' & 0 & 0 \\ 0 & 0 & 1 & 0 & 0 & 0 \\ 0 & -z_0' & 0 & r_h'^2 & 0 & 0 \\ -z_0' & 0 & 0 & 0 & r_h'^2 & 0 \\ 0 & 0 & 0 & 0 & 0 & 0 \end{bmatrix} \tag{B.29}$$

And, as what happen to the stiffness term, $-z_0'$ is null when considering that the center of mass is located on the origin of the reference frame, so the previous equation can be simplified.

$$[\bar{\boldsymbol{\rho}}'] = \rho h\begin{bmatrix} 1 & 0 & 0 & 0 & 0 & 0 \\ 0 & 1 & 0 & 0 & 0 & 0 \\ 0 & 0 & 1 & 0 & 0 & 0 \\ 0 & 0 & 0 & r_h'^2 & 0 & 0 \\ 0 & 0 & 0 & 0 & r_h'^2 & 0 \\ 0 & 0 & 0 & 0 & 0 & 0 \end{bmatrix} \tag{B.30}$$

So, equation B.28 can be expressed as

$$\int_\Omega \{\delta\mathbf{u}'\}^T\rho\{\ddot{\mathbf{u}}'\}d\Omega = \int_S \{\delta\bar{\mathbf{u}}'\}^T[\bar{\boldsymbol{\rho}}']\{\ddot{\mathbf{u}}'\}dS \tag{B.31}$$

- **External body and volume forces**

$$\int_\Omega \{\delta \mathbf{u'}\}^T \left(\rho\{\mathbf{b'}\} + \{\mathbf{q'}\}\right) d\Omega = \int_\Omega \{\delta \bar{\mathbf{u}}'\}^T [\mathbf{D}]^T \left(\rho\{\mathbf{b'}\} + \{\mathbf{q'}\}\right) d\Omega \tag{B.32}$$

$$= \int_S \{\delta \bar{\mathbf{u}}'\}^T \left(\int_{-h/2}^{h/2} [\mathbf{D}]^T \left(\rho\{\mathbf{b'}\} + \{\mathbf{q'}\}\right) dz'\right) dS \tag{B.33}$$

Considering that **b'** is uniform over the thickness, the force per unit of volume can be computed as

$$\{\bar{\mathbf{f}}'\} = \int_{-h/2}^{h/2} [\mathbf{D}]^T \left(\rho\{\mathbf{b'}\} + \{\mathbf{q'}\}\right) dz' = [\bar{\boldsymbol{\rho}}'] \begin{Bmatrix} \bar{b}_{x'} \\ \bar{b}_{y'} \\ \bar{b}_{z'} \\ 0 \\ 0 \\ 0 \end{Bmatrix} + \begin{Bmatrix} \bar{q}_{x'} \\ \bar{q}_{y'} \\ \bar{q}_{z'} \\ \bar{m}_{x'} \\ \bar{m}_{y'} \\ 0 \end{Bmatrix} = [\bar{\boldsymbol{\rho}}']\{\bar{\mathbf{b}}'\} + \{\bar{\mathbf{q}}'\} \tag{B.34}$$

Where $\{\bar{\mathbf{q}'}\}$ are the distributed loads over the shell and can be expressed as

$$\bar{q}_{x'} = \int_{-h/2}^{h/2} q_{x'} dz' \qquad \bar{m}_{x'} = \int_{-h/2}^{h/2} -z' q_{y'} dz' \tag{B.35}$$

$$\bar{q}_{y'} = \int_{-h/2}^{h/2} q_{y'} dz' \qquad \bar{m}_{y'} = \int_{-h/2}^{h/2} z' q_{x'} dz' \tag{B.36}$$

$$\bar{q}_{z'} = \int_{-h/2}^{h/2} q_{z'} dz' \tag{B.37}$$

Finally, equation B.32 can be expressed as

$$\int_\Omega \{\delta \mathbf{u'}\}^T \left(\rho\{\mathbf{b'}\} + \{\mathbf{q'}\}\right) d\Omega = \int_S \{\delta \bar{\mathbf{u}}'\}^T \left([\bar{\boldsymbol{\rho}}']\{\bar{\mathbf{b}}'\} + \{\bar{\mathbf{q}}'\}\right) dS \tag{B.38}$$

- **External surface forces**

$$\int_{\Gamma_\sigma} \{\delta \mathbf{u}'\}^T \{\mathbf{t}'\} d\Gamma_\sigma = \underbrace{\int_S \{\delta \mathbf{u}'\}^T \{\mathbf{t}'_S\} dS}_{Distributed\ loads\ over\ surfaces} + \underbrace{\int_l \{\delta \mathbf{u}'\}^T \{\mathbf{t}'_l\} dl}_{Distributed\ loads\ over\ lines} \tag{B.39}$$

$$= \int_{S^+} \{\delta \mathbf{u}'_+\}^T \{\mathbf{t}'_+\} dS + \int_{S^-} \{\delta \mathbf{u}'_-\}^T \{\mathbf{t}'_-\} dS + \int_l \{\delta \mathbf{u}'\}^T \{\mathbf{t}'_l\} dl \tag{B.40}$$

$$= \int_S \{\delta \bar{\mathbf{u}}'\}^T \{\bar{\mathbf{t}}'_S\} dS + \int_l \{\delta \bar{\mathbf{u}}'_l\}^T \left(\int_{-h/2}^{h/2} [\mathbf{D}]^T \{\mathbf{t}'_l\} dz' \right) dl \tag{B.41}$$

$$= \int_S \{\delta \bar{\mathbf{u}}'\}^T \{\bar{\mathbf{t}}'_S\} dS + \int_l \{\delta \bar{\mathbf{u}}'_l\}^T \{\bar{\mathbf{f}}'_l\} dl \tag{B.42}$$

Then, substituting each term for the expressions obtained in equations B.27, B.31, B.38 and B.42 in equation B.19, the resulting system yields

$$\int_S \{\delta \bar{\varepsilon}'\}^T [\bar{\mathbf{C}}'] \{\delta \bar{\varepsilon}'\} dS + \int_S \{\delta \bar{\mathbf{u}}'\}^T [\bar{\boldsymbol{\rho}}'] \{\ddot{\mathbf{u}}'\} dS = \int_S \{\delta \bar{\mathbf{u}}'\}^T \left([\bar{\boldsymbol{\rho}}'] \{\bar{\mathbf{b}}'\} + \{\bar{\mathbf{q}}'\} \right) dS +$$
$$+ \int_S \{\delta \bar{\mathbf{u}}'\}^T \{\bar{\mathbf{t}}'_S\} dS + \int_l \{\delta \bar{\mathbf{u}}'_l\}^T \{\bar{\mathbf{f}}'_l\} dl + \{\delta \bar{\mathbf{u}}'(x^{(i)})\}^T \{\hat{\mathbf{F}}^{(i)}\} \tag{B.43}$$

Reorganising the terms, the previous expression can be written as

$$\int_S \{\delta \bar{\varepsilon}'\}^T [\bar{\mathbf{C}}'] \{\delta \bar{\varepsilon}'\} dS + \int_S \{\delta \bar{\mathbf{u}}'\}^T [\bar{\boldsymbol{\rho}}'] \{\ddot{\mathbf{u}}'\} dS = \int_S \{\delta \bar{\mathbf{u}}'\}^T \left([\bar{\boldsymbol{\rho}}'] \{\bar{\mathbf{b}}'\} + \{\bar{\mathbf{q}}'\} + \{\bar{\mathbf{t}}'_S\} \right) dS +$$
$$+ \int_l \{\delta \bar{\mathbf{u}}'_l\}^T \{\bar{\mathbf{f}}'_l\} dl + \{\delta \bar{\mathbf{u}}'(x^{(i)})\}^T \{\hat{\mathbf{F}}^{(i)}\} \tag{B.44}$$

Then, considering that the forces applied on the surfaces of the flat shell can be known as $\{\bar{\mathbf{f}}'_S\}$, equation B.44 can be expressed as

$$\int_S \{\delta \bar{\varepsilon}'\}^T [\bar{\mathbf{C}}'] \{\delta \bar{\varepsilon}'\} dS + \int_S \{\delta \bar{\mathbf{u}}'\}^T [\bar{\boldsymbol{\rho}}'] \{\ddot{\mathbf{u}}'\} dS = \int_S \{\delta \bar{\mathbf{u}}'\}^T \{\bar{\mathbf{f}}'_S\} dS + \int_l \{\delta \bar{\mathbf{u}}'_l\}^T \{\bar{\mathbf{f}}'_l\} dl + \{\delta \bar{\mathbf{u}}'(x^{(i)})\}^T \{\hat{\mathbf{F}}^{(i)}\} \tag{B.45}$$

Finally, equation B.45 is another way of expressing the weak form.

B.2.6 Stiffness Term

As shown in equation B.27, the stiffness term can be defined as

$$\int_S \{\delta\bar{\varepsilon}'\}^T[\bar{\mathbf{C}}']\{\delta\bar{\varepsilon}'\}dS \tag{B.46}$$

Moreover, this term can be further decomposed into different components with physical meaning [8].

$$\begin{aligned}\int_S \{\delta\bar{\varepsilon}'\}^T[\bar{\mathbf{C}}']\{\delta\bar{\varepsilon}'\}dS = \underbrace{\int_S \{\delta\bar{\varepsilon}'_m\}^T[\bar{\mathbf{C}}'_m]\{\delta\bar{\varepsilon}'_m\}dS}_{Membrane\ component} + \underbrace{\int_S \{\delta\bar{\varepsilon}'_b\}^T[\bar{\mathbf{C}}'_b]\{\delta\bar{\varepsilon}'_b\}dS}_{Bending\ component} + \\ + \underbrace{\int_S \{\delta\bar{\varepsilon}'_s\}^T[\bar{\mathbf{C}}'_s]\{\delta\bar{\varepsilon}'_s\}dS}_{Shear\ component} + \underbrace{\int_S \{\delta\bar{\varepsilon}'_t\}^T[\bar{\mathbf{C}}'_t]\{\delta\bar{\varepsilon}'_t\}dS}_{Fictitious\ component}\end{aligned} \tag{B.47}$$

Where the different terms of equation B.47 are

$$\{\bar{\varepsilon}'_m\} = \begin{Bmatrix} \bar{u}_{x',x'} \\ \bar{u}_{y',y'} \\ \bar{u}_{x',y'} + \bar{u}_{y',x'} \end{Bmatrix} \qquad [\bar{\mathbf{C}}'_m] = \frac{hE}{1-\nu^2}\begin{bmatrix} 1 & \nu & 0 \\ \nu & 1 & 0 \\ 0 & 0 & \frac{(1-\nu)}{2} \end{bmatrix} \tag{B.48}$$

$$\{\bar{\varepsilon}'_b\} = \begin{Bmatrix} \theta_{y',x'} \\ \theta_{x',y'} \\ \theta_{y',y'} - \theta_{x',x'} \end{Bmatrix} \qquad [\bar{\mathbf{C}}'_b] = \frac{h^3E}{12(1-\nu^2)}\begin{bmatrix} 1 & \nu & 0 \\ \nu & 1 & 0 \\ 0 & 0 & \frac{(1-\nu)}{2} \end{bmatrix} \tag{B.49}$$

$$\{\bar{\varepsilon}'_s\} = \begin{Bmatrix} \bar{u}_{z',x'} + \theta_{y'} \\ \bar{u}_{z',y'} - \theta_{x'} \end{Bmatrix} \qquad [\bar{\mathbf{C}}'_s] = \frac{5hE}{12(1+\nu)}\begin{bmatrix} 1 & 0 \\ 0 & 1 \end{bmatrix} \tag{B.50}$$

$$\{\bar{\varepsilon}'_t\} = \begin{Bmatrix} \theta_{z'} \end{Bmatrix} \qquad [\bar{\mathbf{C}}'_t] = \frac{5hE}{12(1+\nu)}\begin{bmatrix} 1 \end{bmatrix} \tag{B.51}$$

B.2.7 Quadrilateral elements integration

The case of study consists in a discretisation of a structure in quadrilateral shell elements whose shape functions and its derivative are [8]

$$N^{(e,1)}(\xi,\eta) = \frac{1}{4}(1-\xi)(1-\eta) \tag{B.52}$$
$$N^{(e,2)}(\xi,\eta) = \frac{1}{4}(1+\xi)(1-\eta) \tag{B.53}$$
$$N^{(e,3)}(\xi,\eta) = \frac{1}{4}(1+\xi)(1+\eta) \tag{B.54}$$
$$N^{(e,4)}(\xi,\eta) = \frac{1}{4}(1-\xi)(1+\eta) \tag{B.55}$$

$$N^{(e,1)}_{,\xi}(\xi,\eta) = -\frac{1}{4}(1-\eta) \qquad N^{(e,1)}_{,\eta}(\xi,\eta) = -\frac{1}{4}(1-\xi) \tag{B.56}$$
$$N^{(e,2)}_{,\xi}(\xi,\eta) = \frac{1}{4}(1-\eta) \qquad N^{(e,2)}_{,\eta}(\xi,\eta) = -\frac{1}{4}(1+\xi) \tag{B.57}$$
$$N^{(e,3)}_{,\xi}(\xi,\eta) = \frac{1}{4}(1+\eta) \qquad N^{(e,3)}_{,\eta}(\xi,\eta) = \frac{1}{4}(1+\xi) \tag{B.58}$$
$$N^{(e,4)}_{,\xi}(\xi,\eta) = -\frac{1}{4}(1+\eta) \qquad N^{(e,4)}_{,\eta}(\xi,\eta) = \frac{1}{4}(1-\xi) \tag{B.59}$$

Then, the jacobian matrix can be computed as the following [8]

$$[\mathbf{J}'^{(e)}] = \begin{bmatrix} \dfrac{\partial x'}{\partial \xi} & \dfrac{\partial y'}{\partial \xi} \\ \dfrac{\partial x'}{\partial \eta} & \dfrac{\partial y'}{\partial \eta} \end{bmatrix} = \sum_i \begin{Bmatrix} N^{(e,i)}_{,\xi}(\xi,\eta) \\ N^{(e,i)}_{,\eta}(\xi,\eta) \end{Bmatrix} \{\hat{\mathbf{x}}^{(e,i)}\}^T \tag{B.60}$$

So finally the shape functions expressed in local derivatives are

$$\begin{Bmatrix} N^{(e,i)}_{,x'} \\ N^{(e,i)}_{,y'} \end{Bmatrix} = [\mathbf{J}'^{(e)}]^{-1} \begin{Bmatrix} N^{(e,i)}_{,\xi} \\ N^{(e,i)}_{,\eta} \end{Bmatrix} \tag{B.61}$$

B.2.8 Stiffness and mass equations

Once computed $N^{(e,i)}$, $N^{(e,i)}_{,x'}$ and $N^{(e,i)}_{,y'}$, $[\mathbf{B}'^{(e)}_m]$, $[\mathbf{B}'^{(e)}_b]$, $[\mathbf{B}'^{(e)}_s]$ and $[\mathbf{B}'^{(e)}_t]$ can be calculated as following for each node i from 1 to 4.

$$[\mathbf{B}'^{(e,i)}_m] = \begin{bmatrix} N^{(e,i)}_{1,x'} & 0 & 0 & 0 & 0 & 0 \\ 0 & N^{(e,i)}_{1,y'} & 0 & 0 & 0 & 0 \\ N^{(e,i)}_{1,y'} & N^{(e,i)}_{1,x'} & 0 & 0 & 0 & 0 \end{bmatrix} \tag{B.62}$$

$$[\mathbf{B}'^{(e,i)}_b] = \begin{bmatrix} 0 & 0 & 0 & 0 & N^{(e,i)}_{4,x'} & 0 \\ 0 & 0 & 0 & N^{(e,i)}_{4,y'} & 0 & 0 \\ 0 & 0 & 0 & -N^{(e,i)}_{4,x'} & N^{(e,i)}_{4,y'} & 0 \end{bmatrix} \tag{B.63}$$

$$[\mathbf{B}'^{(e,i)}_s] = \begin{bmatrix} 0 & 0 & N^{(e,i)}_{1,x'} & 0 & N^{(e,i)}_{1} & 0 \\ 0 & 0 & N^{(e,i)}_{1,y'} & -N^{(e,i)}_{1} & 0 & 0 \end{bmatrix} \tag{B.64}$$

$$[\mathbf{B}'^{(e,i)}_t] = \begin{bmatrix} 0 & 0 & 0 & 0 & 0 & N^{(e,i)}_{1} \end{bmatrix} \tag{B.65}$$

and the corresponding elementary matrix are

$$[\mathbf{B}'^{(e)}_m] = \begin{bmatrix} [\mathbf{B}'^{(e,1)}_m] & [\mathbf{B}'^{(e,2)}_m] & [\mathbf{B}'^{(e,3)}_m] & [\mathbf{B}'^{(e,4)}_m] \end{bmatrix} \tag{B.66}$$

$$[\mathbf{B}'^{(e)}_b] = \begin{bmatrix} [\mathbf{B}'^{(e,1)}_b] & [\mathbf{B}'^{(e,2)}_b] & [\mathbf{B}'^{(e,3)}_b] & [\mathbf{B}'^{(e,4)}_b] \end{bmatrix} \tag{B.67}$$

$$[\mathbf{B}'^{(e)}_s] = \begin{bmatrix} [\mathbf{B}'^{(e,1)}_s] & [\mathbf{B}'^{(e,2)}_s] & [\mathbf{B}'^{(e,3)}_s] & [\mathbf{B}'^{(e,4)}_s] \end{bmatrix} \tag{B.68}$$

$$[\mathbf{B}'^{(e)}_t] = \begin{bmatrix} [\mathbf{B}'^{(e,1)}_t] & [\mathbf{B}'^{(e,2)}_t] & [\mathbf{B}'^{(e,3)}_t] & [\mathbf{B}'^{(e,4)}_t] \end{bmatrix} \tag{B.69}$$

Now it is time to compute the stiffness and the mass matrix using Gauss quadrature.

$$\begin{aligned}[\mathbf{K}_m^{(e)}] &= [\hat{\mathbf{R}}^{(e)}]^T \int_{S^{(e)}} [\mathbf{B}_m'^{(e)}]^T [\bar{\mathbf{C}}_m'^{(e)}][\mathbf{B}_m'^{(e)}] dS [\hat{\mathbf{R}}^{(e)}] \\ &= [\hat{\mathbf{R}}^{(e)}]^T \left(\sum_{k=1}^{N_G} w_k |\mathbf{J}'^{(e)}| [\mathbf{B}_m'^{(e)}]^T [\bar{\mathbf{C}}_m'^{(e)}][\mathbf{B}_m'^{(e)}] \right) [\hat{\mathbf{R}}^{(e)}] \end{aligned} \tag{B.70}$$

$$\begin{aligned}[\mathbf{K}_b^{(e)}] &= [\hat{\mathbf{R}}^{(e)}]^T \int_{S^{(e)}} [\mathbf{B}_b'^{(e)}]^T [\bar{\mathbf{C}}_b'^{(e)}][\mathbf{B}_b'^{(e)}] dS [\hat{\mathbf{R}}^{(e)}] \\ &= [\hat{\mathbf{R}}^{(e)}]^T \left(\sum_{k=1}^{N_G} w_k |\mathbf{J}'^{(e)}| [\mathbf{B}_b'^{(e)}]^T [\bar{\mathbf{C}}_b'^{(e)}][\mathbf{B}_b'^{(e)}] \right) [\hat{\mathbf{R}}^{(e)}] \end{aligned} \tag{B.71}$$

$$\begin{aligned}[\mathbf{K}_s^{(e)}] &= [\hat{\mathbf{R}}^{(e)}]^T \int_{S^{(e)}} [\mathbf{B}_s'^{(e)}]^T [\bar{\mathbf{C}}_s'^{(e)}][\mathbf{B}_s'^{(e)}] dS [\hat{\mathbf{R}}^{(e)}] \\ &= [\hat{\mathbf{R}}^{(e)}]^T \left(\sum_{k=1}^{N_G} w_k |\mathbf{J}'^{(e)}| [\mathbf{B}_s'^{(e)}]^T [\bar{\mathbf{C}}_s'^{(e)}][\mathbf{B}_s'^{(e)}] \right) [\hat{\mathbf{R}}^{(e)}] \end{aligned} \tag{B.72}$$

$$\begin{aligned}[\mathbf{K}_t^{(e)}] &= [\hat{\mathbf{R}}^{(e)}]^T \int_{S^{(e)}} [\mathbf{B}_t'^{(e)}]^T [\bar{\mathbf{C}}_t'^{(e)}][\mathbf{B}_t'^{(e)}] dS [\hat{\mathbf{R}}^{(e)}] \\ &= [\hat{\mathbf{R}}^{(e)}]^T \left(\sum_{k=1}^{N_G} w_k |\mathbf{J}'^{(e)}| [\mathbf{B}_t'^{(e)}]^T [\bar{\mathbf{C}}_t'^{(e)}][\mathbf{B}_t'^{(e)}] \right) [\hat{\mathbf{R}}^{(e)}] \end{aligned} \tag{B.73}$$

$$\begin{aligned}[\mathbf{M}^{(e)}] &= [\hat{\mathbf{R}}^{(e)}]^T \int_{S^{(e)}} [\mathbf{N}^{(e)}]^T [\bar{\boldsymbol{\rho}}'^{(e)}][\mathbf{N}^{(e)}] dl [\hat{\mathbf{R}}^{(e)}] \\ &= [\hat{\mathbf{R}}^{(e)}]^T \left(\sum_{k=1}^{N_G} w_k |\mathbf{J}'^{(e)}| [\mathbf{N}^{(e)}]^T [\bar{\boldsymbol{\rho}}'^{(e)}][\mathbf{N}^{(e)}] \right) [\hat{\mathbf{R}}^{(e)}] \end{aligned} \tag{B.74}$$

where $[\hat{\mathbf{R}}^{(e)}]$ is the rotation matrix corresponding to the inclination of each element, $|\mathbf{J}'^{(e)}|$ is the determinant of the jacobian matrix and $[\mathbf{B}_t'^{(e)}]$ is a function of (ξ, η). Finally, the stiffness matrix is computed from the sum of all different stress components [8].

$$[\mathbf{K}] = [\mathbf{K}_m] + [\mathbf{K}_b] + [\mathbf{K}_s] + [\mathbf{K}_t] \tag{B.75}$$

Matrix	[**M**]	[$\mathbf{K}_m$]	[$\mathbf{K}_b$]	[$\mathbf{K}_s$]	[$\mathbf{K}_t$]
N_G	4	1	4	1	1

N_G	k	w_k	ξ_k	η_k
1	1	4	0	0
4	1	1	$-1/\sqrt{3}$	$-1/\sqrt{3}$
	2	1	$+1/\sqrt{3}$	$-1/\sqrt{3}$
	3	1	$+1/\sqrt{3}$	$+1/\sqrt{3}$
	4	1	$-1/\sqrt{3}$	$+1/\sqrt{3}$

FIGURE B.7: Recommended Gauss quadrature for the different matrices [8].

B.3 Vibrations formulation

Systems of N-degrees-of-freedom (NDOF) are the ones dynamically defined from the movement of a total NDOF and in which the system of equations can be reduced to

$$[\mathbf{M}]\{\ddot{\mathbf{u}}\} + [\mathbf{C}]\{\dot{\mathbf{u}}\} + [\mathbf{K}]\{\mathbf{u}\} = \{\mathbf{f}\} \tag{B.76}$$

where $\{\mathbf{u}\}$, $\{\dot{\mathbf{u}}\}$ and $\{\ddot{\mathbf{u}}\}$ are the displacements, velocities and accelerations vectors of the different NDOF respectively. Moreover, the previous expression can be transformed into the frequency domain by doing the Fourier Transform.

$$(-\omega^2[\mathbf{M}] + i\omega[\mathbf{C}] + [\mathbf{K}])\{\mathbf{U}\} = \{\mathbf{F}\} \tag{B.77}$$

where $\{\mathbf{U}\}$ is the vibrations displacements vector. This section presents a summary of the vibrations formulation used in this report extracted from references [9], [26] and [27].

B.3.1 Free vibration of an NDOF system

Typically, the study of free vibrations of NDOF systems is done by considering null the damping matrix. In this case, equations B.76 and B.77 are being reduced to

$$[\mathbf{M}]\{\ddot{\mathbf{u}}\} + [\mathbf{K}]\{\mathbf{u}\} = 0 \tag{B.78}$$

$$(-\omega^2[\mathbf{M}] + [\mathbf{K}])\{\mathbf{U}\} = 0 \tag{B.79}$$

As $\{\mathbf{U}\}$ cannot be equal to 0, the solution of the system can be obtained by making zero the parenthesis. For that reason, the non-trivial solution of this expression is given by the set of eigenvalues λ.

$$det(-\lambda[\mathbf{M}] + [\mathbf{K}]) = 0 \tag{B.80}$$

where $\lambda = \omega^2$. For a system of N-degrees-of-freedom, there are N values of λ that satisfy the previous condition, consequentially, those values are called natural frequencies ω_n^2. The eigenvalue matrix is of the form [9]

$$[\boldsymbol{\lambda}] = \begin{bmatrix} \omega_{n1}^2 & & & \\ & \omega_{n2}^2 & & \\ & & \ddots & \\ & & & \omega_{nN}^2 \end{bmatrix} \tag{B.81}$$

where the eigenvalues follow this indexing ω_{nj}^2 in which j correspond to each of the NDOF. Furthermore, replacing any of the eigenvalues in equation B.79 the system results to be linearly dependent and the expression for a generic eigenvalue λ_j results in

$$(-\lambda_j[\mathbf{M}] + [\mathbf{K}])\{\boldsymbol{\phi}\}_j = 0 \tag{B.82}$$

where $\{\boldsymbol{\phi}\}_j$ is the eigenvector associated to each eigenvalue λ_j. An eigenvector defines the amplitude and phase relation between the different NDOF of the system. This means that the importance of this matrix fall into the relations between them whereas its value itself. Moreover, Not having considered damping the information of the phase between the different degrees of freedom will only inform if the movement between them is in phase (same sign) or in counter-phase (opposite sign) [9]. Finally, the eigenvectors matrix is of the form

$$[\boldsymbol{\phi}] = \begin{bmatrix} \{\phi\}_1 & \{\phi\}_j & \cdots & \{\phi\}_N \end{bmatrix} \tag{B.83}$$

$$[\boldsymbol{\phi}] = \begin{bmatrix} \phi_{11} & \phi_{12} & \cdots & \phi_{1N} \\ \phi_{21} & \phi_{22} & \cdots & \vdots \\ \cdots & \cdots & \ddots & \vdots \\ \phi_{N1} & \phi_{N2} & \cdots & \phi_{NN} \end{bmatrix} \tag{B.84}$$

Finally, the free movement of the studied system will be defined by the resulting superposition of the N normal modes. Each of the modes generate an specific vibration according to its eigenvector and natural frequency associated.

B.3.2 Forced vibration of an NDOF system

The forced vibration response is characterised by equation B.77. It should be noted that this system of equations will have to be solved for each of the frequencies in which the excitation of the system is significantly different from zero [9].

B.3.2.1 Direct method

Direct method solves directly equation B.77 by reorganising the terms

$$\{\mathbf{U}\} = (-\omega^2[\mathbf{M}] + i\omega[\mathbf{C}] + [\mathbf{K}])^{-1}\{\mathbf{F}\} \tag{B.85}$$

$$\{\mathbf{U}\} = [\mathbf{H}]\{\mathbf{F}\} \tag{B.86}$$

where $[\mathbf{H}]$ is called receptance matrix and it is defined by the following expression.

$$[\mathbf{H}] = (-\omega^2[\mathbf{M}] + i\omega[\mathbf{C}] + [\mathbf{K}])^{-1} \tag{B.87}$$

Moreover, as the mass, damping and stiffness matrix are symmetric, receptance matrix results to be a function of frequency and symmetric as well. Even though using the inverse to compute the matrix receptance is very intuitive, computationally speaking it is not the most practical and efficient way to do it. For that reason, as the geometry of study is quite complex, modal method will be implemented instead.

B.3.2.2 Modal method

Modal synthesis is a technique that applies a change of basis to the equations of motion of the system based on the eigenvector matrix. It causes that the system will no longer be based on the independent coordinates $\{\mathbf{u}\}$ and will be represented as a function of modal coordinates $\{\mathbf{q}\}$. Thanks to the orthogonal properties of the eigenvectors shown in reference [9], this transformation permit decoupling the system of equations simplifying drastically its resolution.

Moreover, modal and independent coordinates are related using the following expression

$$\{\mathbf{u}\} = [\boldsymbol{\phi}]\{\mathbf{q}\} \tag{B.88}$$

Applying this base transformation to the equations of motion of an NDOF system, equation B.78 results in

$$[\boldsymbol{\phi}]^T[\mathbf{M}][\boldsymbol{\phi}]\{\ddot{\mathbf{q}}\} + [\boldsymbol{\phi}]^T[\mathbf{K}][\boldsymbol{\phi}]\{\mathbf{q}\} = 0 \tag{B.89}$$

$$[\tilde{\mathbf{M}}]\{\ddot{\mathbf{q}}\} + [\tilde{\mathbf{K}}]\{\mathbf{q}\} = 0 \tag{B.90}$$

where $[\tilde{\mathbf{M}}]$ and $[\tilde{\mathbf{K}}]$ are called modal mass matrix and modal stiffness matrix respectively. As explained in section B.3.1, the eigenvectors matrix $\{\boldsymbol{\phi}\}$ is arbitrary escalated so, consequentially, $[\tilde{\mathbf{M}}]$ and $[\tilde{\mathbf{K}}]$ are arbitrary escalated too. To avoid this arbitrariness, eigenvector matrix normalization mechanisms are employed in which the most commonly used is the mass-normalization.

$$[\boldsymbol{\psi}] = [\boldsymbol{\phi}]\begin{bmatrix} \frac{1}{\sqrt{m_{r1}}} & & & \\ & \frac{1}{\sqrt{m_{r2}}} & & \\ & & \ddots & \\ & & & \frac{1}{\sqrt{m_{rN}}} \end{bmatrix} \tag{B.91}$$

Mass-normalized eigenvector matrix is represented by the notation $[\boldsymbol{\psi}]$ and satisfies the following conditions [9].

$$[\boldsymbol{\psi}]^T[\mathbf{M}][\boldsymbol{\psi}] = [\mathbf{I}] \tag{B.92}$$

$$[\boldsymbol{\psi}]^T[\mathbf{K}][\boldsymbol{\psi}] = \begin{bmatrix} \omega_{n1}^2 & & & \\ & \omega_{n2}^2 & & \\ & & \ddots & \\ & & & \omega_{nN}^2 \end{bmatrix} \tag{B.93}$$

Consequentially, if working with the mass-normalised eigenvector matrix, the modal mass matrix $[\tilde{\mathbf{M}}]$ ends up being equal to the identity matrix $[\mathbf{I}]$ and the modal stiffness matrix $[\tilde{\mathbf{K}}]$ is equal to the eigenvalue matrix $[\boldsymbol{\lambda}]$.

B.3.2.3 Application of the modal method in the case of structural damping

In order to apply the modal method in the case of structural damping it must be worked with the equations of motion expressed on the frequency domain. Furthermore, for structural damping, the damping matrix is computed from the complex terms of the stiffness matrix. For this specific case, equation B.77 is transformed into the following expression obtained from reference [9].

$$(-\omega^2[\boldsymbol{\psi}]^T[\mathbf{M}][\boldsymbol{\psi}] + i[\boldsymbol{\psi}]^T Im([\mathbf{K}])[\boldsymbol{\psi}] + [\boldsymbol{\psi}]^T Re([\mathbf{K}])[\boldsymbol{\psi}])\{\mathbf{Q}\} = [\boldsymbol{\psi}]^T\{\mathbf{F}\} \tag{B.94}$$

where the modal damping matrix $[\tilde{C}]$ corresponds to

$$[\tilde{\mathbf{C}}] = [\boldsymbol{\psi}]^T Im([\mathbf{K}])[\boldsymbol{\psi}] = 2 \cdot \begin{bmatrix} \tilde{\eta}_1\omega_{n1}^2 & & & \\ & \tilde{\eta}_2\omega_{n2}^2 & & \\ & & \ddots & \\ & & & \tilde{\eta}_N\omega_{nN}^2 \end{bmatrix} \tag{B.95}$$

In matrix form, modal displacements Q_j can be written as

$$\begin{Bmatrix} Q_1 \\ Q_2 \\ \vdots \\ Q_N \end{Bmatrix} = \begin{bmatrix} \tilde{H}_1 & & & \\ & \tilde{H}_2 & & \\ & & \ddots & \\ & & & \tilde{H}_N \end{bmatrix} \begin{Bmatrix} \tilde{F}_1 \\ \tilde{F}_2 \\ \vdots \\ \tilde{F}_N \end{Bmatrix} \tag{B.96}$$

$$\{\mathbf{Q}\} = [\tilde{\mathbf{H}}]\{\tilde{\mathbf{F}}\} \tag{B.97}$$

So the system of questions B.94 is completely decoupled and results in

$$(-\omega^2 + 2i\omega_{njj}^2 + \omega_{nj}^2)Q_j = \tilde{F}_j \qquad for \quad j = 1, \cdots, N \tag{B.98}$$

Furthermore, the modal receptance $\tilde{H}_j$ is obtained using the expression bellow.

$$\tilde{H}_j = \frac{1}{(\omega_{nj}^2 - \omega^2 + 2i\omega_{njj}^2)} \tag{B.99}$$

Finally, undoing the transformation the displacements in the independent coordinates can be calculated.

$$\{\mathbf{U}\} = [\boldsymbol{\psi}]\{\mathbf{Q}\} = [\mathbf{H}]\{\mathbf{F}\} = [\boldsymbol{\psi}][\tilde{\mathbf{H}}][\boldsymbol{\psi}]^T\{\mathbf{F}\} \tag{B.100}$$

B.3.2.4 Modal Projection

In order to implement a more efficient MATLAB program, modal projection method extracted from reference [26] has been chosen to compute the approximated displacements. Considering that the equation of movement of an NDOF system is

$$[\mathbf{M}]\{\ddot{\mathbf{u}}\} + [\mathbf{K}]\{\mathbf{u}\} = \{\mathbf{f}\} \tag{B.101}$$

The homogeneous solution of this system follows

$$[\mathbf{M}]\{\ddot{\mathbf{u}}_h\} + [\mathbf{K}]\{\mathbf{u}_h\} = \{\mathbf{0}\} \tag{B.102}$$

and it can be expressed as a sum of the each modal projection obtained for the different NDOF that conform the structure.

$$\{\mathbf{u}_h\} = \sum_{j=1}^{N_{dof}} \{\boldsymbol{\psi}_j\} e^{i\sqrt{\lambda_j}t} \tag{B.103}$$

$$\{\ddot{\mathbf{u}}_h\} = \sum_{j=1}^{N_{dof}} -\lambda_j \{\boldsymbol{\psi}_j\} e^{i\sqrt{\lambda_j}t} \tag{B.104}$$

where λ_j are the solutions of the characteristic equation mention in section B.3.1. Furthermore, mass-normalised mode shapes $[\boldsymbol{\psi}]$ are linearly independent which allows us to express any solution of a dynamic system as a linear combination of the associated mode shapes [26].

$$\{\mathbf{u}\} = \sum_{j=1}^{N_{dof}} \{\boldsymbol{\psi}_j\} q_j(t) \tag{B.105}$$

In other words, an uncouple equation can be obtained from each eigenvector from which the modal amplitude can be computed.

$$\{\boldsymbol{\psi}_j\}^T[\mathbf{M}]\{\boldsymbol{\psi}_j\}\ddot{q}_j + \{\boldsymbol{\psi}_j\}^T[\mathbf{K}]\{\boldsymbol{\psi}_j\}q_j = \{\boldsymbol{\psi}_j\}^T\{\mathbf{f}\} \tag{B.106}$$

Then, considering equations B.92 and B.93, the previous equation can be reduced to

$$\ddot{q}_j + \lambda_j q_j = \{\boldsymbol{\psi}_j\}^T\{\mathbf{f}\} \tag{B.107}$$

$$(-\omega^2 + \lambda_j)q_j = \{\boldsymbol{\psi}_j\}^T\{\mathbf{f}\} \tag{B.108}$$

$$q_j = \frac{\{\boldsymbol{\psi}_j\}^T\{\mathbf{f}\}}{(-\omega^2 + \lambda_j)} \tag{B.109}$$

This approach consists in an order-reduction method in which the relevant modes must be solved in order to get an approximated solution.

$$\{\mathbf{u}^*\} = \sum_{j=1}^{N<N_{dof}} \{\boldsymbol{\psi}_j\}q_j(t) \tag{B.110}$$

B.3.2.5 Cumulative effective mass for the modes

The cumulative effective mass for the nodes will give an idea of the relevance of the nodes and the impact they have on the final solution. The formulation behind the computation of the modal effective mass of an NDOF system has been extracted from references [27] and [28] where it is proposed to depict the displacements vector on a basis of 6 rigid modes $[\boldsymbol{\psi}_r]$ with $\{\ \mathbf{u}_{I_f}\} = \{\ 1\}$ and elastic modes $[\boldsymbol{\psi}_p]$ with $\{\ \mathbf{u}_{I_f}\} = \{\ 0\}$. Reference [27] states that the rigid modes have to follow that

$$[\mathbf{K}]\{\boldsymbol{\psi}_r\} = \{\mathbf{0}\} \tag{B.111}$$

and the elastic modes are the ones obtained from the eigenvalue problem which is solved in section B.3.1. Once computed both, the modal effective mass of a certain mode can be computed using the following expression

$$m_{eff,k} = \frac{L_k^2}{m_k} \tag{B.112}$$

where $L_k = \{\boldsymbol{\psi}_{p,k}\}^T[M]\{\boldsymbol{\psi}_r\}$ and $m_k = \{\boldsymbol{\psi}_{p,k}\}^T[M]\{\boldsymbol{\psi}_{p,k}\}$. The cumulative effective mass is the sum of the effective mass of a certain mode and the ones obtained from previous modes. Finally, dividing the cumulative effective mass of each mode with the total cumulative effective mass obtained for the last mode evaluated, the percentage of the cumulative mass is computed. Finally, reference [24] mentions that a a percentage of the cumulative effective mass around 0.97% is good enough to get an accurate approximation.

B.3.3 Types of forced vibrations

In this section, two types of vibration excitation will be studied: harmonic force excitation and random force excitation.

B.3.3.1 Harmonic force excitation

In order to study the harmonic excitation it will be first necessary to characterise a generic sinusoidal force of the form

$$\{\mathbf{f}\} = \{\|\mathbf{A}\|\}\cos\left(\omega_e t + \{\boldsymbol{\varphi}\}\right) = Re\left(\{\mathbf{A}\}e^{i\omega_e t}\right) \tag{B.113}$$

Developing equation B.113, the harmonic force can also be written as

$$\{\mathbf{f}\} = \{\|\mathbf{A}\|\}\cos\left(\omega_e t + \{\boldsymbol{\varphi}\}\right) = \frac{1}{2}\{\|\mathbf{A}\|\}\left(e^{i(\omega_e t+\{\boldsymbol{\varphi}\})} + e^{-i(\omega_e t+\{\boldsymbol{\varphi}\})}\right) = \frac{1}{2}\left(\{\mathbf{A}\}e^{i\omega_e t} + \{\mathbf{A}^*\}e^{-i\omega_e t}\right) \tag{B.114}$$

where $\{\mathbf{A}\}$ is a vector of complex amplitudes characterised by the modulus of its amplitudes $\{\|\mathbf{A}\|\}$ and the phase $\{\boldsymbol{\varphi}\}$ [9]. The resulting force in the frequency domain is obtained by applying the Fourier Transform to the sinusoidal force expressed in time domain.

$$\{\mathbf{F}\} = \frac{1}{2}\left(\int_{-\infty}^{+\infty}\{\mathbf{A}\}e^{i\omega_e t}e^{-i\omega t}dt + \int_{-\infty}^{+\infty}\{\mathbf{A}^*\}e^{-i\omega_e t}e^{-i\omega t}dt\right) \tag{B.115}$$

$$\{\mathbf{F}\} = \pi\{\mathbf{A}\}\delta(\omega - \omega_e) + \pi\{\mathbf{A}^*\}\delta(\omega + \omega_e) \tag{B.116}$$

The harmonic force will be dependant of the frequency in which the applied force oscillates.

$$\{\mathbf{F}\} = \{\mathbf{F}(\omega_e)\} \tag{B.117}$$

Finally, the displacement in the frequency domain can be obtained using equation B.100 considering $\omega = \omega_e$.

$$\{\mathbf{U}(\omega_e)\} = [\mathbf{H}(\omega_e)]\{\mathbf{F}(\omega_e)\} \tag{B.118}$$

From this results, it can be concluded that the response of an harmonic force excitation with an angular frequency ω_e describes an harmonic movement with the same oscillation ω_e but different amplitude [9].

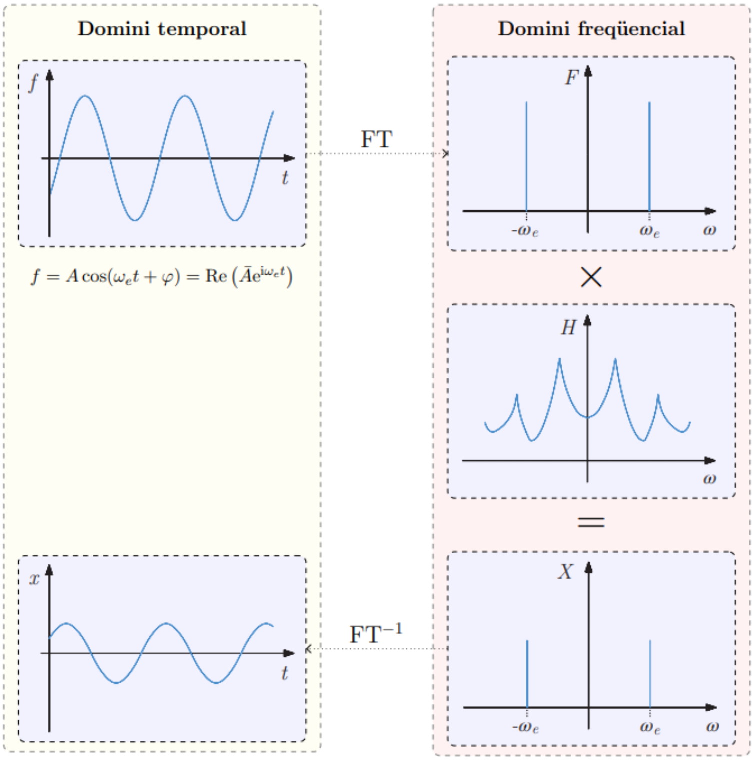

FIGURE B.8: Methodology used to compute the response of an harmonic force excitation [9].

B.3.3.2 Random force excitation

Random excitation is the most general case of excitation in which the force applied follows a completely arbitrary temporary function.

Figure B.9 presents the computational scheme one must follow to obtain the displacements in time domain when applying a random vibration. At first, the force must be transformed from time domain to frequency domain thanks to the Fourier Transforms. Then, the displacements in the frequency domain U are computed by multiplying the receptance H and the force in the frequency domain F [9]. Finally, with the use of the inverse of the Fourier Transform the displacements can be calculated in time domain.

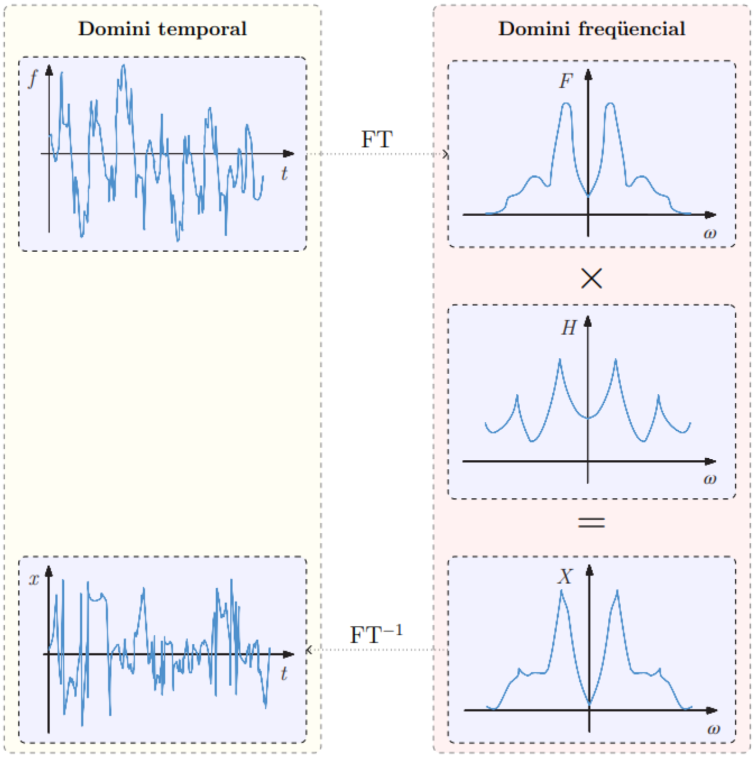

FIGURE B.9: Methodology used to compute the response of a random excitation [9].

Moreover, to evaluate a random vibration test, some parameters must be calculated such as Energy Spectral Density (ESD) and Power Spectral Density (PSD). In order to do so, once obtained the displacements in the frequency domain U, the acceleration in the frequency domain $\ddot{U}$ can be computed thanks to the definition of the FT of a derived [9].

$$\int_{-\infty}^{\infty} \frac{d^n u}{dt^n} e^{-i\omega t} dt = (i\omega)^n U \tag{B.119}$$

$$\dot{U} = i\omega U \tag{B.120}$$

$$\ddot{U} = -\omega^2 U \tag{B.121}$$

B.4 Shock formulation

The shock test is commonly used to prove that a certain assembly or subassembly of an spacecraft will be capable to withstand the shock loads caused by the separation of the spacecraft from the rocket or the burn up of the rocket stages [29] [30].

The Shock Response Spectrum (SRS) is computed by submitting the evaluated structures to a half-sine pulse (HSP). In order to reproduce the half-sine impact, it can be performed two different tests [31] [32] [33]:

- To use a hammer of a pendulum. In this case, thanks to the fall of a mass concentration, the pulse is generated. Moreover, the amplitude depends on the height and the weight of the dropped mass.
- To use a ringing plate to mount the unit tested. In this case, the plate is excited by a falling weight. Furthermore, the loads can be modified by changing the location at which the weight falls.

B.4.1 Transient modal dynamics analysis

In order to evaluate the response of a structure under a time-dependent load, a transient analysis is carried out. First, the eigenvalues and natural frequencies are determined by means of a modal analysis. Then, the response is computed with a transient modal analysis dynamics.

B.4.1.1 Shock Response Spectrum

The Shock Response Spectrum (SRS) is a calculation function based on the acceleration time history [10] in which the acceleration input is applied as a base excitation to a single-degree-of-freedom (SDOF) systems. Figure B.10 shows the SRS model assuming that there is no mass-loading effect on the base input.

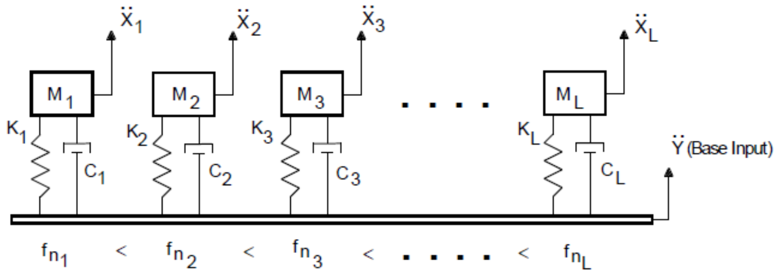

FIGURE B.10: Shock Response Spectrum model [10].

where $\ddot{Y}$ is the acceleration input for each system, $\ddot{X}$ is what in this report is called $\ddot{U}$ and it is the acceleration response, f_{n_i} is the natural frequency of each system, M_i is the mass, C_i is the damping coefficient and K_i is the stiffness of each system.

Moreover, the damping of each system is assumed to be 5% which is equivalent to $Q = 10$. This value is specified in ISO 18431 [34].

B.4.2 Time-dependent solution

First, applying the Newton's law to a free-body system as shown in figure B.11, the resulting governing differential equation of motion is [10]:

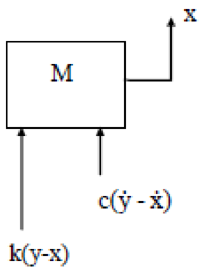

FIGURE B.11: Free-body Diagram [10].

$$m\ddot{u} + c\dot{u} + ku = c\dot{y} + ky \tag{B.122}$$

Furthermore, defining the relative displacement as $z = u - y$, the previous equation results in

$$m\ddot{z} + c\dot{z} + kz = -m\ddot{y} \tag{B.123}$$

Then, substituting

$$\frac{c}{m} = 2\zeta\omega_n \tag{B.124}$$

$$\frac{k}{m} = \omega_n^2 \tag{B.125}$$

equation B.123 ends up being

$$\ddot{z} + 2\zeta\omega_n\dot{z} + \omega_n^2 z = -\ddot{y} \tag{B.126}$$

Additionally, the absolute displacement u can be calculated with

$$\ddot{u} = \ddot{z} + \ddot{y} = -2\zeta\omega_n\dot{z} - \omega_n^2 z \tag{B.127}$$

Moreover, using displacement and velocity initial conditions ($z(0)$ and $\dot{z}(0)$), the solution of equation B.126 can be expressed as [27]

$$z = z(0)e^{-\zeta\omega_n t}\left[\cos(\omega_d t) + \frac{\zeta}{\sqrt{1-\zeta^2}}\sin(\omega_d t)\right] + \dot{z}(0)e^{-\zeta\omega_n t}\frac{\sin(\omega_d t)}{\omega_d} - \int_0^t e^{-\zeta\omega_n\tau}\frac{\sin(\omega_d\tau)}{\omega_d}\ddot{y}(t-\tau)d\tau \tag{B.128}$$

where $\omega_d = \omega_n\sqrt{1-\zeta^2}$. For Shock Response Spectrum calculations, the initial conditions of the displacements and the velocity are null. In other words, $z(0) = 0$ and $\dot{z}(0) = 0$. This hypothesis transforms the previous equation into the following

$$z = -\int_0^t e^{-\zeta\omega_n\tau}\frac{\sin(\omega_d\tau)}{\omega_d}\ddot{y}(t-\tau)d\tau \tag{B.129}$$

$$z = -\int_0^t e^{-\zeta\omega_n(t-\tau)}\frac{\sin(\omega_d(t-\tau))}{\omega_d}\ddot{y}(\tau)d\tau \tag{B.130}$$

Then, when differentiating equation B.130 with respect to time, the relative velocity $\dot{z}$ becomes

$$\dot{z} = -\zeta\omega_n z - \int_0^t e^{-\zeta\omega_n(t-\tau)}\cos(\omega_d(t-\tau))\ddot{y}(\tau)d\tau \tag{B.131}$$

Finally, the absolute acceleration $\ddot{u}$ can be obtained substituting the relative displacement z and the relative velocity $\dot{z}$ defined in equations B.130 and B.131 in equation B.127.

$$\ddot{u} = 2\zeta\omega_n\int_0^t e^{-\zeta\omega_n(t-\tau)}\cos(\omega_d(t-\tau))\ddot{y}(\tau)d\tau + \omega_n(2\zeta^2-1)z \tag{B.132}$$

The Shock Response Spectrum is the plot that depicts the maximum acceleration $\ddot{u}$ obtained for every SDOF system against a range of natural frequencies. In other words, the maximum acceleration $\ddot{u}$ can be computed using the natural frequencies at which each SDOF is in resonance and then those results can be plotted versus the frequency. Some parameters are of the uttermost importance when calculating the SRS [27]:

- The damping ratio ζ of the SDOF dynamic system. Generally, it has a value of 5% which is the equivalent to $Q = 10$.
- The number of SDOF systems for which the maximum response is computed.

- The time frame of the transient period T_{min}. It will be chosen the highest value between $T_{min} \geq \frac{1}{f_{min}}$ and twice the maximum shock time $T_{min} \geq 2t_{shock}$.
- The time step.
- The mesh element type and size.

B.4.3 Numerical calculation of the SRS of a SDOF system

The numerical calculation method of the SRS has been extracted from reference [27] in which the piece wise exact method is explained using two different techniques elaborated by Nigam and Ebeling on the first hand, and Kelly on the other hand. In both methods the input acceleration is assumed to vary linearly in a piece wise fashion and, based on this assumption, an exact solution is determined.

First, from section B.4.2, equation B.126 relates the relative z motion of the SDOF dynamic system with the base acceleration input as the following.

$$\ddot{z} + 2\zeta\omega_n\dot{z} + \omega_n^2 z = -\ddot{y} \tag{B.133}$$

Moreover, a linear variation of the input acceleration $\ddot{y}$ is assumed. For that reason the time and acceleration step can be defined by

$$\Delta t^n = t^{n+1} - t^n \tag{B.134}$$

$$\Delta\ddot{y}(t^n) = \ddot{y}(t^{n+1}) - \ddot{y}(t^n) \tag{B.135}$$

So the acceleration in an arbitrary time between t^n and t^{n+1} can be expressed as

$$\ddot{y}(t) = \ddot{y}(t^n) + \frac{\Delta\ddot{y}(t^n)}{\Delta t^n}(t - t^n) \qquad \text{for} \quad t^n \leq t \leq t^{n+1} \tag{B.136}$$

Rewritten equation B.133 by substituting equation B.136 in it

$$\ddot{z} + 2\zeta\omega_n\dot{z} + \omega_n^2 z = -\ddot{y}(t^n) - \frac{\Delta\ddot{y}(t^n)}{\Delta t^n}(t - t^n) \qquad \text{for} \quad t^n \leq t \leq t^{n+1} \tag{B.137}$$

The solution of the previous expression is

$$
\begin{aligned}
z(t) = z(t^n)e^{-\zeta\omega_n(t-t^n)} &\left[\cos\left(\omega_d(t-t^n)\right) + \frac{\zeta}{\sqrt{1-\zeta^2}}\sin\left(\omega_d(t-t^n)\right)\right] \\
&+ \dot{z}(t^n)e^{-\zeta\omega_n(t-t^n)}\frac{\sin\left(\omega_d(t-t^n)\right)}{\omega_d} - \int_{t^n}^{t} e^{-\zeta\omega_n(t-\tau)}\frac{\sin\left(\omega_d(t-\tau)\right)}{\omega_d}\ddot{y}(\tau)d\tau
\end{aligned}
\tag{B.138}
$$

On the one hand, the integral given by Kelly in his work is the following [35]

$$
\begin{aligned}
\int_{t^n}^{t} e^{-\zeta\omega_n(t-\tau)}\frac{\sin\left(\omega_d(t-\tau)\right)}{\omega_d}\ddot{y}(\tau)d\tau = &-\frac{\ddot{y}(t^n)}{\omega_n^2}\left[1-e^{-\zeta\omega_n(t-t^n)}\left[\cos\left(\omega_d(t-t^n)\right)+\frac{\zeta}{\sqrt{1-\zeta^2}}\sin\left(\omega_d(t-t^n)\right)\right]\right] \\
&-\frac{\Delta\ddot{y}(t^n)}{\omega_n^2}\left[1-\frac{2\zeta}{\omega_n(t-t^n)}\left[1-e^{-\zeta\omega_n(t-t^n)}\cos\left(\omega_d(t-t^n)\right)\right]\right] \\
&+\frac{\Delta\ddot{y}(t^n)}{\omega_n^2}\left[\frac{(1-2\zeta^2)}{\omega_d(t-t^n)}e^{-\zeta\omega_n(t-t^n)}\sin\left(\omega_d(t-t^n)\right)\right]
\end{aligned}
\tag{B.139}
$$

On the other hand, Nigam proposed in his work [36] that the state vector $\{z, \dot{z}\}^T$ at time t^{n+1} can be expressed by the state vector at time t^n and the piece wise linear given base acceleration $\ddot{y}$ at both, t^n and t^{n+1}.

$$
\begin{Bmatrix} z(t^{n+1}) \\ \dot{z}(t^{n+1}) \end{Bmatrix} = [A]\begin{Bmatrix} z(t^n) \\ \dot{z}(t^n) \end{Bmatrix} + [B]\begin{Bmatrix} \ddot{y}(t^n) \\ \ddot{y}(t^{n+1}) \end{Bmatrix}
\tag{B.140}
$$

where

$$
[A] = \begin{bmatrix} a_{11} & a_{12} \\ a_{21} & a_{22} \end{bmatrix} \longrightarrow
\left\{
\begin{aligned}
a_{11} &= e^{-\zeta\omega_n\Delta t^n}\left[\cos\left(\omega_d\Delta t^n\right) + \frac{\zeta}{\sqrt{1-\zeta^2}}\sin\left(\omega_d\Delta t^n\right)\right] \\
a_{12} &= e^{-\zeta\omega_n\Delta t^n}\left[\frac{\sin\left(\omega_d\Delta t^n\right)}{\omega_d}\right] \\
a_{21} &= -e^{-\zeta\omega_n\Delta t^n}\left[\frac{\omega_n}{\sqrt{1-\zeta^2}}\sin\left(\omega_d\Delta t^n\right)\right] \\
a_{22} &= e^{-\zeta\omega_n\Delta t^n}\left[\cos\left(\omega_d\Delta t^n\right) - \frac{\zeta}{\sqrt{1-\zeta^2}}\sin\left(\omega_d\Delta t^n\right)\right]
\end{aligned}
\right.
\tag{B.141}
$$

$$[B] = \begin{bmatrix} b_{11} & b_{12} \\ b_{21} & b_{22} \end{bmatrix} \longrightarrow \begin{cases} b_{11} = e^{-\zeta\omega_n\Delta t^n}\left[\left(\dfrac{2\zeta^2-1}{\omega_n^2\Delta t^n} + \dfrac{\zeta}{\omega_n}\right)\dfrac{\sin(\omega_d\Delta t^n)}{\omega_d} + \left(\dfrac{2\zeta}{\omega_n^3\Delta t^n} + \dfrac{1}{\omega_n^2}\right)\cos(\omega_d\Delta t^n)\right] \\ \quad -\dfrac{2\zeta}{\omega_n^3\Delta t^n} \\ b_{12} = e^{-\zeta\omega_n\Delta t^n}\left[\left(\dfrac{2\zeta^2-1}{\omega_n^2\Delta t^n}\right)\dfrac{\sin(\omega_d\Delta t^n)}{\omega_d} + \left(\dfrac{2\zeta}{\omega_n^3\Delta t^n}\right)\cos(\omega_d\Delta t^n)\right] \\ \quad -\dfrac{1}{\omega_n^2} + \dfrac{2\zeta}{\omega_n^3\Delta t^n} \\ b_{21} = e^{-\zeta\omega_n\Delta t^n}\left(\dfrac{2\zeta^2-1}{\omega_n^2\Delta t^n} + \dfrac{\zeta}{\omega_n}\right)\left[\cos(\omega_d\Delta t^n) - \dfrac{\zeta}{\sqrt{1-\zeta^2}}\sin(\omega_d\Delta t^n)\right] \\ \quad -e^{-\zeta\omega_n\Delta t^n}\left(\dfrac{2\zeta}{\omega_n^3\Delta t^n} + \dfrac{1}{\omega_n^2}\right)\left[\omega_d\sin(\omega_d\Delta t^n) + \zeta_n\cos(\omega_d\Delta t^n)\right] + \dfrac{1}{\omega_n^2\Delta t^n} \\ b_{22} = -e^{-\zeta\omega_n\Delta t^n}\left(\dfrac{2\zeta^2-1}{\omega_n^2\Delta t^n}\right)\left[\cos(\omega_d\Delta t^n) - \dfrac{\zeta}{\sqrt{1-\zeta^2}}\sin(\omega_d\Delta t^n)\right] \\ \quad -e^{-\zeta\omega_n\Delta t^n}\left(-\dfrac{2\zeta}{\omega_n^3\Delta t^n}\right)\left[\omega_d\sin(\omega_d\Delta t^n) + \zeta_n\cos(\omega_d\Delta t^n)\right] - \dfrac{1}{\omega_n^2\Delta t^n} \end{cases} \tag{B.142}$$

Moreover, Gupta [37] transformed expressions b_{21} and b_{22} as a function of the rest

$$b_{21} = -\frac{a_{11}-1}{\omega_n^2\Delta t^n} - a_{12} \tag{B.143}$$

$$b_{22} = -b_{21} - a_{12} \tag{B.144}$$

Additionally, Kelly proposed in his work [35] a similar numerical approach

$$z(t^{n+1}) = B_1 z(t^n) + B_2\dot{z}(t^n) + B_3\ddot{y}(t^n) + B_4\Delta\ddot{y}(t^n) \tag{B.145}$$

$$\dot{z}(t^{n+1}) = B_5 z(t^n) + B_6\dot{z}(t^n) + B_7\ddot{y}(t^n) + B_8\Delta\ddot{y}(t^n) \tag{B.146}$$

where

$$B_1 = e^{-\zeta\omega_n\Delta t^n}\left[\cos(\omega_d\Delta t^n) + \frac{\zeta}{\sqrt{1-\zeta^2}}\sin(\omega_d\Delta t^n)\right] \tag{B.147}$$

$$B_2 = e^{-\zeta\omega_n\Delta t^n}\left[\frac{\sin(\omega_d\Delta t^n)}{\omega_d}\right] \tag{B.148}$$

$$B_3 = \frac{1}{\omega_n^2}(1 - B_1) \tag{B.149}$$

$$B_4 = \frac{1}{\omega_n^2}\left[1 - \frac{2\zeta}{\omega_n\Delta t^n}\left[1 - e^{-\zeta\omega_n\Delta t^n}\cos(\omega_d\Delta t^n)\right] - \left[\frac{(1-2\zeta^2)}{\omega_d\Delta t^n}e^{-\zeta\omega_n\Delta t^n}\sin(\omega_d\Delta t^n)\right]\right] \tag{B.150}$$

$$B_5 = -\omega_n B_2 \tag{B.151}$$

$$B_6 = \frac{e^{-\zeta\omega_n\Delta t^n}}{\omega_n}\left[\cos(\omega_d\Delta t^n) - \frac{\zeta}{\sqrt{1-\zeta^2}}\sin(\omega_d\Delta t^n)\right] \tag{B.152}$$

$$B_7 = -\frac{B_2}{\omega_n} \tag{B.153}$$

$$B_8 = \frac{B_1 - 1}{\omega_n^3\Delta t^n} \tag{B.154}$$

Finally, the absolute acceleration $\ddot{u}$ is computed using the following expression independently of the methodology used to compute z and $\dot{z}$.

$$\ddot{u}(t^{n+1}) = -2\zeta\omega_n\dot{z}(t^{n+1}) - \omega_n^2 z(t^{n+1}) \tag{B.155}$$

B.4.4 Transient study of a NDOF system

In order to compute a transient study of a NDOF system, first the system of equations will be written considering that the force depends on time.

$$[\mathbf{M}]\{\ddot{\mathbf{u}}\} + [\mathbf{C}]\{\dot{\mathbf{u}}\} + [\mathbf{K}]\{\mathbf{u}\} = \{\mathbf{f}(t)\} \tag{B.156}$$

Then, the previous system will be reduced to the free DOFs (I_f).

$$[\mathbf{M}_{I_f,I_f}]\{\ddot{\mathbf{u}}_{I_f}\}+[\mathbf{C}_{I_f,I_f}]\{\dot{\mathbf{u}}_{I_f}\}+[\mathbf{K}_{I_f,I_f}]\{\mathbf{u}_{I_f}\} = \{\mathbf{f}(t)_{I_f}\}-[\mathbf{M}_{I_f,I_p}]\{\ddot{\mathbf{u}}_{I_p}\}+[\mathbf{C}_{I_f,I_p}]\{\dot{\mathbf{u}}_{I_p}\}+[\mathbf{K}_{I_f,I_p}]\{\mathbf{u}_{I_p}\} \tag{B.157}$$

As the prescribed displacements, velocities and accelerations are null, the previous equation can be simplified in:

$$[\mathbf{M}_{I_f,I_f}]\{\ddot{\mathbf{u}}_{I_f}\} + [\mathbf{C}_{I_f,I_f}]\{\dot{\mathbf{u}}_{I_f}\} + [\mathbf{K}_{I_f,I_f}]\{\mathbf{u}_{I_f}\} = \{\mathbf{f}(t)_{I_f}\} \tag{B.158}$$

To make it easier to understand the notation will be changed.

$$[\mathbf{M}] = [\mathbf{M}_{I_f,I_f}] \qquad \{\ddot{\mathbf{u}}\} = \{\ddot{\mathbf{u}}_{I_f}\} \tag{B.159}$$

$$[\mathbf{C}] = [\mathbf{C}_{I_f,I_f}] \qquad \{\dot{\mathbf{u}}\} = \{\dot{\mathbf{u}}_{I_f}\} \tag{B.160}$$

$$[\mathbf{K}] = [\mathbf{K}_{I_f,I_f}] \qquad \{\mathbf{u}\} = \{\mathbf{u}_{I_f}\} \tag{B.161}$$

$$\{\mathbf{f}(t)\} = \{\mathbf{f}(t)_{I_f}\} \tag{B.162}$$

$$[\mathbf{M}]\{\ddot{\mathbf{u}}\} + [\mathbf{C}]\{\dot{\mathbf{u}}\} + [\mathbf{K}]\{\mathbf{u}\} = \{\mathbf{f}(t)\} \tag{B.163}$$

Moreover, modal and independent coordinates are related using the following expression

$$\{\mathbf{u}\} = [\boldsymbol{\psi}]\{\mathbf{q}\} \tag{B.164}$$

Applying this base transformation to the equations of motion of an NDOF system, equation B.163 results in

$$[\boldsymbol{\psi}]^T[\mathbf{M}][\boldsymbol{\psi}]\{\ddot{\mathbf{q}}\} + [\boldsymbol{\psi}]^T[\mathbf{C}][\boldsymbol{\psi}]\{\dot{\mathbf{q}}\} + [\boldsymbol{\psi}]^T[\mathbf{K}][\boldsymbol{\psi}]\{\mathbf{q}\} = [\boldsymbol{\psi}]^T\{\mathbf{f}(t)\} \tag{B.165}$$

$$[\tilde{\mathbf{M}}]\{\ddot{\mathbf{q}}\} + [\tilde{\mathbf{C}}]\{\dot{\mathbf{q}}\} + [\tilde{\mathbf{K}}]\{\mathbf{q}\} = [\boldsymbol{\psi}]^T\{\mathbf{f}(t)\} \tag{B.166}$$

where,

$$[\tilde{\mathbf{M}}] = [\mathbf{I}] \tag{B.167}$$

$$[\tilde{\mathbf{C}}] = 2 \cdot \varepsilon \cdot \begin{bmatrix} \omega_{n1} & & & \\ & \omega_{n2} & & \\ & & \ddots & \\ & & & \omega_{nN} \end{bmatrix} \tag{B.168}$$

$$[\tilde{\mathbf{K}}] = \begin{bmatrix} \omega_{n1}^2 & & & \\ & \omega_{n2}^2 & & \\ & & \ddots & \\ & & & \omega_{nN}^2 \end{bmatrix} \tag{B.169}$$

For this study a damping factor $\varepsilon = 0.05$ is used which is the same as a qual factor $Q = 10$. Furthermore, considering equations B.167, B.168 and B.169, equation B.166 results in

$$\{\ddot{\mathbf{q}}\} + [\tilde{\mathbf{C}}]\{\dot{\mathbf{q}}\} + [\tilde{\mathbf{K}}]\{\mathbf{q}\} = [\boldsymbol{\psi}]^T\{\mathbf{f}(t)\} \tag{B.170}$$

The next step is to solve the differential equation. However, as MATLAB can not solve a second order differential equation, a change of variable has been made as the following.

$$\{\ddot{\mathbf{q}}_1\} = -[\tilde{\mathbf{C}}]\{\dot{\mathbf{q}}_1\} - [\tilde{\mathbf{K}}]\{\mathbf{q}_1\} + [\boldsymbol{\psi}]^T\{\mathbf{f}(t)\} \tag{B.171}$$

$$\{\dot{\mathbf{q}}_1\} = \{\mathbf{q}_2\} \tag{B.172}$$

$$\{\ddot{\mathbf{q}}_1\} = \{\dot{\mathbf{q}}_2\} \tag{B.173}$$

$$\{\dot{\mathbf{q}}_1\} = \{\mathbf{q}_2\} \tag{B.174}$$

$$\{\dot{\mathbf{q}}_2\} = -[\tilde{\mathbf{C}}]\{\mathbf{q}_2\} - [\tilde{\mathbf{K}}]\{\mathbf{q}_1\} + [\boldsymbol{\psi}]^T\{\mathbf{f}(t)\} \tag{B.175}$$

Then, equations B.174 and B.175 can be rewritten together as below.

$$\begin{Bmatrix} \{\dot{\mathbf{q}}_1\} \\ \{\dot{\mathbf{q}}_2\} \end{Bmatrix} = \begin{bmatrix} [\mathbf{0}] & [\mathbf{I}] \\ -[\tilde{\mathbf{K}}] & -[\tilde{\mathbf{C}}] \end{bmatrix} \begin{Bmatrix} \{\mathbf{q}_1\} \\ \{\mathbf{q}_2\} \end{Bmatrix} + \begin{bmatrix} [\mathbf{0}] \\ [\boldsymbol{\psi}]^T \end{bmatrix} \{\mathbf{f}(t)\} \tag{B.176}$$

$$\{\dot{\mathbf{q}}\} = [\mathbf{A}]\{\mathbf{q}\} + [\mathbf{B}]\{\mathbf{f}(t)\} \tag{B.177}$$

Finally, equation B.177 can be computed with MATLAB using function *ode45* [38]. This function permits obtaining the displacements and the velocity distribution in time domain so, in order to compute the acceleration as well, equation B.170 will be used for every time step.

B.4.5 Preprocess parameters

Moreover, the determination of mesh element size and type as well as the time step used are of the uttermost importance in a transient dynamic analysis. In other words, the mesh and the time step must be adequate selected in order to compute an accurate enough response without losing any information and avoid errors.

B.4.5.1 Mesh

The mesh element size and type should be determined according to the maximum frequency of the range at which the structure is evaluated, in this case, 500 Hz. With the highest frequency, the smallest wavelength is computed considering that, in every structure, three types of waves take place: shear, flexural and compression waves. The theory behind a pyroshock test proposed in thesis [11] recommends having at least 8 elements per wavelength. The different wavelengths can be computed using the following expressions:

$$\lambda_{Compression} = \sqrt{\frac{E}{\rho}\frac{1}{f}} \tag{B.178}$$

$$\lambda_{Shear} = \sqrt{\frac{G}{\rho}\frac{1}{f}} \tag{B.179}$$

$$\lambda_{Flexural} = \sqrt[4]{\frac{Et^2}{12\rho}}\sqrt{\frac{2\pi}{f}} \tag{B.180}$$

where E is the Young's modulus, G is the shear modulus, ρ is the density, t is the thickness of the material and f is the maximum frequency at which it is evaluated.

B.4.5.2 Time step

Ideally, the computation time step used should be as small as possible in order to provide the most precise solution, nevertheless, the smaller time step, the more computational cost. In order to achieve an optimal balance between accuracy and efficiency, the time step should be determined with the maximum frequency at which the structure will be evaluated. The increment time step should be less than the 10% of the reciprocal value of the maximum frequency f_{max} and the minimum number of time steps have to be computed as well. Both conditions have been extracted from reference [11] and are defined by the following expressions.

$$\Delta t \leq \frac{0.1}{f_{max}} \tag{B.181}$$

$$n_{min} = \frac{T_{min}}{\Delta t} = 10\frac{f_{max}}{f_{min}} \tag{B.182}$$

Moreover, in dynamics analysis it is necessary to check the Courant Condition in order to maintain the numerical consistency. This conditions consists in verifying that the distance travelled by the wave within the finite element model is less than the element length [11].

$$\textit{Courant Condition} \quad \longrightarrow \quad \frac{c_F \cdot \Delta t}{\Delta x} \leq 1 \tag{B.183}$$

B.4.5.3 Boundary conditions

Although there are several types of pyroshock, in this report the force will be generated by the impact of a hammer. As reference [11] states, the force that the hammer generates to the structure can be described by a half-sine pulse as shown in figure B.12.

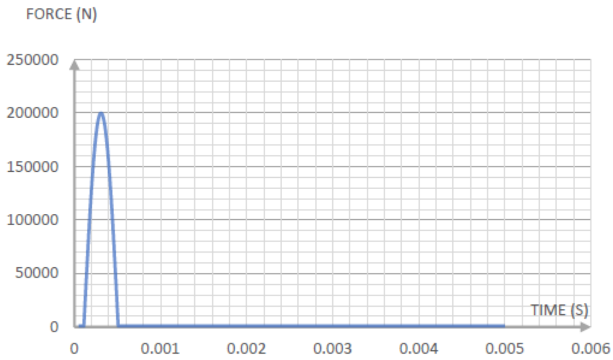

FIGURE B.12: Half-sine force input [11].

Furthermore, in order to adapt the test as much as possible to the one performed in a laboratory, the structure will have free boundary conditions.

Appendix C

Reports

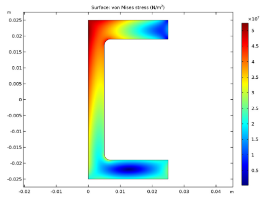

POLYTECHNIC UNIVERSITY OF CATALONIA
Structural Mechanics
Matlab and Comsol

C.1 Report 1: Channel Beam

The aim of this report is to compare the analytical solution of the cantilever beam problem with the numerical one computed with COMSOL. The report will be divided in two studies. At first, Von Mises stress will be analytically obtained and compared with COMSOL results. Then, it will be carried on a second study which consists in varying the profile parameters and orientation to know how those parameters affect Von Misses stress along the beam.

C.1.1 Model Definition

First, the geometry, the material and the boundary conditions at which the cantilever beam is studied will be defined.

Geometry

- Beam length, L = 1 m.
- Cross-section area $A = 4.90 \cdot 10^{-4} m^2$ (from the cross section library)
- Area moment of inertia in stiff direction, $I_{zz} = 1.69 \cdot 10^{-7} m^4$.
- Area moment of inertia in weak direction, $I_{yy} = 2.77 \cdot 10^{-8} m^4$.
- Torsional constant, $J = 5.18 \cdot 10^{-9} m^4$.
- Position of the shear center (SC) with respect to the area center of gravity (CG), ez = 0.0148 m.
- Torsional section modulus $W_t = 8.64 \cdot 10^{-7} m^3$.
- Ratio between maximum and average shear stress for shear in y direction, $\mu_y = 2.44$.
- Ratio between maximum and average shear stress for shear in z direction,$\mu_y = 2.38$.

Material

- Young's modulus, E = 210 GPa.
- Poisson's ratio, $\eta = 0.25$.
- Mass density, $\rho = 7800 kg/m^3$.

Boundary Conditions

- One end of the beam is fixed.
- A punctual load is applied in the other end of the beam.
  - Axial force FX = 10 kN
  - Transverse forces FY = 100 N and FZ = -50 N
  - Twisting moment MX = -10 Nm

C.1.2 First Study

In the first place, it has been carried on a comparative study between the analytical and numerical (COMSOL) solutions obtained for the cantilever beam problem. In this case, the dimensions of the section of the beam, as well as, the area moments of inertia (I_y and I_z) will be considered known.

Diagrams

In order to calculate the Von Misses stress along the beam it has first been necessary to compute the load diagrams considering a punctual force located on the coordinate (1,0,0) m. Once obtained the analytical solution, it has been compared with the graphics plotted with COMSOL.

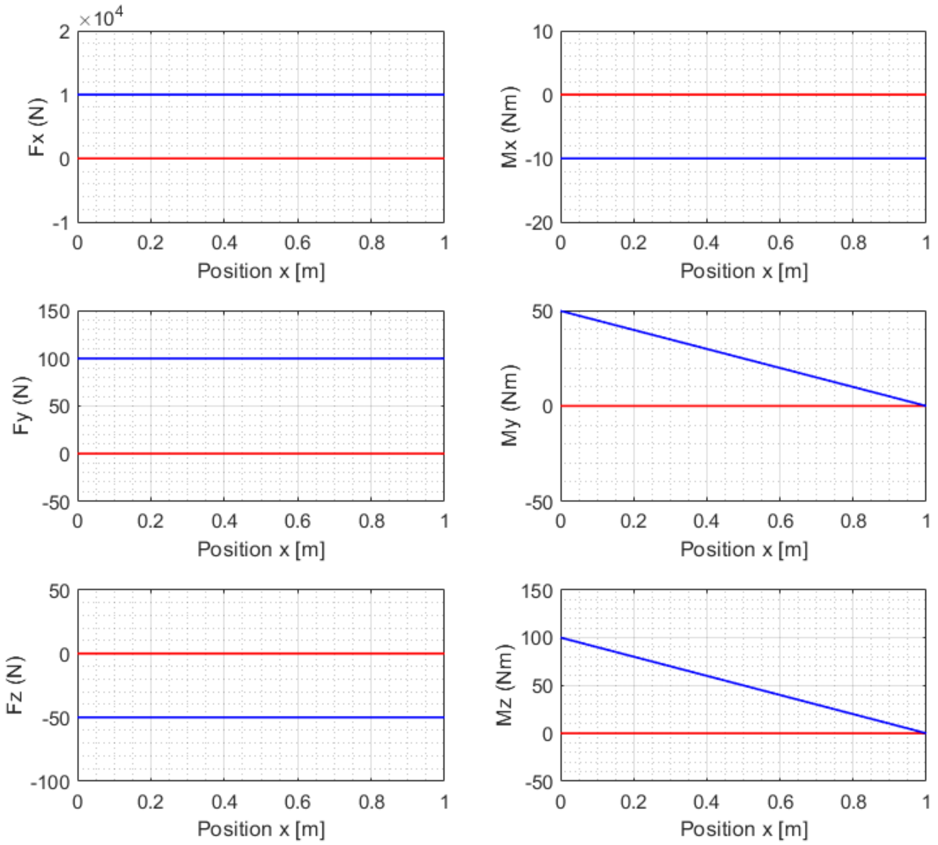

FIGURE C.1: Load diagrams obtained analytically [MATLAB].

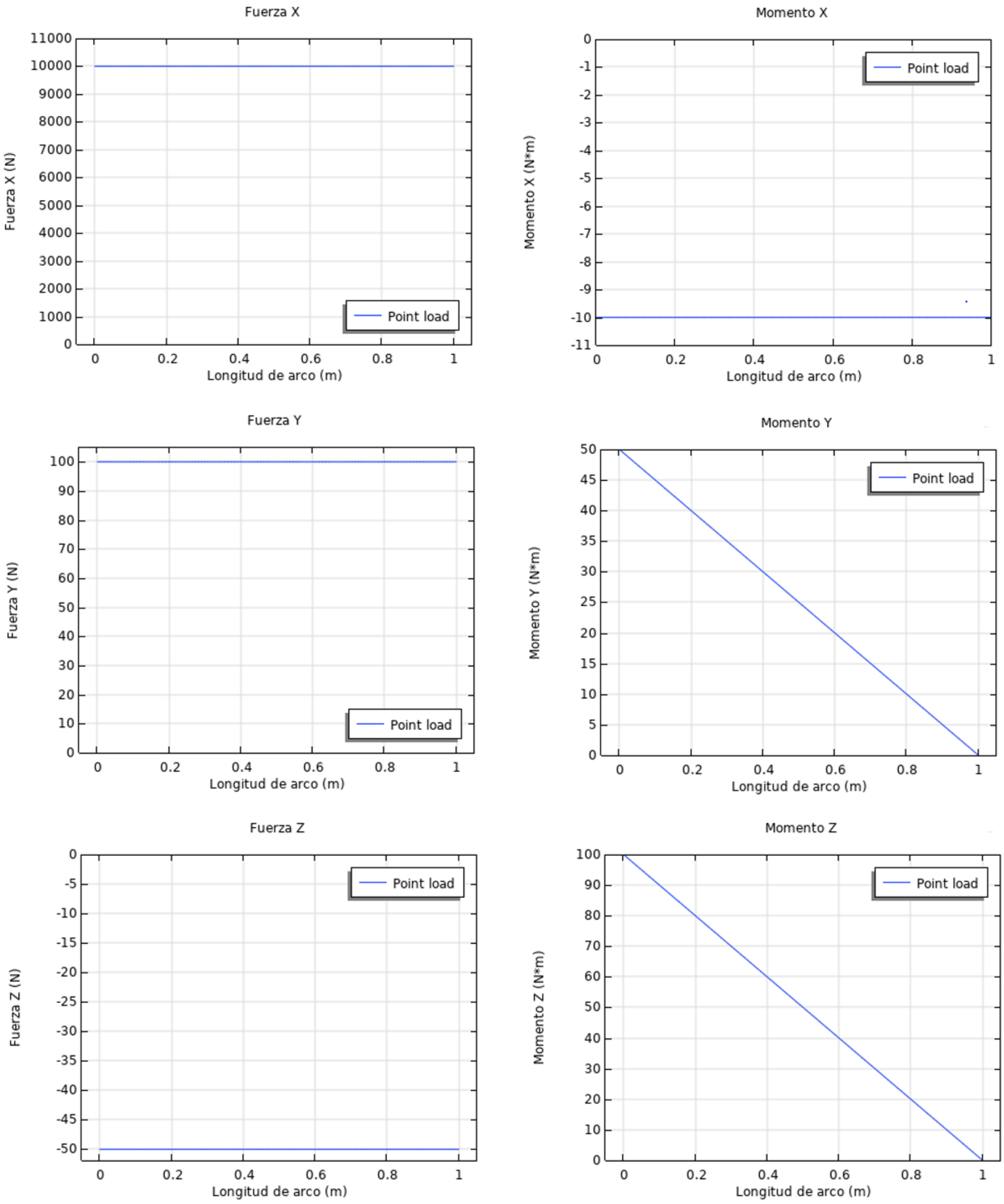

FIGURE C.2: Load diagrams [COMSOL].

Comparing figures C.1 and C.2, it can be considered that the results obtained using both methods agree. As seen in both figures, the axial force remains constant and equal to 10000 N and the forces in the y and z-direction also are constant along the beam and equal to 100 N and -50 N respectively. Moreover, although the torsion moment remains constant and equal to -10 Nm along the beam, bending moments present a linear distribution with a maximum located on the beginning of the beam and a minimum equal to 0 Nm at its end.

Total axial stress

Axial Stress is a measure of the axial force acting on a beam. However, not only is axial force the only external load contributing to the total axial stress, but also bending moments (y and z). The expression used to compute the total axial stress along the beam is:

$$\sigma = \frac{F_x}{A} - \frac{M_z}{I_{zz}} \cdot y + \frac{M_y}{I_{yy}} \cdot z \tag{C.1}$$

Considering that the locations of the most critical points of the section are its corners, the previous expression will be plotted by each of them in order to define the coordinate at which the axial stress is maximum.

$$P1 = (-0.025, -0.0164) \qquad P3 = (0.025, -0.0164) \tag{C.2}$$

$$P2 = (-0.025, 0.0086) \qquad P4 = (0.025, 0.0086) \tag{C.3}$$

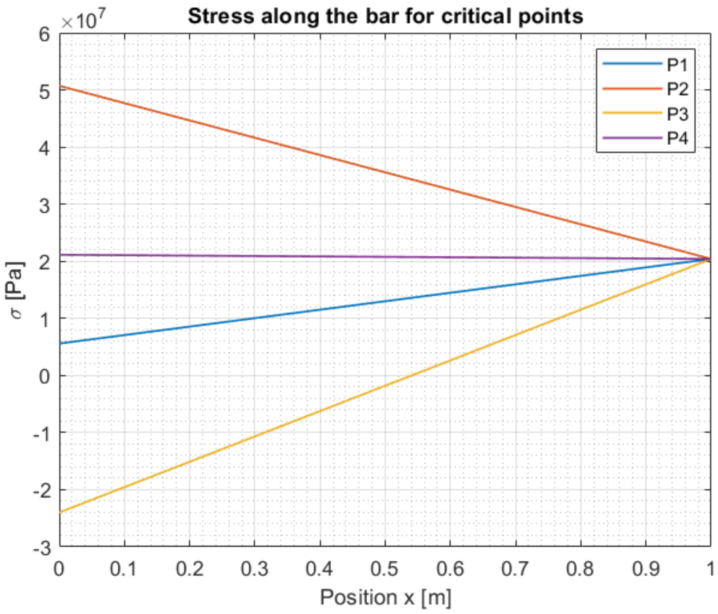

FIGURE C.3: Axial stress distribution obtained for the four most demanding points of the section [MATLAB].

Figure C.3 shows the axial stress distribution along the beam for the four most demanding points of the section. Whereas in x=0m the axial stress of the four points is far for being the same, at the end of the beam, where x=1m, the axial stress of the four point is the same and equal to 2Pa. Finally, comparing the different axial stress distributions of the four points evaluated, the second point is the most critical one in terms of axial stress.

Total shear stress τ

Shear stress is the component of stress co-planar with a material cross section. It arises from the shear force, the component of the force vector parallel to the material cross section, and from the torsion moment. Furthermore, total shear stress can be computed in two directions: y and z. The expression used to compute the shear stress in both directions is:

$$\tau_{xy} = \mu_y \frac{F_y}{A} + \frac{M_x}{W_t} \tag{C.4}$$

$$\tau_{xz} = \mu_z \frac{F_z}{A} + \frac{M_x}{W_t} \tag{C.5}$$

Von Misses Stress

Von Mises stress is a value used to determine if a given material will yield or fracture. It is mostly used for ductile materials, such as metals. Von Mises yield criterion states that if the Von Mises stress of a material under a certain load is equal or greater than the yield limit of the same material under simple stress, then the material will yield.

Usually in a beam only 3 of the 6 components of the stress tensor are different from zero: the normal stress in the cross section and two independent components associated with the tangential stress, in this case the main stresses turn out to be:

$$\sigma_1 = \frac{\sigma + \sqrt{\sigma^2 + 4 \cdot (\tau_{xy}^2 + \tau_{xz}^2)}}{2} \tag{C.6}$$

$$\sigma_2 = 0 \tag{C.7}$$

$$\sigma_3 = \frac{\sigma - \sqrt{\sigma^2 + 4 \cdot (\tau_{xy}^2 + \tau_{xz}^2)}}{2} \tag{C.8}$$

Von Mises stress can be computed with the following expression using the axial stress distribution obtained for the second point which is the most critical.

$$\sigma_{VM} = \sqrt{\sigma^2 + 3 \cdot \tau_{xy}^2 + 3 \cdot \tau_{xz}^2} \tag{C.9}$$

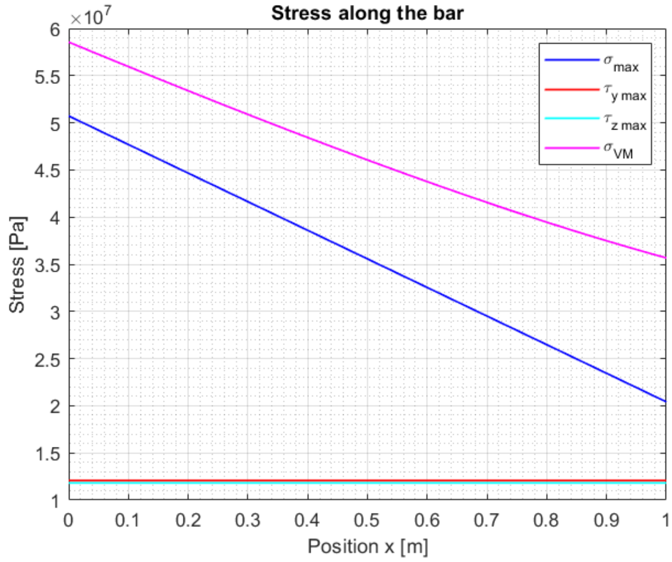

FIGURE C.4: Von Mises stress, total axial stress and both shear moment distributions along the beam [MATLAB].

Figure C.4 shows graphically the Von Mises stress, the total axial stress and both shear moment distributions along the beam. Whereas the axial stress presents a linear distribution with its maximum at the beginning of the beam and a minimum at its end, the shear moment distributions along the beam remain constant. Furthermore, Von Mises stress distribution is maximum at the beginning of the beam and minimum at the end.

Finally, figure C.5 compares the results obtained analytically and numerically using COMSOL.

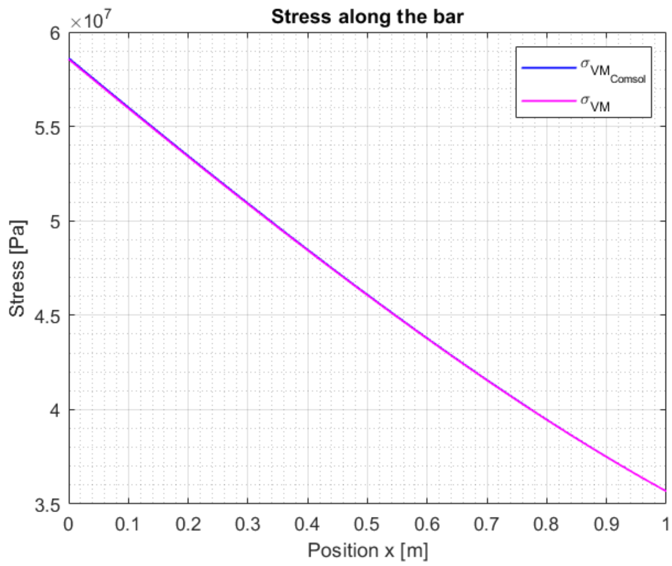

FIGURE C.5: Von Misses distribution along the beam computed analytically and numerically with the use of COMSOL [MATLAB].

Figure C.5 shows the convergence of the analytical and numerical solution. Von Mises stress distribution along the beam decreases when moving to the end of the bar. Its maximum is located at the beginning of the beam where x=0m, whereas its minimum is located at the free end where x=1m. Figure C.6 is made with COMSOL and shows the Von Mises stress distribution along the cantilever beam with the color bar, as well as, the deformation of the beam in the xy plane.

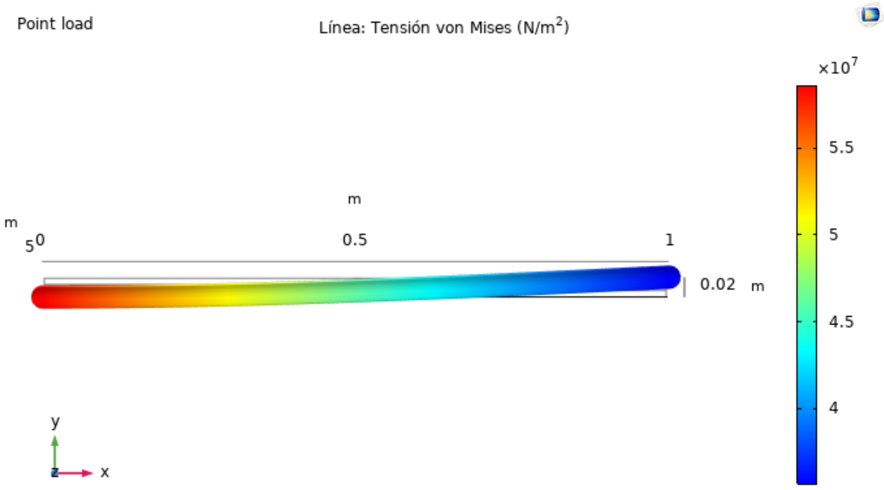

FIGURE C.6: Von Misses distribution along the beam computed with COMSOL and its deformation [COMSOL].

C.1.3 Second Study

The aim of the second study is to observe what happens when changing the dimensions of the section of the beam as well as its orientation. So, in this case, the moments of inertia will be computed for each case separately depending on the dimensions of the section.

Area of the section

In the first place, it will be studied the impact that the dimensions of the section of the cantilever beam have on the Von Mises stress distribution. In this case, the area of the section will change throughout the study. Some parameters such as h_1, h_2 and t will vary in order to see how the Von Mises stress distributions changes. For that reason it is necessary to define a general expression to compute the area in each iteration of the program.

$$A = (h_1 - 2t) \cdot t + 2h_2 t \tag{C.10}$$

Center of gravity

The center of mass or the center of gravity of a certain mass distribution in space is the unique point where the weighted relative position of the distributed mass sum is equal to zero. In this case, as the geometry of the section results to be symmetric in the xz plane, the cdg will be located in that plane of symmetry ($y_{cdg} = 0$). Furthermore, the following expression as a function of h_1, h_2 and t will be used to compute z_{cdg} in each iteration of the program.

$$z_{cdg} = \frac{(h_1 - 2t) \cdot t \cdot \left(-\frac{h_2}{2} + \frac{t}{2} \right)}{2h_2 t + (h_1 - 2t) \cdot t} \tag{C.11}$$

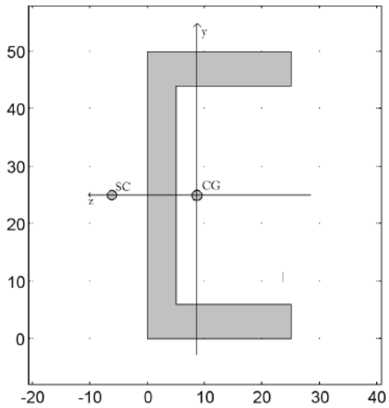

FIGURE C.7: Section of the beam [COMSOL].

Inertia

Another point worth considering is that the area inertial moment will also change when varying the height or the thickness of the profile. Consequentially, it will be needed a general expression. The I_{zz} and the I_{yy} general expressions for the section presented in figure C.11 are the following.

$$I_{zz_1} = \frac{t \cdot h_2^3}{12} + h_2 \cdot t \cdot z_{cdg}^2 \tag{C.12}$$

$$I_{zz_2} = \frac{(h_1 - 2t) \cdot t^3}{12} + (h_1 - 2t) \cdot t \cdot \left(z_{cdg} - \frac{h_2}{2} + \frac{t}{2} \right)^2 \tag{C.13}$$

$$I_{zz} = 2 \cdot I_{zz_1} + I_{zz_2} \tag{C.14}$$

$$I_{yy_1} = \frac{t^3 \cdot h_2}{12} + h_2 \cdot t \cdot \left(\frac{h_1}{2} - \frac{t}{2}\right)^2 \quad (C.15)$$

$$I_{yy_2} = \frac{(h_1 - 2t)^3 \cdot t}{12} \quad (C.16)$$

$$I_{yy} = 2 \cdot I_{yy_1} + I_{yy_2} \quad (C.17)$$

Von Mises stress

Finally, the Von Mises stress distribution for the critical point of the profile (P2) considering different dimensions of the profile have been calculated and the results obtained have been the following.

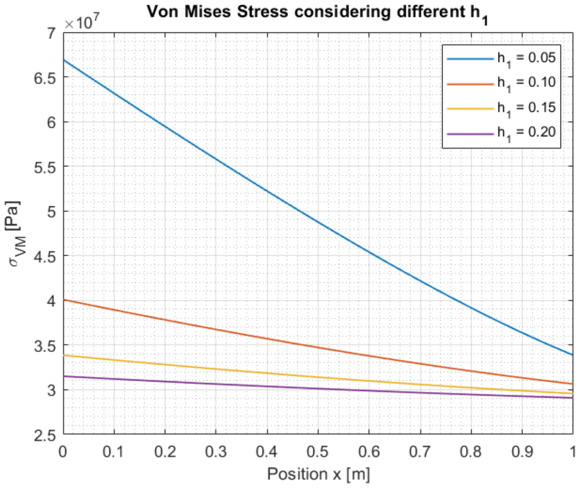

FIGURE C.8: Von Mises stress distribution along the cantilever beam for different heights of the profile [MATLAB].

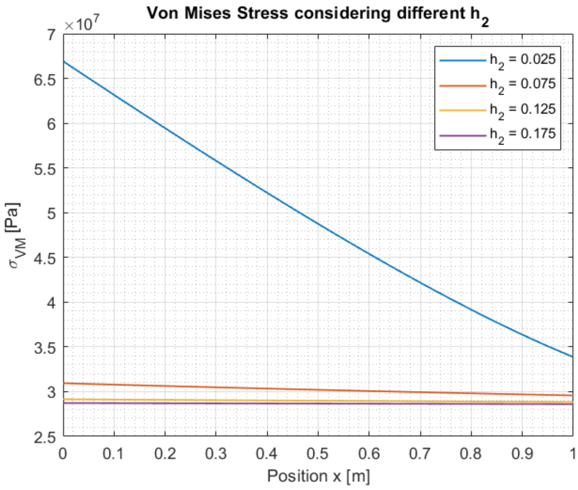

FIGURE C.9: Von Mises stress distribution along the cantilever beam for different widths of the profile [MATLAB].

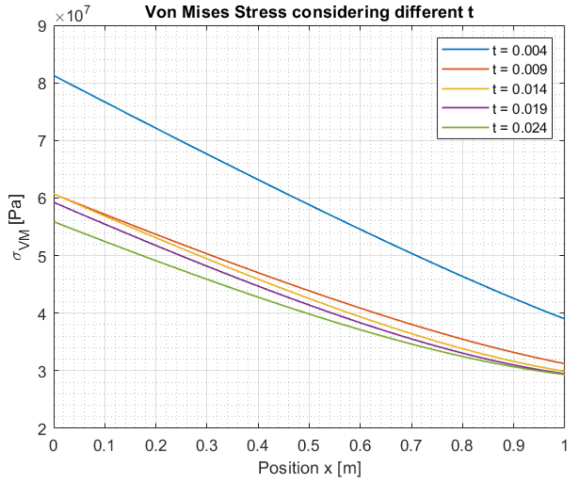

FIGURE C.10: Von Mises stress distribution along the cantilever beam for different thickness of the profile [MATLAB].

Figures C.12, C.13 and C.14 show the Von Mises stress distributions obtained for different values of height, width and thickness of the profile of the beam respectively. When decreasing the height, the width or the thickness of the section, Von Mises stress along the beam increases which means that the structure could break easily.

Center of gravity

The next step is to orientate the section differently in order to study the Von Misses stress distribution along the beam for different orientations. In this case, as the geometry of the section results to be symmetric in the xy plane, the cdg will be located in that plane of symmetry ($z_{cdg} = 0$). Furthermore, the following expression as a function of h_1, h_2 and t will be used to compute y_{cdg} in each iteration of the program.

$$y_{cdg} = \frac{(h_1 - 2t) \cdot t \cdot \left(-\frac{h_2}{2} + \frac{t}{2}\right)}{2h_2 t + (h_1 - 2t) \cdot t} \tag{C.18}$$

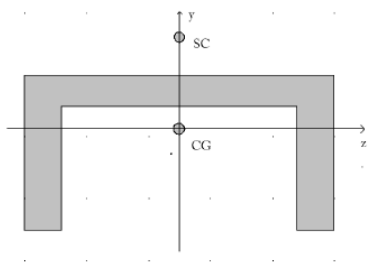

FIGURE C.11: Reoriented section of the beam [COMSOL].

Inertia

Another point worth considering is that the area inertial moment will also change when varying the height or the thickness of the profile. Consequentially, the I_{zz} and the I_{yy} general expressions for the section presented in figure C.11 are the following.

$$I_{yy_1} = \frac{t \cdot h_2^3}{12} + h_2 \cdot t \cdot y_{cdg}^2 \tag{C.19}$$

$$I_{yy_2} = \frac{(h_1 - 2t) \cdot t^3}{12} + (h_1 - 2t) \cdot t \cdot \left(z_{cdg} - \frac{h_2}{2} + \frac{t}{2} \right)^2 \tag{C.20}$$

$$I_{yy} = 2 \cdot I_{yy_1} + I_{yy_2} \tag{C.21}$$

$$I_{zz_1} = \frac{t^3 \cdot h_2}{12} + h_2 \cdot t \cdot \left(\frac{h_1}{2} - \frac{t}{2} \right)^2 \tag{C.22}$$

$$I_{zz_2} = \frac{(h_1 - 2t)^3 \cdot t}{12} \tag{C.23}$$

$$I_{zz} = 2 \cdot I_{zz_1} + I_{zz_2} \tag{C.24}$$

Von Mises stress

Finally, the Von Mises stress distribution for the critical point of the profile (P2) considering different dimensions of the profile have been calculated and the results obtained have been the following.

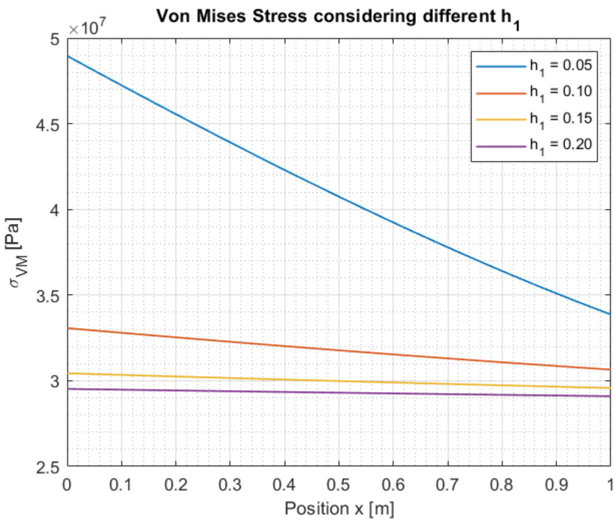

FIGURE C.12: Von Mises stress distribution along the reoriented cantilever beam for different heights of the profile [MATLAB].

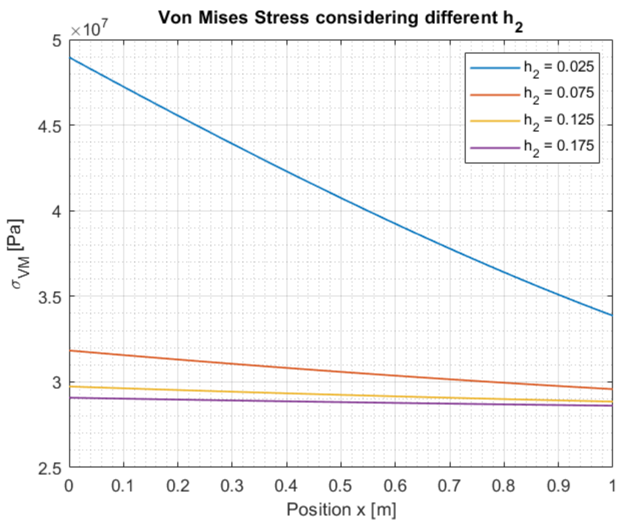

FIGURE C.13: Von Mises stress distribution along the reoriented cantilever beam for different widths of the profile [MATLAB].

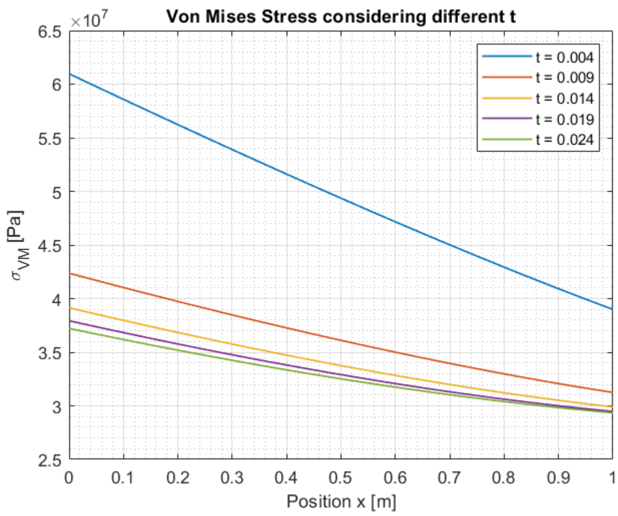

FIGURE C.14: Von Mises stress distribution along the reoriented cantilever beam for different thickness of the profile [MATLAB].

As a result of orientating the section differently, the Von Misses stress obtained for the same height, width and thickness decreases. It means that, by orientating the section in a different way, the beam presents a lower stress distribution due to the fact that in y-direction the component of the force applied is much higher than the z-component. As a result, the correct positioning of the profile should be this second studied orientation.

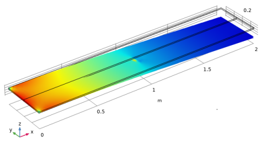

POLYTECHNIC UNIVERSITY OF CATALONIA
Structural Mechanics
Comsol

C.2 Report 2: Thin Plate

The aim of this study is to evaluate a thin plate under certain load conditions and, in order to study its behaviour, it has been considered to divide the report in different parts. At first, it will be plotted the Von Mises stress distribution along the shell considering three different boundary conditions. Then, the convergence of the mesh has been studied in order to get a better perspective of what occurs when changing it. As a third study, the shear force along the shell has been plotted considering different punctual loads along its center line. In addition, the different momentum components have been plotted as well considering a distributed face load applied on the surface of the shell. Finally, it has been carried on a complete study in which it has been applied punctual loads and moments and a distributed face load.

C.2.1 Model definition

First, the geometry and the material of the rectangular thin plate studied will be defined.

Geometry

- Shell dimensions: 2,00 x 0,40 m
- Shell thickness: 0.01 m

Material

- Material used: structural steel.
- Young's modulus, E = 200 GPa.
- Poisson's ratio, $\nu = 0.33$.
- Mass density, $\rho = 7850 kg/m^3$.

C.2.2 Von Mises distribution for different loads

Then, a brief study applying three different boundary conditions has been carried on. The main reason for doing so is the necessity of knowing what effects have loads separately on the shell. So, the displacements and the Von Mises stress distributions will be plotted and analysed for three different load conditions: a punctual load applied at the end of the shell, a punctual moment applied on the middle of the shell and a distributed load applied along the surface of the shell.

Boundary Conditions 1

- The beginning of the shell is fixed (x=0 m).
- In the middle of the ending edge of the shell a punctual force is applied (Fz = -500 N).

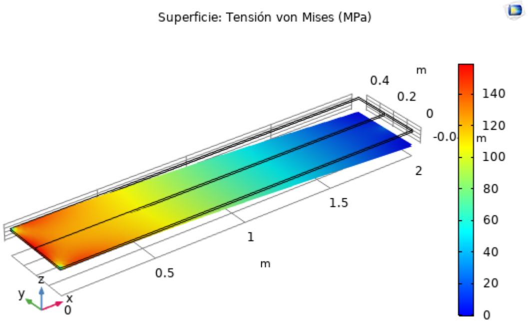

FIGURE C.15: Von Mises stress distribution along the thin plate considering boundary conditions 1 [COMSOL].

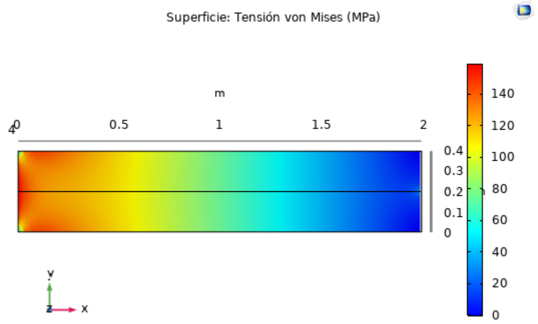

FIGURE C.16: Von Mises stress distribution along the thin plate considering boundary conditions 1 [COMSOL].

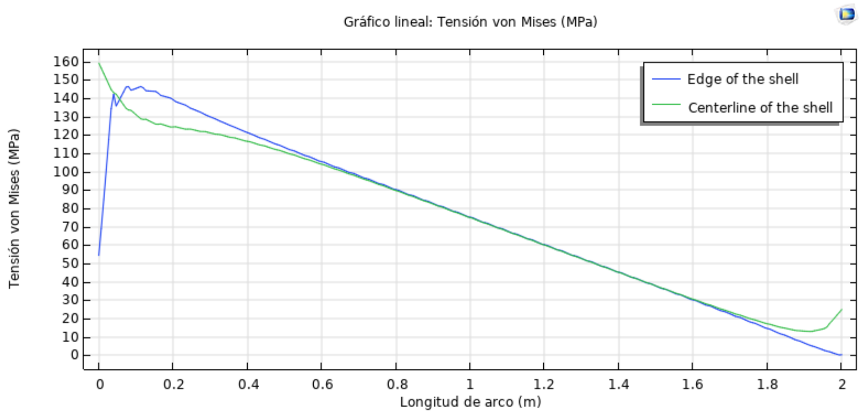

FIGURE C.17: Von Mises stress distribution along the center line and an edge of the thin plate considering boundary conditions 1 [COMSOL].

Figure C.15 shows the displacement distribution of the shell as well as the Von Mises stress distribution. It can be seen that, whereas the displacement is maximum at the end of the shell, Von Mises stress is maximum at the beginning of the shell where it is fixed. Furthermore, figure C.17 presents the Von Mises stress distributions obtained for two different lines of the shell: one edge of the shell and its center line. Although both functions converge in the middle positions of the shell, at the beginning and at the end of the shell there is not an agreement of both plots. The Von Mises stress distribution obtained for the edge of the shell presents its maximum at x=0.1 m and its minimum at the end of the thin plate, whereas the Von Mises stress distribution obtained for the center line of the plate presents its maximum at the beginning where x=0 m and its minimum where x=1.9 m approximately.

Boundary Conditions 2

- The beginning of the shell is fixed (x=0m).
- In the middle of the shell a punctual moment is applied (My = 500 Nm).

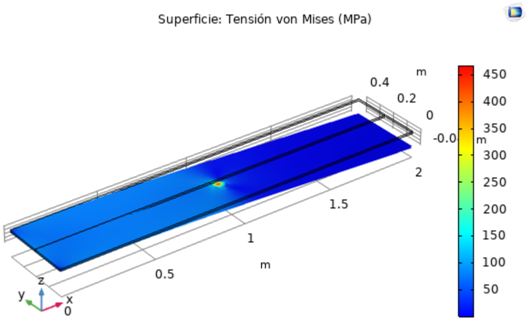

FIGURE C.18: Von Mises stress distribution along the thin plate considering boundary conditions 2 [COMSOL].

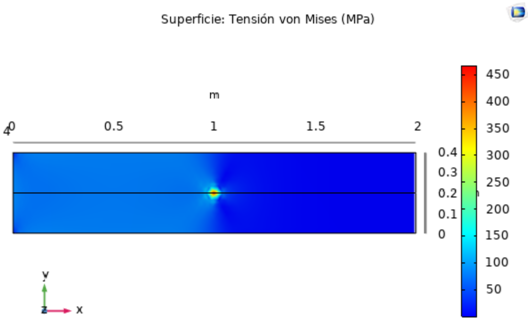

FIGURE C.19: Von Mises stress distribution along the thin plate considering boundary conditions 2 [COMSOL].

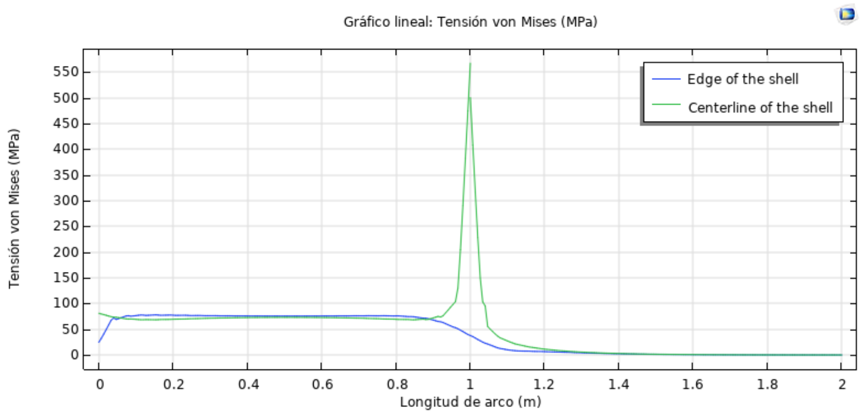

FIGURE C.20: Von Mises stress distribution along the center line and an edge of the thin plate considering boundary conditions 2 [COMSOL].

Figure C.18 shows the displacement distribution of the shell as well as the Von Mises stress distribution. It can be seen that, whereas the displacement is maximum at the end of the shell, Von Mises stress is maximum in the middle where the punctual moment is applied. Furthermore, figure C.20 presents the Von Mises stress distributions obtained for two different lines of the shell: one edge of the shell and its center line. Although both functions almost fully converge, in the middle positions of the shell where the punctual moment is applied there is not total agreement of both plots. The Von Mises stress distribution obtained for the edge of the shell presents its maximum in the first half of the shell, before the moment is applied, and the second half of the function remains constant and equal to 0. In contrast, the Von Mises stress distribution obtained for the center line of the shell presents its maximum in the middle of the shell where x=1 m, point at which the punctual moment is applied.

Boundary Conditions 3

- The beginning of the shell is fixed (x=0 m).
- Over the whole shell a face load of 5 kPa is applied.

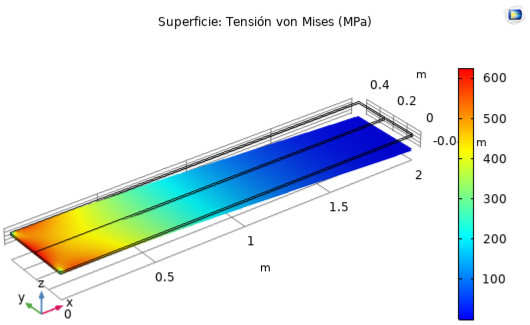

FIGURE C.21: Von Mises stress distribution along the thin plate considering boundary conditions 3 [COMSOL].

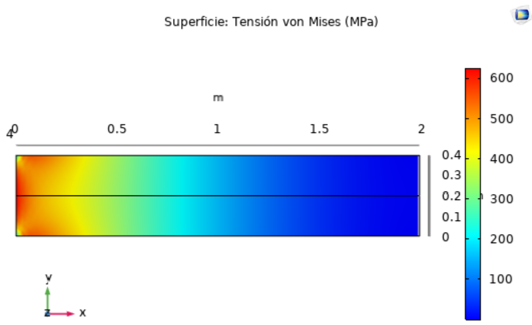

FIGURE C.22: Von Mises stress distribution along the thin plate considering boundary conditions 3 [COMSOL].

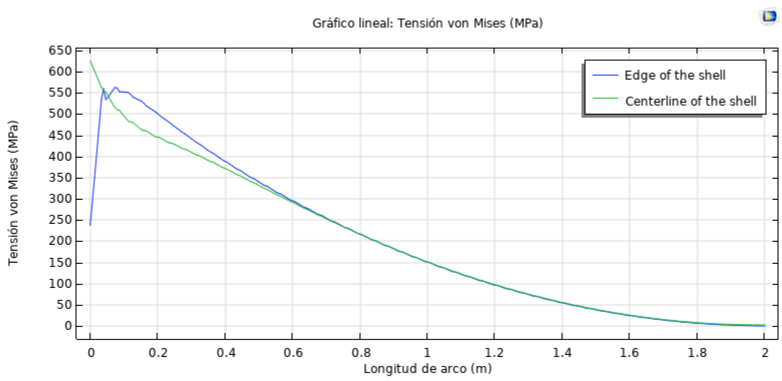

FIGURE C.23: Von Mises stress distribution along the center line and an edge of the thin plate considering boundary conditions 3 [COMSOL].

Figure C.21 shows the displacement distribution of the shell as well as the Von Mises stress distribution for boundary conditions 3. It can be seen that, whereas the displacement is maximum at the end of the shell, Von Mises stress is maximum at the beginning. Moreover, figure C.23 presents the Von Mises stress distributions obtained for two different lines of the shell: one edge of the shell and its center line. Although both functions almost fully converge, at the beginning positions of the shell there is not complete agreement of both plots. The Von Mises stress distribution obtained for the edge of the shell presents its maximum at x=0.1 m and its minimum at the end of the shell, whereas the Von Mises stress distribution obtained for the center line of the shell presents its maximum at the beginning where x=0 m and its minimum at the end of the shell.

C.2.3 Von Mises distribution for different meshes

In this second section it will be studied the differences obtained in the Von Mises stress distribution due to the mesh used in each case. Second boundary condition from the previous section will be considered and evaluated for different mesh distributions. Finally, the results obtained with COMSOL have been the following.

- **Triangular mesh 1.** Maximum element size = 0.5 m

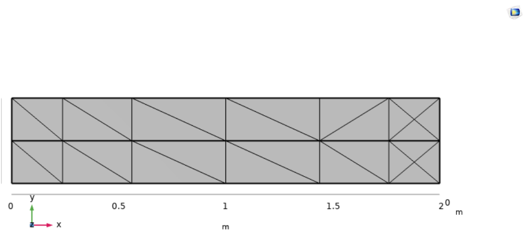

FIGURE C.24: Triangular mesh 1 [COMSOL].

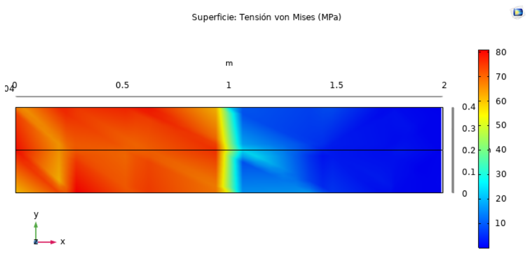

FIGURE C.25: Von Mises stress distribution along the shell obtained using the triangular mesh 1 [COMSOL].

- **Triangular mesh 2.** Maximum element size = 0.25 m

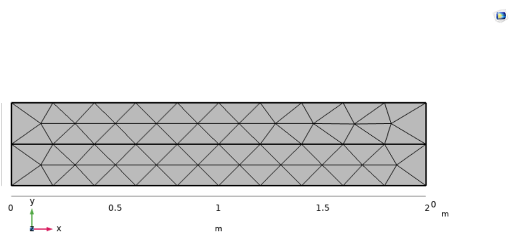

FIGURE C.26: Triangular mesh 2 [COMSOL].

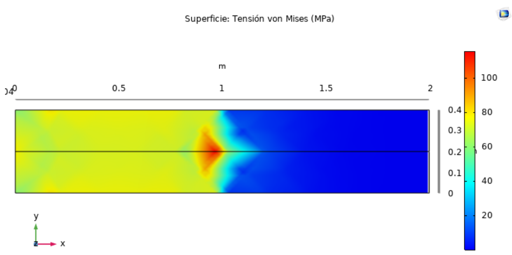

FIGURE C.27: Von Mises stress distribution along the shell obtained using the triangular mesh 2 [COMSOL].

- **Triangular mesh 3.** Maximum element size = 0.125 m

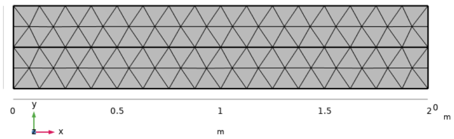

FIGURE C.28: Triangular mesh 3 [COMSOL].

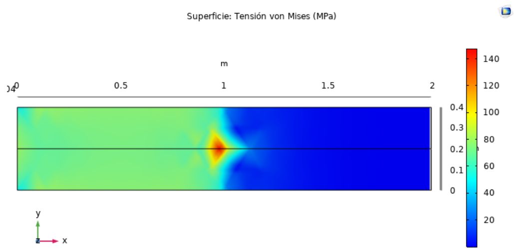

FIGURE C.29: Von Mises stress distribution along the shell obtained using the triangular mesh 3 [COMSOL].

- **Triangular mesh 4.** Maximum element size = 0.0625 m

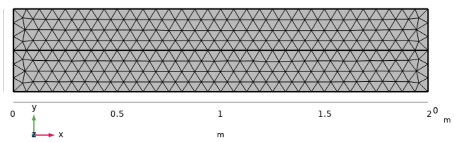

FIGURE C.30: Triangular mesh 4 [COMSOL].

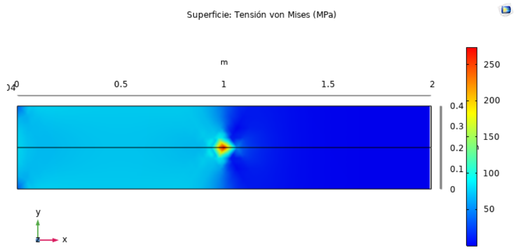

FIGURE C.31: Von Mises stress distribution along the shell obtained using the triangular mesh 4 [COMSOL].

- **Triangular mesh 5.** Maximum element size = 0.03125 m

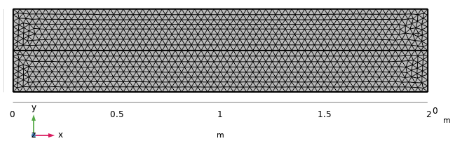

FIGURE C.32: Triangular mesh 5 [COMSOL].

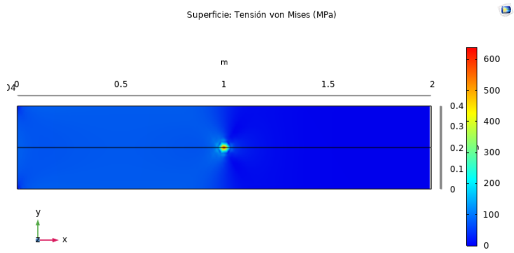

FIGURE C.33: Von Mises stress distribution along the shell obtained using the triangular mesh 5 [COMSOL].

- **Triangular mesh 6.** Maximum element size = 0.015625 m

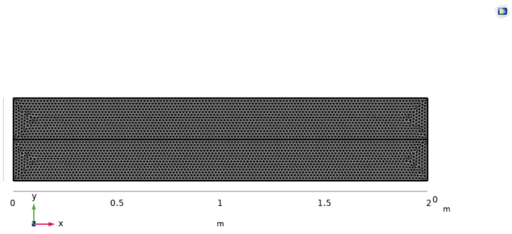

FIGURE C.34: Triangular mesh 6 [COMSOL].

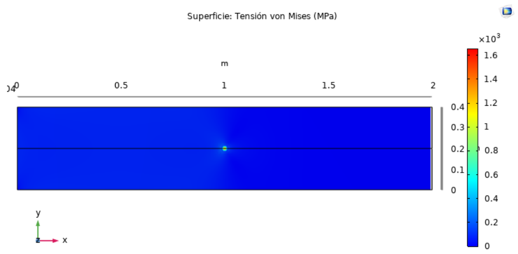

FIGURE C.35: Von Mises stress distribution along the shell obtained using the triangular mesh 6 [COMSOL].

Then, the different Von Mises stress distributions along the shell obtained for the six meshes used have been plotted in two graphics. The first plot consists in the Von Mises stress distribution of the lateral edge of the shell and, the second one, the Von Mises stress distribution obtained for the center line of the shell.

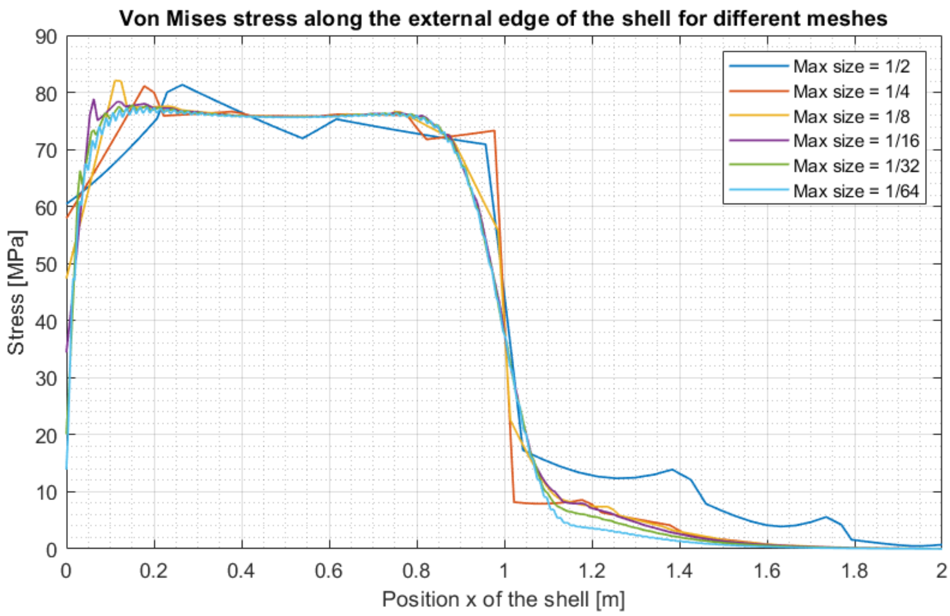

FIGURE C.36: Von Mises stress distribution along the external edge of the shell using different triangular element meshes [MATLAB].

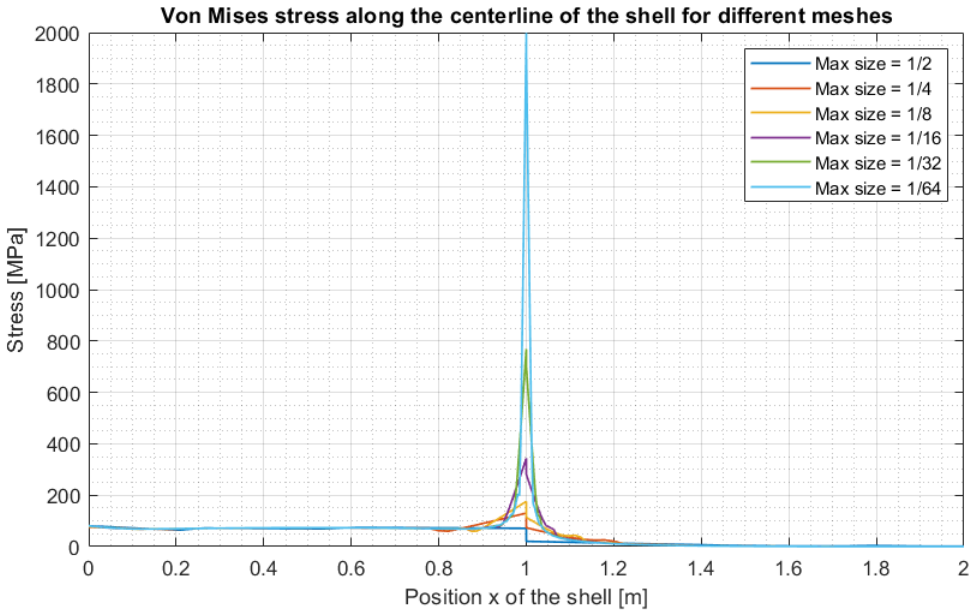

FIGURE C.37: Von Mises stress distribution along the center line of the shell using different triangular element meshes [MATLAB].

Figure C.36 shows the Von Mises stress distribution obtained along the external edge of the shell considering different meshes. It can be concluded that the more number of discretisations used, the more precision is obtained. Moreover, for smaller sizes than 1/16 the function obtained remains almost the same. Furthermore, figure C.37 presents the Von Mises stress distribution obtained along the center line of the shell considering different meshes. In this case, with the decrease of the element size, the maximum Von Mises stress located in the middle of the plate increases.

Then, it has been carried on the same study considering a quadrilateral element discretisation instead of using triangular elements.

- **Quadrilateral mesh 1.** Maximum element size = 0.5 m

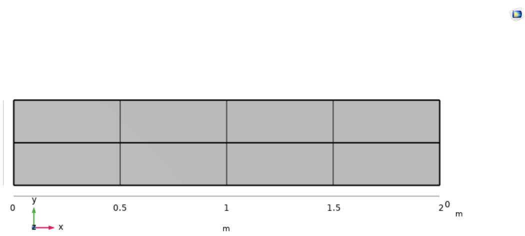

FIGURE C.38: Quadrilateral mesh 1 [COMSOL].

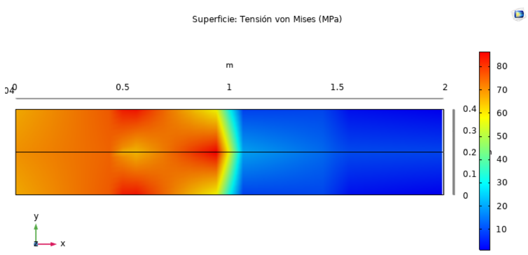

FIGURE C.39: Von Mises stress distribution along the shell obtained using the quadrilateral mesh 1 [COMSOL].

- **Quadrilateral mesh 2.** Maximum element size = 0.25 m

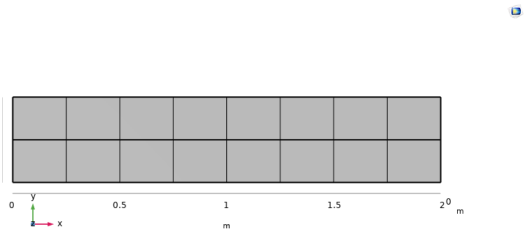

FIGURE C.40: Quadrilateral mesh 2 [COMSOL].

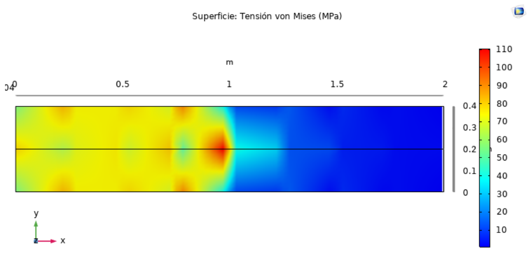

FIGURE C.41: Von Mises stress distribution along the shell obtained using the quadrilateral mesh 2 [COMSOL].

- **Quadrilateral mesh 3.** Maximum element size = 0.125 m

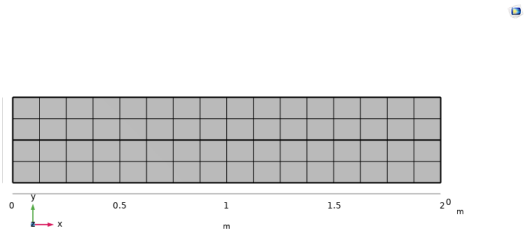

FIGURE C.42: Quadrilateral mesh 3 [COMSOL].

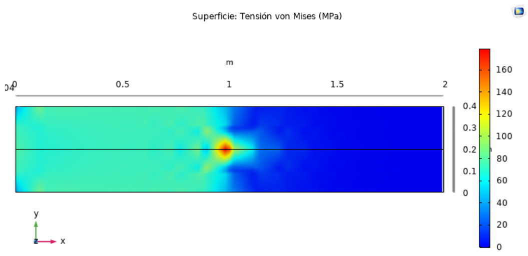

FIGURE C.43: Von Mises stress distribution along the shell obtained using the quadrilateral mesh 3 [COMSOL].

- **Quadrilateral mesh 4.** Maximum element size = 0.0625 m

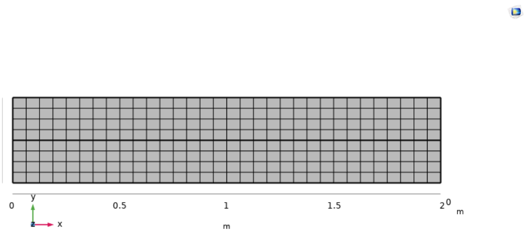

FIGURE C.44: Quadrilateral mesh 4 [COMSOL].

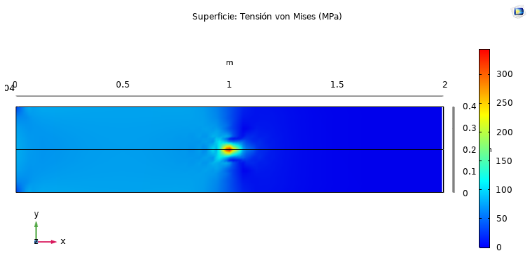

FIGURE C.45: Von Mises stress distribution along the shell obtained using the quadrilateral mesh 4 [COMSOL].

- **Quadrilateral mesh 5.** Maximum element size = 0.03125 m

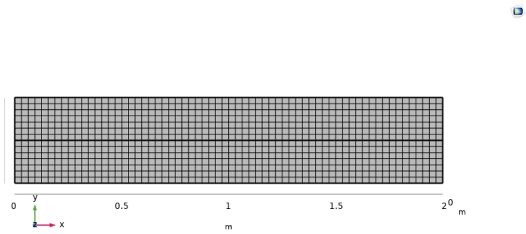

FIGURE C.46: Quadrilateral mesh 5 [COMSOL].

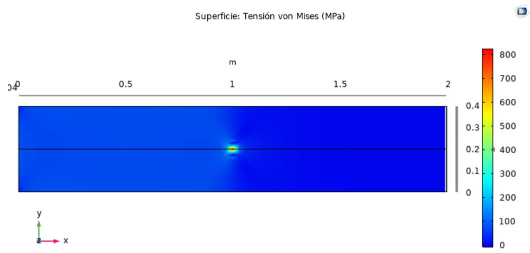

FIGURE C.47: Von Mises stress distribution along the shell obtained using the quadrilateral mesh 5 [COMSOL].

- **Quadrilateral mesh 6.** Maximum element size = 0.015625 m

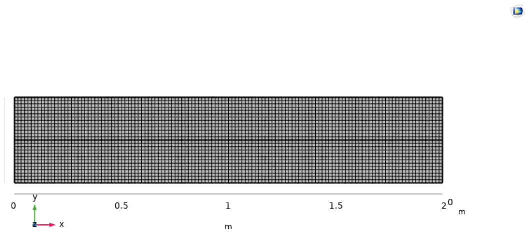

FIGURE C.48: Quadrilateral mesh 6 [COMSOL].

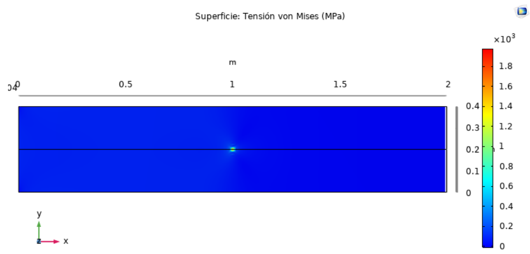

FIGURE C.49: Von Mises stress distribution along the shell obtained using the quadrilateral mesh 6 [COMSOL].

Then, the different Von Mises stress distributions along the shell obtained for the six different meshes have been plotted in two graphics. The first plot consists in the stress distribution of the lateral edge of the shell and, the second one, of the stress distribution on the center line of the shell.

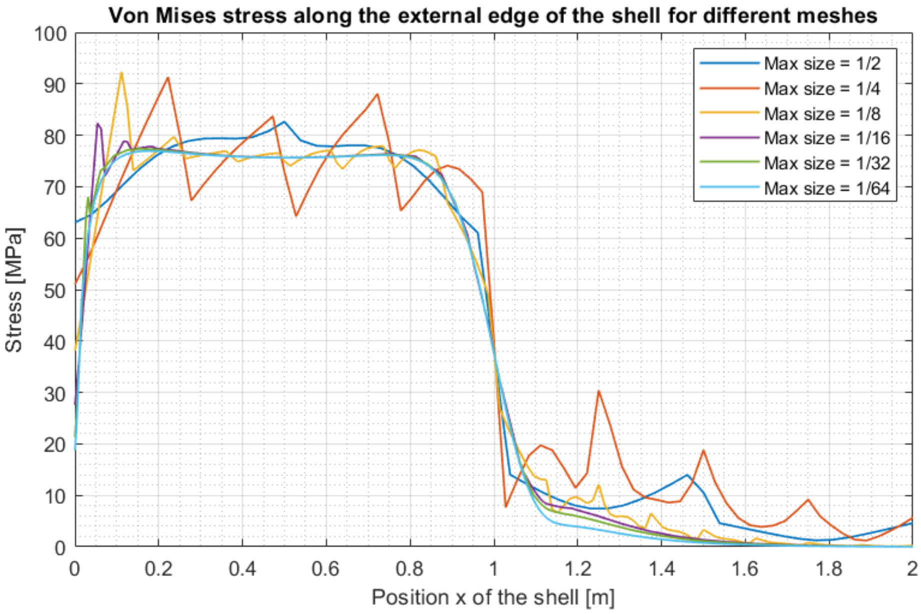

FIGURE C.50: Von Mises stress distribution along the external edge of the shell using different quadrilateral element meshes [MATLAB].

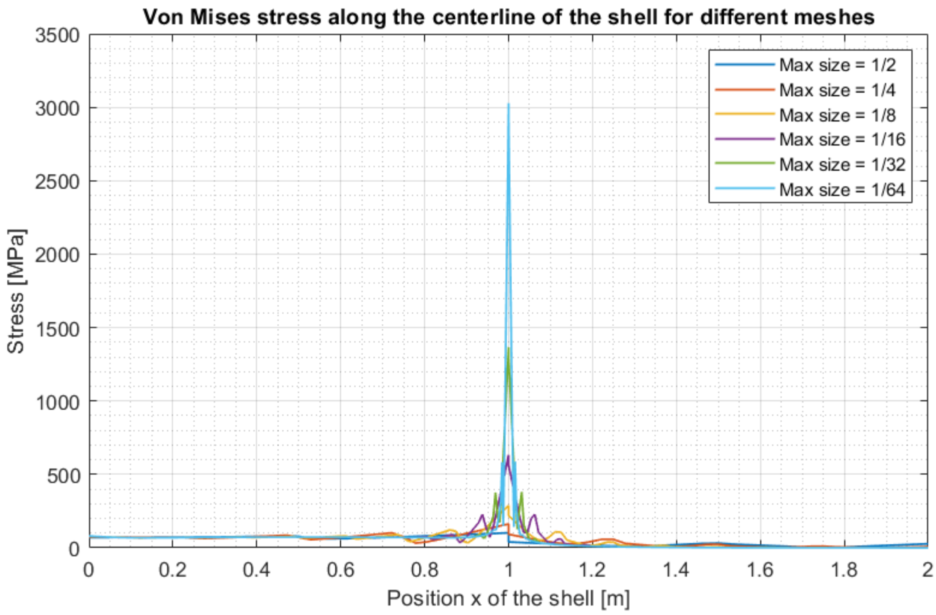

FIGURE C.51: Von Mises stress distribution along the center line of the shell using different quadrilateral element meshes [MATLAB].

Figure C.50 shows the Von Mises stress distribution obtained along the external edge of the shell considering different quadrilateral meshes. It can be concluded that the more number of discretisations used, the more precision is obtained. Moreover, for smaller sizes than 1/16 the stress distributions obtained remains almost the same. Furthermore, figure C.51 presents the Von Mises stress distribution obtained along the center line of the shell considering different meshes. In this case, with the decrease of the element size, the maximum located in the middle of the shell increases.

C.2.4 Shear force study

Furthermore, the shear force along the shell will be studied by applying different punctual loads along the shell. In figure C.52 is schematised the different loads applied on the shell for this study.

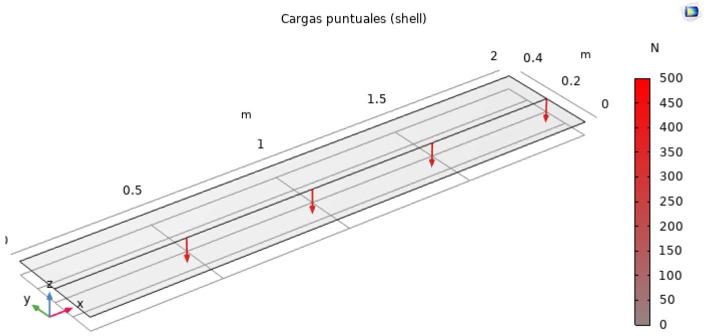

FIGURE C.52: Punctual loads applied on the center line of the shell [COMSOL].

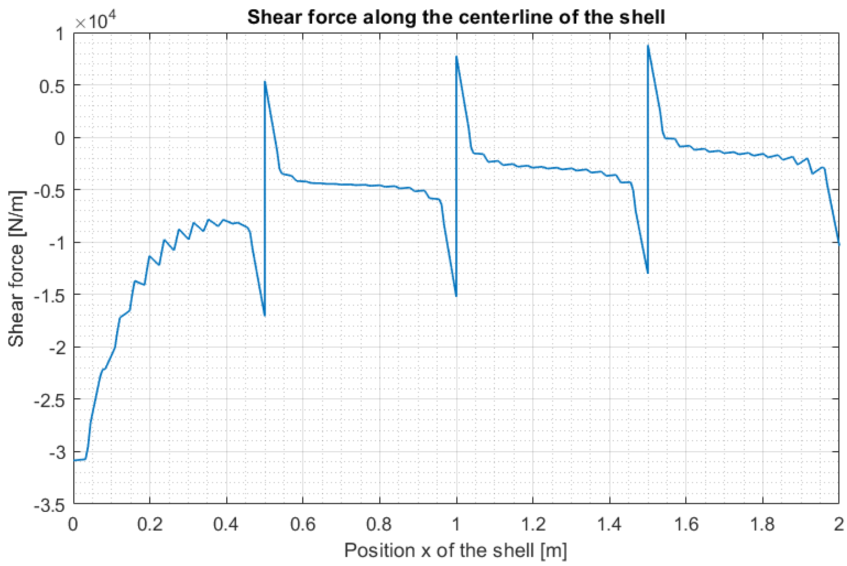

FIGURE C.53: Shear force distribution of the center line of the shell computed with COMSOL [MATLAB].

Figure C.53 shows the shear force distribution along the center line of the shell obtained with COMSOL. It can be seen that where a punctual load is applied, the shear force increases.

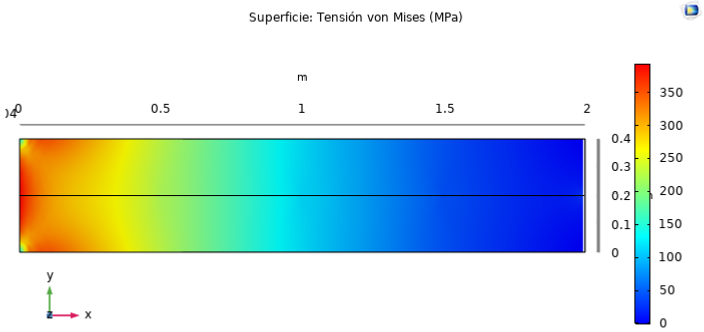

FIGURE C.54: Von Mises stress distribution along the shell [COMSOL].

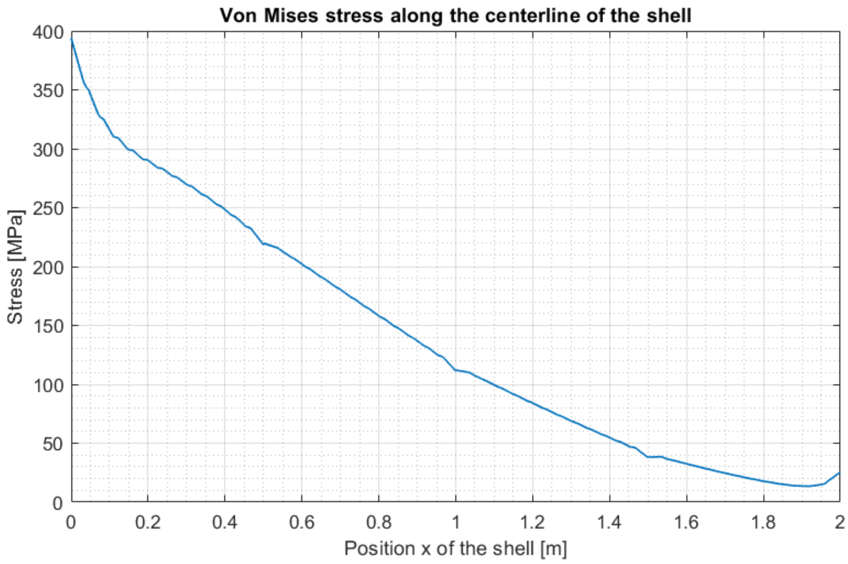

FIGURE C.55: Von Mises stress distribution in the center line of the shell computed with COMSOL [MATLAB].

Furthermore, figure C.55 presents the Von Mises stress distribution obtained along the center line of the shell with COMSOL. The stress decreases when moving to the end of the shell. Moreover, the points at which a force is applied present an small decreasing slope.

C.2.5 Momentum study

In addition, the momentum along the shell will be studied by applying a distributed face load all along the surface of the shell as shown in figure C.56. Additionally, it will be considered that the beginning edge where x=0 m is fixed.

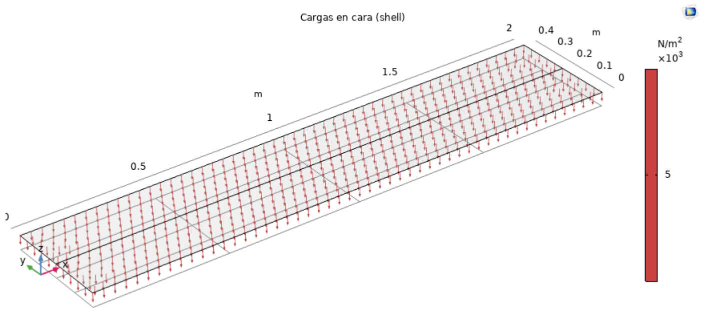

FIGURE C.56: Distributed load applied on the surface of the shell [COMSOL].

Moreover, the Von Mises stress distribution along the surface of the shell has been computed using COMSOL and it can be seen in figure C.57.

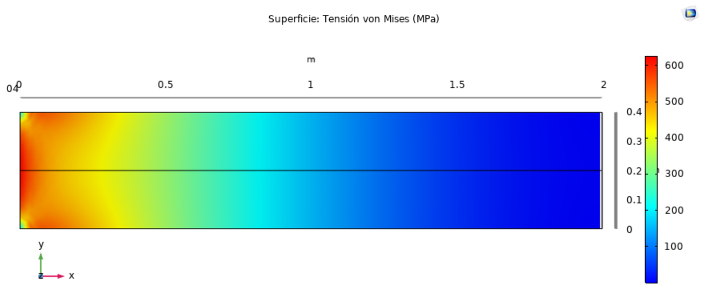

FIGURE C.57: Von Mises stress distribution along the shell when a face load is applied [COMSOL].

As shown in figure C.57, the maximum stress is located on the middle of the beginning edge where x=0 m, whereas its minimum is located at the ending edge where the shell is completely free.

Then, the different components of the momentum have been plotted considering the face load boundary conditions.

- Momentum component 11

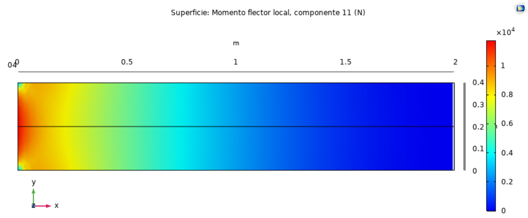

FIGURE C.58: Momentum component 11 along the shell [COMSOL].

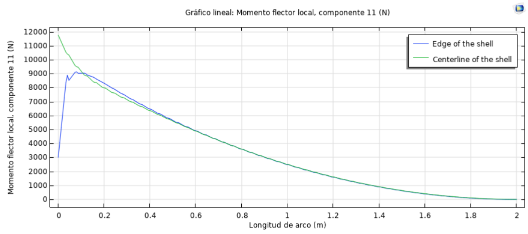

FIGURE C.59: Momentum component 11 along the center line and an external edge of the shell [COMSOL].

- Momentum component 12

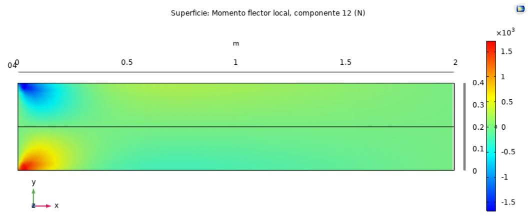

FIGURE C.60: Momentum component 12 along the shell [COMSOL].

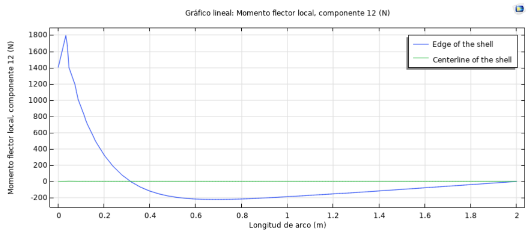

FIGURE C.61: Momentum component 12 along the center line and an external edge of the shell [COMSOL].

- Momentum component 13

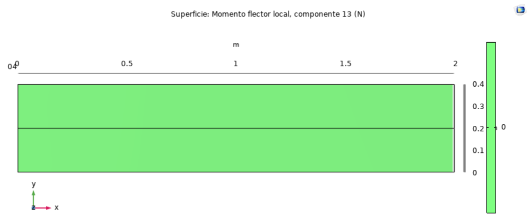

FIGURE C.62: Momentum component 13 along the shell [COMSOL].

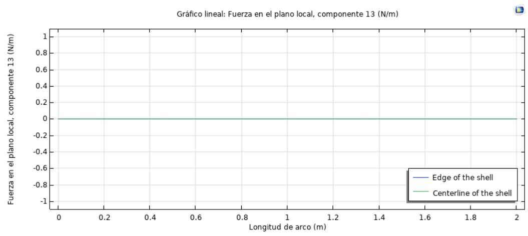

FIGURE C.63: Momentum component 13 along the center line and an external edge of the shell [COMSOL].

- Momentum component 22

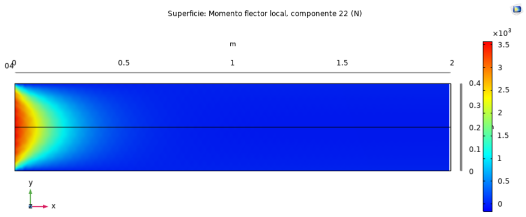

FIGURE C.64: Momentum component 22 along the shell [COMSOL].

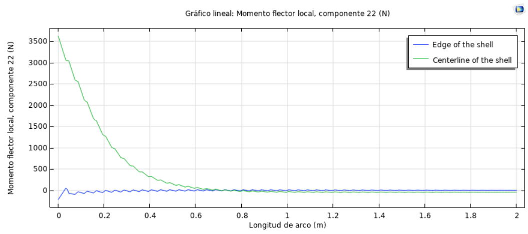

FIGURE C.65: Momentum component 22 along the center line and an external edge of the shell [COMSOL].

- Momentum component 23

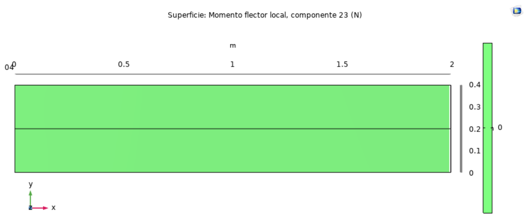

FIGURE C.66: Momentum component 23 along the shell [COMSOL].

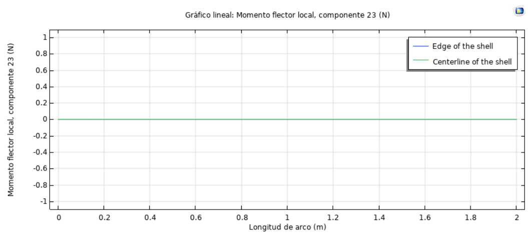

FIGURE C.67: Momentum component 23 along the center line and an external edge of the shell [COMSOL].

- Momentum component 33

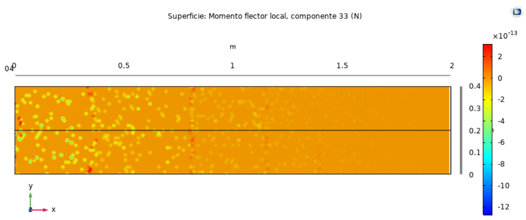

FIGURE C.68: Momentum component 33 along the shell [COMSOL].

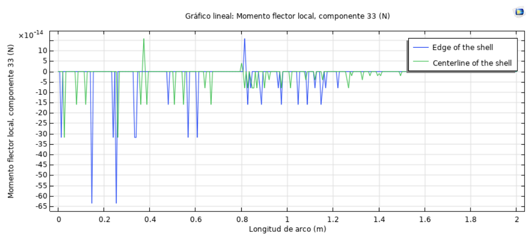

FIGURE C.69: Momentum component 33 along the center line and an external edge of the shell [COMSOL].

Figure C.58 shows the distribution of the momentum component 11 along the shell which is maximum at the beginning edge of the shell where x=0 m and minimum equal to 0 at the end of the shell. In contrast, figures C.60 and C.62 present the distributions of the momentum components 12 and 13 respectively which almost remain constant and equal to 0 along the shell. Moreover, figure C.64 shows the distribution of the momentum component 22 along the shell which is maximum in the middle of the beginning edge of the shell where x=0 m and minimum equal to 0 at the end of the shell. In contrast, figures C.66 and C.68 present the distributions of the momentum components 23 and 33 respectively which remain constant and equal to 0 along the shell.

C.2.6 Complete study

Finally, a complete study has been carried on in which the boundary conditions used have been the ones listed below.

Boundary Conditions

- The beginning of the shell is fixed (x=0 m).
- In the middle point of the ending edge a punctual force is applied (Fz = -500 N).
- In the middle of the shell a punctual moment is applied (My = 500 Nm).
- Over the whole shell a face load of 5kPa is applied.

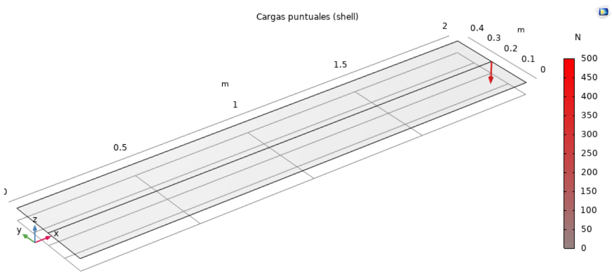

FIGURE C.70: Punctual force applied on the ending edge of the shell [COMSOL].

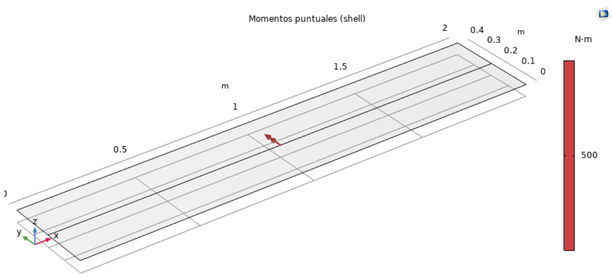

FIGURE C.71: Punctual moment applied on the center of the shell [COMSOL].

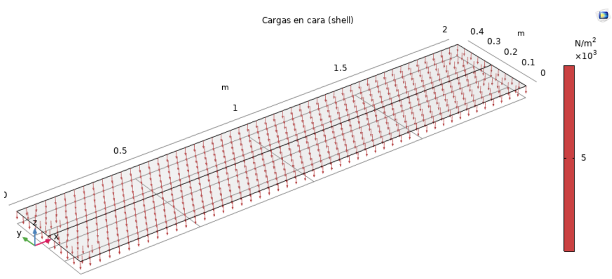

FIGURE C.72: Distributed load applied on the surface of the shell [COMSOL].

Von Mises stress and displacements distributions

Once applied the different boundary conditions on the shell, the following results have been obtained with COMSOL.

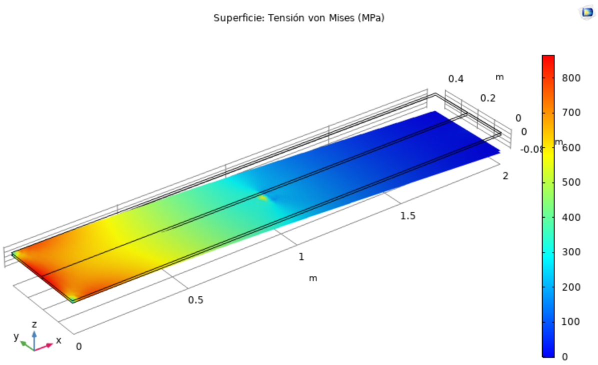

FIGURE C.73: Von Mises stress distribution along the shell for the complete study [COMSOL].

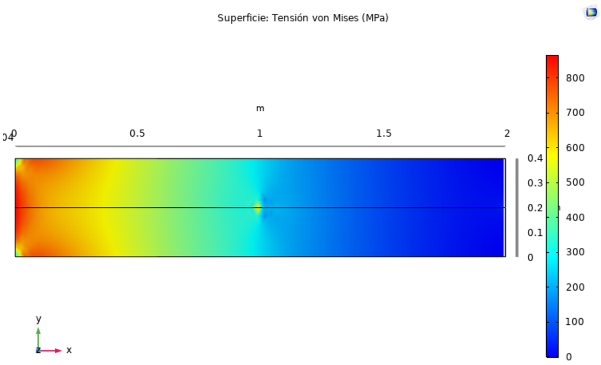

FIGURE C.74: Von Mises stress distribution along the shell for the complete study [COMSOL].

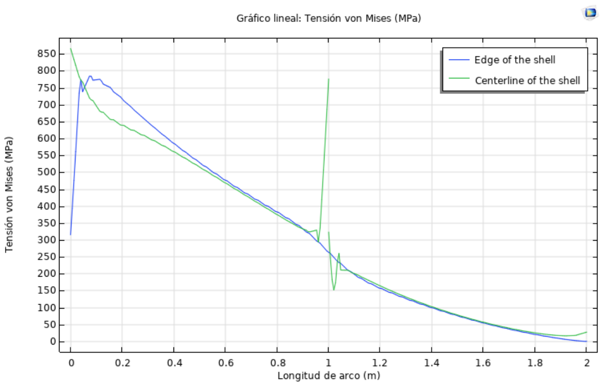

FIGURE C.75: Von Mises stress along two edges of the shell: an external edge and the center line of the shell [COMSOL].

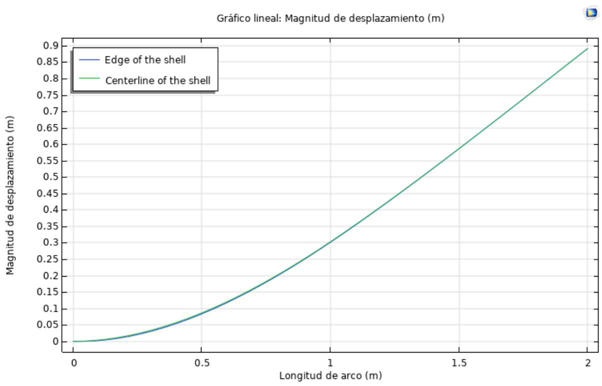

FIGURE C.76: Displacements of two edges of the shell: an external edge and the center line of the shell [COMSOL].

Figures C.75 and C.76 show the Von Mises and the displacements distributions obtained with COMSOL respectively. Both graphics include two different functions, one for the distributions obtained for the edge of the shell and the other for its center line. It can be seen that Von Mises stress is maximum at the beginning of the shell and minimum at the end where the edge is free. In contrast, for the displacements distribution, the maximum displacement is located at the free end where x=2 m.

Shear force

To continue with, the shear force distribution have been computed using COMSOL. As shown in figure C.77, the shear force can be divided in two different components first being in the z-direction and the second in the y-direction.

The z-direction component of the shear force has been plotted for two different lines of the shell: the edge of the shell and its center line. The maximum of the distribution obtained for the edge of the shell is located at the beginning where x=0 m, whereas for the center line the maximum is located in the middle where the punctual moment is applied. Moreover, both functions present its minimum at the end of the shell where x=2 m with a value of 0 N/m.

Furthermore, the y-direction component of the shear force has also been plotted for two different lines: the edge of the shell and its center line. Even though there is a maximum at the beginning of the edge of the shell with a value of -500 kN/m, both functions tent to remain constant and equal to 0 along the shell.

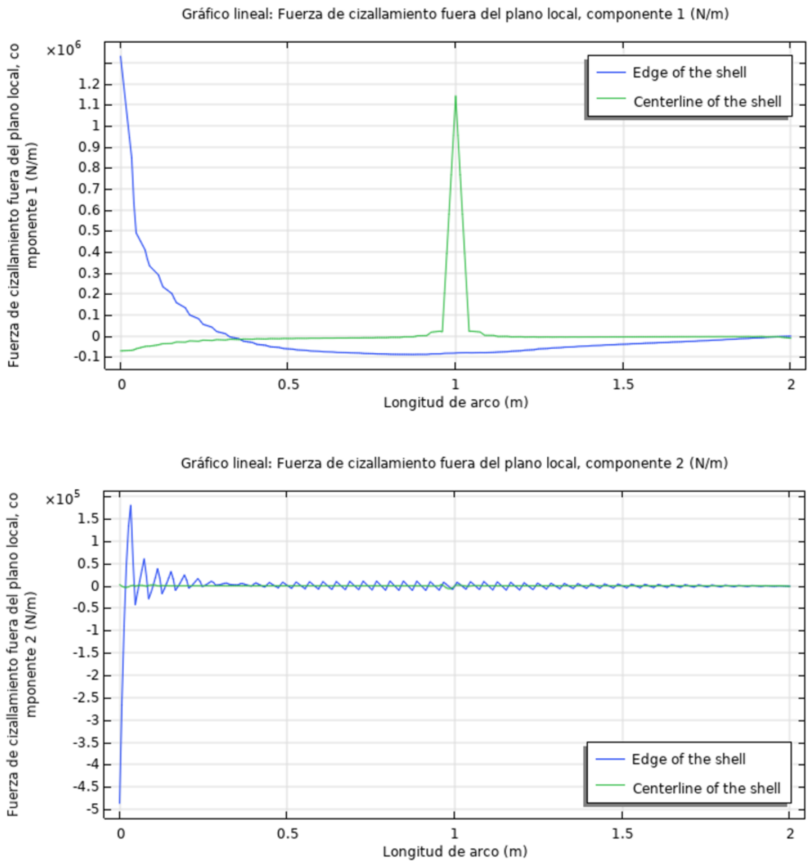

FIGURE C.77: Shear force distribution along two edges of the shell: an external edge and the center line of the shell [COMSOL].

Momentum components

Finally, the different components of the momentum have been plotted considering the previous boundary conditions.

- Momentum component 11

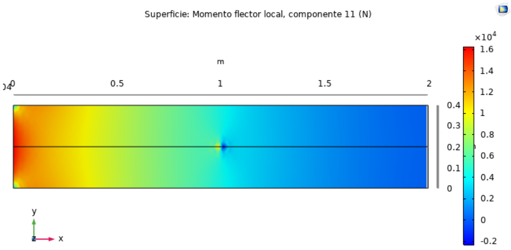

FIGURE C.78: Momentum component 11 along the shell [COMSOL].

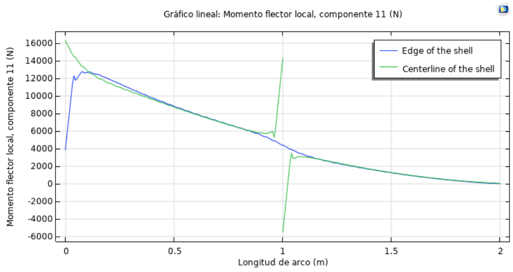

FIGURE C.79: Momentum component 11 along the center line and an external edge of the shell [COMSOL].

- Momentum component 12

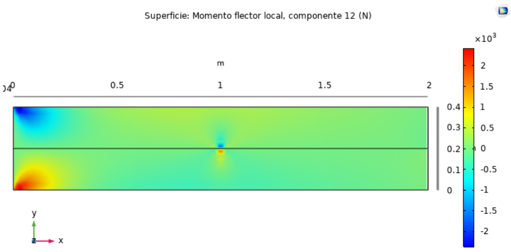

FIGURE C.80: Momentum component 12 along the shell [COMSOL].

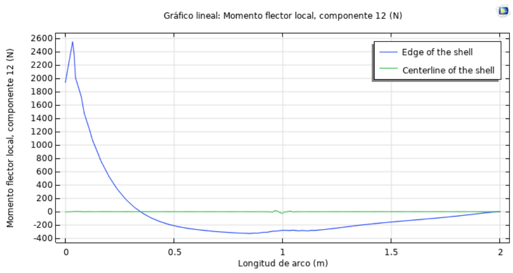

FIGURE C.81: Momentum component 12 along the center line and an external edge of the shell [COMSOL].

- Momentum component 13

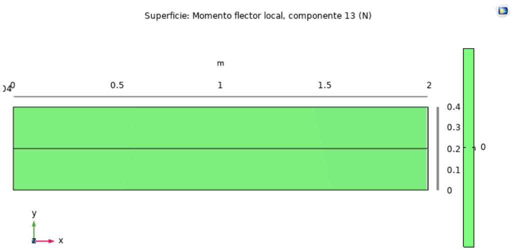

FIGURE C.82: Momentum component 13 along the shell [COMSOL].

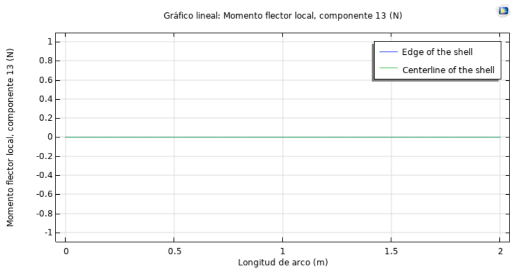

FIGURE C.83: Momentum component 13 along the center line and an external edge of the shell [COMSOL].

- Momentum component 22

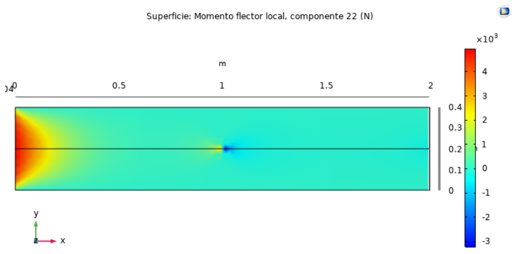

FIGURE C.84: Momentum component 22 along the shell [COMSOL].

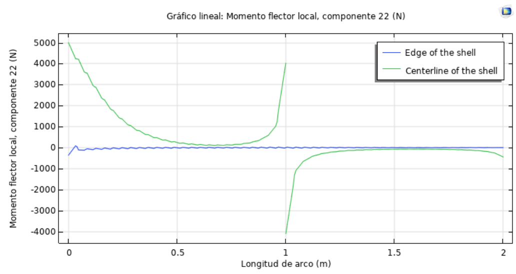

FIGURE C.85: Momentum component 22 along the center line and an external edge of the shell [COMSOL].

- Momentum component 23

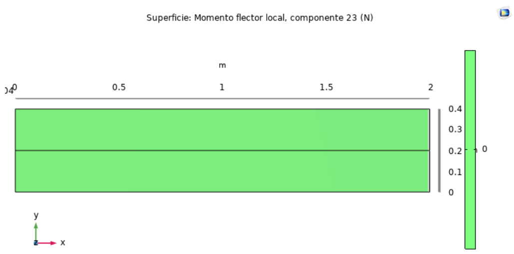

FIGURE C.86: Momentum component 23 along the shell [COMSOL].

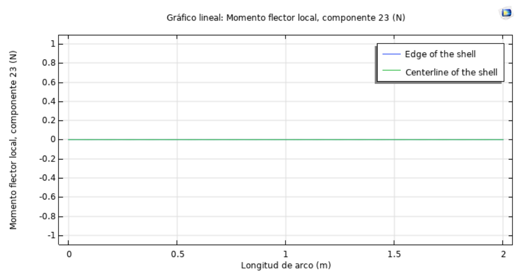

FIGURE C.87: Momentum component 23 along the center line and an external edge of the shell [COMSOL].

- Momentum component 33

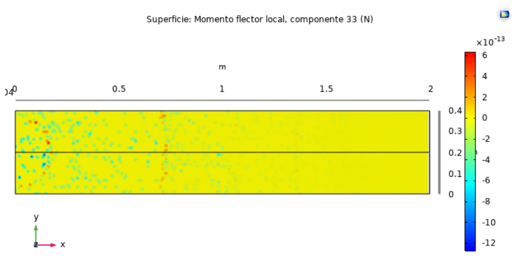

FIGURE C.88: Momentum component 33 along the shell [COMSOL].

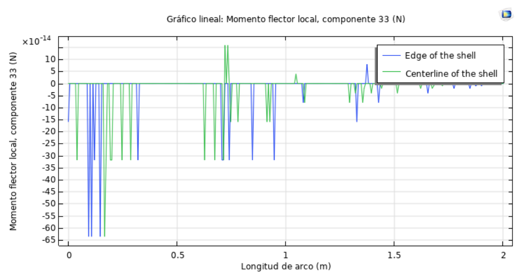

FIGURE C.89: Momentum component 33 along the center line and an external edge of the shell [COMSOL].

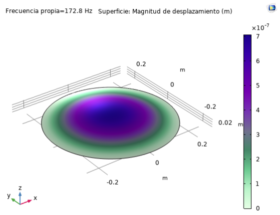

POLYTECHNIC UNIVERSITY OF CATALONIA

Structural Mechanics

Comsol

C.3 Report 3: Vibrating Membrane

The aim of this study is to determine the natural frequencies and modes of a circular membrane as well as to determine the vibration obtained when applying an external load.

C.3.1 Model definition

First, the geometry, the material and the boundary conditions at which the circular membrane is studied will be defined.

Geometry

- Membrane radius: R=0.25m.
- Membrane thickness: h=0.2m.

Material

- Material used: structural steel.
- Young's modulus, E = 200 GPa.
- Poisson's ratio, $\nu = 0.33$.
- Mass density, $\rho = 7850 kg/m^3$.

Boundary Conditions

- The outer edge of the membrane is supported in the transverse direction. Two points have constraints in the in-plane direction in order to avoid rigid body motions.

C.3.2 Natural frequencies

The first study consists in obtaining the eigenvalues of a circular membrane and its modes. In order to do so, the membrane has been dimensioned using COMSOL and then a modal test has been carried on. Table C.1 lists the first 6 natural frequencies obtained.

TABLE C.1: Natural frequencies of a vibrating membrane [COMSOL].

Harmonic	**Natural frequency [Hz]**
1st	172.8
2nd	275.33
3rd	275.33
4th	396.03
5th	396.03
6th	396.72

Moreover, figures C.90, C.91, C.92, C.93, C.94 and C.95 show the first 6 modes obtained using COMSOL.

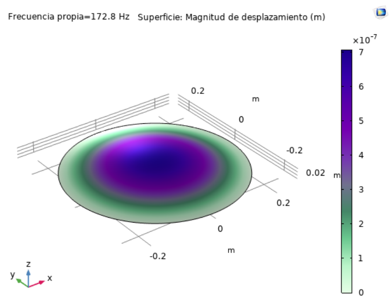

FIGURE C.90: Displacement of the first harmonic [COMSOL].

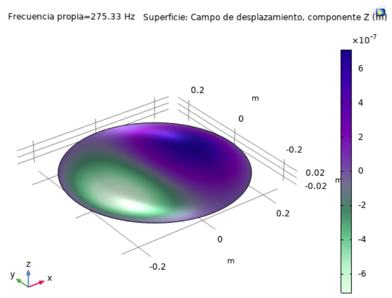

FIGURE C.91: Displacement of the second harmonic [COMSOL].

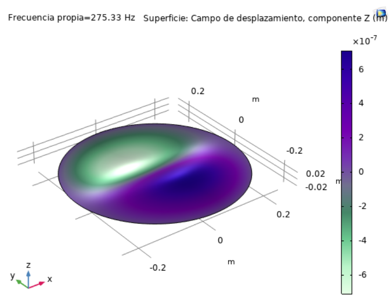

FIGURE C.92: Displacement of the third harmonic [COMSOL].

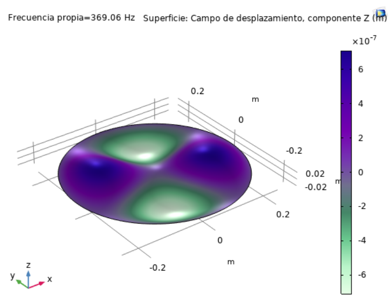

FIGURE C.93: Displacement of the fourth harmonic [COMSOL].

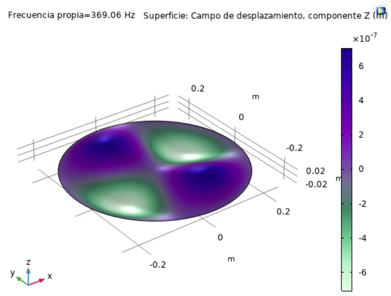

FIGURE C.94: Displacement of the fifth harmonic [COMSOL].

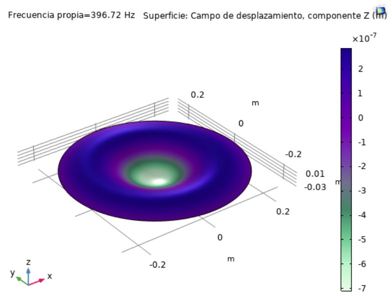

FIGURE C.95: Displacement of the sixth harmonic [COMSOL].

C.3.3 Displacement caused by an external load

Then, it has been prepared a second study where the pres-stress is instead computed from an external load. For doing so, it has been necessary to add a spring with an arbitrary small stiffness in order to suppress the out-of-plane singularity of the unstressed membrane. The natural frequencies obtained are listed in table C.2 and the first six modes are plotted in figures C.96, C.97, C.98, C.99, C.100 and C.101.

TABLE C.2: Natural frequencies of a vibrating membrane under an external load boundary condition [COMSOL].

Harmonic	Natural frequency [Hz]
1st	172.8
2nd	275.33
3rd	275.33
4th	396.03
5th	396.03
6th	396.72

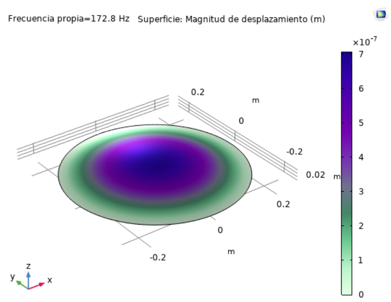

FIGURE C.96: Displacement of the first harmonic under an external load condition [COMSOL].

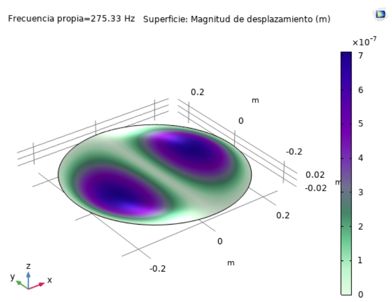

FIGURE C.97: Displacement of the second harmonic under an external load condition [COMSOL].

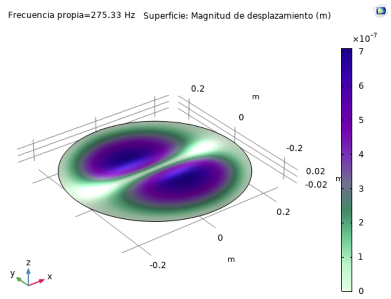

Figure C.98: Displacement of the third harmonic under an external load condition [COMSOL].

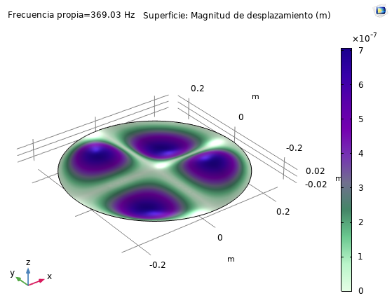

Figure C.99: Displacement of the fourth harmonic under an external load condition [COMSOL].

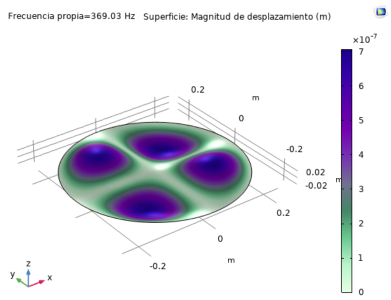

Figure C.100: Displacement of the fifth harmonic under an external load condition [COMSOL].

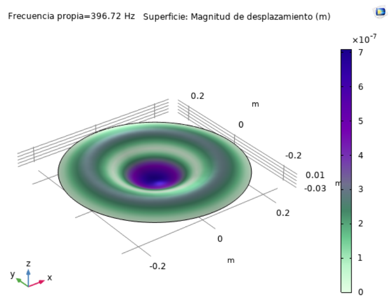

Figure C.101: Displacement of the sixth harmonic under an external load condition [COMSOL].

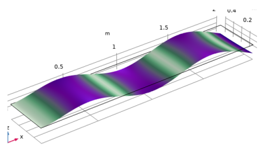

POLYTECHNIC UNIVERSITY OF CATALONIA
Structural Mechanics
Comsol

C.4 Report 4: Vibrating Shell

The aim of this study is to evaluate the behaviour of a thin plate under certain boundary conditions. First, a modal analysis study will be carried on in order to determine the natural frequencies and modes of the shell. Then, a resonance study will be computed in order to verify that the shell is in resonance when the natural frequencies are applied. For a third study, an external periodical load will be applied at the ending edge of the shell and it will be study the behaviour of the shell for several frequencies of the external load. Finally, it will be compared the results obtained for different time steps.

C.4.1 Model definition

Geometry

- Shell dimensions: 2,00 x 0,40 m
- Shell thickness: 0.01 m

Material

- Material used: structural steel.
- Young's modulus, E = 200 GPa.
- Poisson's ratio, $\nu = 0.33$.
- Mass density, $\rho = 7850 kg/m^3$.

Boundary conditions

- The beginning of the shell is fixed (x=0m).
- In the ending edge of the shell is located a distributed load of q=-500 N/m.

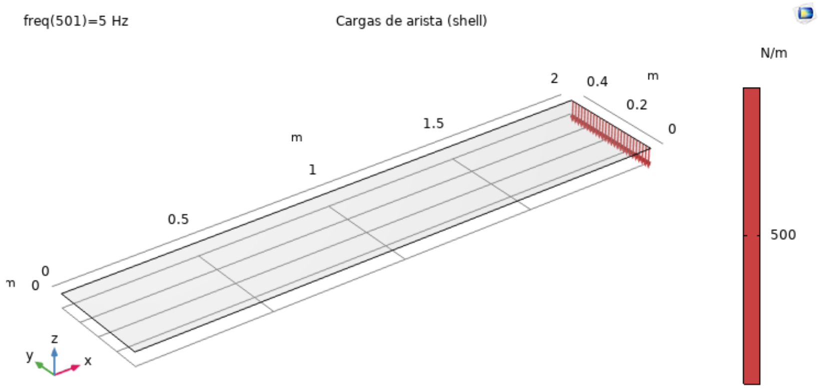

FIGURE C.102: Loads applied on the shell [COMSOL].

C.4.2 Natural frequencies

The first study have consisted in obtaining the eigenfrequency values of a thin plate and its modes when a distributed load on the extreme edge is applied. In table C.3 there are listed the first 6 natural frequencies of the shell.

TABLE C.3: Natural frequencies of a vibrating shell [COMSOL].

Harmonic	Natural frequency [Hz]
1st	2.0695
2nd	12.95
3rd	20.25
4th	36.338
5th	61.993
6th	71.469

Then the modes obtained are shown in figures C.103, C.104, C.105, C.106, C.107 and C.108.

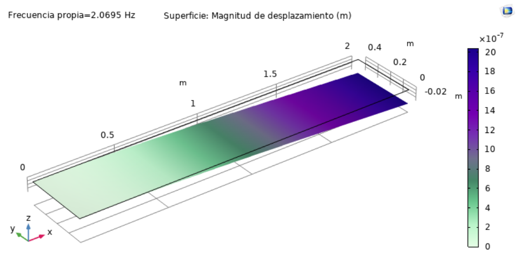

FIGURE C.103: Mode 1 when f=2.0695 Hz [COMSOL].

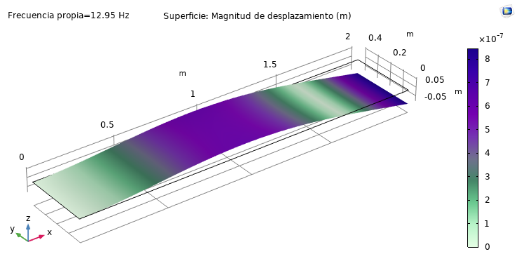

FIGURE C.104: Mode 2 when f=12.95 Hz [COMSOL].

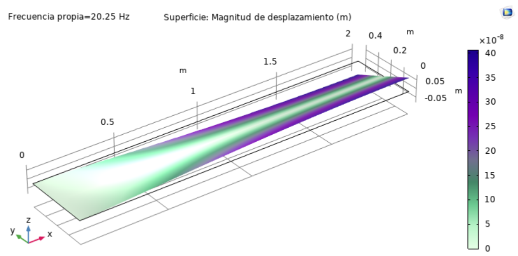

FIGURE C.105: Mode 3 when f=20.25 Hz [COMSOL].

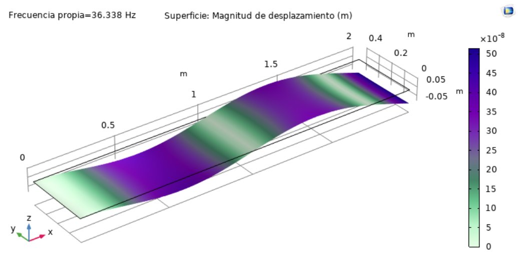

FIGURE C.106: Mode 4 when f=36.338 Hz [COMSOL].

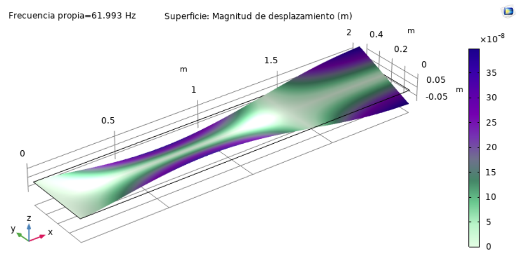

FIGURE C.107: Mode 5 when f=61.993 Hz [COMSOL].

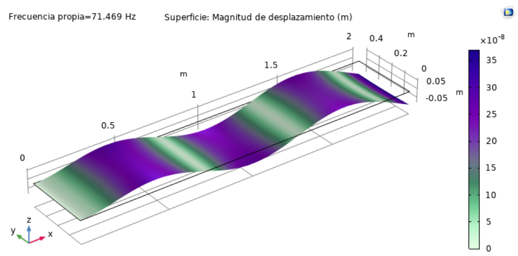

FIGURE C.108: Mode 6 when f=71.469 Hz [COMSOL].

C.4.3 Resonance study

In the second study, the shell have been made vibrate for a certain range of frequencies. Moreover, the external force applied at the ending edge of the shell have remained the same.

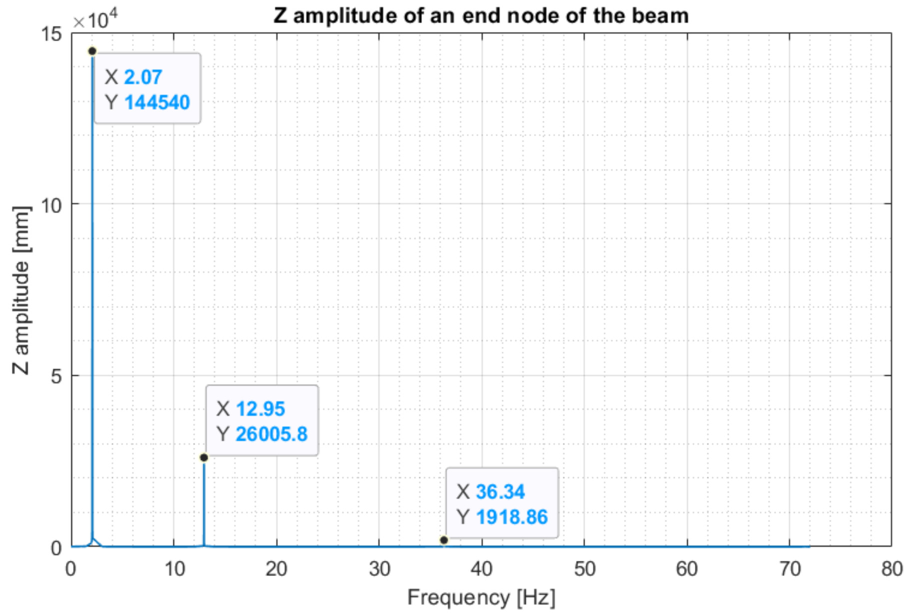

FIGURE C.109: Amplitude of the displacement in the z-direction obtained for an ending node evaluated in a range of frequencies [MATLAB].

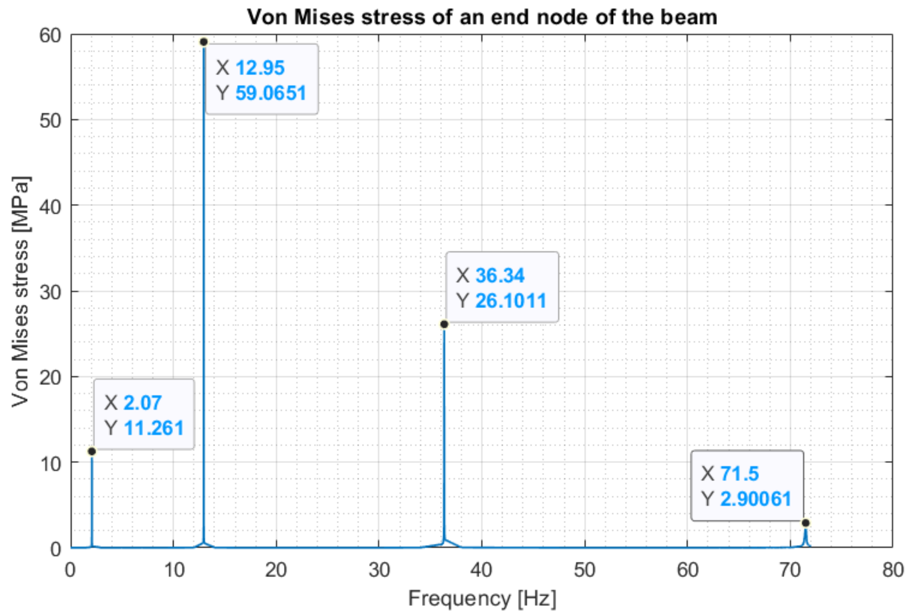

FIGURE C.110: Von Mises stress obtained for an ending node evaluated in a range of frequencies [MATLAB].

Figure C.109 shows the amplitude of the displacement in the z-direction obtained for an ending node evaluated in a range of frequencies. Due to the frequency step used, not all the natural frequencies can been seen in the graphic, however, the first, the second and the fourth natural frequencies obtained can be seen as an amplitude peaks in figure C.109.

C.4.4 Harmonic force response

The third study have consisted in applying an external periodical load on the ending edge of the shell with a varying frequency.

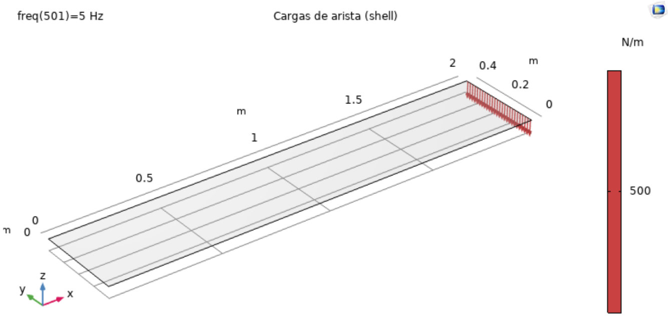

FIGURE C.111: Loads applied on the shell [COMSOL].

$$F_z = 500 \cdot \sin(2\pi f \cdot t) \tag{C.25}$$

Freq = 10 Hz

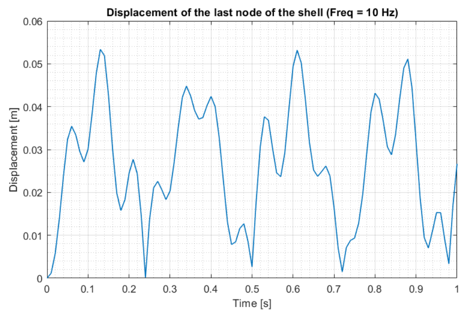

FIGURE C.112: Displacement of the last node of the shell when applying an harmonic load of 10 Hz [MATLAB].

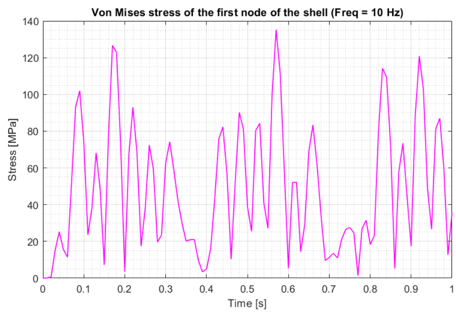

FIGURE C.113: Stress of the first node of the shell when applying an harmonic load of 10 Hz [MATLAB].

Freq = 20 Hz

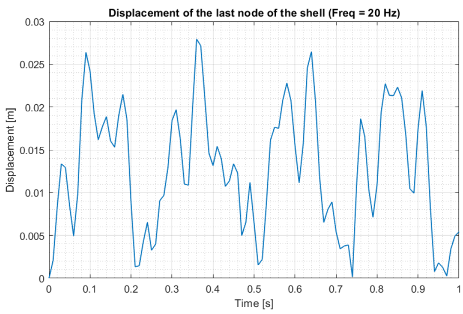

FIGURE C.114: Displacement of the last node of the shell when applying an harmonic load of 20 Hz [MATLAB].

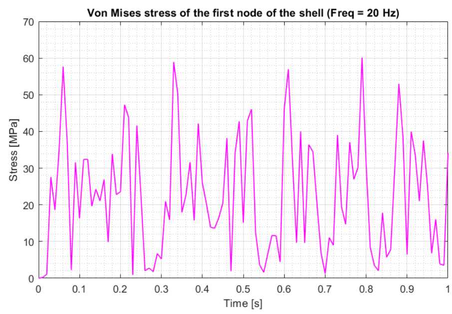

FIGURE C.115: Stress of the first node of the shell when applying an harmonic load of 20 Hz [MATLAB].

Freq = 40 Hz

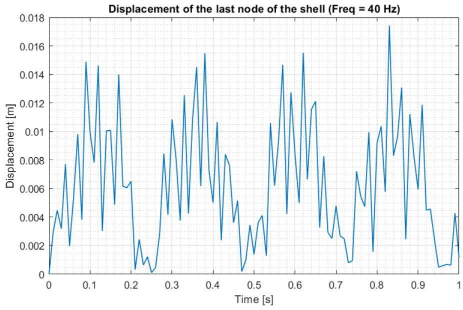

FIGURE C.116: Displacement of the last node of the shell when applying an harmonic load of 40 Hz [MATLAB].

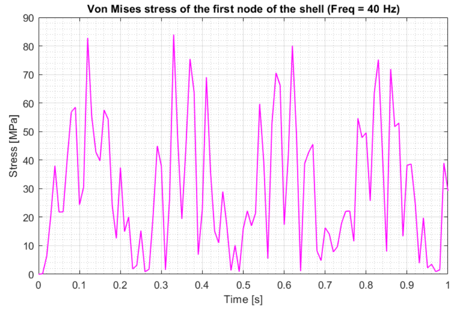

FIGURE C.117: Stress of the first node of the shell when applying an harmonic load of 40 Hz [MATLAB].

Freq = 80 Hz

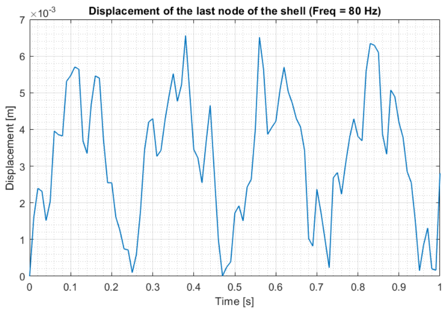

FIGURE C.118: Displacement of the last node of the shell when applying an harmonic load of 80 Hz [MATLAB].

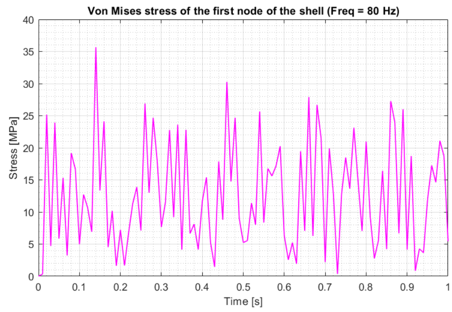

FIGURE C.119: Stress of the first node of the shell when applying an harmonic load of 80 Hz [MATLAB].

Freq = 70 Hz. Near resonance.

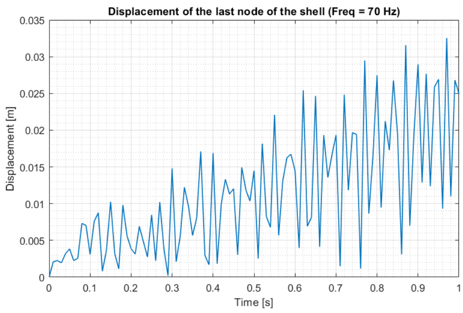

FIGURE C.120: Displacement of the last node of the shell when applying an harmonic load of 70 Hz [MATLAB].

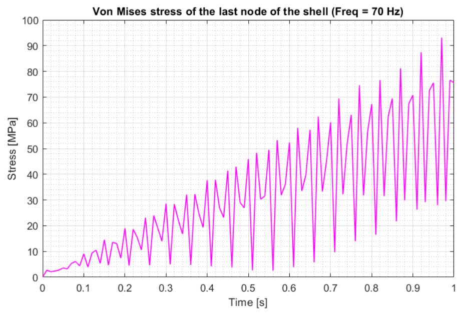

FIGURE C.121: Stress of the first node of the shell when applying an harmonic load of 70 Hz [MATLAB].

Figures C.120 and C.121 show the displacement of the ending node and the Von Misses stress of the first node distributions along time domain. As the sixth natural frequency obtained in table C.3 is close to 70Hz, it can be seen how the shell is close to resonance and keeps increasing its displacement over time. Contrary to the results obtained for the frequency of 70Hz, the other frequencies are far from being in resonance and present a displacement distribution that can be considered kind of periodical over time.

C.4.5 Study of the time step

Finally, it has been applied an harmonic force of 10 Hz on the ending edge of the shell in order to study what happens when using different time steps.

- $\Delta t = 0.1$ s

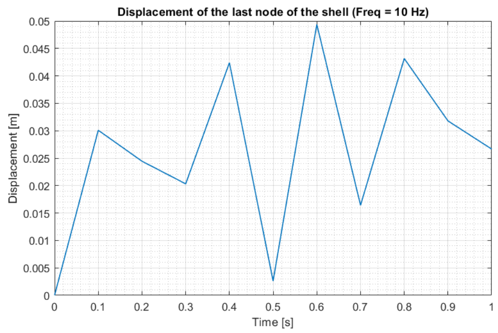

FIGURE C.122: Displacement of the last node of the shell when using $\Delta t = 0.1$ s [MATLAB].

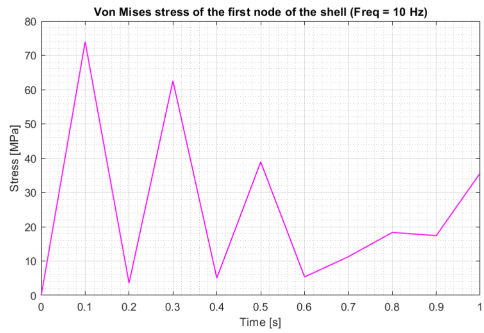

FIGURE C.123: Stress of the first node of the shell when using $\Delta t = 0.1$ s [MATLAB].

- $\Delta t = 0.05$ s

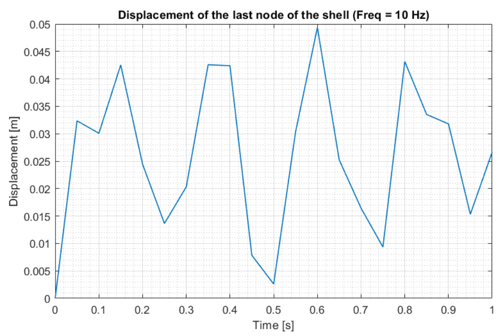

FIGURE C.124: Displacement of the last node of the shell when using $\Delta t = 0.05$ s [MATLAB].

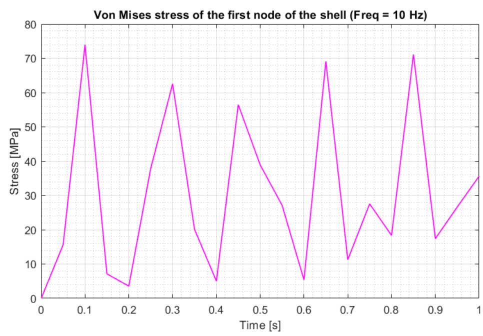

FIGURE C.125: Stress of the first node of the shell when using $\Delta t = 0.05$ s [MATLAB].

- $\Delta t = 0.025$ s

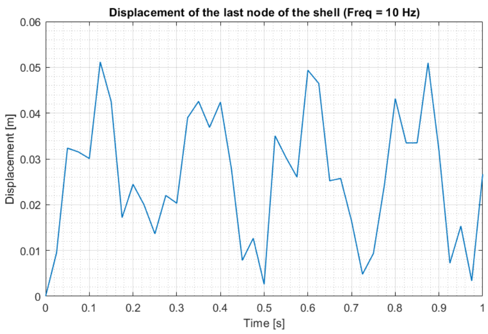

FIGURE C.126: Displacement of the last node of the shell when using $\Delta t = 0.025$ s [MATLAB].

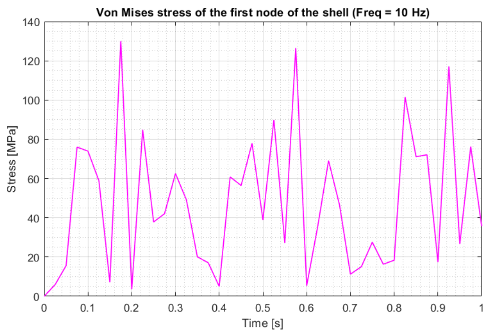

FIGURE C.127: Stress of the first node of the shell when using $\Delta t = 0.025$ s [MATLAB].

- $\Delta t = 0.0125$ s

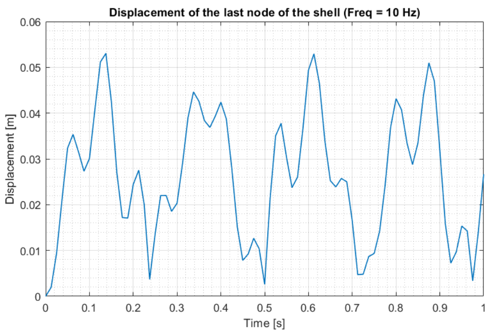

FIGURE C.128: Displacement of the last node of the shell when using $\Delta t = 0.0125$ s [MATLAB].

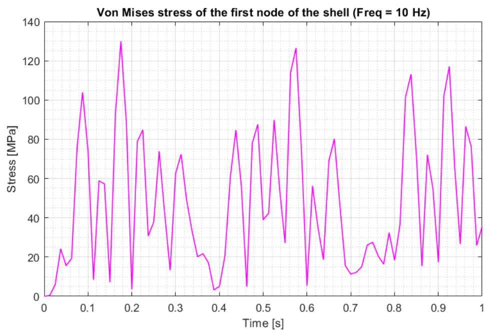

FIGURE C.129: Stress of the first node of the shell when using $\Delta t = 0.0125$ s [MATLAB].

- $\Delta t = 0.00625$ s

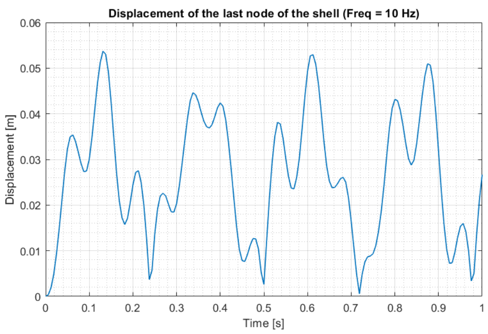

FIGURE C.130: Displacement of the last node of the shell when using $\Delta t = 0.00625$ s [MATLAB].

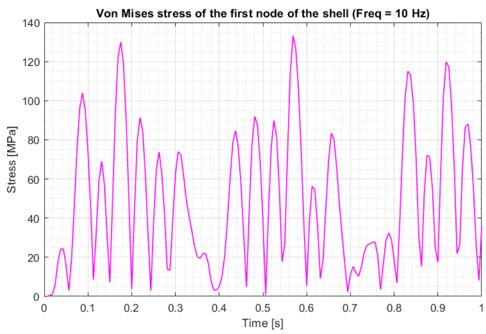

FIGURE C.131: Stress of the first node of the shell when using $\Delta t = 0.00625$ s [MATLAB].

C.4.6 Conclusions

From this study it can be easily seen that the minor time step, the more precision is obtained. When reducing the time step, more and more peaks are captured by the step used and less information is lost.

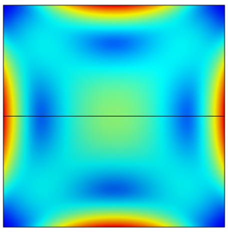

POLYTECHNIC UNIVERSITY OF CATALONIA
Structural Mechanics
Matlab and Comsol

C.5 Report 5: Convergence study

The aim of this report is to compare the analytical solution obtained for a flat shell under certain boundary conditions with the numerical one computed with both, COMSOL and MATLAB. At first, Von Mises maximum stress and the maximum displacement in the z-direction will be analytically obtained. Secondly, with the use of COMSOL and MATLAB, the Von Mises stress and the displacement in the z-direction distribution will be computed and compared.

Furthermore, the analytical, COMSOL and MATLAB solutions are not calculated following the same theory as shown in table C.4.

TABLE C.4: Theory used to compute the displacements [7] [8] [12] [16] [17].

	Theory
Analytical	Kirchhoff thin plate theory [12]
	Timoshenko plate theory [16]
COMSOL	Reissner-Mindlin plate theory [17]
MATLAB	Reissner-Mindlin flat shell theory [7] [8]

C.5.1 Model definition

Geometry

- Shell dimensions: 2,00 x 2,00 m
- Shell thickness: 0.05 m

Material

- Young's modulus, E = 69 GPa.

- Poisson's ratio, $\nu = 0.3$.
- Mass density, $\rho = 2700kg/m^3$.

Boundary conditions

- The four edges of the shell are embedded. All direction displacements and rotations are equal to 0.
- A distributed load of $-1 \cdot 10^6\ N/m^2$ is applied on the surface.
- Gravity is also considered in the problem.

C.5.2 Analytical Solution

Kirchhoff thin plate theory

The analytical solution using Kirchhoff thin plate theory for the flat shell problem considering little displacements and a lineal case is given by the following equations extracted from reference [12].

$$\sigma_{max} = \beta q \left(\frac{c}{h}\right)^2 \tag{C.26}$$

$$\frac{w_{max}}{h} = \delta \frac{q}{E} \left(\frac{c}{h}\right)^4 \tag{C.27}$$

where:

- c is the shortest edge of the plate
- h is the thickness
- σ_{max} is the maximum stress
- E is Young's modulus
- ν is Poisson's module
- q is the distributed load applied on the plate
- w_{max} is the maximum displacement of the plate
- β and δ coefficients

In order to compute β and δ coefficients it must be first taken into account the shape of the plate and, as the plate has a square shape, α parameter is equal to 1.

$$\alpha = \frac{c}{l} = 1 \tag{C.28}$$

Furthermore, when calculating the β coefficient analytically it must be taken into consideration where the stress is computed, at the centre of the plate or at one of the recessed edges. If all of the edges of the square plate are embedded, β at the center and at one edge is computed using the following expressions from figure C.132.

$$\beta_c = \frac{1}{4\left(1+\alpha^4\right)} = 0.125 \qquad \sigma_c = \beta_c q \left(\frac{c}{h}\right)^2 = 2 \cdot 10^8 \ Pa \tag{C.29}$$

$$\beta_e = \frac{1}{2\left(1+\alpha^4\right)} = 0.25 \qquad \sigma_{e\ max} = \beta_e q \left(\frac{c}{h}\right)^2 = 4 \cdot 10^8 \ Pa \tag{C.30}$$

Finally, when calculating δ coefficient and the maximum displacement a previous parameter must be computed (δ_0) using the equations provided in figure C.132.

$$\delta_0 = 32\left(1+\alpha^4\right) \qquad \delta = \frac{1-\nu^2}{\delta_0} \tag{C.31}$$

$$w_{max} = h\delta \frac{q}{E}\left(\frac{c}{h}\right)^4 = h\frac{1-\nu^2}{32\left(1+\alpha^4\right)}\frac{q}{E}\left(\frac{c}{h}\right)^4 = -0.0264 \ m \tag{C.32}$$

Forma		Lados	δ_o	$1/\beta_c$ centro	$1/\beta_e$ empotramiento
c	1	Apoyados	$85{,}333 \frac{1+\nu}{5+\nu}$	$\frac{10{,}667}{3+\nu}$	//////////////
	2	Empotrados	$85{,}333$	$\frac{10{,}667}{1+\nu}$	$5{,}333$
c, ℓ	3	Apoyados	$6{,}37 + 5{,}91\,\alpha + 8{,}63\,\alpha^4$	$1{,}33+1{,}9\,\alpha^{2,2}$	//////////////
c: lado menor, $\alpha = c/\ell$	4	Empotrados	$32+53{,}33\,\alpha^3$	$4+4{,}2\,\alpha^3$	$2+3{,}33\,\alpha^3$
c, ℓ	5	Apoyados	$6{,}4+14{,}3\,\alpha^3$	$1{,}33+2{,}2\,\alpha^{2,8}$	//////////////
	6	Empotrados	$32\left(1+\alpha^4\right)$	$4\left(1+\alpha^4\right)$	$2\left(1+\alpha^4\right)$
c: lado menor	7	Cortos apoyados Largos empotrados	$32+9{,}8\,\alpha^4$	$4+\alpha^5$	$2+0{,}4\,\alpha^5$
$\alpha = c/\ell$, $0<\alpha\leq 1$	8	Cortos empotrados Largos apoyados	$6{,}4+37{,}4\,\alpha^{3,5}$	$\alpha<0{,}8 \rightarrow 1{,}3+5{,}6\,\alpha^{3,2}$ $\alpha\geq 0{,}8 \rightarrow 3+2\,\alpha^3$	$1{,}33+1{,}1\,\alpha^{3,6}$

FIGURE C.132: Equations to compute the different coefficients for small deformations problem [12].

Timoshenko plate theory

Then, using Timoshenko analytical solution for an embedded flat shell with a distributed load extracted from reference [16], the maximum displacement can be computed as follows:

$$D = \frac{Eh^3}{12(1-\nu^2)} = 7.898 \cdot 10^5 \qquad \omega = 0.00126\frac{qL^4}{D} = -0.0255 \ m \tag{C.33}$$

C.5.3 Numerical solution

Von Mises stress

Furthermore, Von Mises stress distribution has been computed at first with COMSOL, shown in figure C.133, and then with MATLAB, shown in figure C.134, to finally plot and compare the results obtained.

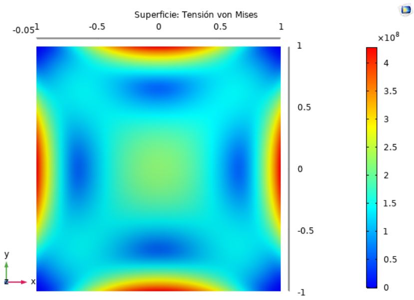

FIGURE C.133: Von Mises tension distribution [COMSOL].

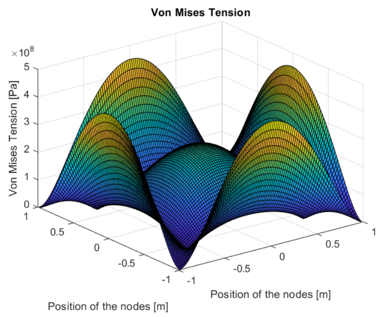

FIGURE C.134: Von Mises tension distribution [MATLAB].

Figure C.135 superposes the stress distributions computed with MATLAB and the ones simulated with COMSOL for two specific lines of the square plate, x=0 m and x=1 m. While the maximum stress of the center line is located at the ends, y=-1m and y=1m, the maximum Von Mises stress of the edges of the plate is located on the centre, y=0 m. Furthermore, the stress is equal to 0 at the corners of the plate. Although both solutions have the same shape, they are slightly different. Probably, with the use of the finite element method (FEM), the mesh should be more dense so that the error decreases.

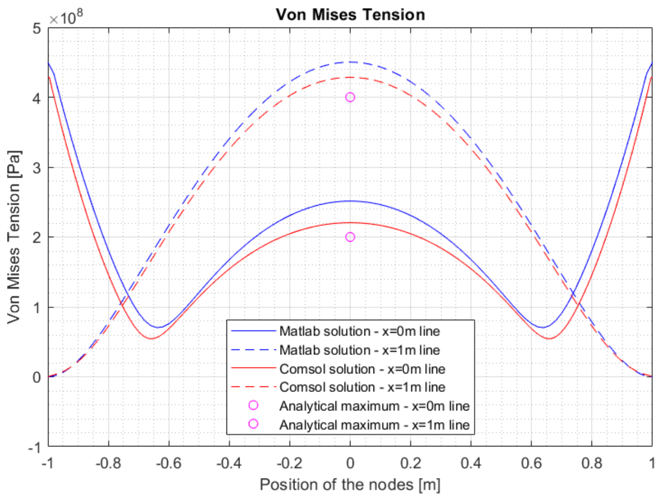

FIGURE C.135: Comparison of the stress distributions obtained with MATLAB and COMSOL for 100^2 elements and the analytical maximum stresses calculated [MATLAB].

Displacements

Then, the displacements in the z-direction, normal to the plane of the plate, have been also calculated and plotted. Figures C.136 and C.137 show the displacement distributions along the plate obtained with both, COMSOL and MATLAB.

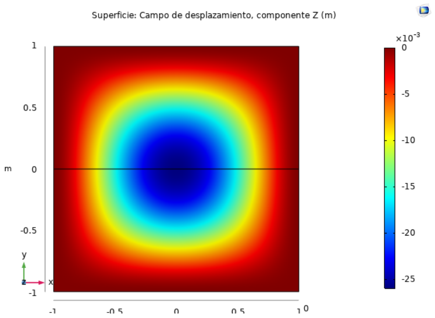

FIGURE C.136: Displacements distribution [COMSOL].

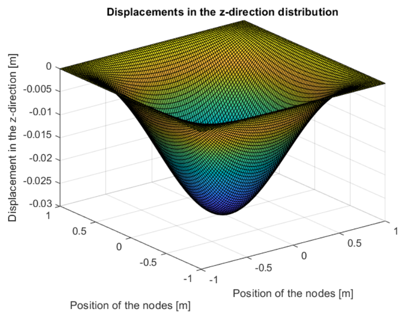

FIGURE C.137: Displacements distribution [MATLAB].

In order to compare the results, figure C.138 superposes the displacement distribution along the center line of the plate obtained using COMSOL and MATLAB. The maximum displacement in the vertical direction is obtained at the center of the plate. Moreover, the displacement is equal to zero along the edges where the plate is embedded. However, even though the displacements distributions obtained with COMSOL and MATLAB had the same shape, the values are quite different and did not fully agree.

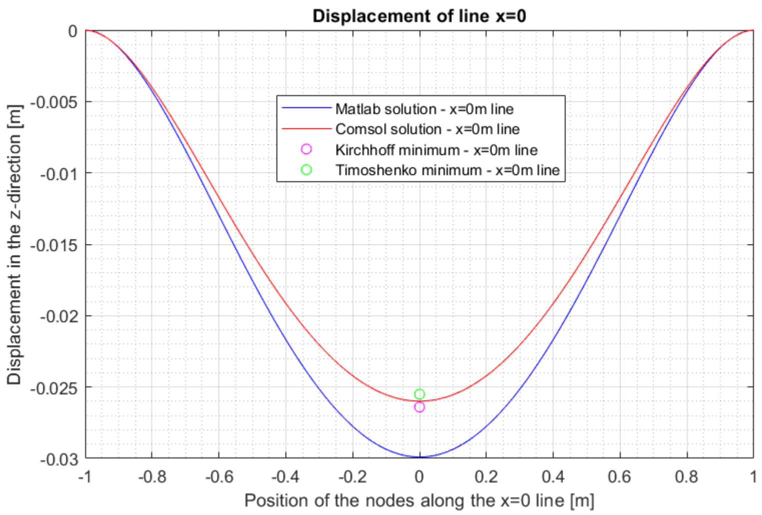

FIGURE C.138: Comparison of the results obtained with MATLAB and COMSOL for 100^2 elements and the analytical minimum displacement calculated [MATLAB].

Finally, all the results have been summarised in table C.5 and, according to them, the results obtained with COMSOL are the closest to the analytical solution, especially when it comes to the maximum displacement in which the values obtained are almost the same.

TABLE C.5: Comparison of the results obtained analytically, with COMSOL and MATLAB [7] [8] [12] [16] [17].

	Theory	σ_c [Pa]	$\sigma_{e\ max}$ [Pa]	w_{max} [m]
Analytical	Kirchhoff thin plate theory [12]	$2 \cdot 10^8$	$4 \cdot 10^8$	-0.0264
	Timoshenko plate theory [16]			-0.0255
COMSOL	Reissner-Mindlin plate theory [17]	$2.2 \cdot 10^8$	$4.3 \cdot 10^8$	-0.0259
MATLAB	Reissner-Mindlin flat shell theory [7] [8]	$2.5 \cdot 10^8$	$4.5 \cdot 10^8$	-0.0299

C.5.4 Convergence study

As the results obtained in the previous section using COMSOL and MATLAB did not completely agree, it has been studied how does the mesh of the MATLAB program affect in the convergence with COMSOL results. To get an accurate solution with COMSOL, it has been used an extremely thin mesh of about 200^2 elements (200 x 200 elements). Then, 4 different mesh divisions of $[20^2, 40^2, 80^2, 160^2]$ elements respectively have been used in order to compute the Von Mises stress and the displacements distributions with MATLAB. In figures C.139, C.140 and C.141, the results of the Von Mises stress and the displacement in the z-direction distributions obtained are compared with both, the COMSOL extremely accurate solution and the analytical one.

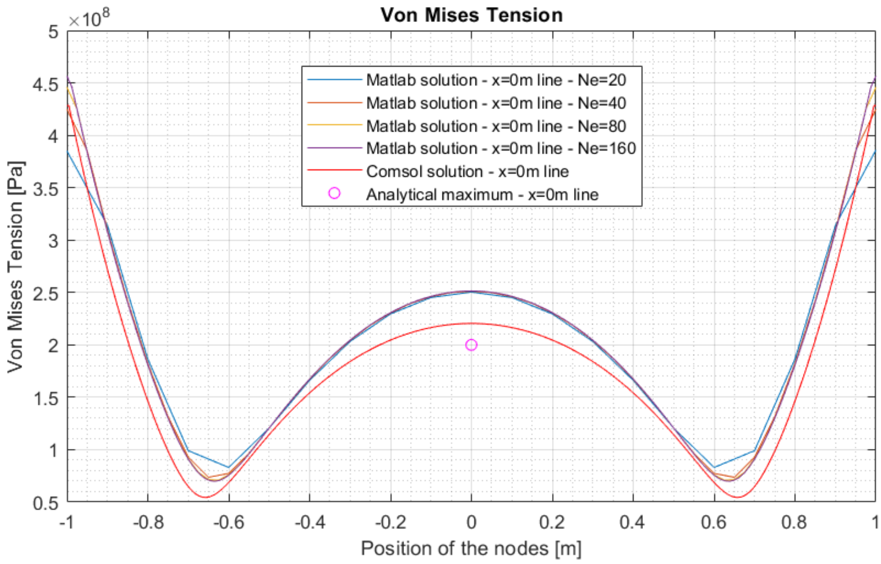

FIGURE C.139: Comparison of the Von Mises stress results obtained for the center line of the shell considering different meshes [MATLAB].

Figure C.139 shows the Von Mises stress distribution obtained for the center line of the shell. However, although considering different meshes, the results obtained with MATLAB seem to describe similar distributions which are quite different from the COMSOL result obtained.

Moreover, figure C.140 presents the Von Mises stress distribution obtained for one edge of the shell. In contrast with figure C.139, the more elements used, the higher Von Mises stress is obtained. In other words, for the different meshes, different results are obtained and there is a tendency to increase the Von Mises stress distribution when increasing the elements used. Furthermore, for the mesh of 40^2 elements, the results obtained with MATLAB and COMSOL are almost the same.

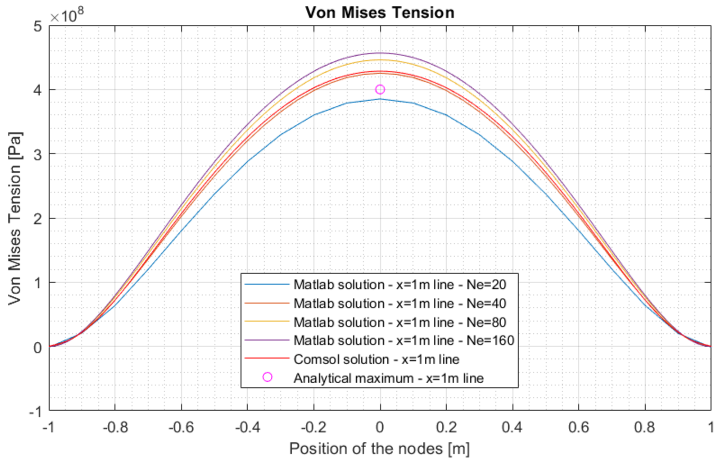

FIGURE C.140: Comparison of the Von Mises stress results obtained for one edge line of the shell considering different meshes [MATLAB].

Finally, figure C.141 shows the displacements distribution obtained for the center line of the shell. As in figure C.139, the results obtained with MATLAB using different meshes are almost the same. That means that, when increasing the elements of the mesh, little difference is seen.

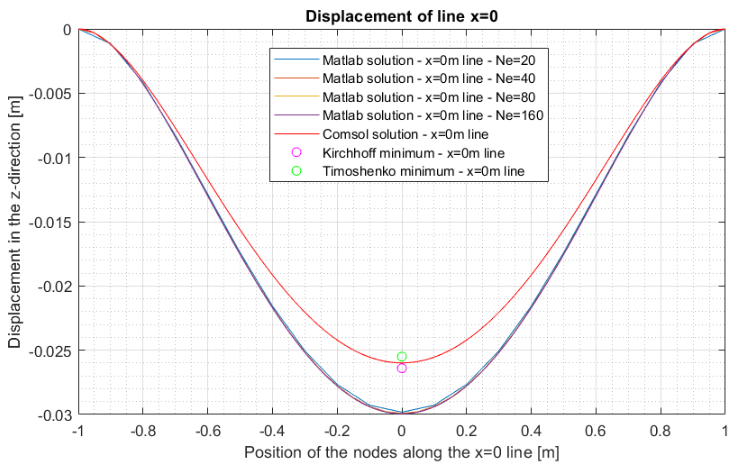

FIGURE C.141: Comparison of the displacements distribution obtained for the center line of the shell considering different meshes [MATLAB].

C.5.5 Case 2: Thinner flat shell study

The reason why there is a difference between the Von Mises stress and the displacements in the z-direction distributions obtained with COMSOL and MATLAB can lie on the thickness of the geometry used. Whereas COMSOL uses a Reissner-Mindlin plate theory that takes into account the thickness of the element, MATLAB uses the Reissner-Mindlin flat shell theory which can only be used for extremely thin geometries. For that reason, a second study has been carried on in which the dimensions of the shell will be redefined.

Geometry

- Shell dimensions: 2,00 x 2,00 m
- Shell thickness: 0.001 m

Material

- Young's modulus, E = 69 GPa.
- Poisson's ratio, $\nu = 0.3$.
- Mass density, $\rho = 2700 kg/m^3$.

Boundary conditions

- The four edges of the shell are embedded. All direction displacements and rotations are equal to 0.
- A distributed load of $-1 \cdot 10^6 \ N/m^2$ is applied on the surface.
- Gravity is also considered in the problem.

Analytical Solution

Following the process and equations used in the previous sections, the analytical solution for the maximum displacement and maximum Von Mises stress using Kirchhoff theory for a flat shell of a 0.001 m of thickness has been calculated. As the plate has a square shape, α parameter is equal to 1. Then, β is computed for the center of the plate and one of the recessed edges using the expressions from figure C.132 and the maximum stress is calculated as well in both positions.

$$\beta_c = \frac{1}{4\left(1+\alpha^4\right)} = 0.125 \qquad \sigma_c = \beta_c q \left(\frac{c}{h}\right)^2 = 5 \cdot 10^{11} \ Pa \tag{C.34}$$

$$\beta_e = \frac{1}{2\left(1+\alpha^4\right)} = 0.25 \qquad \sigma_{e \ max} = \beta_e q \left(\frac{c}{h}\right)^2 = 1 \cdot 10^{12} \ Pa \tag{C.35}$$

Finally, δ coefficient is calculated as well as the maximum displacement as the following.

$$\delta = \frac{1-\nu^2}{\delta_0} \qquad w_{max} = h\delta \frac{q}{E}\left(\frac{c}{h}\right)^4 = h\frac{1-\nu^2}{32\left(1+\alpha^4\right)}\frac{q}{E}\left(\frac{c}{h}\right)^4 = -3297 \ m \tag{C.36}$$

Then, using Timoshenko analytical solution for an embedded flat shell with a distributed load, the maximum displacement can be computed as follows:

$$\omega = 0.00126\frac{12(1-\nu^2)qL^4}{Eh^3} = -3190\ m \tag{C.37}$$

Numerical Solution

As what happened to the previous geometry, there is still a difference between the numerical solutions computed with COMSOL and MATLAB as can be seen in figures C.142 and C.143, which present the Von Mises stress and the displacements in the z-direction distributions respectively.

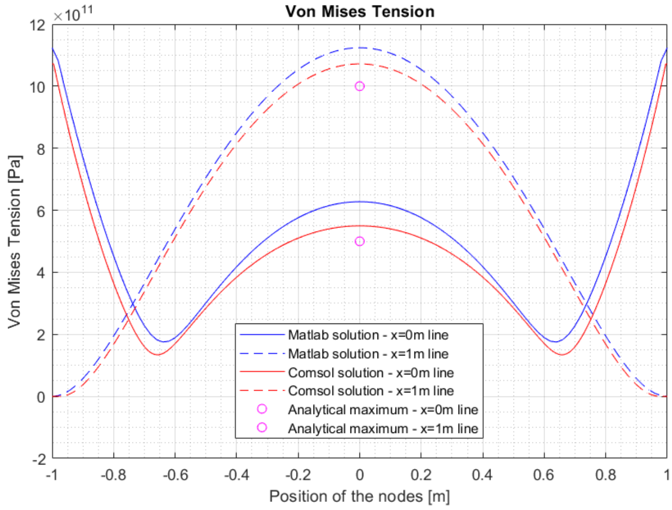

FIGURE C.142: Comparison of the stress distribution results obtained with MATLAB and COMSOL for 100^2 elements and the analytical maximum stresses calculated [MATLAB].

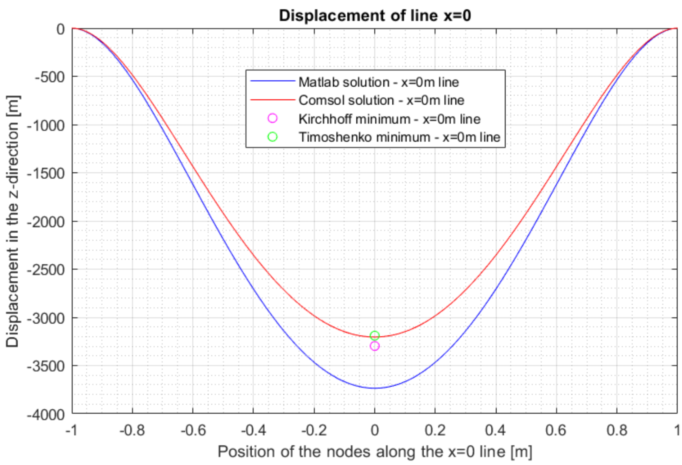

FIGURE C.143: Comparison of the results obtained with MATLAB and COMSOL for 100^2 elements and the analytical minimum displacement calculated [MATLAB].

C.5.6 Case 3: Extremely thin flat shell study

Finally, a third study has been carried on in which the dimensions of the shell will be redefined.

Geometry

- Shell dimensions: 2,00 x 2,00 m
- Shell thickness: $1 \cdot 10^{-4}$ m

Material

- Young's modulus, E = 69 GPa.
- Poisson's ratio, $\nu = 0.3$.
- Mass density, $\rho = 2700 kg/m^3$.

Boundary conditions

- The four edges of the shell are embedded. All direction displacements and rotations are equal to 0.
- A distributed load of $-0.1\ N/m^2$ is applied on the surface.
- Gravity is also considered in the problem.

Analytical Solution

Following the process and equations used in section C.5.2, the analytical solution for the maximum displacement and maximum Von Mises stress using Kirchhoff theory for a flat shell of a 0.001 m of thickness has been calculated. First, as the plate has a square shape, α parameter is equal to 1.

$$\alpha = \frac{c}{l} = 1 \tag{C.38}$$

Then, β is computed for the center of the plate and one of the recessed edges using the expressions from figure C.132 and the maximum stress is calculated as well in both positions.

$$\beta_c = \frac{1}{4\left(1+\alpha^4\right)} = 0.125 \qquad \sigma_c = \beta_c q \left(\frac{c}{h}\right)^2 = 5 \cdot 10^6\ Pa \tag{C.39}$$

$$\beta_e = \frac{1}{2\left(1+\alpha^4\right)} = 0.25 \qquad \sigma_{e\ max} = \beta_e q \left(\frac{c}{h}\right)^2 = 10 \cdot 10^6\ Pa \tag{C.40}$$

Finally, when calculating δ coefficient and the maximum displacement a previous parameter must be computed (δ_0) using the equations provided in figure C.132.

$$\delta_0 = 32\left(1+\alpha^4\right) \qquad \delta = \frac{1-\nu^2}{\delta_0} \tag{C.41}$$

$$w_{max} = h\delta \frac{q}{E}\left(\frac{c}{h}\right)^4 = h\frac{1-\nu^2}{32\left(1+\alpha^4\right)}\frac{q}{E}\left(\frac{c}{h}\right)^4 = -0.3297\ m \tag{C.42}$$

Then, using Timoshenko analytical solution for an embedded flat shell with a distributed load, the maximum displacement can be computed as follows:

$$\omega = 0.00126\frac{12(1-\nu^2)qL^4}{Eh^3} = -0.319\ m \tag{C.43}$$

Numerical Solution

As what happened to the previous geometry, there is still a difference between the numerical solutions computed with COMSOL and MATLAB as can be seen in figures C.144 and C.145, which present the Von Mises stress and the displacements in the z-direction distributions respectively.

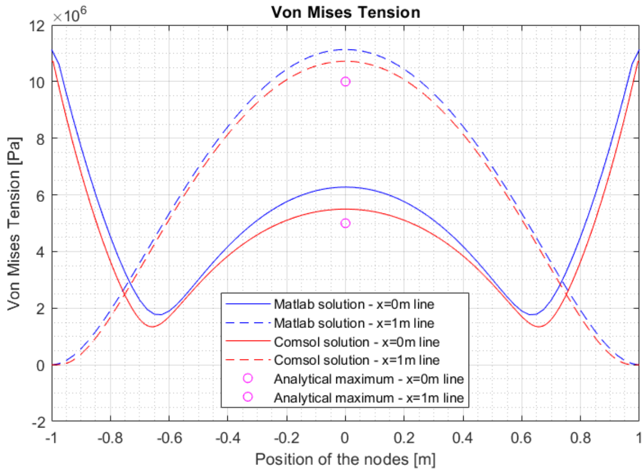

FIGURE C.144: Comparison of the stress distribution results obtained with MATLAB and COMSOL for 100^2 elements and the analytical maximum stresses calculated [MATLAB].

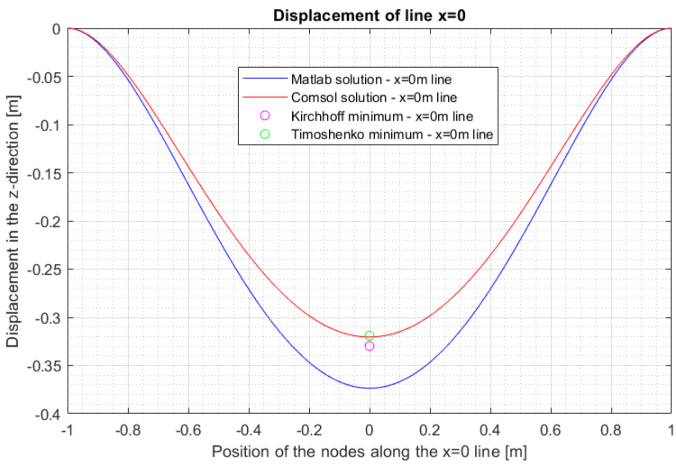

FIGURE C.145: Comparison of the results obtained with MATLAB and COMSOL for 100^2 elements and the analytical minimum displacement calculated [MATLAB].

C.5.7 Results summary

Finally, the maximum displacement obtained for the different geometries studied have been summarised in table C.6. Additionally the error between the different methodologies used has been computed as well.

TABLE C.6: Summary of the results obtained and error calculations [7] [8] [12] [16] [17].

Maximum displacement ω_{max} [m]				
	Theory	**1st Case**	**2nd Case**	**3rd Case**
	Kirchhoff thin plate theory [12]	-0.0264	-3297	-0.3297
	Timoshenko plate theory [16]	-0.0255	-3190	-0.3190
COMSOL	Reissner-Mindlin plate theory [17]	-0.0260	-3200	-0.3200
MATLAB	Reissner-Mindlin flat shell theory [7] [8]	-0.0300	-3735	-0.3735
Error Kirchhoff - COMSOL		1.5 %	2.9 %	2.9 %
Error Timoshenko - COMSOL		1,9 %	**0.3 %**	**0.3 %**
Error Kirchhoff - MATLAB		13.6 %	13.3 %	13.3 %
Error Timoshenko - MATLAB		17.6 %	17.1 %	17.1 %

As shown in table C.6 COMSOl results are the closests to the analytical solutions obtained for the three cases studied. However, MATLAB results don't exceed an error of a 20%.

POLYTECHNIC UNIVERSITY OF CATALONIA
Structural Mechanics
Matlab and Comsol

C.6 Report 6: Receptance of a flat shell

The aim of this report is to understand what the receptance is and to verify its computation with MATLAB. In order to do so, a modal analysis will be performed on a flat squared shell embedded for each of its four edges. Once obtained the frequencies at which the shell will be in resonance, the receptance will be computed. Finally, if the receptance results obtained present a discontinuity on the eigenvalues previously calculated, the computation of the receptance will be verified.

C.6.1 Model definition

This report will be analysing a flat squared shell with the following characteristics.

Geometry

- Shell dimensions: 2,00 x 2,00 m
- Shell thickness: 0.05 m

Material

- Young's modulus, E = 69 GPa.
- Poisson's ratio, $\nu = 0.3$.
- Mass density, $\rho = 2700 kg/m^3$.

Boundary conditions

- The four edges of the shell are embedded. All direction displacements and rotations are equal to 0.

- A distributed load of $-1 \cdot 10^6$ N/m^2 is applied on the surface.
- Gravity is also considered in the problem.

C.6.2 Modes and natural frequencies

The first study at which the flat shell has been submitted is a modal analysis which consisted in obtaining the modes and the natural frequencies of a flat shell embedded for its four edges using COMSOL and MATLAB. On the first place, the modal analysis has been performed in COMSOL and the first 6 natural frequencies obtained are listed in table C.7. Moreover, its respective vibration modes are shown in figures C.146, C.147, C.148, C.149, C.150 and C.151.

TABLE C.7: First 6 natural frequencies [COMSOL].

Mode	**Frequency (Hz)**
1st	108.72
2nd	220.53
3rd	220.53
4th	323.44
5th	392.29
6th	394.32

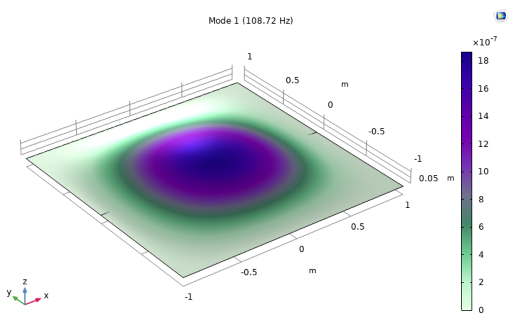

FIGURE C.146: Mode 1 (108.72 Hz) [COMSOL].

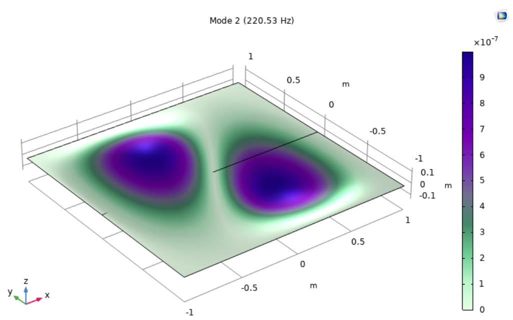

FIGURE C.147: Mode 2 (220.53 Hz) [COMSOL].

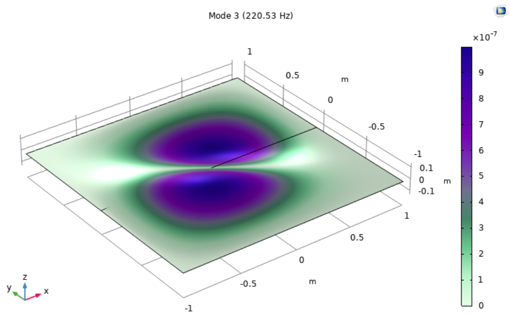

FIGURE C.148: Mode 3 (220.53 Hz) [COMSOL].

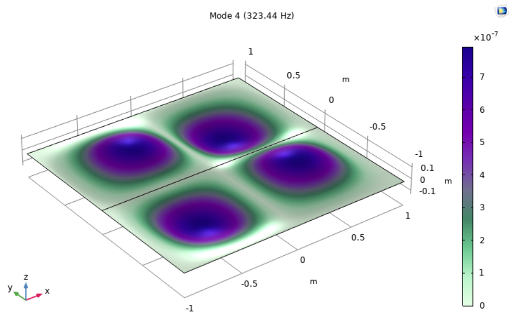

FIGURE C.149: Mode 4 (323.44 Hz) [COMSOL].

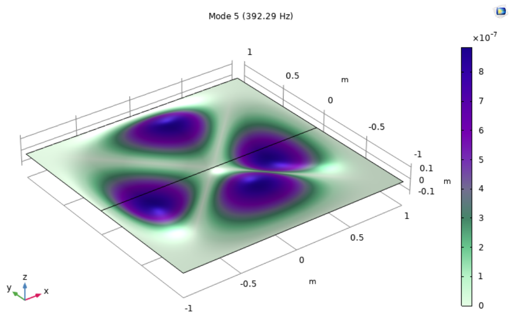

FIGURE C.150: Mode 5 (392.29 Hz) [COMSOL].

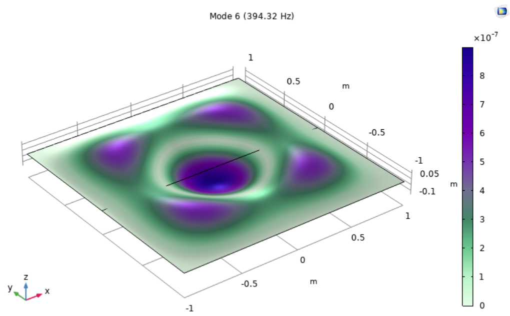

FIGURE C.151: Mode 6 (394.32 Hz) [COMSOL].

Furthermore, the same analysis has been carried on with MATLAB. The first 6 natural frequencies obtained are listed in table C.8 and its respective vibration modes are shown in figure C.152.

TABLE C.8: First 6 natural frequencies [MATLAB].

Mode	**Frequency (Hz)**
1st	104.855
2nd	324.868
3rd	324.868
4th	450.583
5th	451.861
6th	459.721

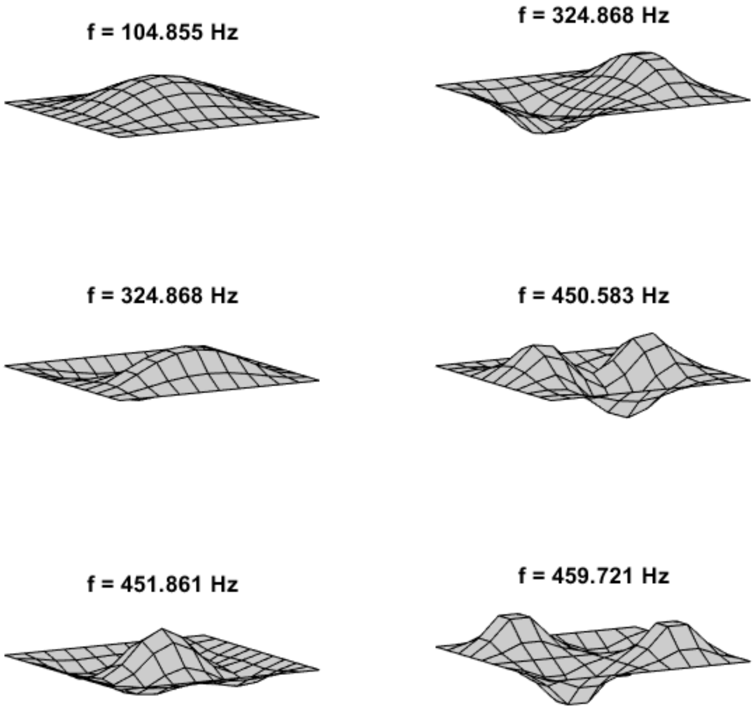

FIGURE C.152: First 6 modes considering a 100 elements mesh (10x10) [MATLAB].

For the modal analysis it can be concluded that, at higher frequencies the eigenvalues obtain tend to disagree. However, for the fist mode, the natural frequency obtained is quite similar.

C.6.3 Receptance

Then, the receptance will be computed in order to evaluate the form of the resulting function versus frequency. If calculations were correct, the resulting plots for the variables in which a certain movement is described (u_z, θ_x and θ_y) will have a similar shape to the results obtained in figure C.153.

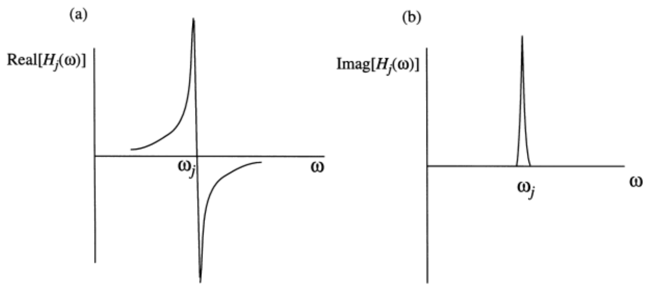

FIGURE C.153: Plots of complex receptance function: (a) real part and (b) imaginary part [13].

The receptance is defined as the division between the displacement obtained and the force applied.

$$[\mathbf{H}(\omega)] = \frac{\{\mathbf{X}(\omega)\}}{\{\mathbf{F}(\omega)\}} \tag{C.44}$$

As the force is the same for all of the nodes of the shell, it has been selected the two nodes at which the maximum displacements and rotations will take place in order to identify easily the maximum receptance and the characteristic shape of the function of the receptance versus frequency shown in figure C.153. Those selected nodes have been P1 in which the displacement in the z-direction is maximum and P2 in which the rotation in x and y-direction are maximum. The location of these two points on the shell are shown in figure C.184.

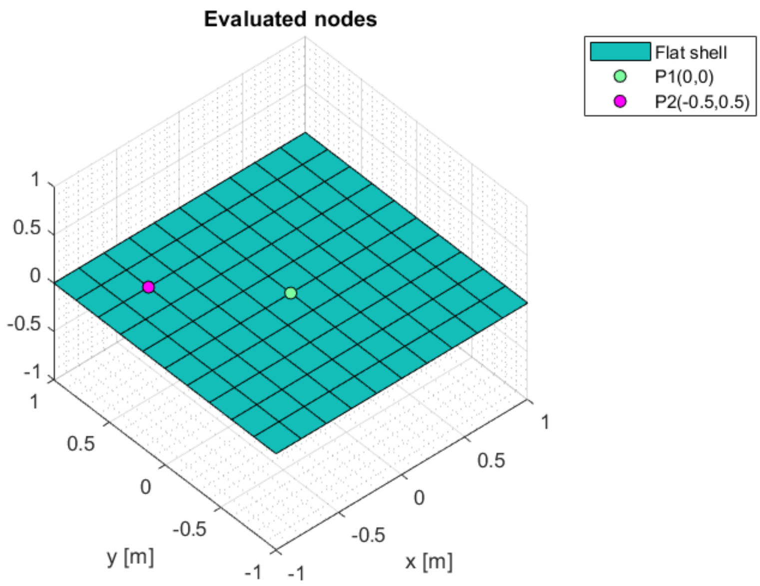

FIGURE C.154: Scheme of the location of the evaluated nodes of the shell [MATLAB].

Then, the receptance distribution along the frequency domain as well as the receptance distribution along the shell for the frequency of 104.8 Hz have been computed for each degree-of-freedom

(u_x, u_y, u_z, θ_x, θ_y and θ_z).

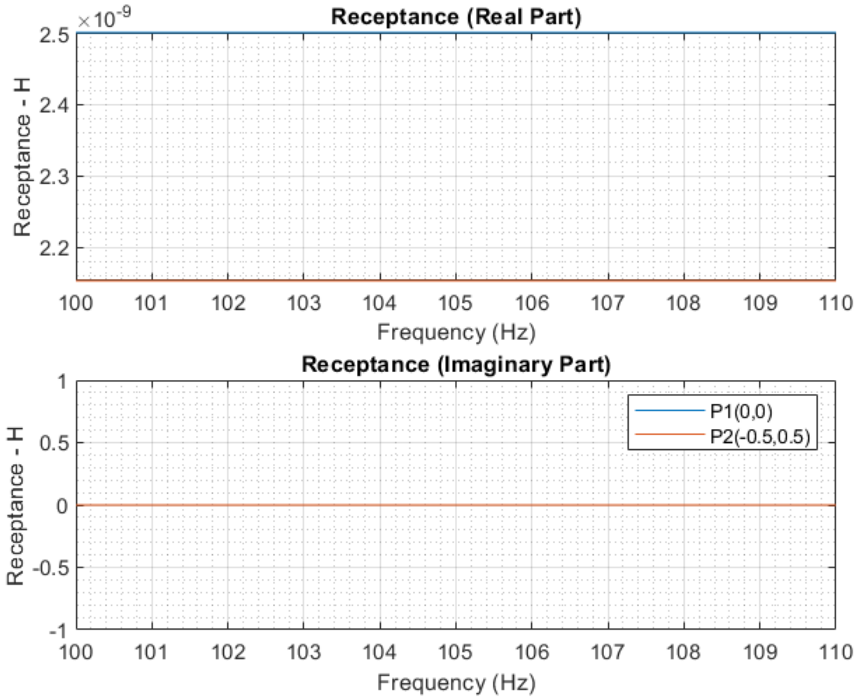

FIGURE C.155: Receptance obtained for u_x degree of freedom for nodes located in the coordinates P1 and P2 as a function of frequency [MATLAB].

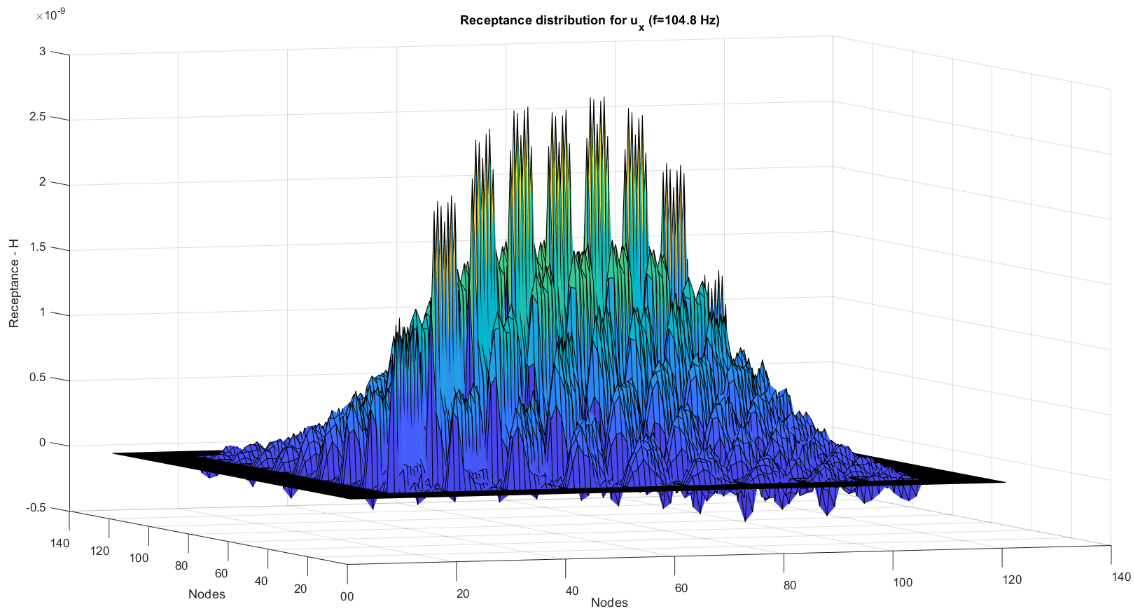

FIGURE C.156: Receptance distribution along the shell obtained for u_x degree of freedom for f=104.8 Hz [MATLAB].

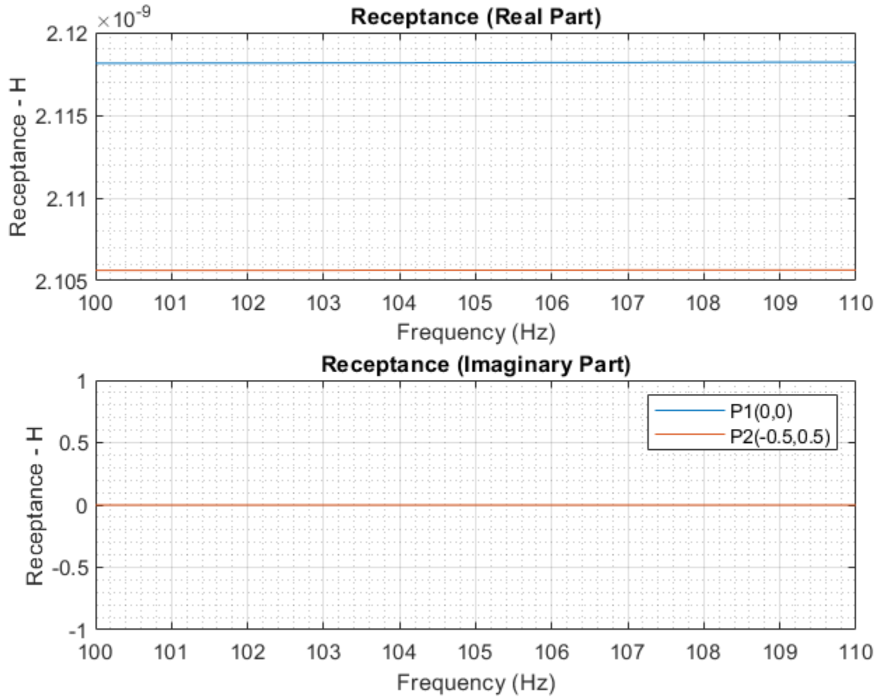

FIGURE C.157: Receptance obtained for u_y degree of freedom for nodes located in the coordinates P1 and P2 as a function of frequency [MATLAB].

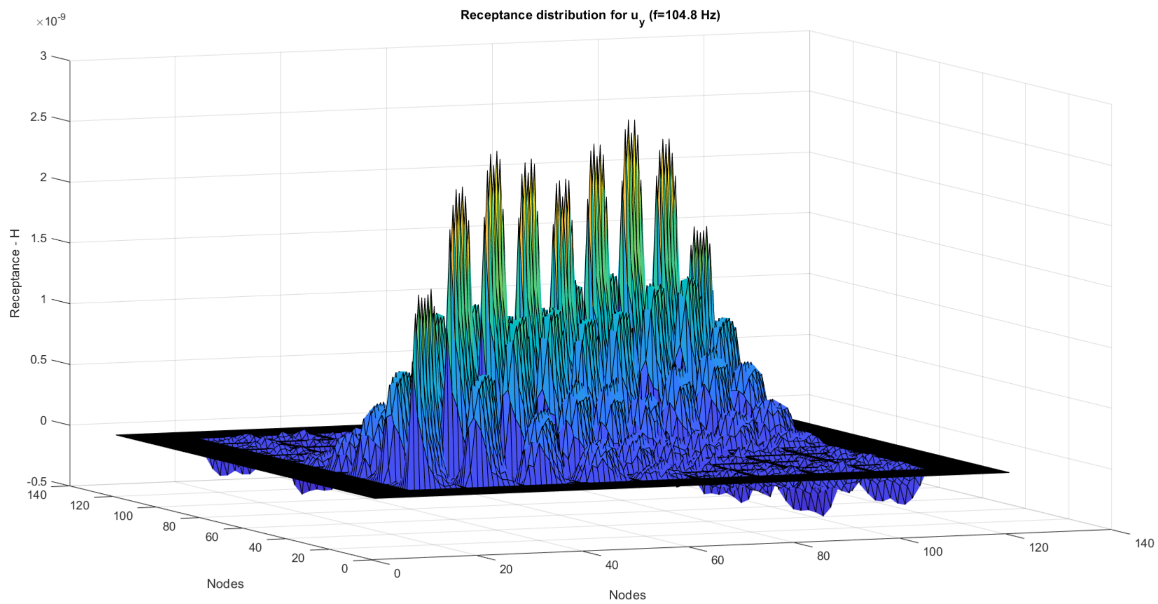

FIGURE C.158: Receptance distribution along the shell obtained for u_y degree of freedom for f=104.8 Hz [MATLAB].

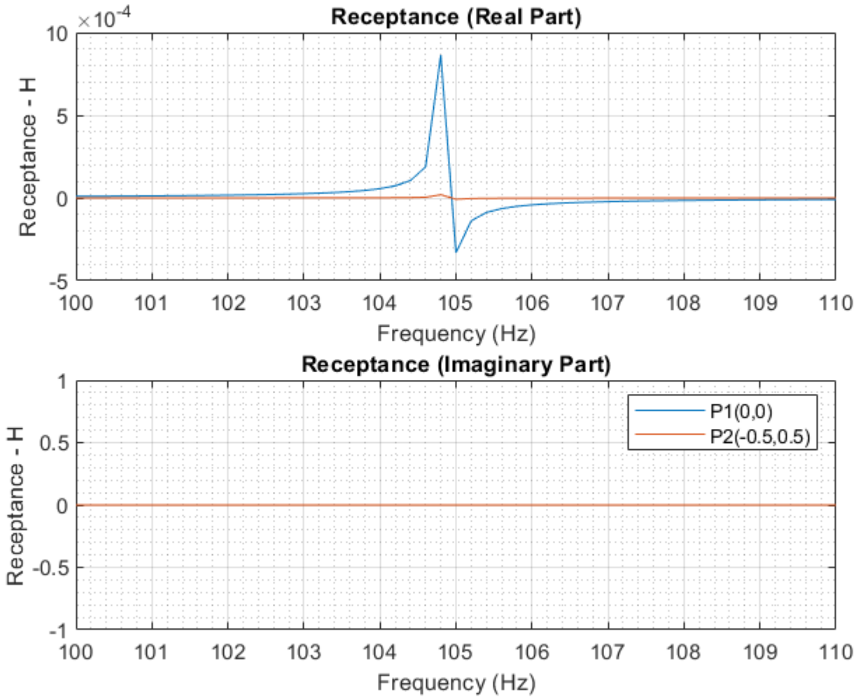

FIGURE C.159: Receptance obtained for u_z degree of freedom for nodes located in the coordinates P1 and P2 as a function of frequency [MATLAB].

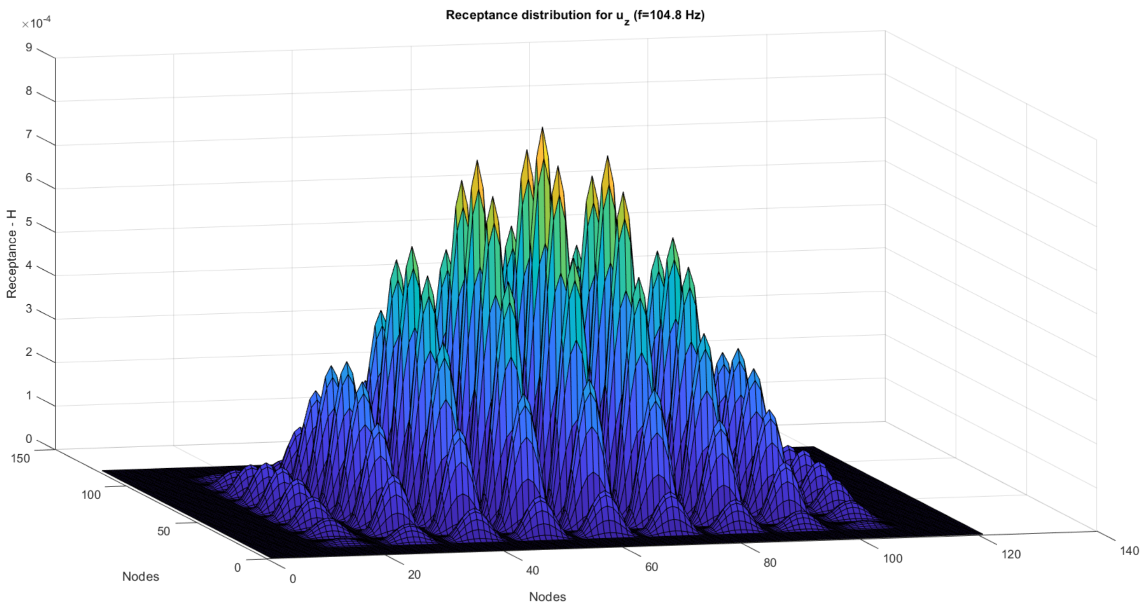

FIGURE C.160: Receptance distribution along the shell obtained for u_z degree of freedom for f=104.8 Hz [MATLAB].

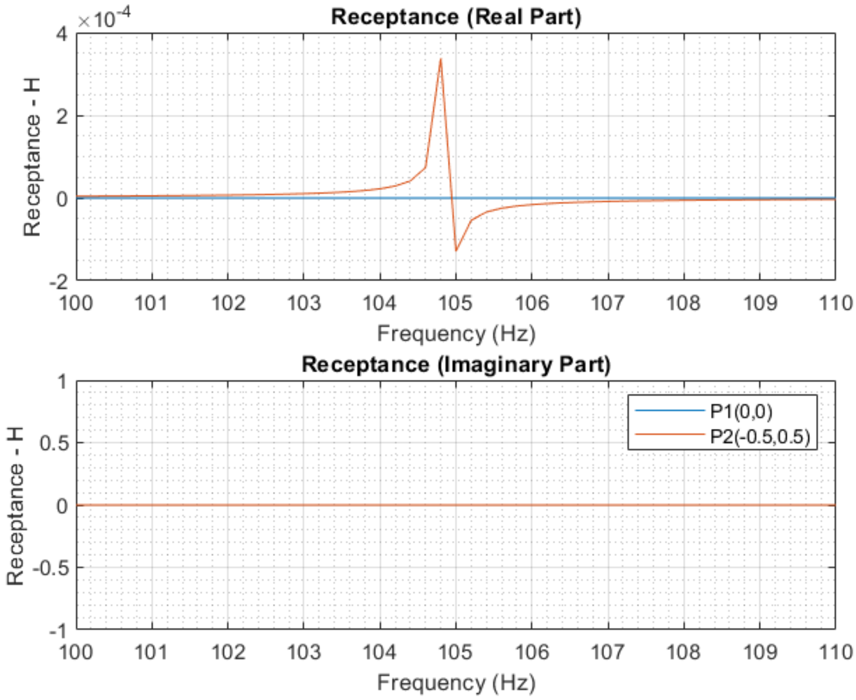

FIGURE C.161: Receptance obtained for θ_x degree of freedom for nodes located in the coordinates P1 and P2 as a function of frequency [MATLAB].

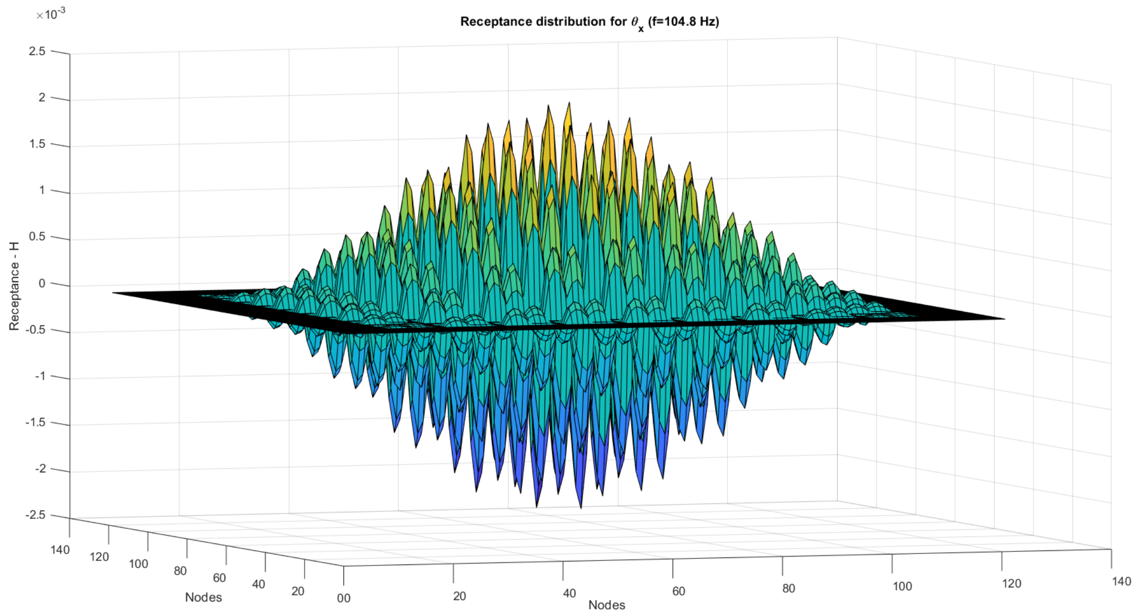

FIGURE C.162: Receptance distribution along the shell obtained for θ_x degree of freedom for f=104.8 Hz [MATLAB].

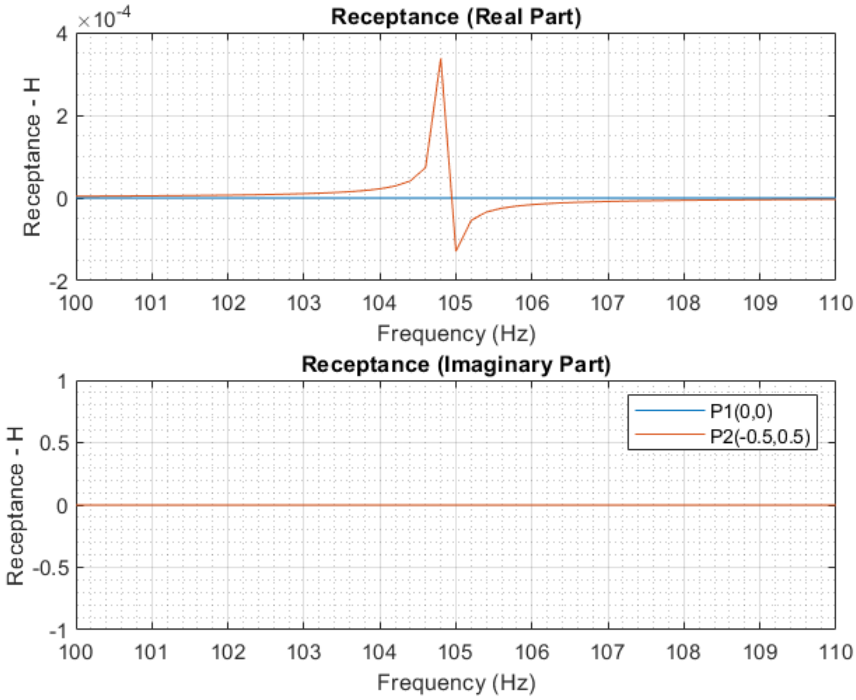

FIGURE C.163: Receptance obtained for θ_y degree of freedom for nodes located in the coordinates P1 and P2 as a function of frequency [MATLAB].

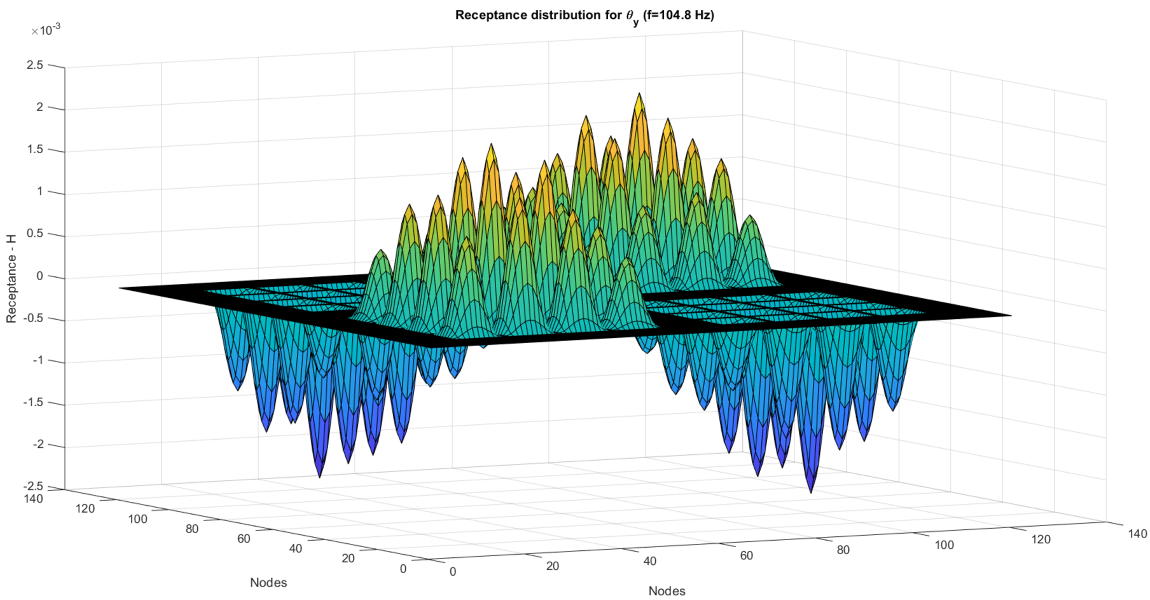

FIGURE C.164: Receptance distribution along the shell obtained for θ_y degree of freedom for f=104.8 Hz [MATLAB].

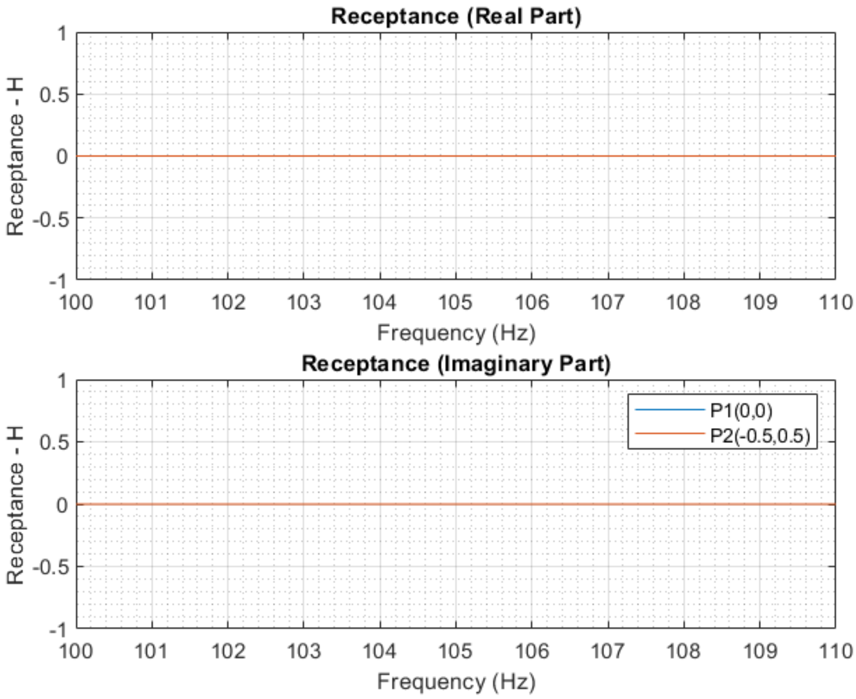

FIGURE C.165: Receptance obtained for θ_z degree of freedom for nodes located in the coordinates P1 and P2 as a function of frequency [MATLAB].

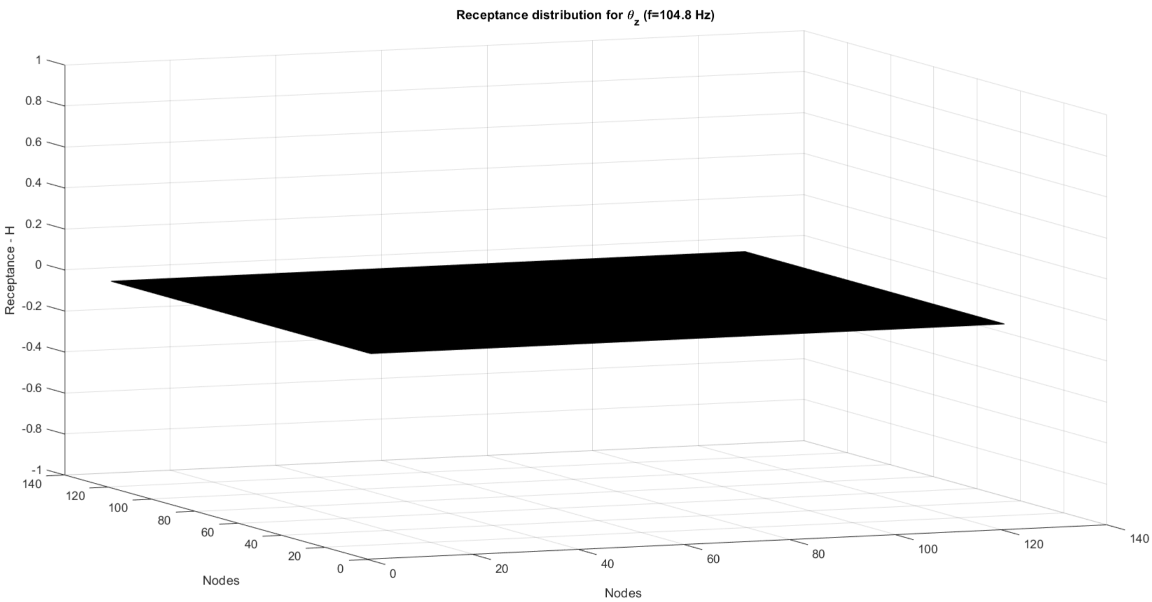

FIGURE C.166: Receptance distribution along the shell obtained for θ_y degree of freedom for f=104.8 Hz [MATLAB].

As expected, the real part of the plots of the variables that describe a certain movement such as u_z, θ_x and θ_y (figures C.159, C.161 and C.163) present the same shape as in figure C.153. However, when comparing the imaginary plot with the one presented in figure C.153, it is quite different, there is no discontinuity. This disagreement happens due to the frequency step used to obtain the plots with MATLAB. The frequency step is not accurate enough to compute the receptance in exactly the natural frequency value.

Furthermore, the receptance computed for the other degrees of freedom u_x, u_y and θ_z doesn't present this characteristic shape due to the fact that these degrees of freedom don't describe any movement along time, in other words, the quadrilateral shell doesn't describe any displacement in the x and y-direction or any rotation in the z-direction.

Figures C.156, C.158, C.160, C.162, C.164 and C.166 represent the receptance obtained from the relation between each movement with the force applied (u_x, u_y, u_z, θ_x, θ_y and θ_z respectively). Not only is the receptance evaluated for each movement, but also for each pair of nodes, in other words, the shell is discretised in 121 nodes (11 x 11 nodes in each edge) so the receptance is calculated 121x121 times to evaluated the relation between all the nodes for a certain movement.

For instance, considering figure C.160, the receptance is computed for 104.8 Hz and only for u_z displacement. X and Y-axis represent the 121 nodes in which the shell is discretised. Finally, Z-axis define the receptance for the z-displacement between the pair of nodes evaluated.

Finally, figure C.167 represents the receptance distribution obtained for u_z, θ_x and θ_y degrees of freedom for a range of frequencies that includes the first 6 natural frequencies. As expected, for the natural frequencies, the plot will present six times the characteristic shape shown in figure C.153 for each natural frequency evaluated. Moreover, it can be seen that the discontinuity is more remarkable for lower natural frequencies.

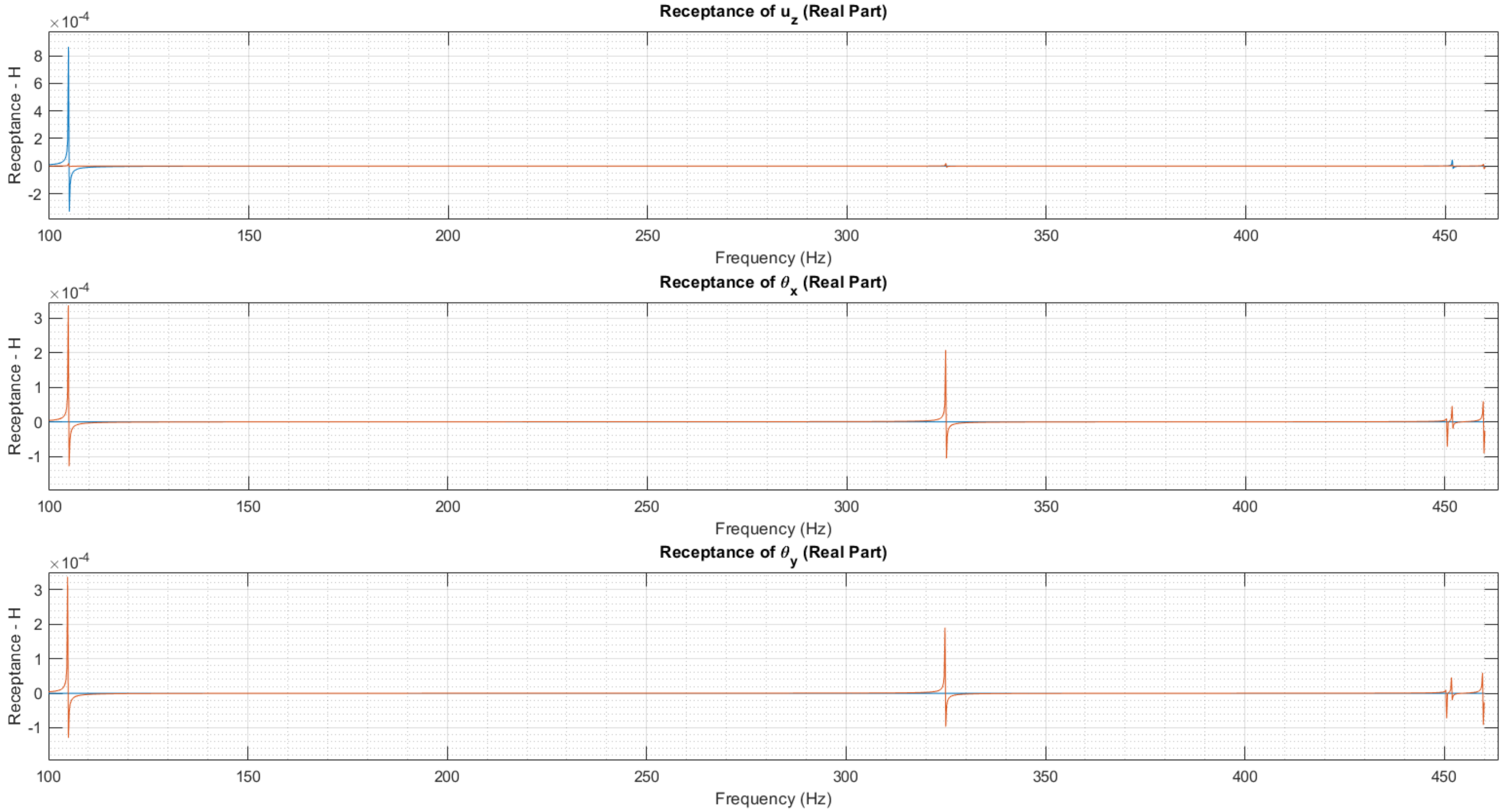

FIGURE C.167: Receptance distribution obtained for u_z, θ_x and θ_y degrees of freedom for a range of frequencies that includes the first 6 natural frequencies [MATLAB].

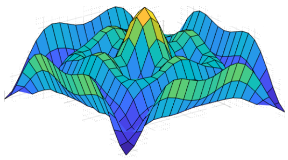

POLYTECHNIC UNIVERSITY OF CATALONIA
Structural Mechanics
Matlab and Comsol

C.7 Report 7: Harmonic and Random Vibration Excitation

The aim of this report is to develop a MATLAB code capable of obtaining the response in the frequency domain of the displacements and the Von Mises stress distributions that a flat shell presents when an harmonic or a random vibration load is applied.

C.7.1 Model definition

Geometry

- Shell dimensions: 2,00 x 2,00 m
- Shell thickness: 0.05 m

Material

- Young's modulus, E = 69 GPa.
- Poisson's ratio, $\nu = 0.3$.
- Mass density, $\rho = 2700 kg/m^3$.

Boundary conditions

- The four edges of the shell are embedded. All direction displacements and rotations are equal to 0.
- An harmonic or a random vibration excitation is applied on the z-direction of the middle node of the shell.

Evaluated nodes

First, it has been selected the two nodes at which the maximum displacements and rotations will be obtained in order to identify easily the maximum displacement and Von Mises stress, the location of the points chosen are shown in figure C.168. Those selected nodes have been P1 in which the displacement in the z-direction will be maximum and P2 in which the rotation in x and y-direction will be maximum.

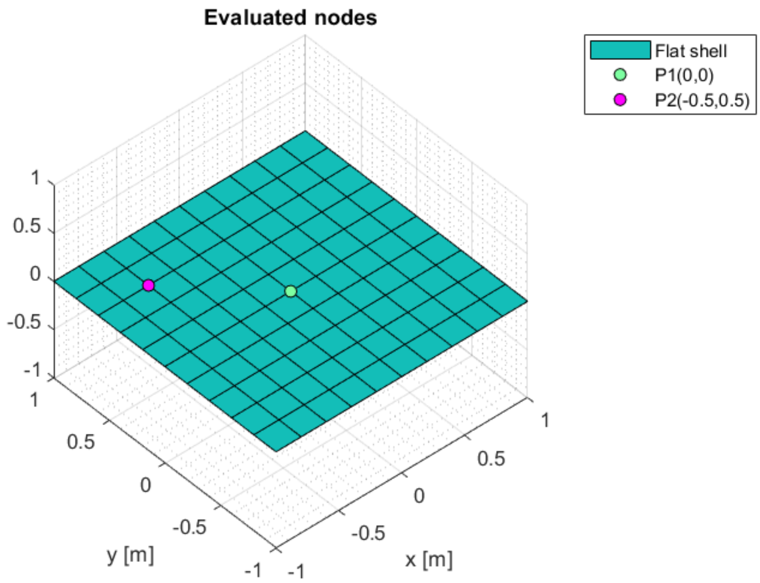

FIGURE C.168: Scheme of the location of the evaluated nodes of the shell [MATLAB].

C.7.2 Harmonic Force Excitation

Then, an harmonic force excitation has been applied on the middle of the shell in order to evaluate its response in the frequency domain. First, two methods has been used to compute the response in order to compare the results obtained for each method and verify its convergence.

The first methodology used is shown in figure C.169. The harmonic vibration of an amplitude of 50 m/s^2 and a frequency of 70 Hz has been first computed in the time domain.

$$s = -50 \cdot \sin(2\pi 70t) \tag{C.45}$$

Then, with the use of the mass matrix and considering that the acceleration is applied on the u_z degree of freedom of the middle node of the shell, the force in time domain has been calculated as well for each time step.

$$\{\mathbf{a}\} = \{\mathbf{a}(DOF, t)\} \tag{C.46}$$

$$\{\mathbf{a}(u_{z\ middle\ node}, :)\} = s \tag{C.47}$$

$$\{\mathbf{f}(:,t)\} = [\mathbf{M}]\{\mathbf{a}(:,t)\} \tag{C.48}$$

Once obtained the force applied to each degree of freedom of the system for every time step considered, the force is computed in the frequency domain thanks to the use of the Fourier Transform.

$$\{\mathbf{F}\} = fft(\{\mathbf{f}\}) \tag{C.49}$$

Figure C.169 shows the results obtained for the middle node along the frequency domain using the first methodology.

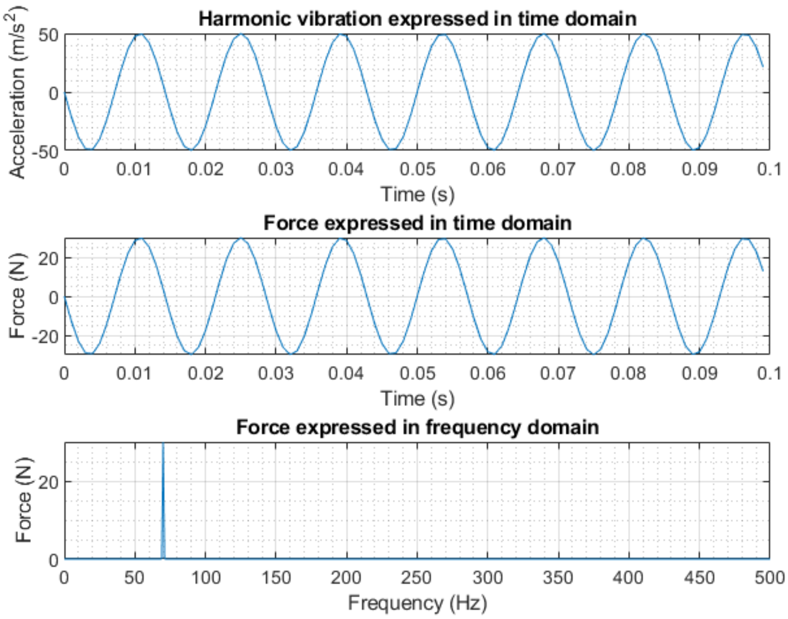

FIGURE C.169: Methodology 1 used to compute the force in the frequency domain [MATLAB].

Once computed the force vector in the frequency domain the displacements in the frequency domain can be calculated with the use of the following equation

$$\{\mathbf{X}(\omega)\} = [\mathbf{H}(\omega)]\{\mathbf{F}(\omega)\} \tag{C.50}$$

As shown in figure C.170, the shell only describes a displacement in the z-direction and a rotation in the x and y-direction. Moreover, as the resulting shape is the same as the Fourier Transform of a sinusoidal function, the shell describes an harmonic movement in the z-direction (u_z) and an harmonic movement for both rotations as well.

The displacements in the time domain for the middle node of the shell P1(0,0) m (left column) and for P2 (-0.5,0.5) m (right column) can be describe as

$$
\begin{aligned}
&P_1 && P_2 \\
&u_x = 0 && u_x = 0 && \text{(C.51)}\\
&u_y = 0 && u_y = 0 && \text{(C.52)}\\
&u_z = 4,1 \cdot 10^{-4} \cdot \sin(2\pi 70t) && u_z = 0.2 \cdot 10^{-4} \cdot \sin(2\pi 70t) && \text{(C.53)}\\
&\theta_x = 0 && \theta_x = -2,6 \cdot 10^{-4} \cdot \sin(2\pi 70t) && \text{(C.54)}\\
&\theta_y = 0 && \theta_y = -2,6 \cdot 10^{-4} \cdot \sin(2\pi 70t) && \text{(C.55)}\\
&\theta_z = 0 && \theta_z = 0 && \text{(C.56)}
\end{aligned}
$$

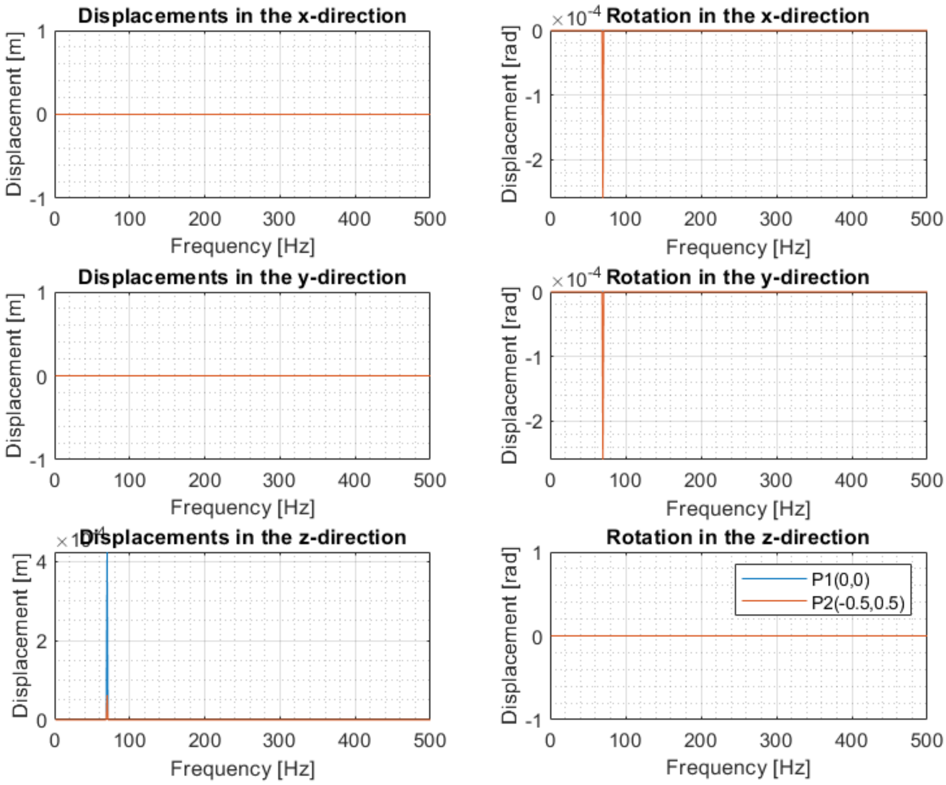

FIGURE C.170: Displacements in the frequency domain obtained when an harmonic force is applied using a 400 element mesh (20x20) [MATLAB].

The second methodology used is shown in figure C.171. The harmonic vibration of an amplitude of 50 m/s^2 and a frequency of 70 Hz has been first computed in the time domain as the first methodology.

$$s = -50 \cdot \sin(2\pi 70t) \quad \text{(C.57)}$$

Then, with the use of the Fourier Transform the acceleration has been transformed from the time domain to the frequency domain.

$$S = fft(s) \tag{C.58}$$

Once obtained the acceleration in the frequency domain, the acceleration has been applied to the u_z degree of freedom of the middle node of the shell.

$$\{\mathbf{A}\} = \{\mathbf{A}(DOF, freq)\} \tag{C.59}$$

$$\{\mathbf{A}\}(u_{z\ middle\ node}, :) = S \tag{C.60}$$

With the mass matrix and the acceleration in the frequency domain, the force in the frequency domain for each frequency step can be computed.

$$\{\mathbf{F}(:, freq)\} = [\mathbf{M}]\{\mathbf{A}(:, freq)\} \tag{C.61}$$

Figure C.171 shows the results obtained in the middle node for each step of the second methodology used to compute the force in the frequency domain.

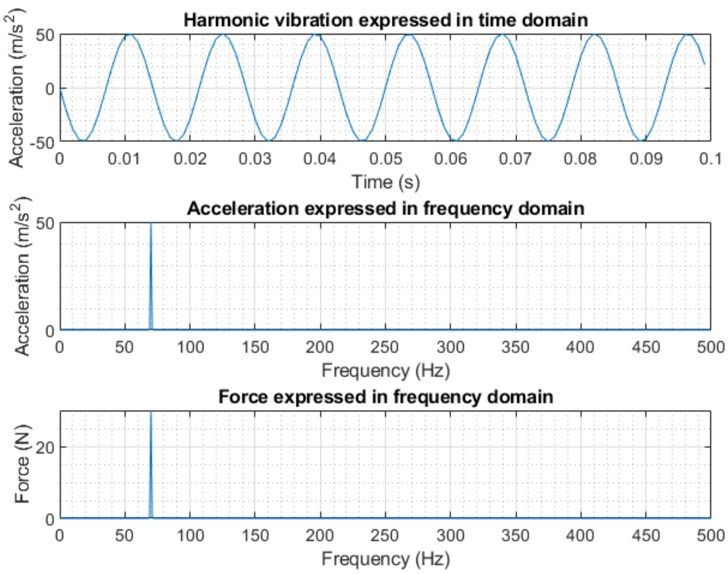

FIGURE C.171: Methodology 2 used to compute the force in the frequency domain [MATLAB].

Once computed the force vector in the frequency domain the displacements in the frequency domain can be calculated with the use of the following equation

$$\{\mathbf{X}(\omega)\} = [\mathbf{H}(\omega)]\{\mathbf{F}(\omega)\} \tag{C.62}$$

Comparing figures C.170 and C.172, the same results are obtained using both computational methods. This conclusion drawn will be useful when considering a random force excitation instead of an harmonic force because it will not be necessary to be working in the time domain when the input is a Power Spectral Density function expressed in the frequency domain.

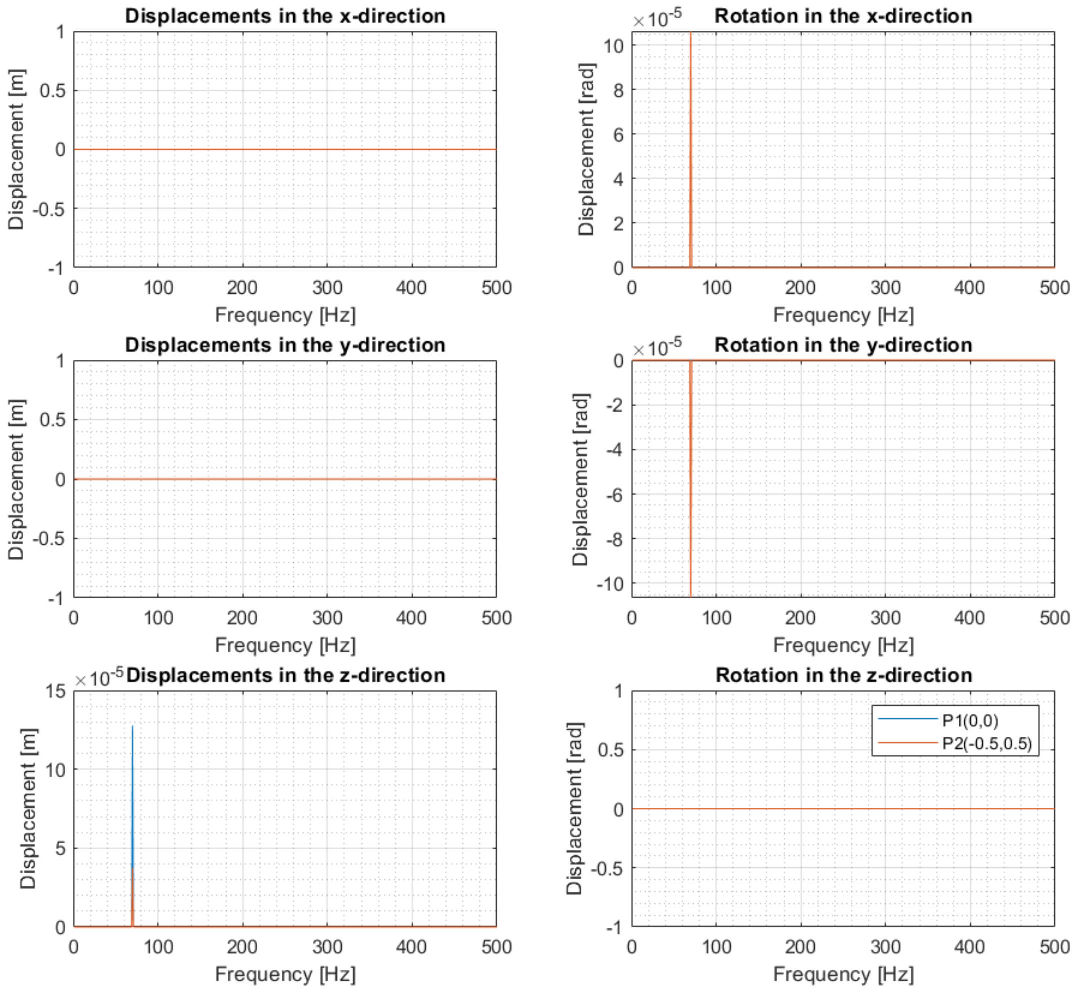

FIGURE C.172: Displacements in the frequency domain obtained when an harmonic force is applied using a 400 element mesh (20x20) [MATLAB].

Moreover, figure C.172 shows that the response of an harmonic force excitation is sinusoidal. In other words, the shape of the displacements in the z-direction and the rotation in both, x and y-direction, agrees with the Fourier Transform of a sinusoidal function. Furthermore, from figure C.172, the frequency at which the maximum displacement is presented is 70 Hz which results to be the same value as the frequency of the harmonic force input applied.

Figure C.173 shows the displacements distribution along the shell when the frequency is equal to 70 Hz. As the four edges of the plate have fixed displacement restrictions, the maximum displacement is located in the middle of the shell with a value of $13 \cdot 10^{-5}$m and coincides with the location at which the harmonic load has been applied. Moreover, although the displacement in x and y-direction as well as the rotation in the z-direction are null, the rotation in both, x and y-direction, changes along the shell and its distribution is presented in figure C.173.

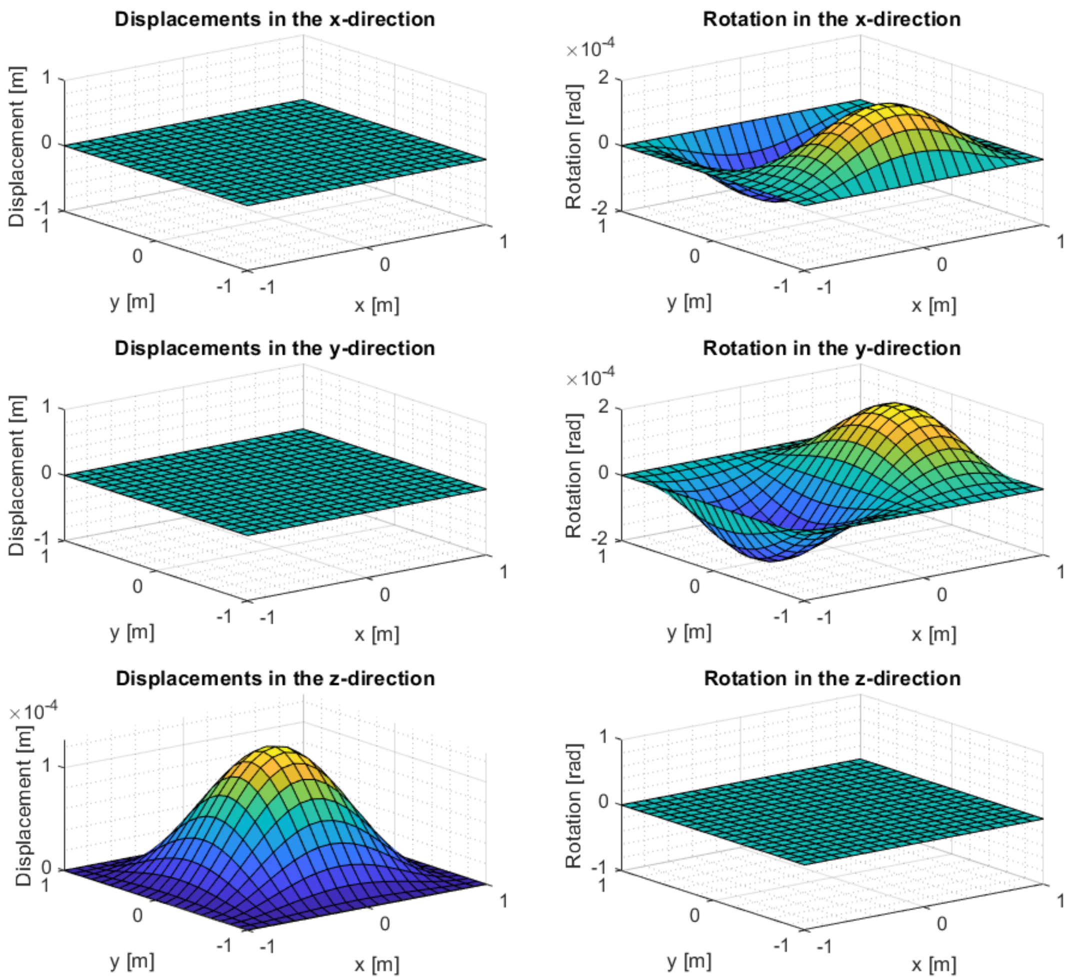

FIGURE C.173: Maximum displacement obtained when the frequency is equal to 70 Hz using a 400 element mesh (20x20) [MATLAB].

Figure C.174 shows the Von Misses stress versus frequency. As what happened to the displacement distribution along the frequency for an harmonic force, the stress distribution describes as well an harmonic oscillation in the frequency domain when the frequency is equal to 70 Hz. In other words, the shape of the Von Mises stress agrees with the Fourier Transform of a sinusoidal function.

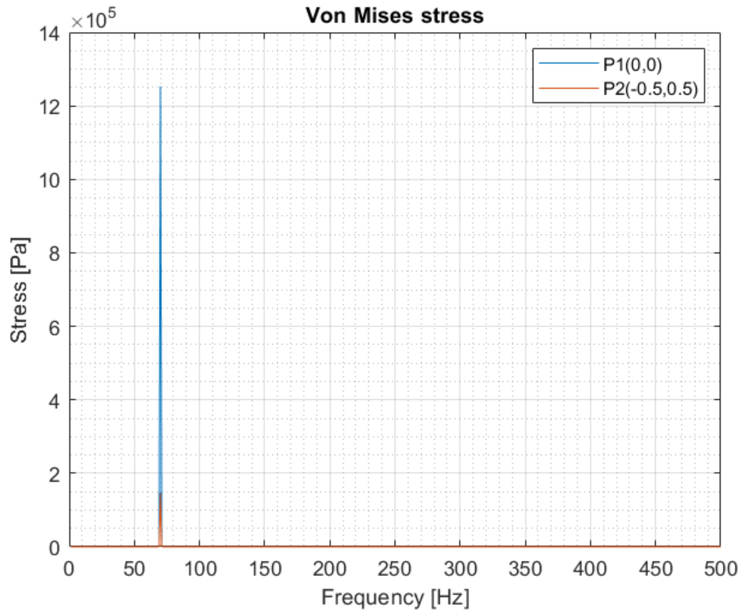

FIGURE C.174: Von Mises stress in the frequency domain obtained for an harmonic force using a 400 element mesh (20x20) [MATLAB].

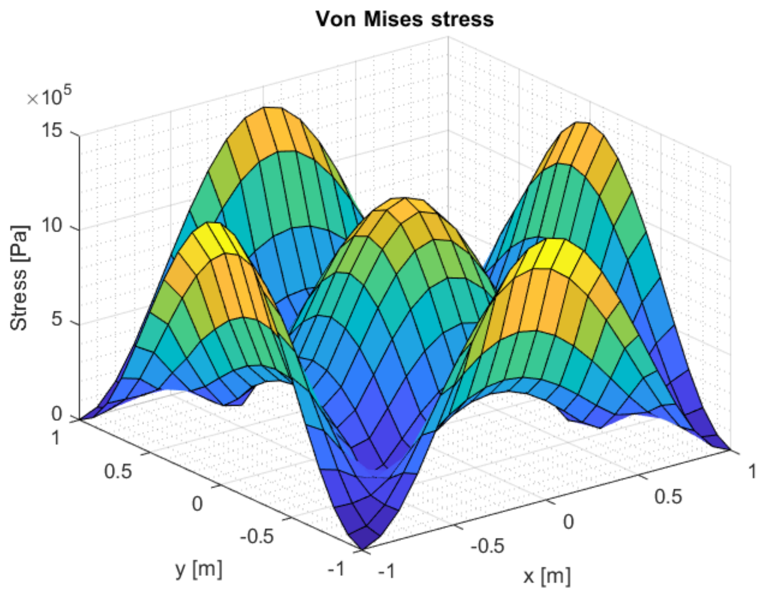

FIGURE C.175: Maximum Von Mises stress obtained when the frequency is equal to 70 Hz using a 400 element mesh (20x20) [MATLAB].

The Von Mises stress distribution along the shell for a frequency of 70 Hz is presented in figure C.175 in which it can be concluded that the maximum stress is located in the middle node of the external edges of the shell with a value of $14 \cdot 10^5$ Pa.

C.7.3 Random Force Excitation

In this section, a random vibration force will be applied in the z-direction of the middle node of the shell and, thanks to the conclusions drawn in the previous section, the force will be computed directly in the frequency domain following the methodology shown in figure C.176.

First, the Power Spectral Density function that describes the acceleration applied is

$$PSD = 6 \cdot log_{10}(freq) + 0.04 - 6 \cdot log_{10}(40) \qquad when\ freq < 40\ Hz \tag{C.63}$$

$$PSD = 0.04 \qquad when\ 40\ Hz \leq freq \leq 450\ Hz \tag{C.64}$$

$$PSD = -6 \cdot log_{10}(freq) + 0.04 + 6 \cdot log_{10}(450) \qquad when\ freq > 450\ Hz \tag{C.65}$$

Then, the acceleration has been computed from the PSD input using the following expression:

$$PSD = \frac{S^2}{\Delta freq} \qquad \longrightarrow \qquad S = \sqrt{PSD \cdot \Delta freq} \tag{C.66}$$

As the acceleration is now expressed in g units, it has been multiplied by 9.81 m/s^2 in order to obtain the acceleration in the international system units. Finally, the acceleration has been applied to the u_z degree of freedom of the middle node of the shell.

$$\{\mathbf{A}\} = \{\mathbf{A}(DOF, freq)\} \tag{C.67}$$

$$\{\mathbf{A}\}(u_{z\ middle\ node}, :) = S \tag{C.68}$$

With the mass matrix and the acceleration in the frequency domain, the force in the frequency domain for each frequency step can be computed.

$$\{\mathbf{F}(:, freq)\} = [\mathbf{M}]\{\mathbf{A}(:, freq)\} \tag{C.69}$$

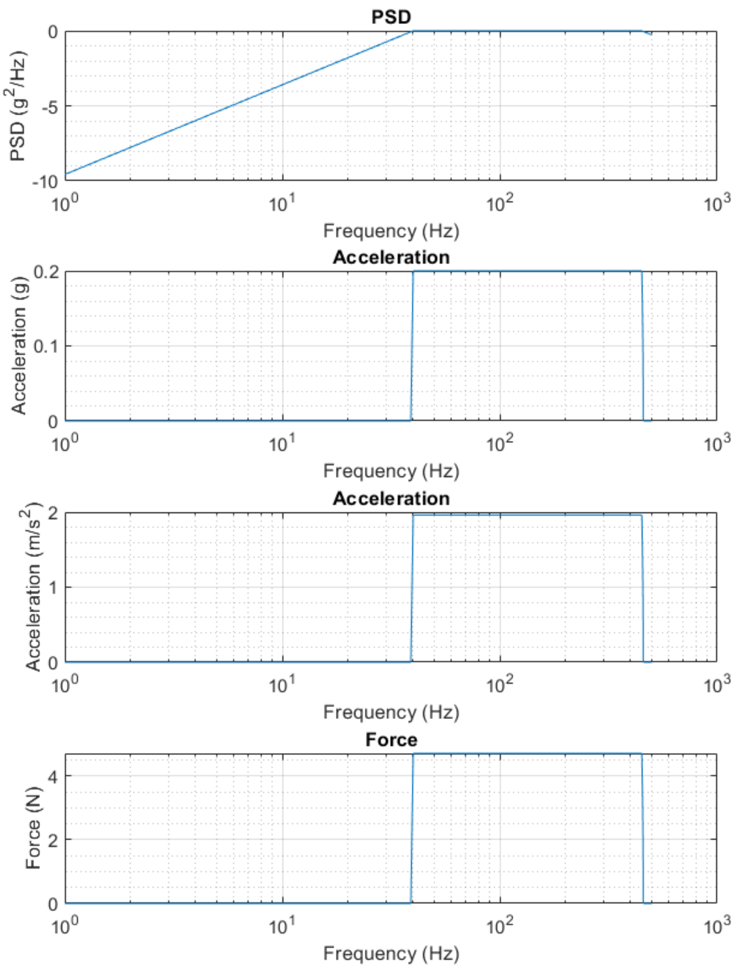

FIGURE C.176: Methodology used to compute the force in the frequency domain for a random vibration excitation [MATLAB].

Figure C.177 shows the displacements in P1 and P2 versus the frequency. The maximum displacement in the z-direction as well as the maximum rotation in both, x and y-direction, is located at the same frequency of 103 Hz.

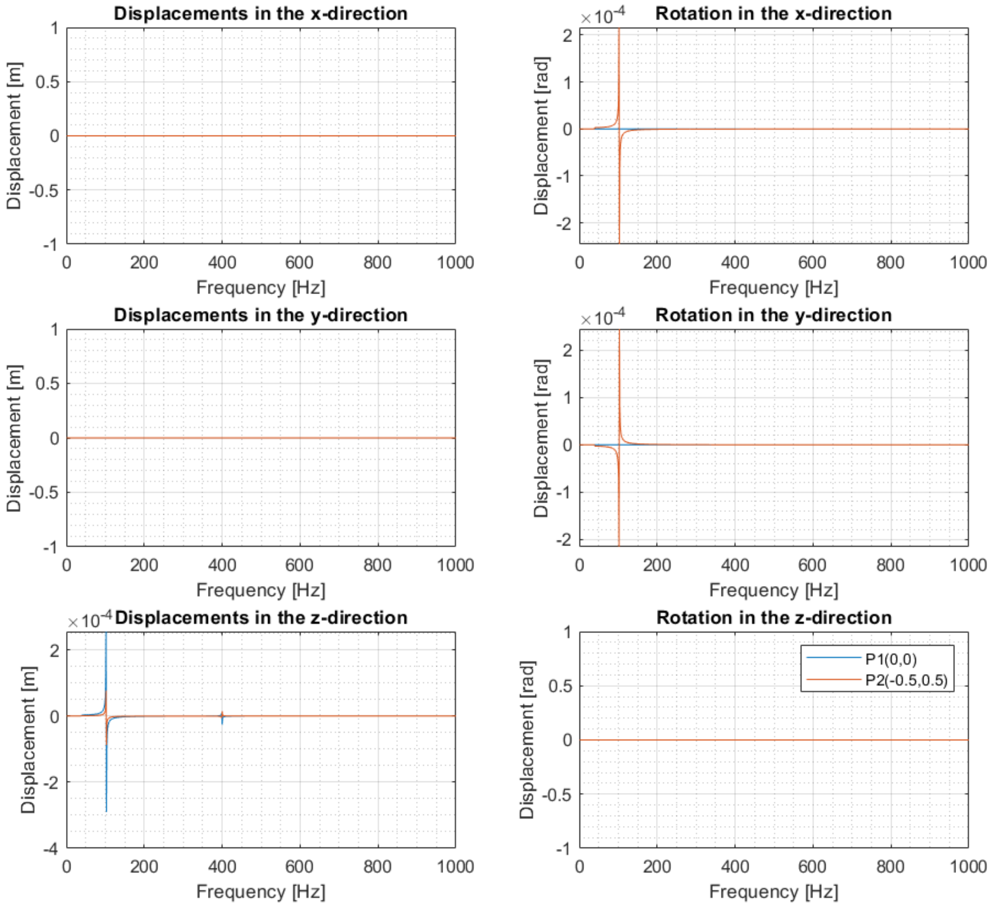

FIGURE C.177: Displacements in the frequency domain obtained for a random vibration force using a 400 element mesh (20x20) [MATLAB].

Furthermore, figure C.178 presents the displacements in P1 and P2 versus the frequency focusing on what is happening in an smaller scale where it can be seen, for instance, that when the frequency is equal to 40 Hz the graphic presents a jump as a results of a variation in the slope of the PSD function in this frequency.

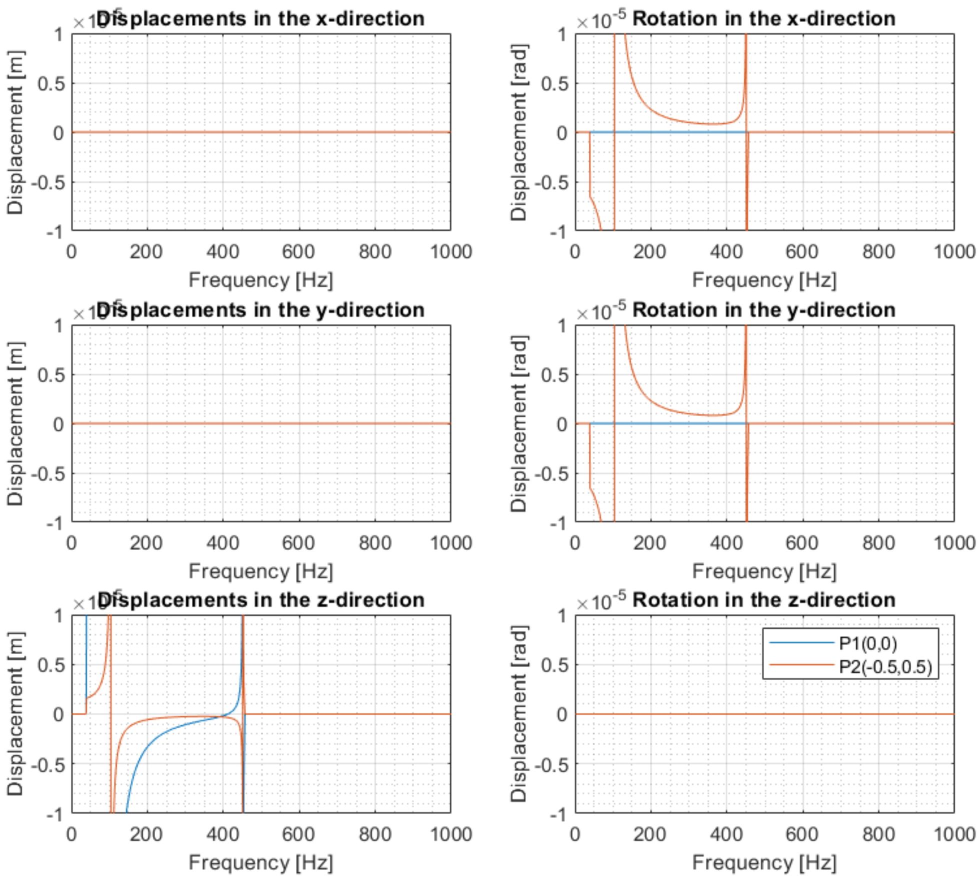

FIGURE C.178: Displacements in the frequency domain obtained for a random vibration force using a 400 element mesh (20x20) [MATLAB].

The displacement and rotation distributions along the shell are plotted in figure C.179 for the frequency of 103 Hz where the maximum displacement takes places. The maximum displacement in the z-direction is located in the middle node of the shell with a value of $2.5 \cdot 10^{-4}$m. Furthermore, figure C.180 shows the displacements distribution along the shell for the frequency of 400 Hz.

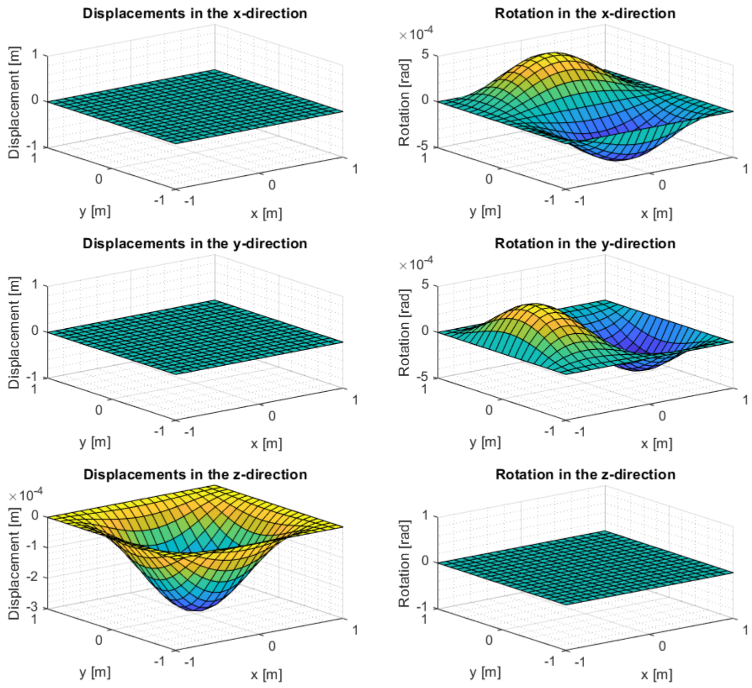

FIGURE C.179: Displacement obtained when the frequency is equal to 103 Hz using a 400 element mesh (20x20) [MATLAB].

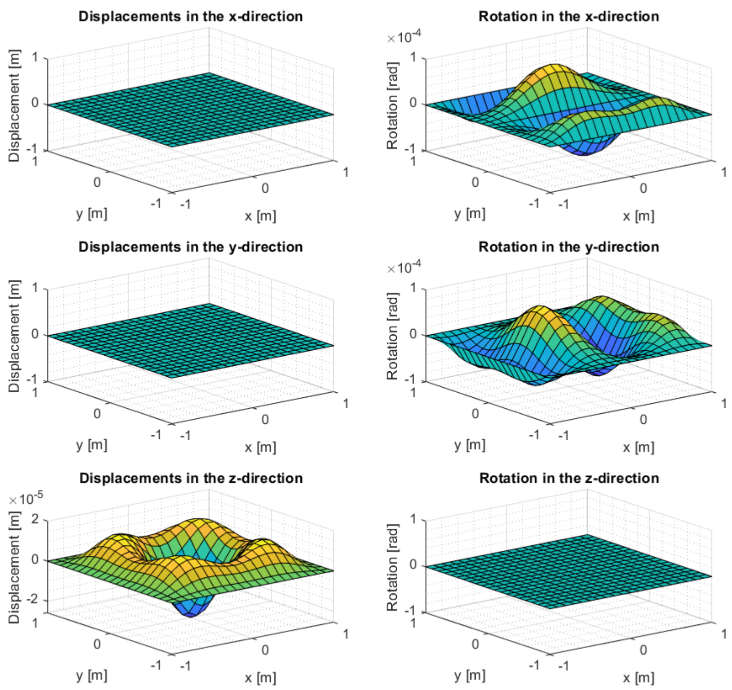

FIGURE C.180: Displacement obtained when the frequency is equal to 400 Hz using a 400 element mesh (20x20) [MATLAB].

Figure C.181 shows the Von Misses stress distribution versus frequency. As what happened to the displacement distribution along the frequency for an harmonic force, the stress distribution has its maximum when the frequency is equal to 103 Hz. Figure C.182 presents the Von Mises stress distribution along the shell for the frequency of 103 Hz in order to obtain where the maximum stress is located. As what happened to the harmonic force vibration, the maximum stress is also located in the middle nodes of the external edges of the shell with a value of $3.2 \cdot 10^6$ Pa. Additionally, the Von Mises stress distribution along the shell has been plotted in figure C.183 for the frequency of 400 Hz where the second maximum takes place.

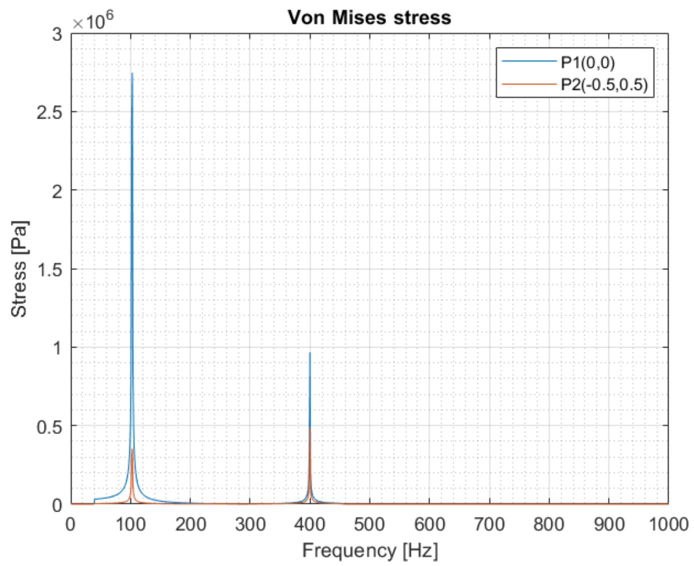

FIGURE C.181: Von Mises stress in the frequency domain obtained for a random vibration force using a 400 element mesh (20x20) [MATLAB].

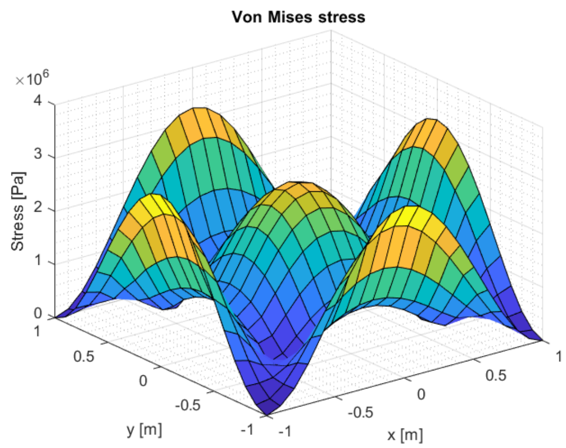

FIGURE C.182: Von Mises stress distribution along the shell obtained when the frequency is equal to 103 Hz using a 400 element mesh (20x20) [MATLAB].

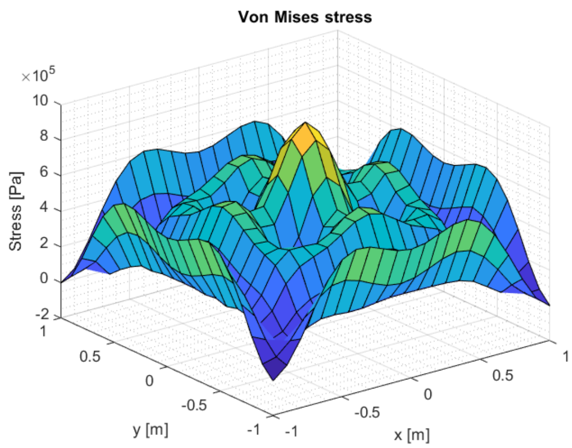

FIGURE C.183: Von Mises stress distribution along the shell obtained when the frequency is equal to 400 Hz using a 400 element mesh (20x20) [MATLAB].

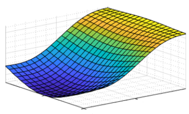

POLYTECHNIC UNIVERSITY OF CATALONIA
Structural Mechanics
Matlab and Comsol

C.8 Report 8: Free Shell

The aim of this report is to validate the MATLAB code created to compute the displacements and the Von Mises stress of a shell when a vibration is imposed on one of its edges. In order to do so, the report has been divided in fours sections. First, a modal analysis will be performed with MATLAB and COMSOL and the natural frequencies and modes obtained will be compared. Then, a quasi-static test will be computed using MATLAB from which the displacement and the Von Mises stress distribution along the shell will be calculated and later compared with the results obtained with COMSOL. In third place, a random vibration test will be also performed and compared with the one done with COMSOL. Once validated the MATLAB code, the dependence on the frequency step for the random vibration test will be studied and the PSDs for the displacements and the Von Mises stress distribution along the shell will be calculated.

C.8.1 Model definition

Geometry

- Shell dimensions: 2,00 x 2,00 m
- Shell thickness: 0.05 m

Material

- Young's modulus, E = 69 GPa.
- Poisson's ratio, $\nu = 0.3$.
- Mass density, $\rho = 2700 kg/m^3$.

Boundary conditions

- None of the four edges of the shell is embedded.
- An acceleration is defined in x=-1m line.

Evaluated nodes

Additionally, the position of the two nodes of the shell that will be analysed during the whole report are depict in figure C.184.

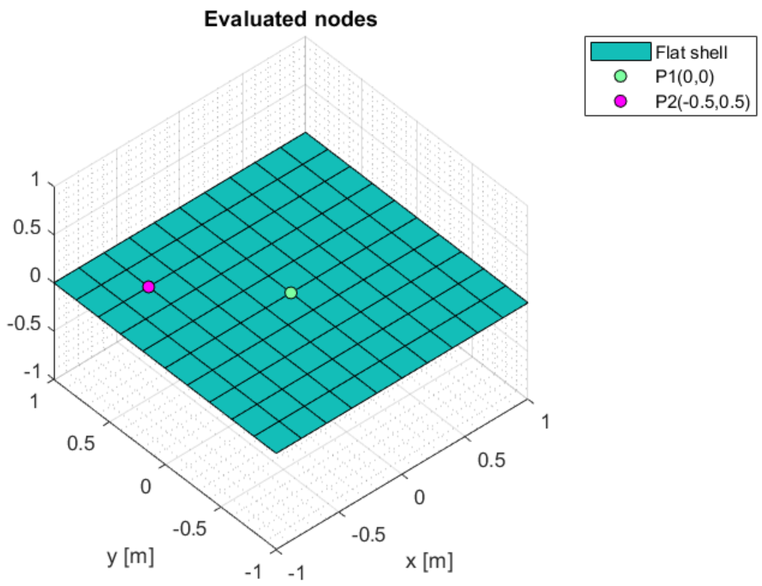

FIGURE C.184: Scheme of the location of the evaluated nodes of the shell [MATLAB].

C.8.2 Modal analysis

First, a modal analysis has been performed in order to identify the first six natural frequencies at which the shell will experiment resonance. Table C.9 shows the first six eigenvalues obtained with MATLAB considering that there is a prescribed displacement in the z-direction of the nodes located in the line x=-1 m. Furthermore, figure C.185 shows the first six vibration modes of the shell.

TABLE C.9: First six natural frequencies [MATLAB].

Mode	Frequency (Hz)
1st	$1.491 \cdot 10^{-4}$
2nd	19.9644
3rd	45.4904
4th	74.0549
5th	77.6737
6th	139.659

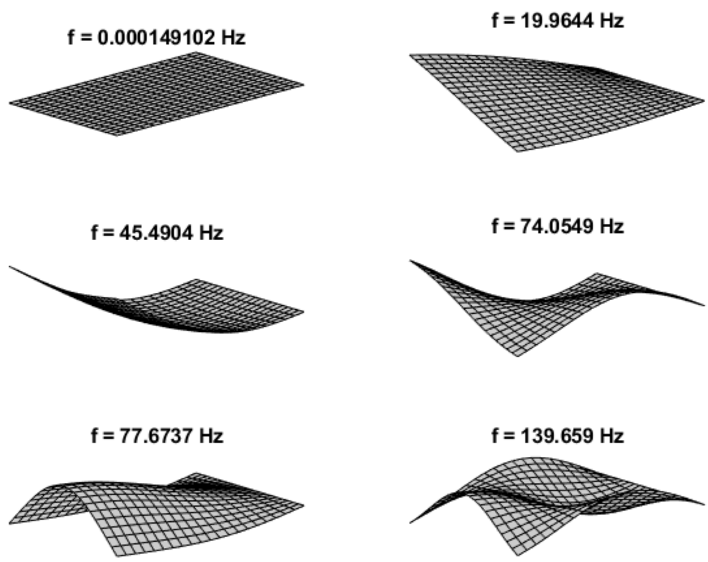

FIGURE C.185: First six natural frequencies and modes of the shell obtained using MATLAB for a 400 elements mesh (20x20) [MATLAB].

Then, the same study has been carried on with COMSOL and the results are listed in table C.10. In comparison with the results obtained with MATLAB, the maximum error between them is 4% for the sixth mode. Furthermore, the different modes have been plotted as well.

Comparing both, MATLAB and COMSOL results, it can be concluded that they agree. Not only the natural frequencies obtained using both programs are almost the same, but also the shape of the first six modes coincides.

TABLE C.10: First six natural frequencies [COMSOL].

Mode	Frequency (Hz)
1st	-
2nd	19.919
3rd	45.231
4th	76.232
5th	78.498
6th	145.47

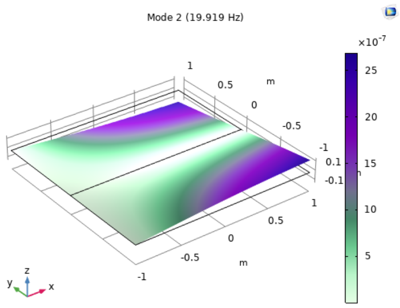

FIGURE C.186: Mode 2 [COMSOL].

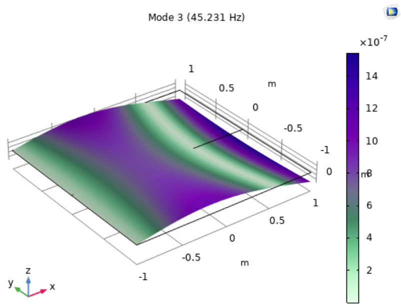

FIGURE C.189: Mode 3 [COMSOL].

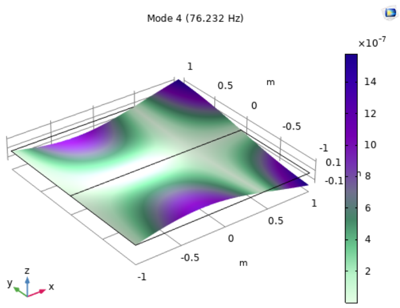

FIGURE C.187: Mode 4 [COMSOL].

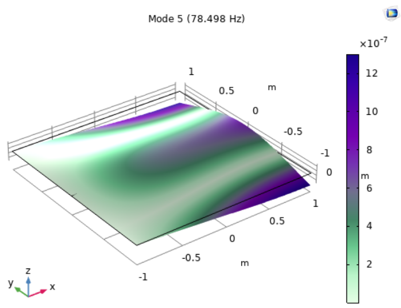

FIGURE C.190: Mode 5 [COMSOL].

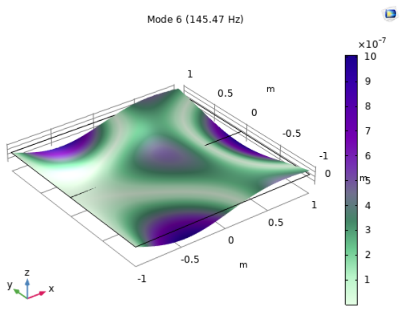

FIGURE C.188: Mode 6 [COMSOL].

C.8.3 Finite element formulation

Then, to compute both, the quasi-static test and the random vibration test, it has been necessary to identify the equation to solve, considering that, in this case, the prescribed movement will be an acceleration applied on the line x=-1 m. First, the equilibrium equation in the matrix form has been defined as the following.

$$[\mathbf{M}]\{\ddot{\mathbf{u}}\} + [\mathbf{K}]\{\mathbf{u}\} = \{\mathbf{F}\} \tag{C.70}$$

$$[\mathbf{M}]\begin{Bmatrix}\ddot{\mathbf{u}}_f\\ \ddot{\mathbf{u}}_r\end{Bmatrix} + [\mathbf{K}]\begin{Bmatrix}\mathbf{u}_f\\ \mathbf{u}_r\end{Bmatrix} = \begin{Bmatrix}\mathbf{F}_f\\ \mathbf{F}_r\end{Bmatrix} \tag{C.71}$$

Then, the classic reduced system can be written as

$$[\mathbf{M}_{ff}]\{\ddot{\mathbf{u}}_f\} + [\mathbf{K}_{ff}]\{\mathbf{u}_f\} = \{\mathbf{F}_f\} - ([\mathbf{M}_{fr}]\{\ddot{\mathbf{u}}_r\} + [\mathbf{K}_{fr}]\{\mathbf{u}_r\}) \tag{C.72}$$

Moreover, equation C.72 expressed in the time domain can be transformed into the frequency domain using the equality below.

$$u_r = A_r e^{i\omega t} \qquad u_f = A_f e^{i\omega t} \tag{C.73}$$

$$\ddot{u}_r = -\omega^2 A_r e^{i\omega t} \qquad \ddot{u}_f = -\omega^2 A_f e^{i\omega t} \tag{C.74}$$

$$(-\omega^2[\mathbf{M}_{ff}] + [\mathbf{K}_{ff}])\{\mathbf{A}_f\}e^{i\omega t} = \{\mathbf{F}_f\} - (-\omega^2[\mathbf{M}_{fr}] + [\mathbf{K}_{fr}])\{\mathbf{A}_r\}e^{i\omega t} \tag{C.75}$$

As there is no force applied on the shell, the previous equation can be simplified as the following.

$$(-\omega^2[\mathbf{M}_{ff}] + [\mathbf{K}_{ff}])\{\mathbf{A}_f\} = (\omega^2[\mathbf{M}_{fr}] - [\mathbf{K}_{fr}])\{\mathbf{A}_r\} \tag{C.76}$$

$$\{\mathbf{A}_f\} = [\mathbf{H}_{ff}](\omega^2[\mathbf{M}_{fr}] - [\mathbf{K}_{fr}])\{\mathbf{A}_r\} \tag{C.77}$$

C.8.4 Quasi-Static Test

MATLAB

The methodology used to perform the quasi-static vibration test is shown in figure C.272. The harmonic vibration of an amplitude of 50 m/s^2 and a frequency of 70 Hz has been first computed in the time domain.

$$s = -50 \cdot \sin(2\pi 70t) \tag{C.78}$$

Then, with the use of the Fourier Transform the acceleration has been transformed from time domain to frequency domain.

$$S = fft(s) \tag{C.79}$$

The acceleration has been applied to the u_z degree of freedom of the nodes located at the line x=-1 m of the shell.

$$\{\mathbf{A}\} = \{\mathbf{A}(DOF, freq)\} \tag{C.80}$$

$$\{\mathbf{A}(u_{z\ x=-1m}, :)\} = S \tag{C.81}$$

Once obtained the acceleration in the frequency domain and using equations C.73 and C.74, the displacements in the frequency domain $\{\mathbf{A}_r\}$ can be computed

$$\{\mathbf{A}_r(:, freq)\} = -\frac{\{\mathbf{A}(:, freq)\}}{(2\pi freq)^2} \tag{C.82}$$

Finally, using equation C.77, the displacements can be computed.

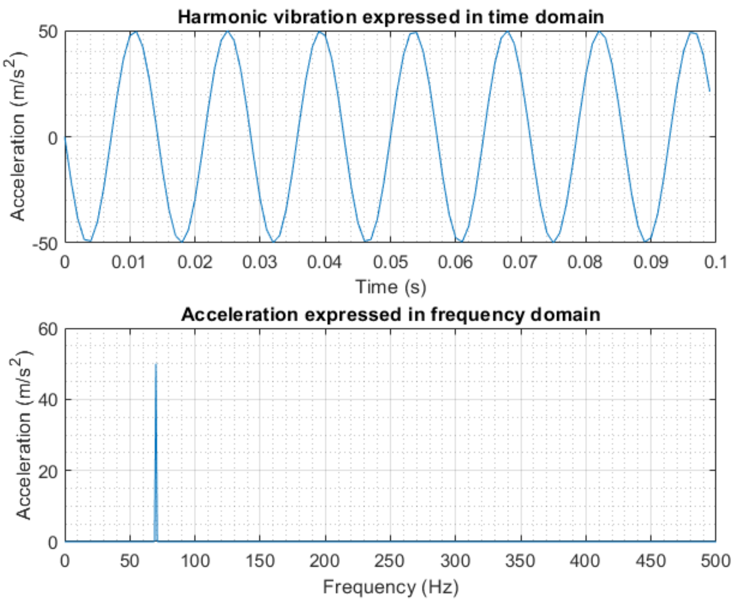

FIGURE C.191: Methodology used to compute the acceleration in the frequency domain [MATLAB].

Figure C.192 shows the displacements versus the frequency for the quasi-static test performed and it can be seen that the response of an harmonic force excitation is sinusoidal. In other words, the shape of the displacements in the z-direction and the rotation in both, x and y-direction, agrees with the Fourier Transform of a sinusoidal function. Furthermore, from figure C.192, the frequency at which the maximum displacement takes place is 70 Hz which results to be the same value as the frequency of the harmonic force applied.

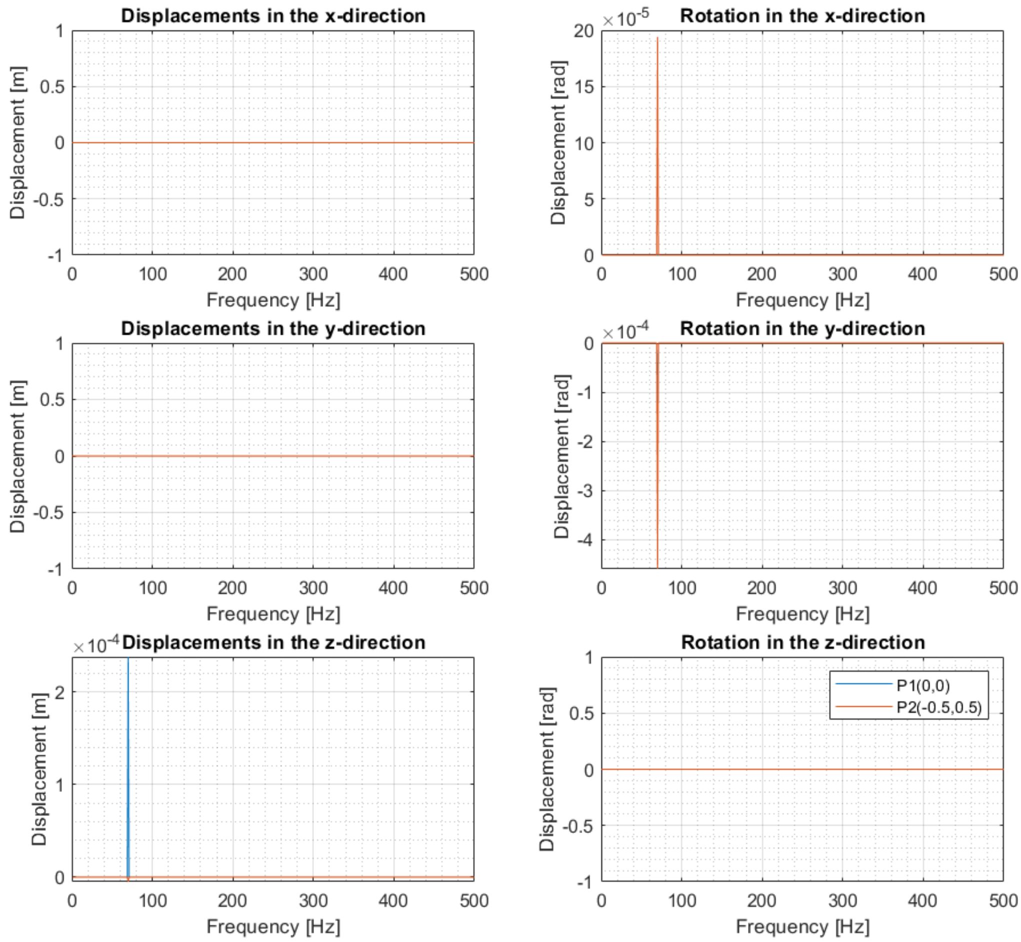

FIGURE C.192: Displacements in the frequency domain obtained for an harmonic acceleration using a 400 element mesh (20x20) [MATLAB].

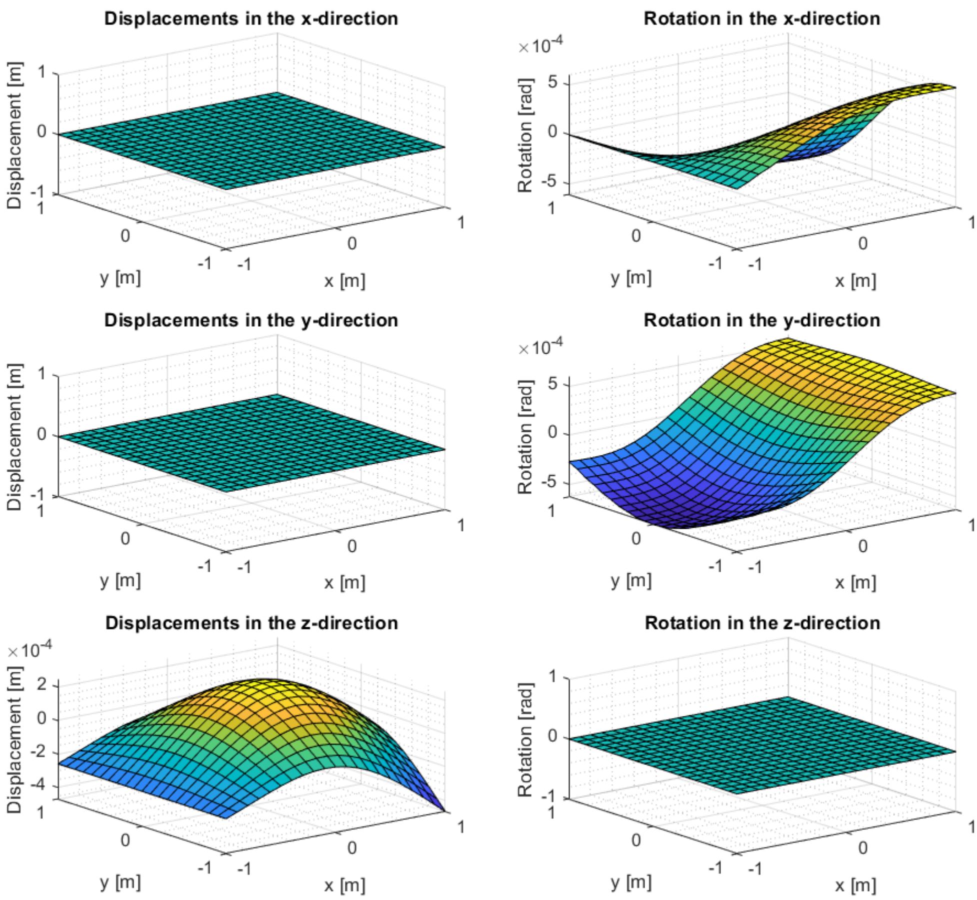

FIGURE C.193: Displacement distribution along the shell when the frequency is equal to 70 Hz using a 400 element mesh (20x20) [MATLAB].

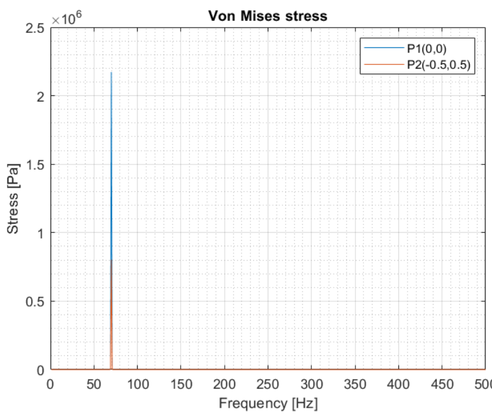

FIGURE C.194: Von Mises stress in the frequency domain obtained for an harmonic acceleration using a 400 element mesh (20x20) [MATLAB].

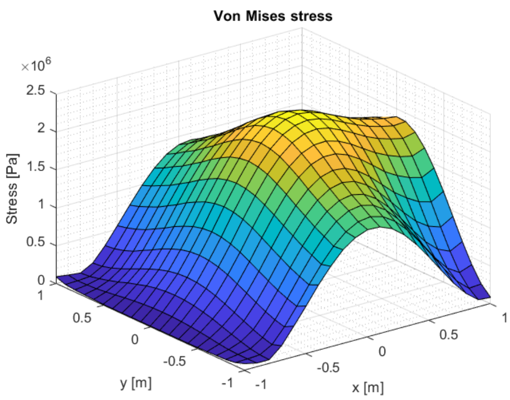

FIGURE C.195: Von Mises stress distribution along the shell when the frequency is equal to 70 Hz using a 400 element mesh (20x20) [MATLAB].

Figure C.194 shows the Von Mises stress distribution of the points P1 and P2 versus the frequency. As there is a maximum where the frequency is equal to 70 Hz, the Von Mises distribution along the shell has been plotted for that specific frequency in figure C.195. Moreover, figure C.197 shows the Von Mises stress distribution along the line y=0m of the shell where the maximum stress takes place. Specifically, the maximum Von Mises stress is located on the coordinates (0.2,0) of the shell with a value of $2.28 \cdot 10^6$ Pa. Figure C.196 shows the displacements distribution in the z-direction along the y=0m line of the shell when the frequency is equal to 70 Hz where the maximum displacement takes place. The maximum displacement is located on the coordinates (-1,0) with a value of $-2.58 \cdot 10^{-4}$ m.

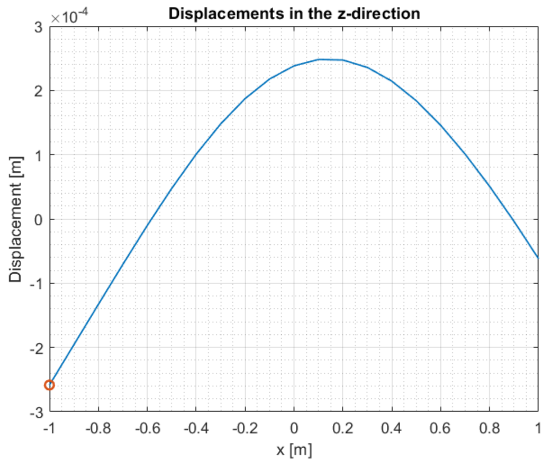

FIGURE C.196: Displacements distribution in the z-direction along y=0m line of the shell when the frequency is equal to 70 Hz using a 400 element mesh (20x20) [MATLAB].

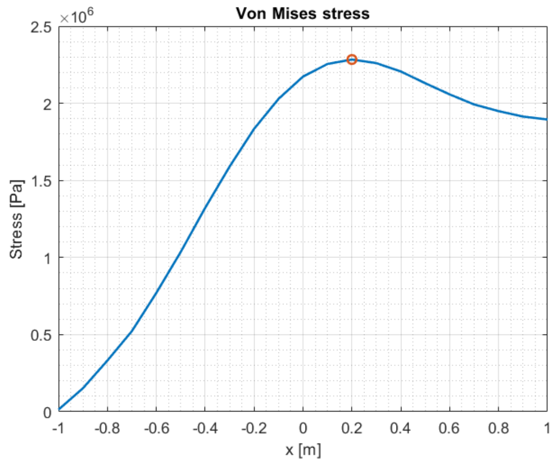

FIGURE C.197: Von Mises stress distribution along y=0m line of the shell when the frequency is equal to 70 Hz using a 400 element mesh (20x20) [MATLAB].

COMSOL

Additionally, the same quasi-static test has been performed with COMSOL in order to, later, do a comparative study between the results obtained with MATLAB and COMSOL. First, the acceleration has been defined as a function of the frequency. As it is a sinusoidal vibration, when using the Fourier Transform the resulting function only presents one peak at the same frequency as the input acceleration in time domain. Figure C.198 shows the acceleration function in the frequency domain. Moreover, this defines the prescribed acceleration in the z-direction of the nodes located on the line x=-1m of the shell.

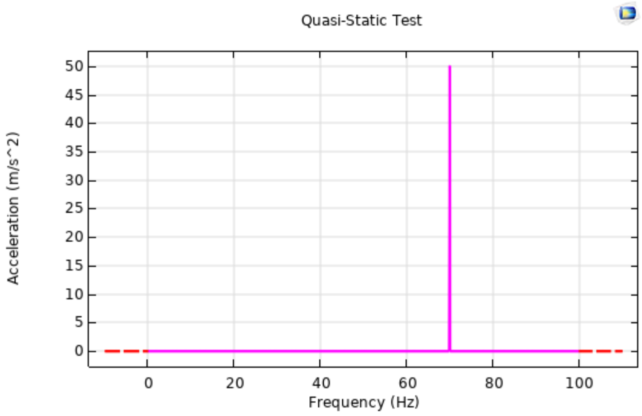

FIGURE C.198: Acceleration input to perform the quasi-static test [COMSOL].

Once performed the quasi-static test, the displacements and the Von Mises stress distributions versus the frequency have been computed and the results are shown in figures C.199 and C.200. As what happened to the quasi-static test performed with MATLAB, the maximum displacement and Von Mises stress takes place when the frequency is equal to 70 Hz.

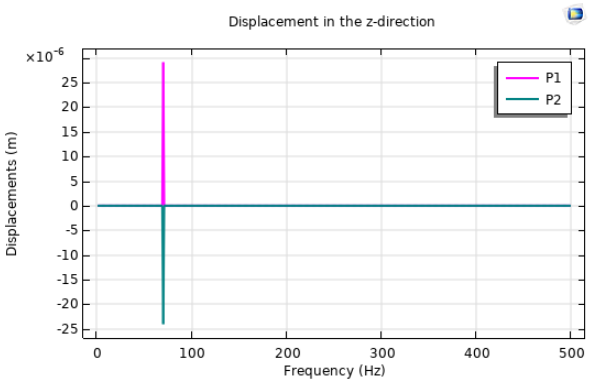

FIGURE C.199: Displacements distribution versus the frequency using a 400 element mesh (20x20) [COMSOL].

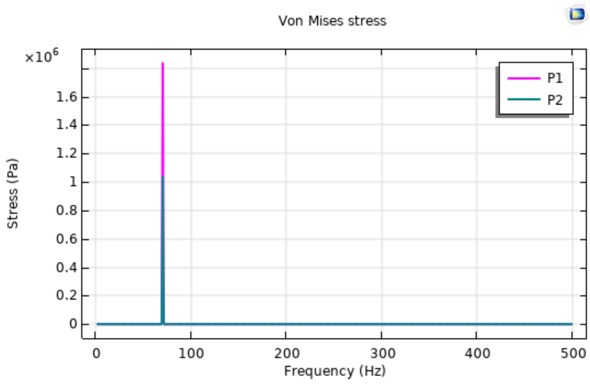

FIGURE C.200: Von Mises stress distribution versus frequency using a 400 element mesh (20x20) [COMSOL].

Figure C.201 shows the Von Mises stress distribution along the shell when the frequency is equal to 70 Hz.

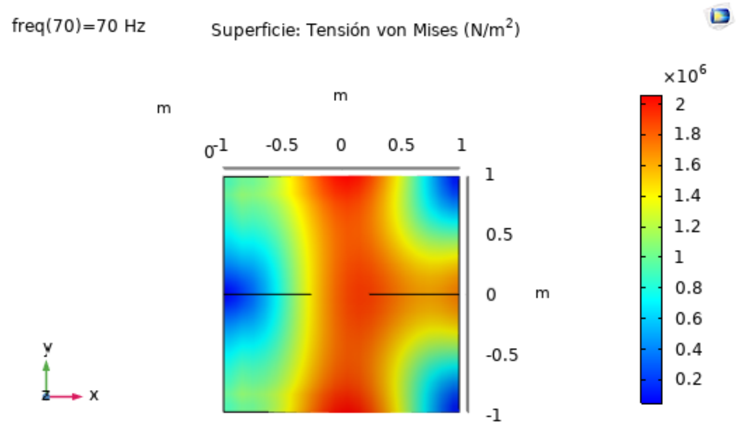

FIGURE C.201: Von Mises stress distribution along the shell when the frequency is equal to 70 Hz using a 400 element mesh (20x20) [COMSOL].

Then, the displacements distribution in the z-direction and the Von Mises stress distribution along the line y=0m have been plotted in order to obtain the exact location and value of both, the maximum displacement and Von Mises stress.

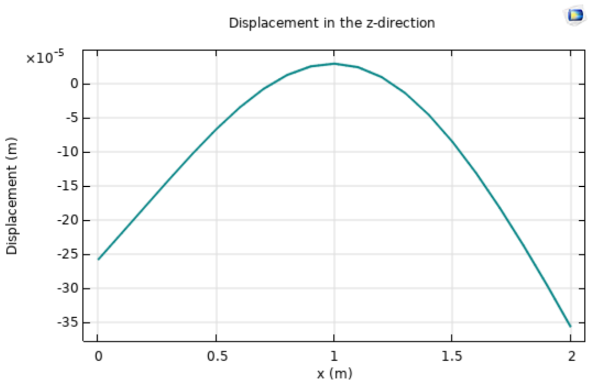

FIGURE C.202: Displacements distribution in the z-direction along y=0m line of the shell when the frequency is equal to 70 Hz using a 400 element mesh (20x20) [COMSOL].

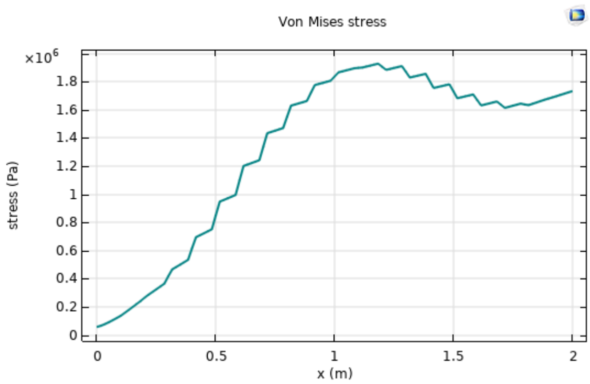

FIGURE C.203: Von Mises stress distribution along y=0m line of the shell when the frequency is equal to 70 Hz using a 400 element mesh (20x20) [COMSOL].

C.8.5 Convergence Study of the Quasi-static Test

To finish the quasi-static test, the results obtained with MATLAB and COMSOL will be compared. Figure C.204 presents the displacements distribution in the z-direction for the nodes located in the line y = 0 m of the shell. As it can be seen, there is no agreement between both results which can be derived from the number of nodes each program uses. Moreover, whereas MATLAB uses a linear quadratic element type with 4 nodes in each element, COMSOL uses 8 nodes in each of the elements. Probably, the deviation of the results has its origin in how many nodes the elements have. Furthermore, figure C.205 shows the Von Mises stress distribution along the line y = 0 m of the shell. In this case, it looks like there is a certain agreement between both results. The maximum error of this plot is located on the maximum Von Mises stress position of both functions and it is about a 18.13%.

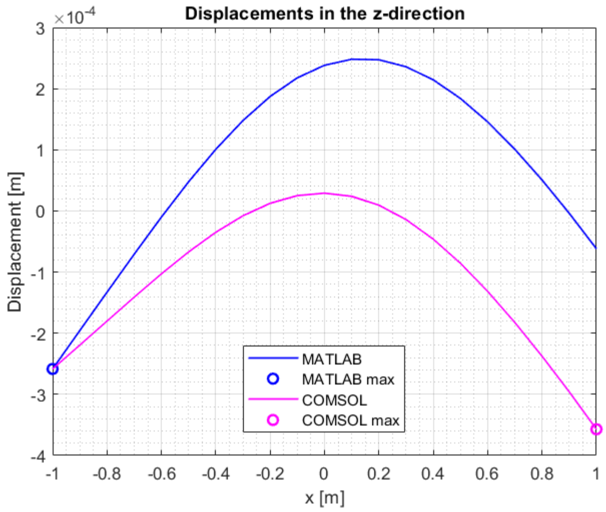

FIGURE C.204: Comparison between the displacements distribution in the line y=0m of the shell obtained with MATLAB and COMSOL [MATLAB].

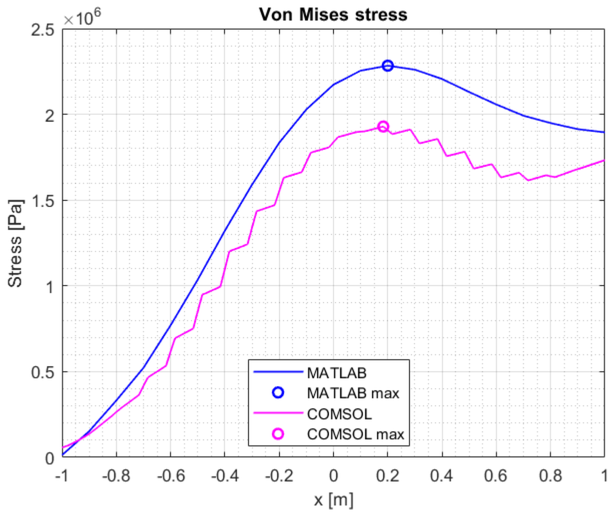

FIGURE C.205: Comparison between the Von Mises stress distribution in the line y=0m of the shell obtained with MATLAB and COMSOL [MATLAB].

Table C.11: Error between the displacements in the z-direction and the Von Mises stress [MATLAB] and [COMSOL].

	Displacements [m]	**Von Mises stress [Pa]**
MATLAB maximum	$-2.58 \cdot 10^{-4}$	$2.28 \cdot 10^{6}$
COMSOL maximum	$-3.61 \cdot 10^{-4}$	$1.93 \cdot 10^{6}$
Error	28.53 %	18.13 %

C.8.6 Random Vibration Test

MATLAB

In this section, a random vibration acceleration will be applied in the z-direction of the nodes located in the line x=-1m of the shell. First, the Power Spectral Density function that describes the acceleration applied is

$$PSD = 6 \cdot log_{10}(freq) + 0.04 - 6 \cdot log_{10}(40) \qquad when\ freq < 40\ Hz \tag{C.83}$$

$$PSD = 0.04 \qquad when\ 40\ Hz \leq freq \leq 450\ Hz \tag{C.84}$$

$$PSD = -6 \cdot log_{10}(freq) + 0.04 + 6 \cdot log_{10}(450) \qquad when\ freq > 450\ Hz \tag{C.85}$$

Then, the acceleration has been computed from the PSD input using the following expression:

$$PSD = \frac{S^2}{\Delta freq} \quad \longrightarrow \quad S = \sqrt{PSD \cdot \Delta freq} \tag{C.86}$$

As the acceleration is now expressed in g units, it has been multiplied by 9.81 m/s^2 in order to obtain the acceleration in the international system units. Finally, the acceleration has been applied to the u_z degree of freedom of the nodes located on the line x=-1 m of the shell.

$$\{\mathbf{A}\} = \{\mathbf{A}(DOF, freq)\} \tag{C.87}$$

$$\{\mathbf{A}(u_{z\ x=-1m}, :)\} = S \tag{C.88}$$

Once obtained the acceleration in the frequency domain and using equations C.73 and C.74, the displacements in the frequency domain $\{\mathbf{A}_r\}$ can be computed

$$\{\mathbf{A}_r(:, freq)\} = -\frac{\{\mathbf{A}(:, freq)\}}{(2\pi freq)^2} \tag{C.89}$$

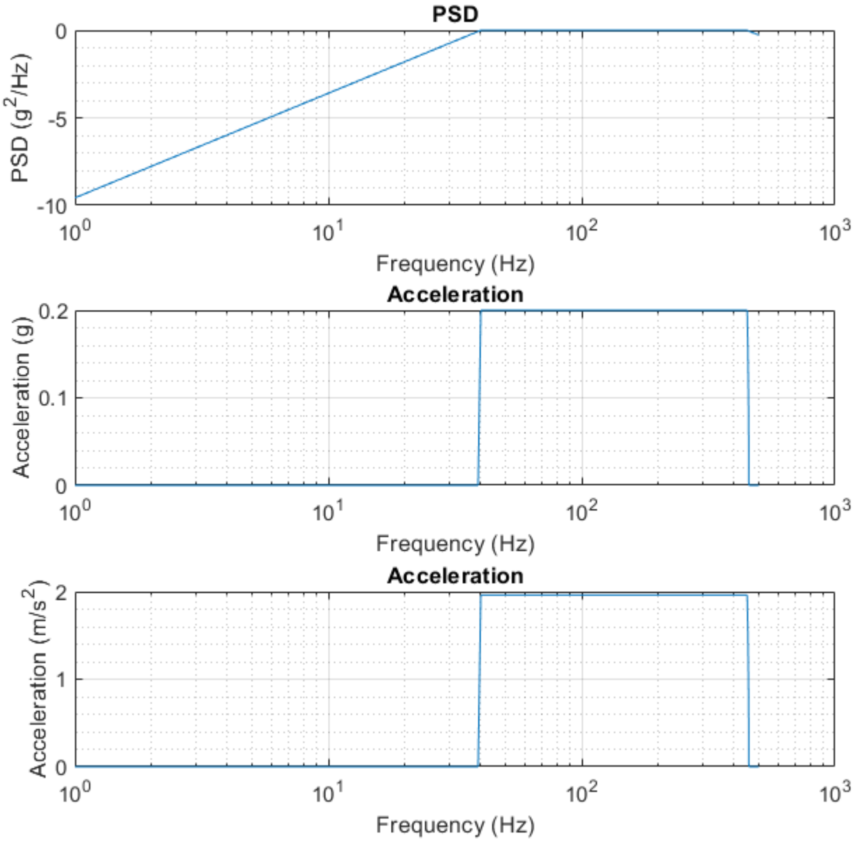

Figure C.206: Methodology used to compute the acceleration in the frequency domain considering $\Delta f = 1$ Hz [MATLAB].

Then, using equation C.77, the displacements can be computed. Figure C.207 shows the displacements distribution of the points P1 and P2 versus the frequency considering a frequency step of 1 Hz. In this case, the maximum displacement in the z-direction takes place at the frequency of 46 Hz.

As shown in figure C.209, the maximum Von Mises stress takes place when the frequency is equal to 153 Hz. However, the displacements and the Von Mises stress distribution along the shell have been plotted for the frequency equal to 46 Hz in order to then compare this results with the ones obtained with COMSOL. The Von Mises stress versus frequency and the Von Mises stress distribution along the shell for a frequency of 46 Hz and are shown in figures C.208 and C.210 respectively considering a frequency step of 1 Hz.

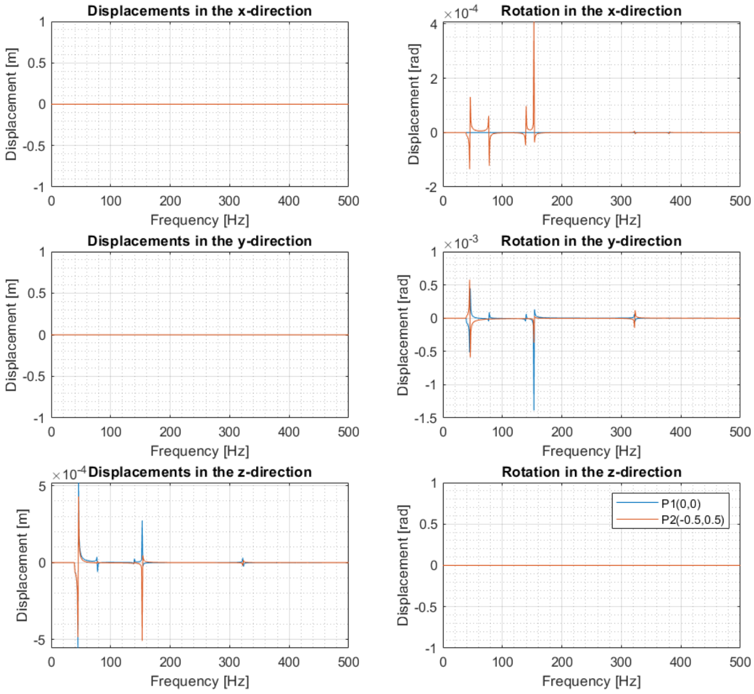

FIGURE C.207: Displacements in the frequency domain obtained for a random vibration acceleration using a 400 element mesh (20x20) and with $\Delta f = 1$ Hz [MATLAB].

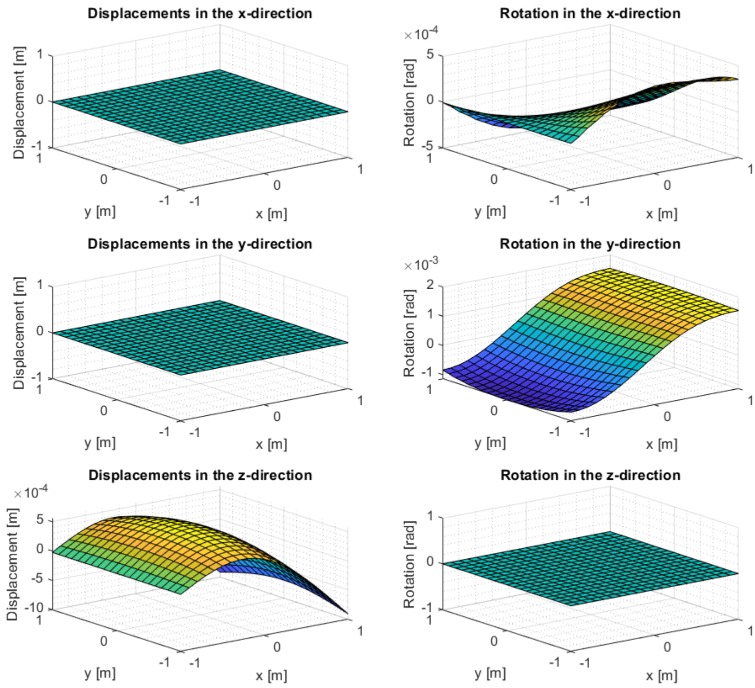

FIGURE C.208: Displacement distribution along the shell when the frequency is equal to 46 Hz using a 400 element mesh (20x20) and with $\Delta f = 1$ Hz [MATLAB].

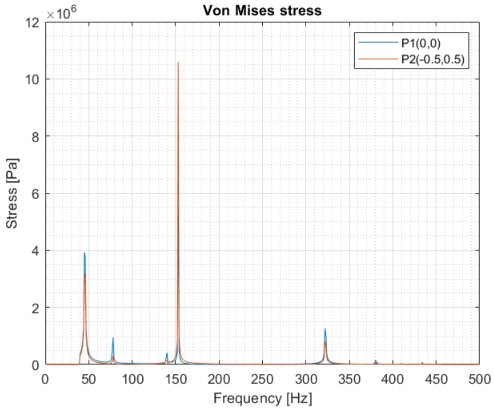

FIGURE C.209: Von Mises stress in the frequency domain obtained for a random vibration acceleration using a 400 element mesh (20x20) and with $\Delta f = 1$ Hz [MATLAB].

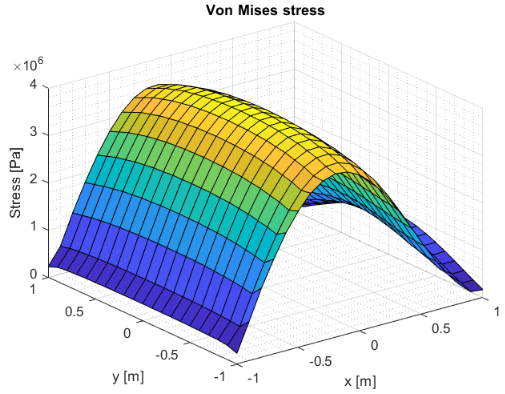

FIGURE C.210: Von Mises stress distribution along the shell when the frequency is equal to 46 Hz using a 400 element mesh (20x20) and with $\Delta f = 1$ Hz [MATLAB].

Moreover, figure C.211 shows the displacements distribution in the z-direction along the y=0 m line of the shell when the frequency is equal to 46 Hz where the maximum displacement takes place. The maximum displacement in the z-direction is located on the coordinates (1,0) with a value of $-6.878 \cdot 10^{-4}$ m. Figure C.212 shows the Von Mises stress distribution along the line y=0 m of the shell where the maximum stress for the $freq = 46$ Hz takes place. Specifically, the maximum Von Mises stress is located in the coordinates (-0.1,0) of the shell with a value of $3.87 \cdot 10^{6}$ Pa.

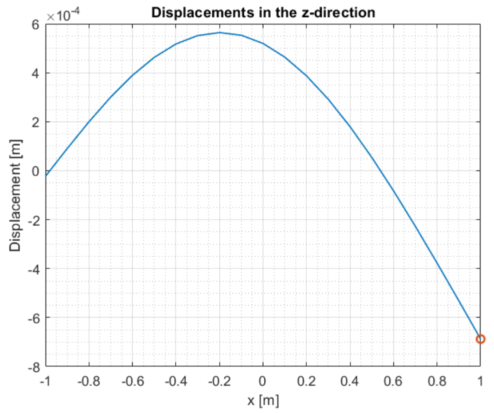

FIGURE C.211: Displacements distribution in the z-direction along y=0m line of the shell when the frequency is equal to 46 Hz using a 400 element mesh (20x20) and with $\Delta f = 1$ Hz [MATLAB].

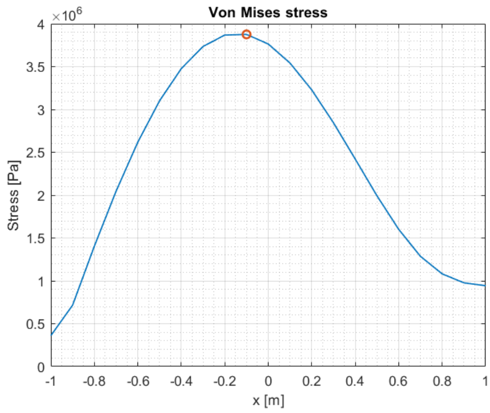

FIGURE C.212: Von Mises stress distribution along y=0m line of the shell when the frequency is equal to 46 Hz using a 400 element mesh (20x20) and with $\Delta f = 1$ Hz [MATLAB].

COMSOL

Additionally, the same random vibration test has been performed with COMSOL in order to, later, do a convergence study between the results obtained with MATLAB and COMSOL. First, the acceleration has been defined as a function of the frequency considering a frequency step of 1 Hz.

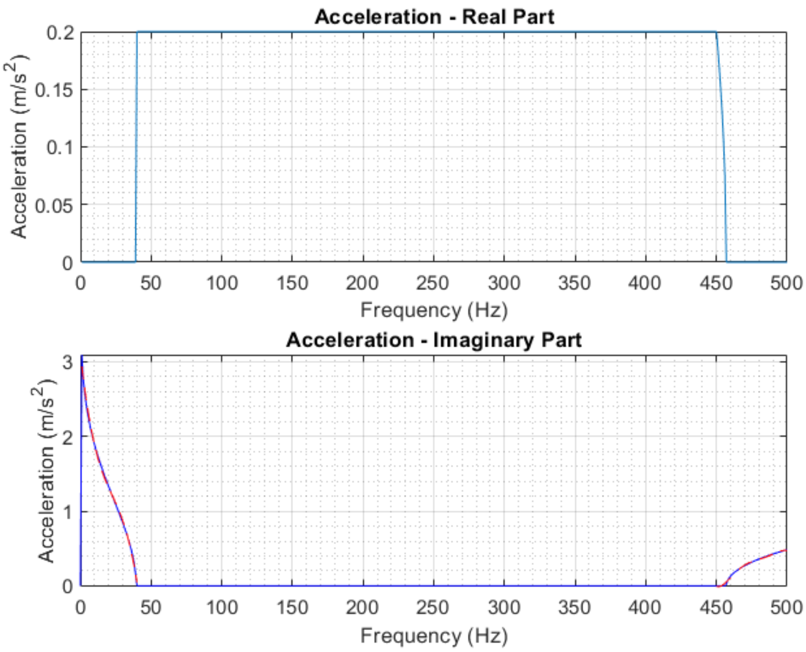

FIGURE C.213: Acceleration distribution along frequency (real and imaginary part) [MATLAB].

$$a = (-(0.001i) \cdot freq^3 + (0.0005 + 0.0057i) \cdot freq^2 - (0.0068 + 0.1702i) \cdot freq + (0.02 + 3.1016i)) \cdot 9.81 \qquad 0 < freq < 40 \tag{C.90}$$

$$a = 0.2 \cdot 9.81 \qquad 40 < freq < 450 \tag{C.91}$$

$$a = (-(8.5279E-14 + 2.3116E-13i)freq^5 + (3.2042E-10 + 8.8858E-10i)freq^4 - (4.7524E-7 + 1.3551E-6i)freq^3 + (0.0003 + 0.001i)freq^2 - (0.1252 + 0.3887i)freq + (17.7714 + 58.3021i)) \cdot 9.81 \qquad 450 < freq < 500 \tag{C.92}$$

Once performed the random vibration test, the displacements and the Von Mises stress distributions versus the frequency have been computed and the results are shown in figures C.214 and C.215.

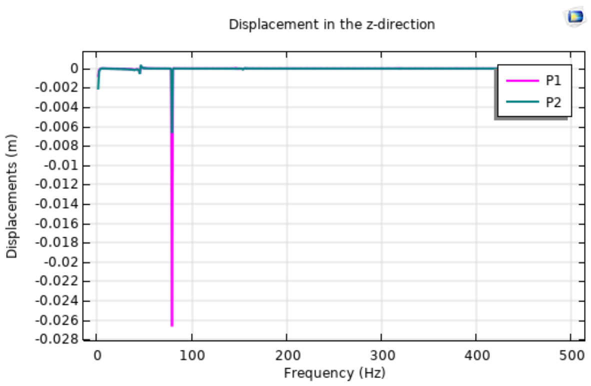

FIGURE C.214: Displacements distribution versus the frequency using a 400 element mesh (20x20) and with $\Delta f = 1$ Hz [COMSOL].

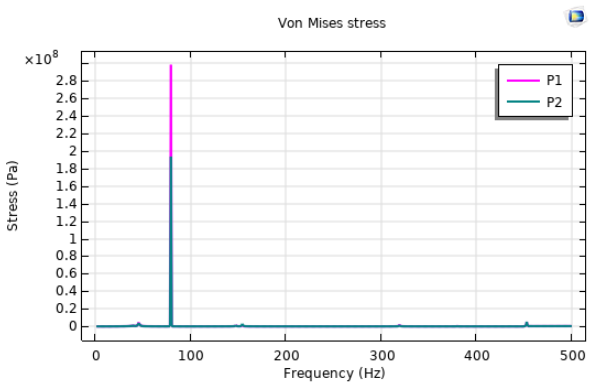

FIGURE C.215: Von Mises stress distribution versus frequency using a 400 element mesh (20x20) and with $\Delta f = 1$ Hz [COMSOL].

In order to later compare Matlab and Comsol reults, all the plots will be made for the frequency of 46 Hz. Figure C.216 shows the Von Mises stress distribution along the shell when the frequency is equal to 46 Hz.

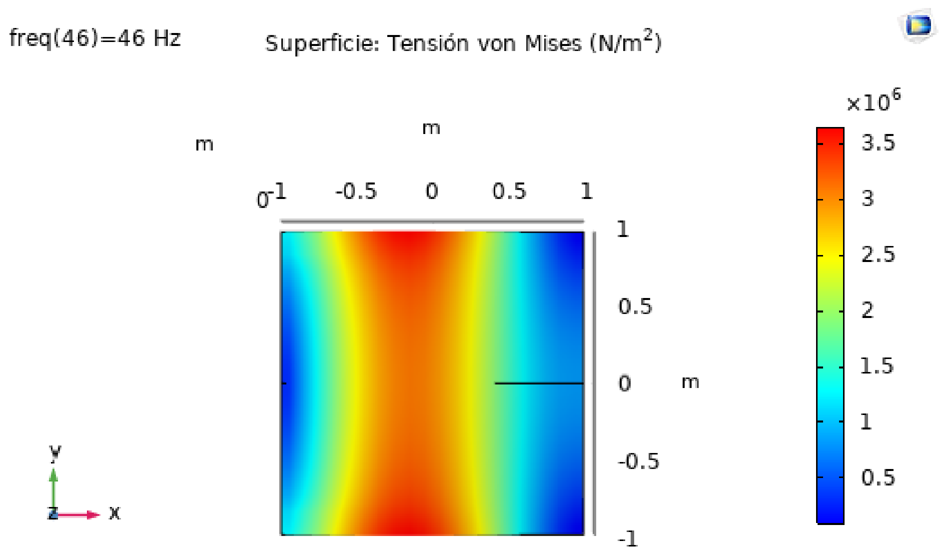

FIGURE C.216: Von Mises stress distribution along the shell when the frequency is equal to 46 Hz using a 400 element mesh (20x20) and with $\Delta f = 1$ Hz [COMSOL].

Then, the displacements distribution in the z-direction and the Von Mises stress distribution along the line y=0m have been plotted in order to obtain the exact location and value of both, the maximum displacement and Von Mises stress.

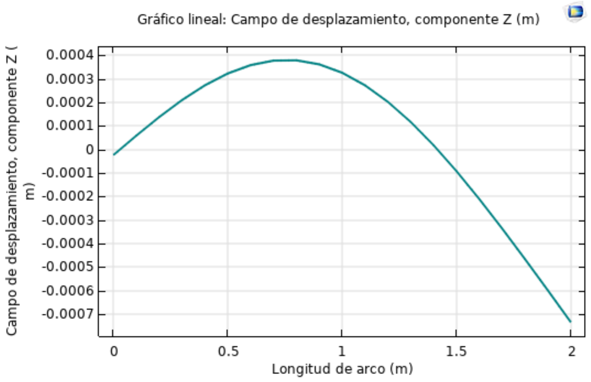

FIGURE C.217: Displacements distribution in the z-direction along y=0m line of the shell when the frequency is equal to 46 Hz using a 400 element mesh (20x20) and with $\Delta f = 1$ Hz [COMSOL].

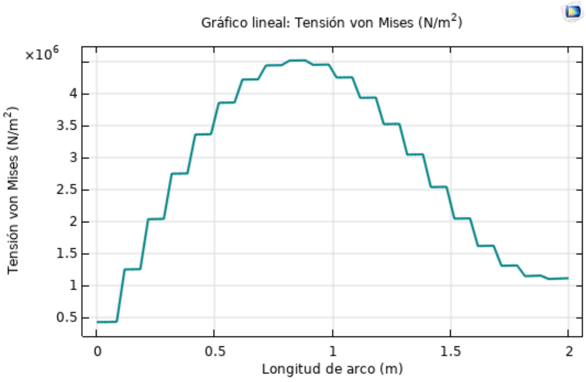

FIGURE C.218: Von Mises stress distribution in the z-direction along y=0m line of the shell when the frequency is equal to 46 Hz using a 400 element mesh (20x20) and with $\Delta f = 1$ Hz [COMSOL].

C.8.7 Convergence Study of the Random Vibration Test

Then, a convergence study between the results obtained with MATLAB and COMSOL has been done considering that the random tests performed had a frequency step of 1 Hz. On the random test, the frequency step used is of the utmost importance when it comes to compare and validate results because, not until the PSD is computed by adimensionalising with the frequency, the results will deviate depending of the frequency step used. The displacements and Von Mises stress distributions along the line y = 0 m of the shell are shown in figures C.219 and C.220 respectively. Table C.12 presents the errors between the maximum displacement and Von Mises stress obtained using MATLAB and COMSOL.

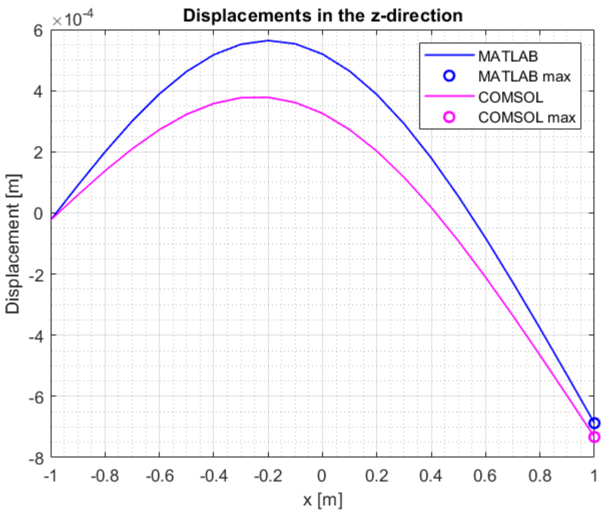

FIGURE C.219: Comparison between the displacements distribution in the line y=0m of the shell obtained with MATLAB and COMSOL for $\Delta f = 1$ Hz [MATLAB].

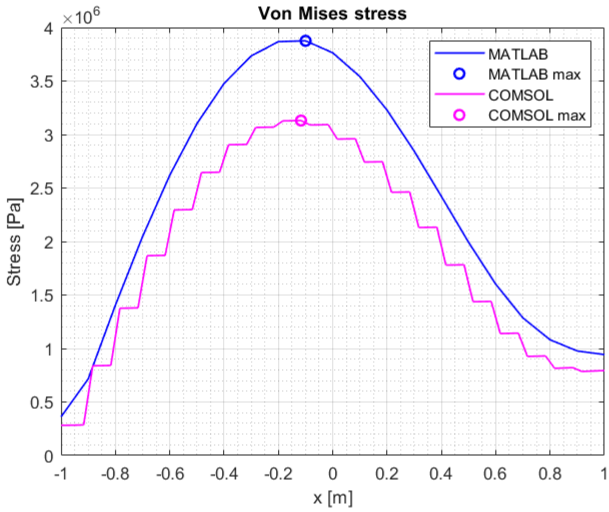

FIGURE C.220: Comparison between the Von Mises stress distribution in the line y=0m of the shell obtained with MATLAB and COMSOL for $\Delta f = 1$ Hz [MATLAB].

TABLE C.12: Error between the displacements in the z-direction and the Von Mises stress [MATLAB] and [COMSOL].

	Displacements [m]	**Von Mises stress [Pa]**
MATLAB maximum	$-4.86 \cdot 10^{-4}$	$2.74 \cdot 10^{6}$
COMSOL maximum	$-5.18 \cdot 10^{-4}$	$2.21 \cdot 10^{6}$
Error	6.18 %	23.98 %

C.8.8 Random vibration test considering different Δf

The last study that will be carried on in this report is to compare the results obtained for different frequency steps when the shell is under a random vibration test. As mentioned before, there is a huge dependence on the frequency step when performing a random test. The origin of this dependence resides in the beginning of the test when the Power Spectral density is transformed into an acceleration. In this transformation Δf appears and it is a degree of freedom of the problem. However, for that reason, the final analysis can not be done using just the displacements or the Von Mises stress directly, at the end of the test, all the results must be converted again to PSD by diving for the frequency step used.

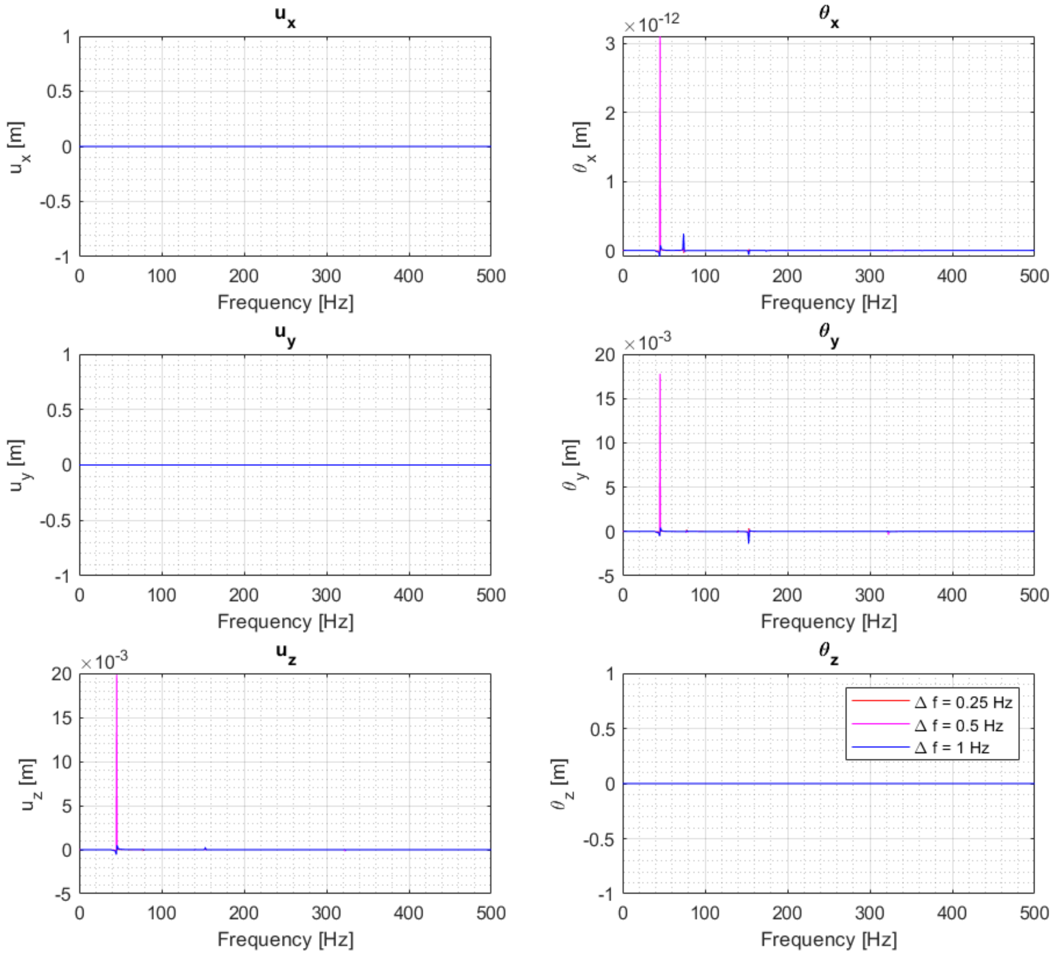

FIGURE C.221: Displacements in the frequency domain obtained for a random vibration acceleration using a 400 element mesh (20x20) and considering three frequency steps: $\Delta f = 0.25$ Hz, $\Delta f = 0.5$ Hz and $\Delta f = 1$ Hz [MATLAB].

Moreover, as shown in figure C.221, depending on the frequency step used the maximum displacement appears in different frequencies. For instance, if the maximum displacement is located on 45.5 Hz and the frequency step used is 1 Hz, when computing the displacements in the frequency domain the maximum will not appear in 45.5 Hz because by using this Δf the function will not be analysed in 45.5 Hz. For that reason, it will be of the uttermost importance the study of the frequency step when it comes to determine the final results.

Figure C.222 presents the displacements in the frequency domain adimensionalised with the frequency step. As mentioned, the higher frequency step, the less precision in the results. In other words, for the frequency step of 1 Hz, as the frequency of 45.5 Hz is not evaluated, the PSD obtained is in disagreement with the rest of the frequency steps anaysed. However, as the frequency steps of 0.25 and 0.5 Hz include the frequency 45.5 where the maximum is located, when adimensionalising, the magnitude is exactly the same for both steps.

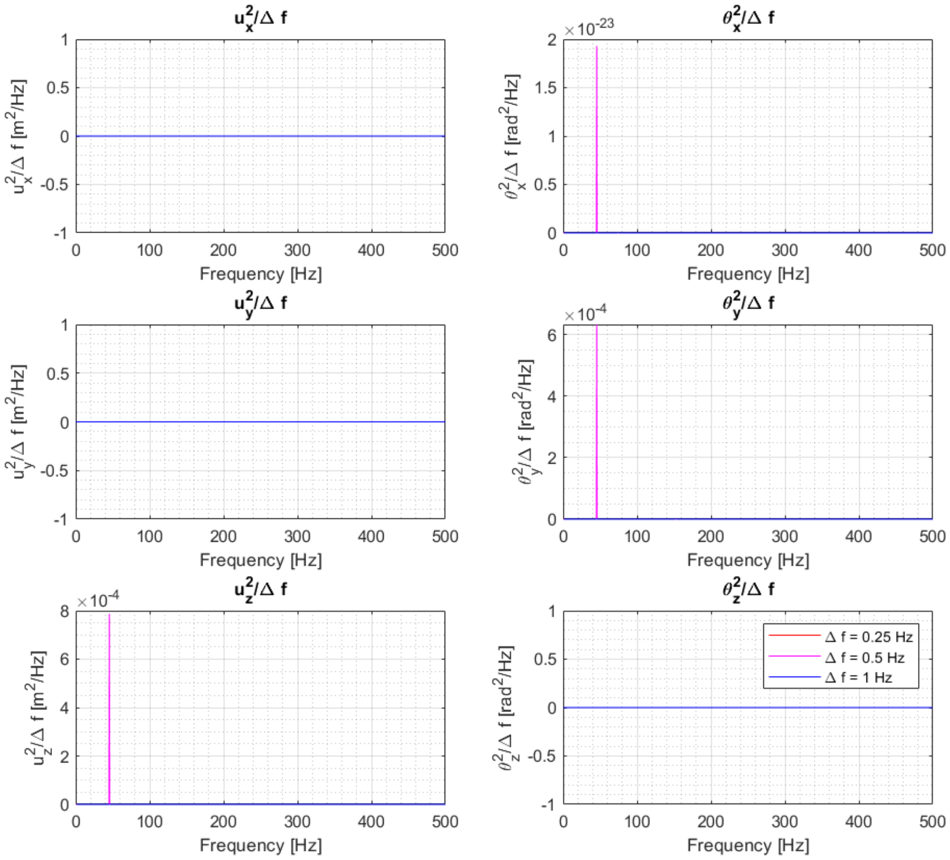

FIGURE C.222: Displacements in the frequency domain adimensionalised with the frequency step obtained for a random vibration acceleration using a 400 element mesh (20x20) and considering three frequency steps: $\Delta f = 0.25$ Hz, $\Delta f = 0.5$ Hz and $\Delta f = 1$ Hz [MATLAB].

In order to compare the three frequency steps, the frequency of 46 have been selected. As it can be seen in figure C.223, the displacement distribution along the line y = 0 m of the shell is different depending on the frequency step used. Nevertheless, when adimensionalising with the frequency step used in each case, all the functions agree. This agreement is shown in figure C.224.

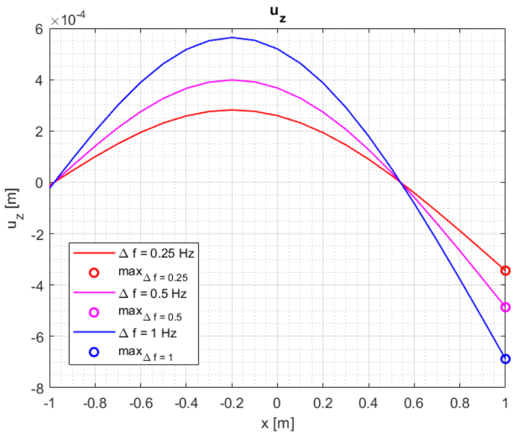

FIGURE C.223: Displacements distribution in the line y = 0 m for a random vibration acceleration using a 400 element mesh (20x20) and considering three frequency steps: Δf = 0.25 Hz, Δf = 0.5 Hz and Δf = 1 Hz [MATLAB].

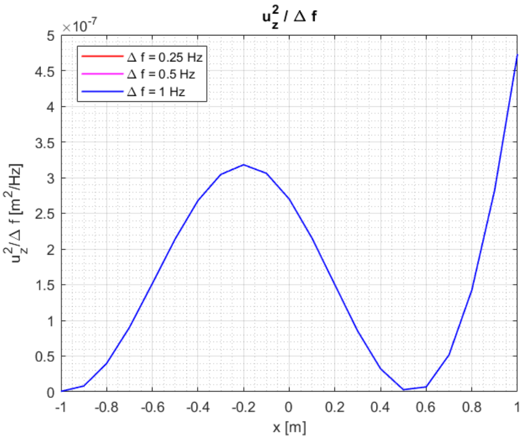

FIGURE C.224: Displacements distribution adimensionalised with the frequency step in the line y = 0 m of the shell for a random vibration acceleration using a 400 element mesh (20x20) and considering three frequency steps: Δf = 0.25 Hz, Δf = 0.5 Hz and Δf = 1 Hz [MATLAB].

The same process has been done for the Von Mises stress. First, the Von Mises stress distribution versus the frequency has been plotted in figure C.225 considering different frequency steps: Δf = 0.25 Hz, Δf = 0.5 Hz and Δf = 1 Hz. As what happened with the displacements distribution, when using the frequency step of 1 Hz the maximum stress is not obtained because it doesn't evaluate decimal numbers. However, as the other frequency steps used evaluate the stress in 45.5 Hz, when adimensionalising with the frequency, the same magnitude of the maximum Von Mises stress is obtained. This phenomenon can be seen in figure C.226.

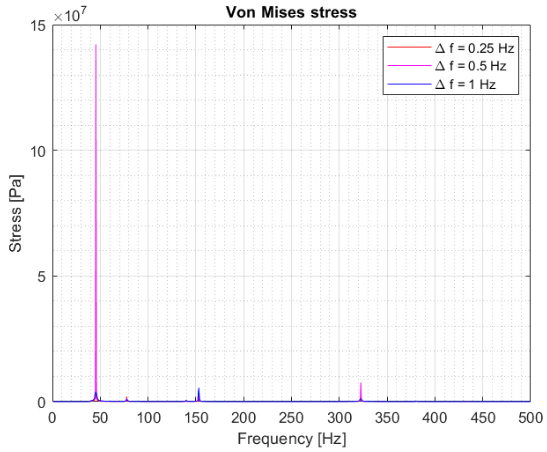

FIGURE C.225: Von Mises stress distribution in the frequency domain obtained for a random vibration acceleration using a 400 element mesh (20x20) and considering three frequency steps: $\Delta f = 0.25$ Hz, $\Delta f = 0.5$ Hz and $\Delta f = 1$ Hz [MATLAB].

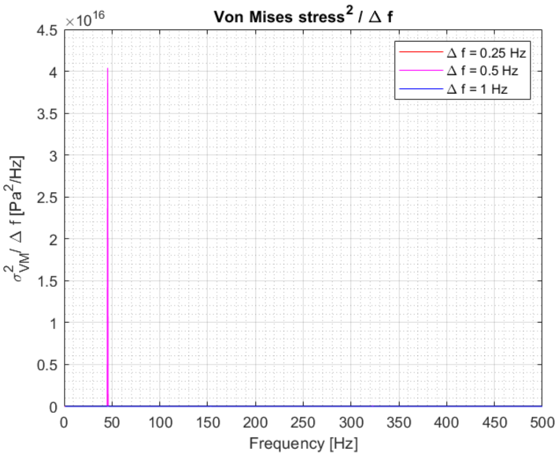

FIGURE C.226: Von Mises stress distribution in the frequency domain adimensionalised with the frequency step for a random vibration acceleration using a 400 element mesh (20x20) and considering three frequency steps: $\Delta f = 0.25$ Hz, $\Delta f = 0.5$ Hz and $\Delta f = 1$ Hz [MATLAB].

Finally, in order to compare the results obtained for the three frequency steps, the frequency of 46 have been selected. As it can be seen in figure C.227, the Von Mises stress distribution along the line y = 0 m of the shell is different depending on the frequency step used. Nevertheless, when adimensionalising with the frequency step used in each case, all functions agree. This convergence is shown in figure C.228.

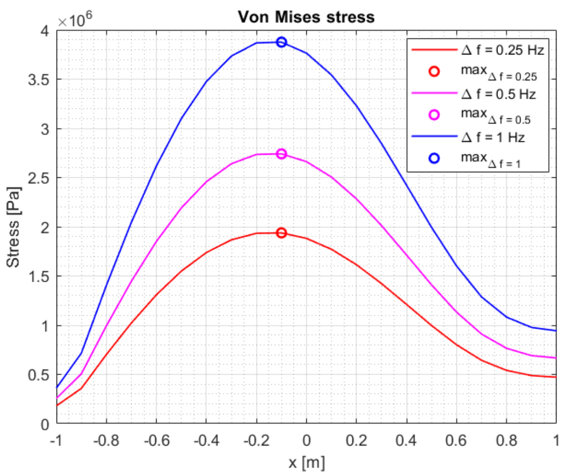

FIGURE C.227: Von Mises stress distribution in the line y = 0 m for a random vibration acceleration using a 400 element mesh (20x20) and considering three frequency steps: $\Delta f = 0.25$ Hz, $\Delta f = 0.5$ Hz and $\Delta f = 1$ Hz [MATLAB].

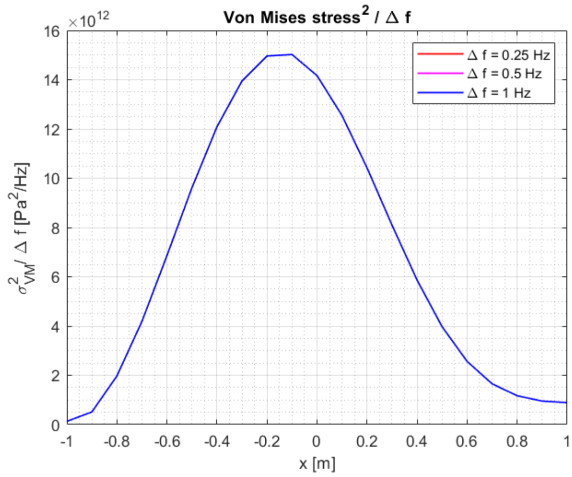

FIGURE C.228: Von Mises stress distribution adimensionalised with the frequency step for the line y = 0 m of the shell for a random vibration acceleration using a 400 element mesh (20x20) and considering three frequency steps: $\Delta f = 0.25$ Hz, $\Delta f = 0.5$ Hz and $\Delta f = 1$ Hz [MATLAB].

C.9 Report 9: First approximation to the wind sensor

The aim of this report is to perform a quasi-static test and a random vibration test on a shell doing an approximation to the sensor's dimensions and properties on each iteration. The first model tested will consist on a shell of 4 m^2 of surface, 0.05 m thickness, a young's modulus of 69 GPa, a Poisson ration of 0.3 and a density of 2700 kg/m^3. Then, for second model, the dimensions of the shell will change to a closer shape to the sensor. In this case the shell will be 0.2 m long, 0.002 m width and 0.001 m thick. However, the properties of the shell will remain the same as the first model. Finally, the last model not only will change its dimensions from model 1, but also its properties. In this case, the shell will be made of printed circuit boards (PCB).

C.9.1 First model definition

The geometric characteristics, the material and the boundary conditions of the first model are the following.

Geometry

- Dimensions: 2,00 x 2,00 m
- Thickness: 0.05 m

Material

- Young's modulus, E = 69 GPa.
- Poisson's ratio, $\nu = 0.3$.
- Density, $\rho = 2700\ kg/m^3$.

Boundary Conditions

- None of the four edges of the shell is embedded.
- An acceleration is defined in x=-1m line.
- To be more time-efficient, $u_x = u_y = \theta_z = 0$.

Quasi-Static Test

First, a quasi-static test will be performed on the first model of the shell. Figure C.229 shows the displacements versus the frequency for the quasi-static test performed and it can be seen that the response of an harmonic force excitation is sinusoidal. In other words, the shape of the displacements in the z-direction and the rotation in both, x and y-direction, agrees with the Fourier Transform of a sinusoidal function. Furthermore, from figure C.229, the frequency at which the maximum displacement takes place is 70 Hz which results to be the same value as the frequency of the harmonic force applied.

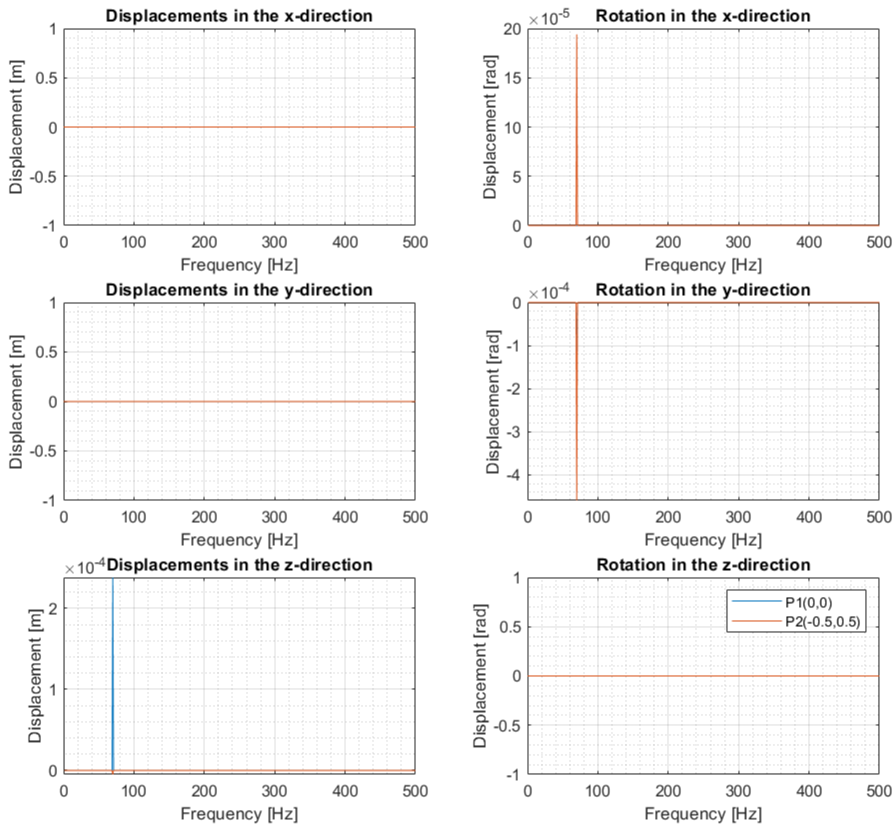

FIGURE C.229: Displacements in the frequency domain obtained for an harmonic acceleration using a 400 element mesh (20x20) [MATLAB].

Figure C.230 depicts the displacement distribution along the shell where the maximum displacement is presented, which coincides with the frequency of 70 Hz. Furthermore, figure C.231 shows the Von Mises stress distribution in the points P1 and P2 versus the frequency. As there is a maximum where the frequency is equal to 70 Hz, the Von Mises distribution along the shell has been plotted for that specific frequency in figure C.232.

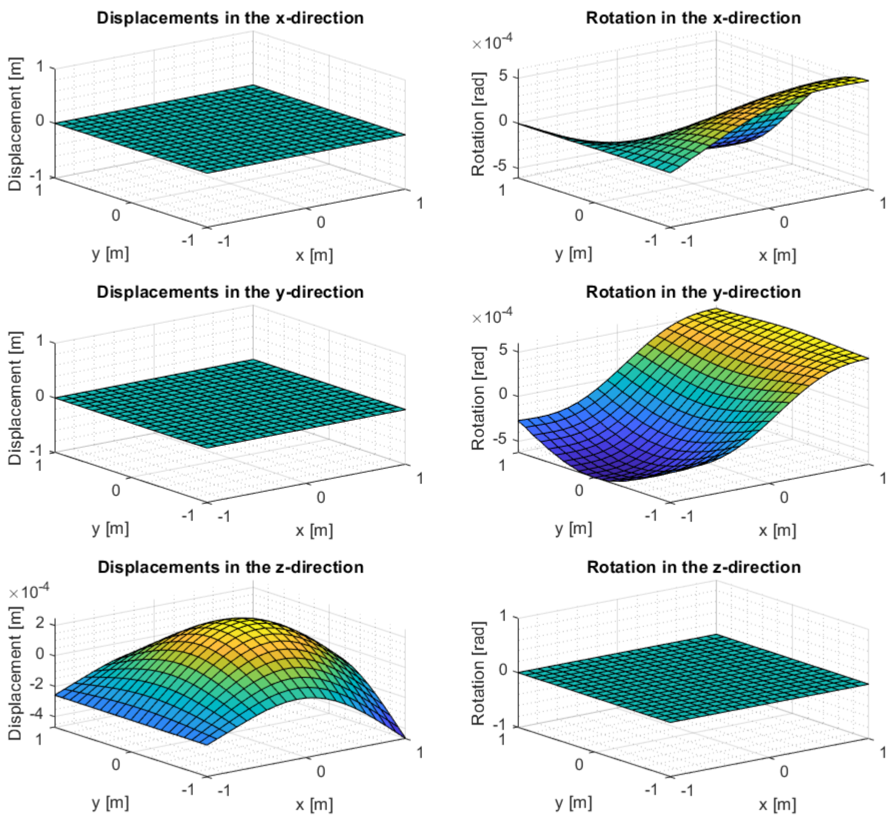

FIGURE C.230: Displacement distribution along the shell when the frequency is equal to 70 Hz using a 400 element mesh (20x20) [MATLAB].

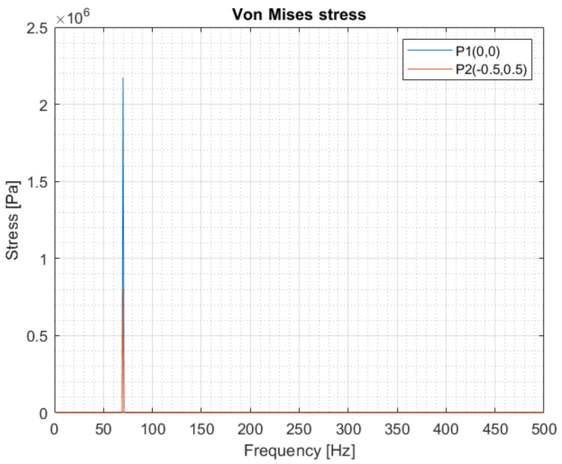

FIGURE C.231: Von Mises stress in the frequency domain obtained for an harmonic acceleration using a 400 element mesh (20x20) [MATLAB].

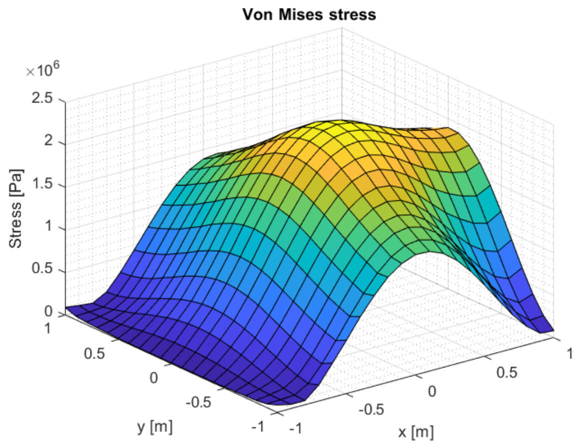

FIGURE C.232: Von Mises stress distribution along the shell when the frequency is equal to 70 Hz using a 400 element mesh (20x20) [MATLAB].

Random Vibration Test

Then, a random vibration test has been performed to the first model of the shell. Figure C.233 shows the displacements distribution of the points P1 and P2 versus the frequency considering a frequency step of 0.5 Hz. In this case, the maximum displacement in the z-direction takes place at the frequency of 45.5 Hz.

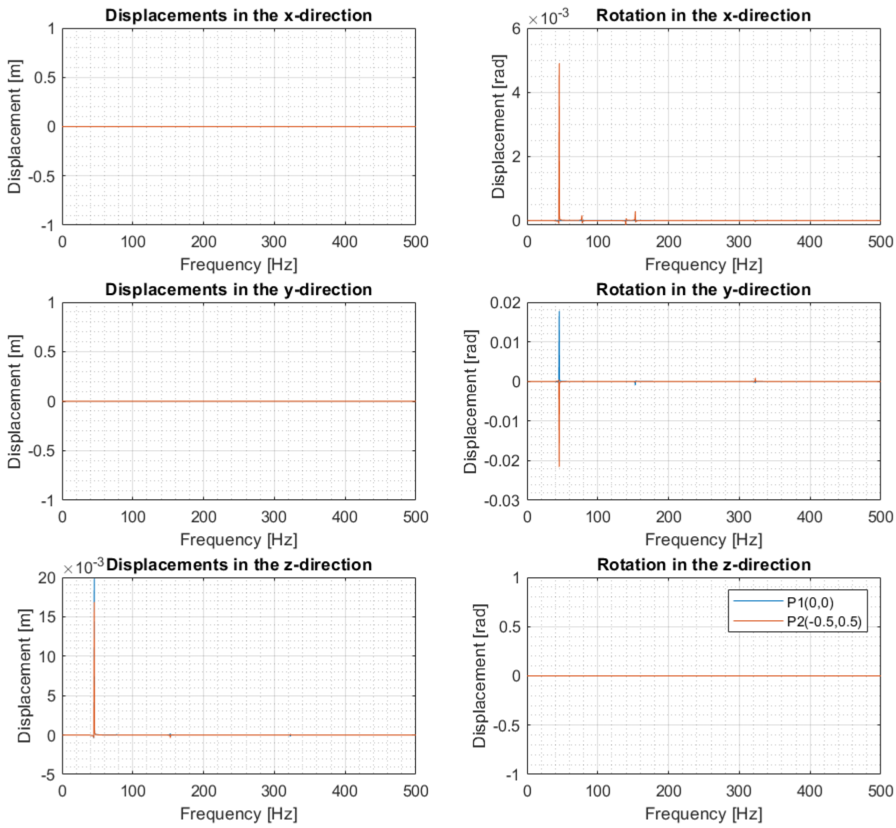

FIGURE C.233: Displacements in the frequency domain obtained for a random vibration acceleration using a 400 element mesh (20x20) and with $\Delta f = 0.5$ Hz [MATLAB].

As the maximum displacement is obtained for the frequency of 45.5 Hz, the displacements distribution along the shell have been computed for this frequency and are plotted in figure C.234. Moreover, as shown in figure C.235, the maximum Von Mises stress takes place when the frequency is equal to 45.5 Hz, so the displacements and the Von Mises stress distribution along the shell have been plotted for this specific frequency. Von Mises stress versus frequency and Von Mises stress distribution along the shell for the frequency of 45.5 Hz are shown in figures C.235 and C.236 respectively considering a frequency step of 0.5 Hz.

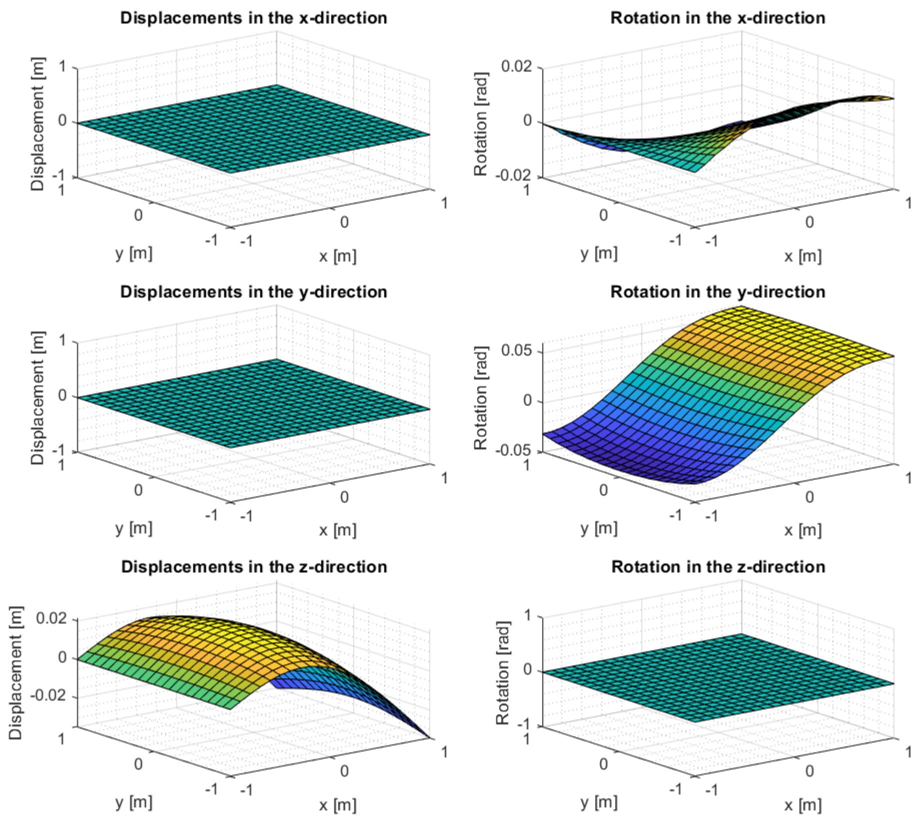

FIGURE C.234: Displacement distribution along the shell when the frequency is equal to 45.5 Hz using a 400 element mesh (20x20) and with $\Delta f = 0.5$ Hz [MATLAB].

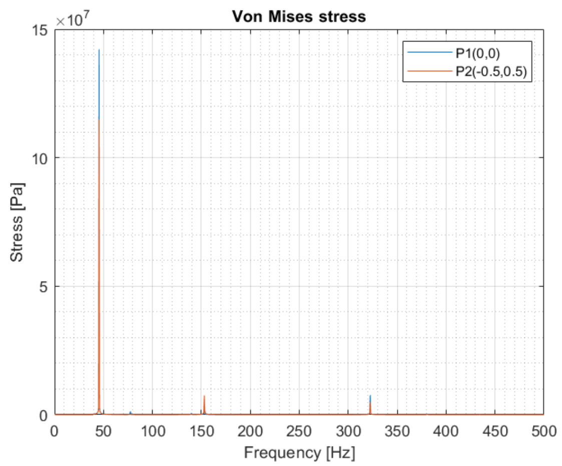

FIGURE C.235: Von Mises stress in the frequency domain obtained for a random vibration acceleration using a 400 element mesh (20x20) and with $\Delta f = 0.5$ Hz [MATLAB].

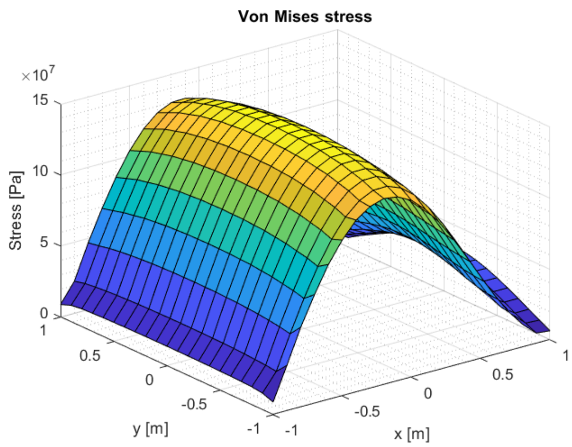

FIGURE C.236: Von Mises stress distribution along the shell when the frequency is equal to 45.5 Hz using a 400 element mesh (20x20) and with $\Delta f = 0.5$ Hz [MATLAB].

C.9.2 Second model definition

Then, for the second model, an approximation from the flat shell to the sensor's dimensions has been done. In this case, the shell will be 0.2 meters long with a width of 0.02 meters and a thickness of 0.001 m. The geometry and properties of the second shell model are listed bellow.

Geometry
- Dimensions: 2,00 x 2,00 m
- Thickness: 0.001 m

Material
- Young's modulus, E = 69 GPa.
- Poisson's ratio, $\nu = 0.3$.
- Density, $\rho = 2700\ kg/m^3$.

Boundary Conditions
- None of the four edges of the shell is embedded.
- An acceleration is defined in x=-1m line.
- To be more time-efficient, $u_x = u_y = \theta_z = 0$.

Quasi-static Test

Then, the quasi- static test has been performed to the second model of the shell. Figure C.237 shows the displacements distribution versus the frequency obtained for the nodes located on P1 and P2. As what happened to the first model, the maximum displacement is located at the same frequency of the harmonic vibration applied, 70 Hz.

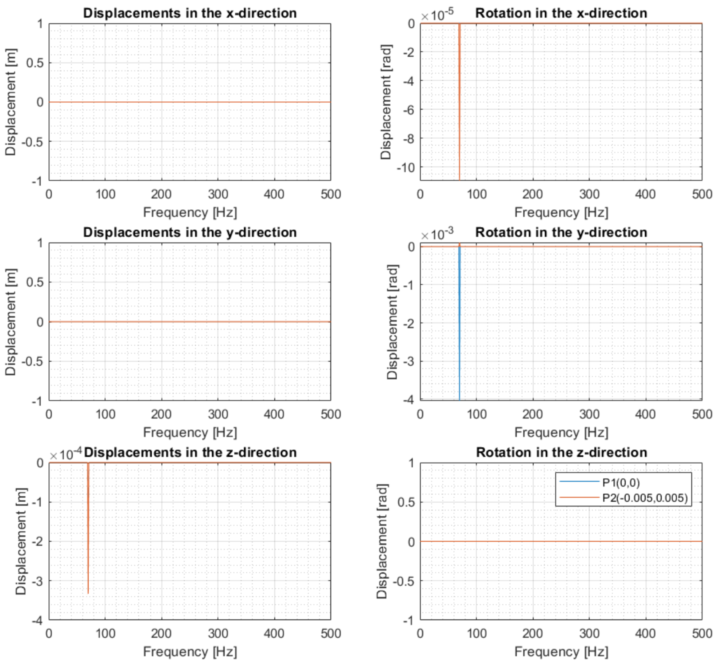

FIGURE C.237: Displacements in the frequency domain obtained for an harmonic vibration using a 400 element mesh (20x20) [MATLAB].

For the frequency at which the maximum displacement takes places, the displacement distribution along the shell has been plotted and can be seen in figure C.238. Moreover, the Von Mises stress distribution in the frequency domain has been computed as well and it is shown in figure C.239. As the maximum Von Mises stress coincides with the frequency equal to 70 Hz, the Von Mises stress distribution along the shell has been plotted for this specific frequency in figure C.240.

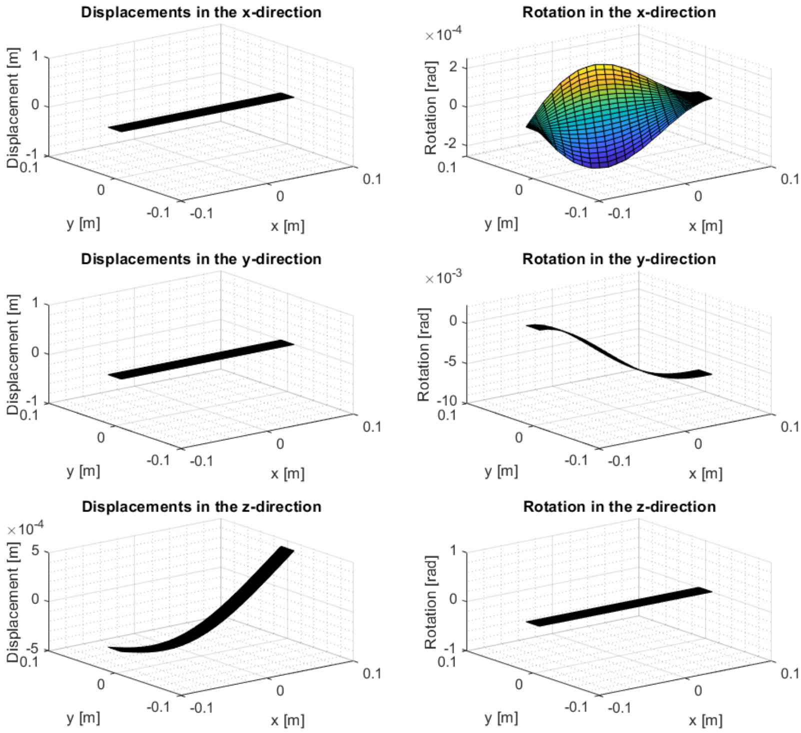

FIGURE C.238: Displacement distribution along the shell when the frequency is equal to 70 Hz using a 400 element mesh (20x20) [MATLAB].

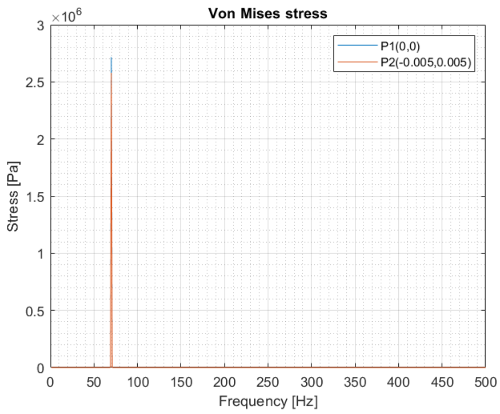

FIGURE C.239: Von Mises stress in the frequency domain obtained for an harmonic vibration using a 400 element mesh (20x20) [MATLAB].

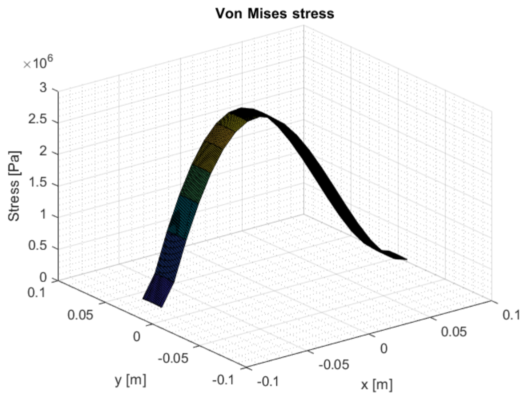

FIGURE C.240: Von Mises stress distribution along the shell when the frequency is equal to 70 Hz using a 400 element mesh (20x20) [MATLAB].

Random Vibration Test

Then, a random vibration test has been performed to the second shell model. Figure C.241 shows the displacements distribution of the points P1 and P2 in the frequency domain. The maximum displacement in the z-direction and both, the maximum rotation in x and y-direction, take place when the frequency is equal to 90 Hz.

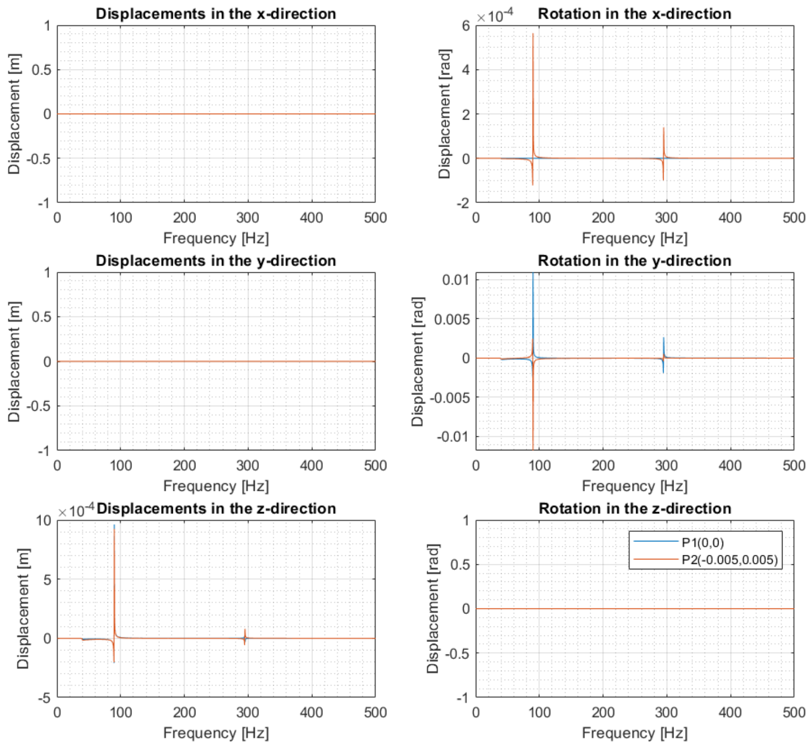

FIGURE C.241: Displacements in the frequency domain obtained for an harmonic vibration using a 400 element mesh (20x20) and with $\Delta f = 0.5$ Hz [MATLAB].

As the maximum displacement is presented at a frequency of 90 Hz, the displacements and rotations distributions along the shell have been plotted for this frequency in figure C.242. Moreover, the Von Mises stress distribution versus the frequency is shown in figure C.243. Figure C.244 presents the Von Mises stress distribution along the shell for the frequency of 90 Hz where the maximum stress takes place.

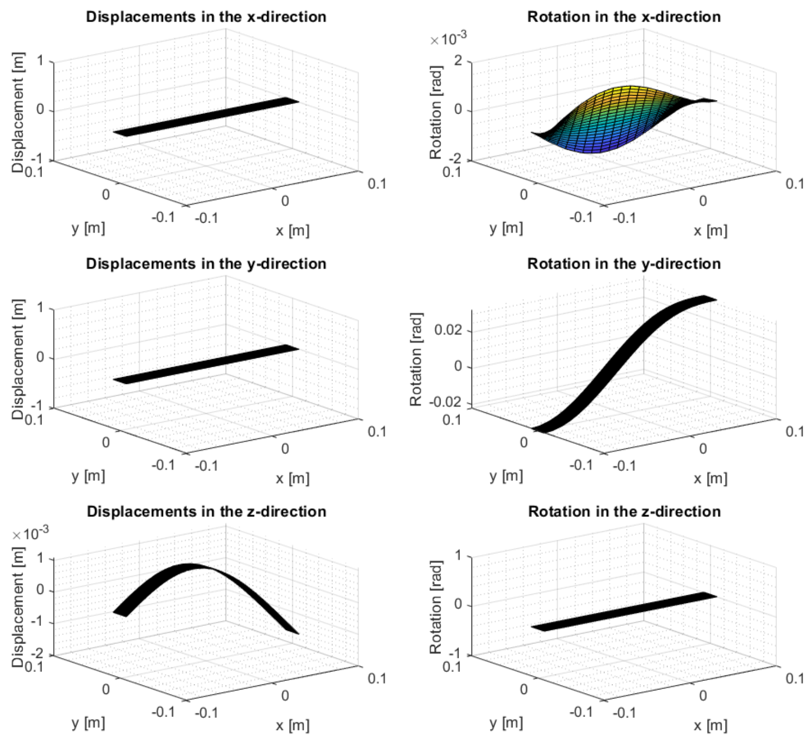

FIGURE C.242: Displacement distribution along the shell when the frequency is equal to 90 Hz using a 400 element mesh (20x20) and with $\Delta f = 0.5$ Hz [MATLAB].

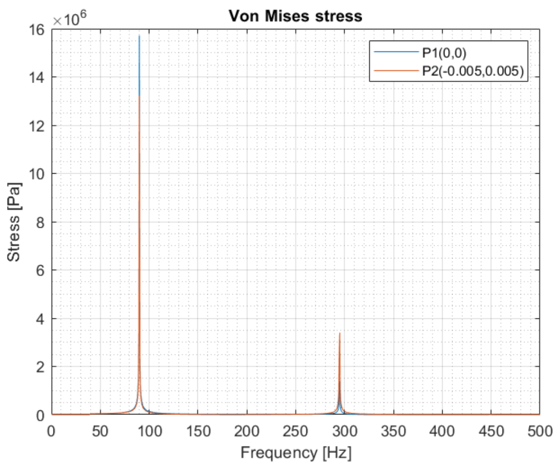

FIGURE C.243: Von Mises stress in the frequency domain obtained for an harmonic vibration using a 400 element mesh (20x20) and with $\Delta f = 0.5$ Hz [MATLAB].

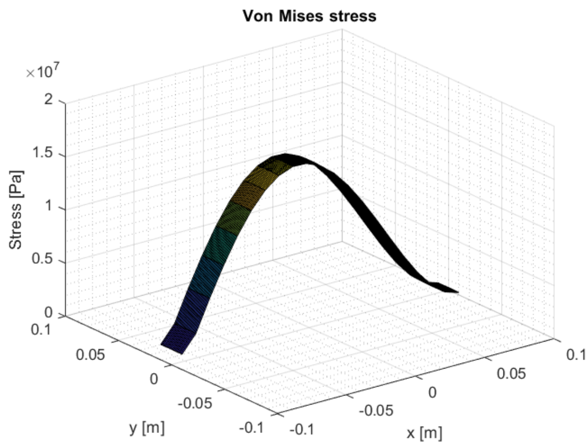

FIGURE C.244: Von Mises stress distribution along the shell when the frequency is equal to 90 Hz using a 400 element mesh (20x20) and with $\Delta f = 0.5$ Hz [MATLAB].

C.9.3 Third model definition

Finally, the last model not only will change the dimensions from the first model, but also its properties. The characteristics of the third model are listed bellow.

Geometry

- Dimensions: 2,00 x 2,00 m
- Thickness: 0.001 m

Material

- Young's modulus, E = 22 GPa.
- Poisson's ratio, $\nu = 0.15$.
- Density, $\rho = 1900\ kg/m^3$.

Boundary Conditions

- None of the four edges of the shell is embedded.
- An acceleration is defined in x=-1m line.
- To be more time-efficient, $u_x = u_y = \theta_z = 0$.

Quasi-static Test

For the third model, first a quasi-static test was performed. Figure C.245 shows the displacements distribution along the frequency domain. The maximum displacement in the z-direction as well as the maximum rotation in both, x and y-direction, is presented when the frequency is equal to 70 Hz.

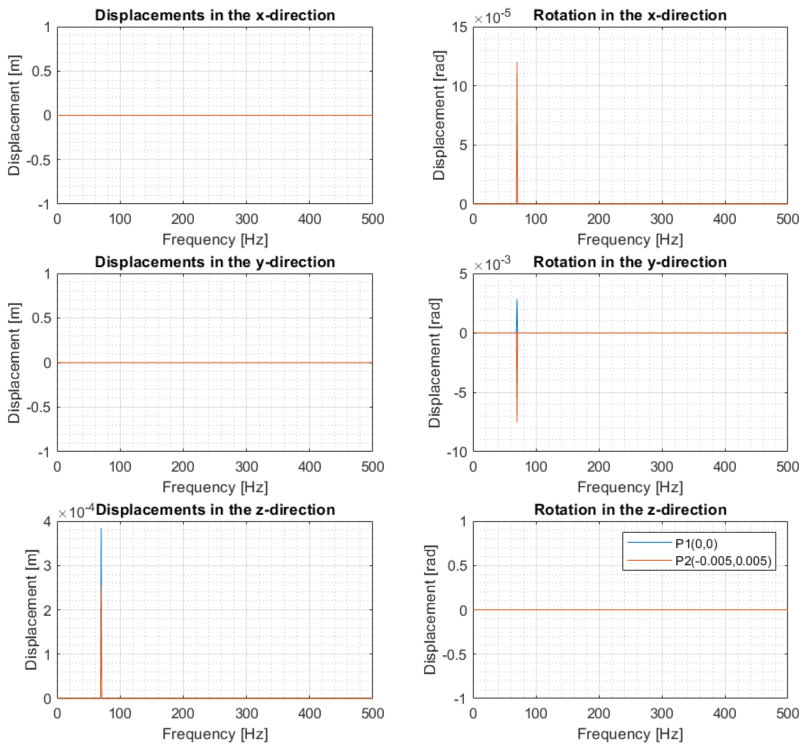

Figure C.245: Displacements in the frequency domain obtained for an harmonic vibration using a 400 element mesh (20x20) [MATLAB].

The displacement distribution along the shell has been plotted in figure C.246 for the frequency equal to 70, when the maximum displacement takes place. Furthermore, the Von Mises stress distribution versus the frequency is shown in figure C.247 and, as the maximum Von Mises stress takes place when the frequency is equal to 70 Hz, the Von Mises stress distribution along the shell has been plotted for this specific frequency in figure C.248.

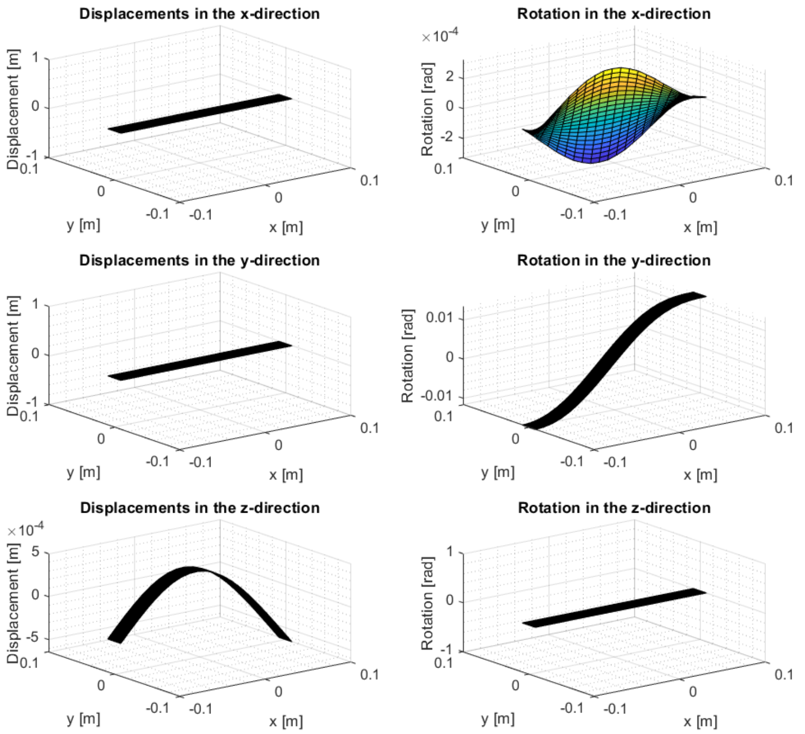

FIGURE C.246: Displacement distribution along the shell when the frequency is equal to 70 Hz using a 400 element mesh (20x20) [MATLAB].

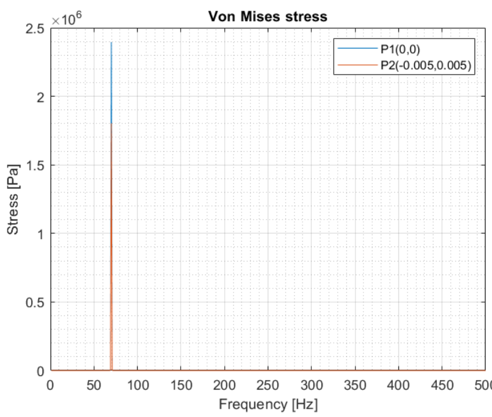

FIGURE C.247: Von Mises stress in the frequency domain obtained for an harmonic vibration using a 400 element mesh (20x20) [MATLAB].

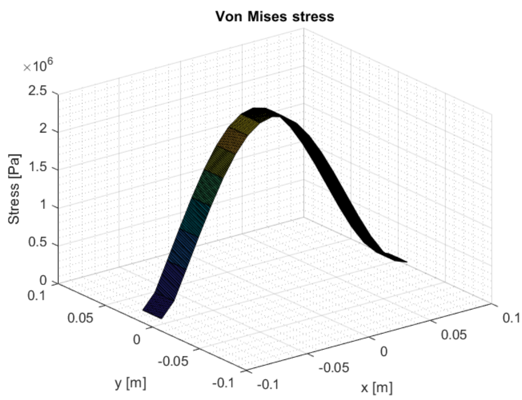

FIGURE C.248: Von Mises stress distribution along the shell when the frequency is equal to 70 Hz using a 400 element mesh (20x20) [MATLAB].

Random Vibration Test

Then, a random vibration test has been performed to the third model of the shell. Figure C.249 presents the displacements distribution versus the frequency. As the maximum displacement in the z-direction as well as the maximum rotation in both, x and y-direction, takes place when the frequency is equal to 60.5 Hz, the displacements distribution has been plotted for this specific frequency and the results can be seen in figure C.250.

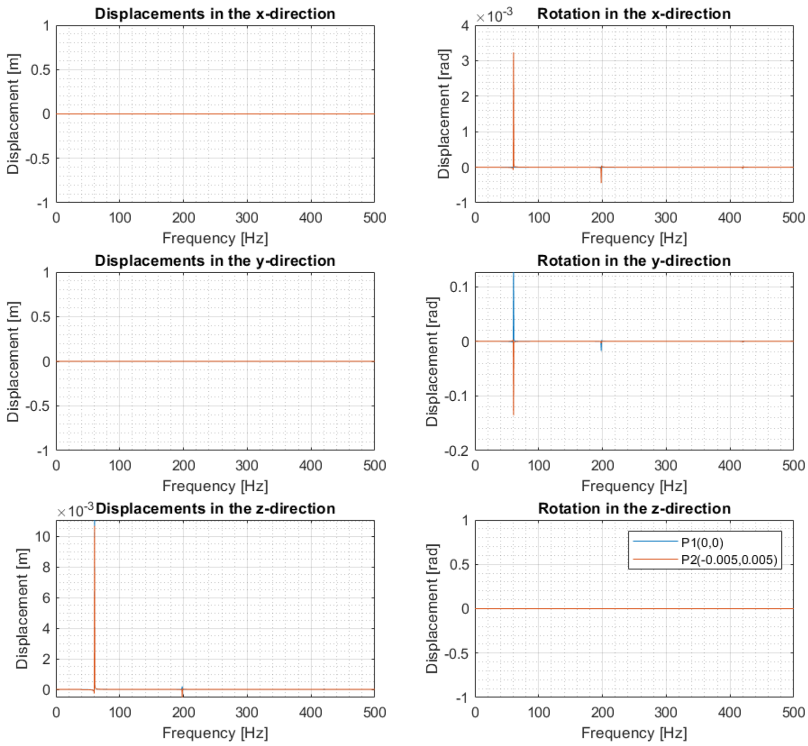

FIGURE C.249: Displacements in the frequency domain obtained for an harmonic vibration using a 400 element mesh (20x20) and with $\Delta f = 0.5$ Hz [MATLAB].

Figure C.251 presents the Von Mises stress distribution versus the frequency obtained for the random vibration test performed on the shell. As the maximum stress appears when the frequency is equal to 60.5 Hz, the Von Mises stress distribution along the shell for this frequency is plotted in figure C.252.

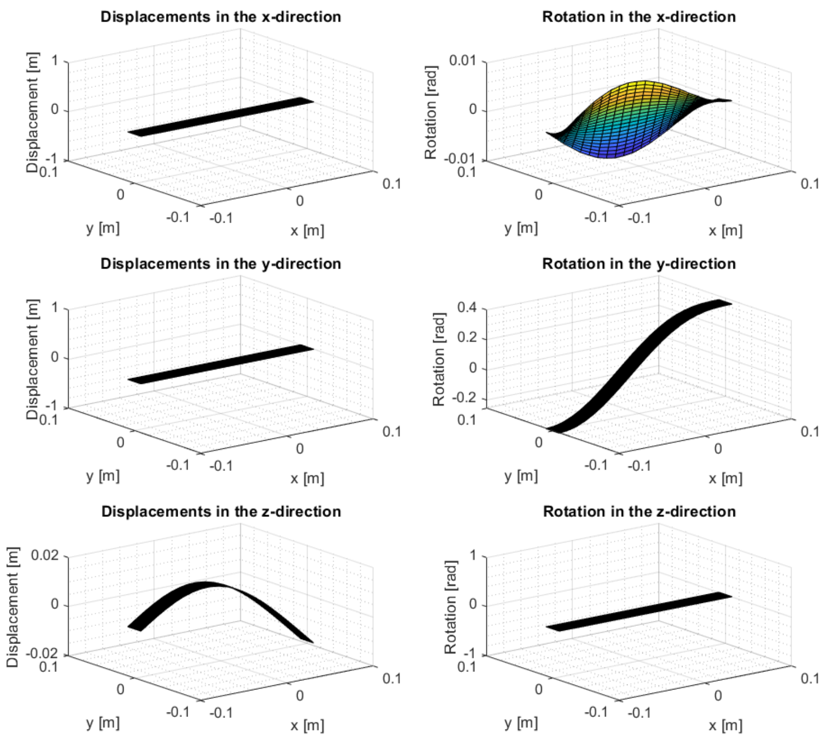

FIGURE C.250: Displacement distribution along the shell when the frequency is equal to 60.5 Hz using a 400 element mesh (20x20) and with $\Delta f = 0.5$ Hz [MATLAB].

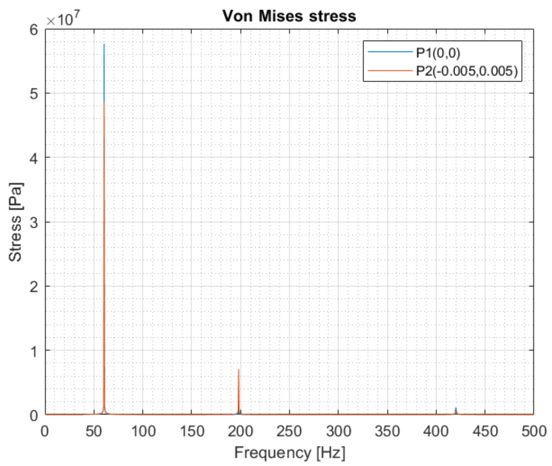

FIGURE C.251: Von Mises stress in the frequency domain obtained for an harmonic vibration using a 400 element mesh (20x20) and with $\Delta f = 0.5$ Hz [MATLAB].

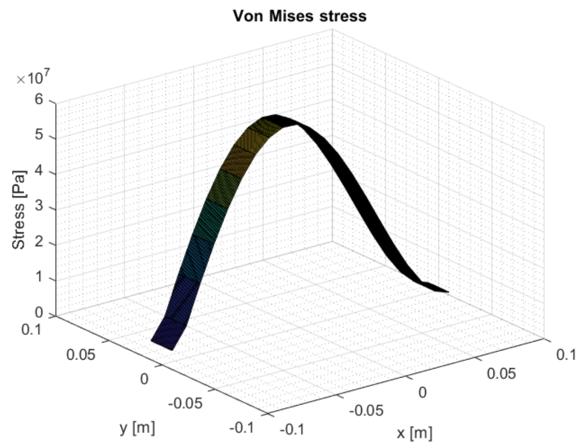

FIGURE C.252: Von Mises stress distribution along the shell when the frequency is equal to 60.5 Hz using a 400 element mesh (20x20) and with $\Delta f = 0.5$ Hz [MATLAB].

C.9.4 Differences between the three models

Finally, the different results obtained during the whole report are organised and listed in table C.13. As shown in the following table, comparing the results of the quasi-static test for the three models, the maximum displacement is obtained always at the same frequency of 70 Hz, which also coincides with the frequency at which the sinusoidal acceleration applied oscillates. In contrast, when comparing the random test results obtained for the three models, there is a complete disagreement in the frequency at which the maximum displacement takes place.

TABLE C.13: Summary of results obtained for the tests performed to the three models.

	Model 1	**Model 2**	**Model 3**
Dimensions			
x (m)	2	0.2	0.2
y (m)	2	0.02	0.02
z (m)	0.05	0.001	0.001
Properties			
E (GPa)	69	69	22
ν	0.3	0.3	0.15
ρ (kg/m^3)	2700	2700	1900
Results Quasi-Static Test			
$freq_{max\ disp}$ (Hz)	70	70	70
$u_{z\ max}$ (m)	$2.58 \cdot 10^{-4}$	$4.188 \cdot 10^{-4}$	$4.017 \cdot 10^{-4}$
$\sigma_{VM\ max}$	$2.28 \cdot 10^{6}$	$2.94 \cdot 10^{6}$	$2.442 \cdot 10^{6}$
Results Random Test			
$freq_{max\ disp}$ (Hz)	45.5	90	60.5
$u_{z\ max}$ (m)	0.0217	$1.63 \cdot 10^{-3}$	0.0125
$\sigma_{VM\ max}$ (Pa)	$146.5 \cdot 10^{6}$	$16.35 \cdot 10^{6}$	$60.007 \cdot 10^{6}$

Moreover, the maximum displacement for the quasi-static test is obtained on the second model of the shell with a value of $4.188 \cdot 10^{-4}$ m. However, the maximum displacement when performing a random vibration test takes place on the first model with a value of 0.0217 m. The maximum Von Mises stress obtained from the quasi-static test takes place on the second model with a value of $2.94 \cdot 10^{6}$ Pa. In contrast, the maximum Von Mises stress when performing a random vibration test appears in the first model with a value of $146.5 \cdot 10^{6}$ Pa. It can be concluded that, by approximating the geometry and the properties of the shell to the sensor, the maximum displacement and Von Mises stress decreases.

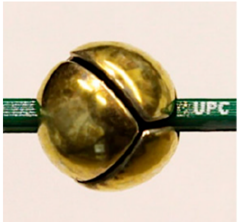

POLYTECHNIC UNIVERSITY OF CATALONIA
Structural Mechanics
Comsol

C.10 Report 10: Second approximation to the wind sensor

The aim of this report is to determine the geometry and composition of the sensor as well as to evaluate the sensor under a periodical load using COMSOL.

C.10.1 Model definition

The sensor is mainly composed by two section: a thin plate composed by circuit boards of PCB and a spherical shell made by Silicon carbide.

Material

- Material of the circuit board: PCB.
  - Young's modulus, E = 22 GPa.
  - Poisson's ratio, $\nu = 0.15$.
  - Mass density, $\rho = 1900 kg/m^3$.
- Material of the sphere: Silicon carbide (SiC).
  - Young's modulus, E = 748 GPa.
  - Poisson's ratio, $\nu = 0.45$.
  - Mass density, $\rho = 3216 kg/m^3$.

Sensor dimensions and geometry

Figures C.253 and C.254 show an schematic sketch of the positions of the different sectors as well as the shape of the PCB structure which holds the different sectors. Moreover, figure C.255 presents an overview of the sensor and figure C.256 defines the sensor dimensions.

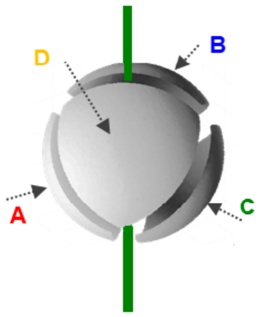

FIGURE C.253: Schematic sketch of the position of each of the four sectors of the wind sensor [14].

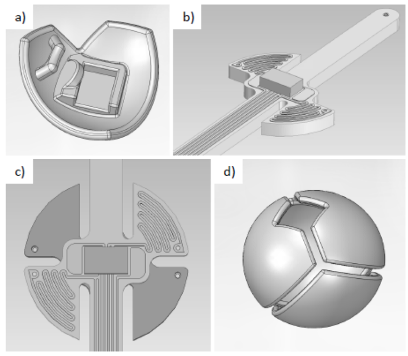

FIGURE C.254: Images of the complex geometry of the wind sensor [15].

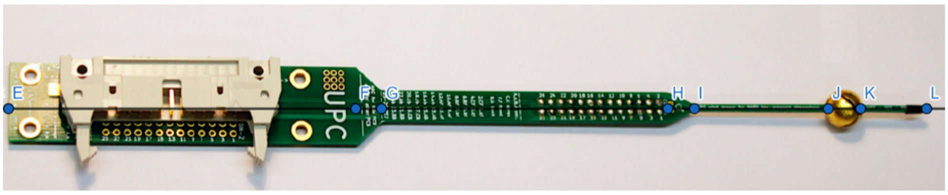

FIGURE C.255: Overview of the wind sensor [14].

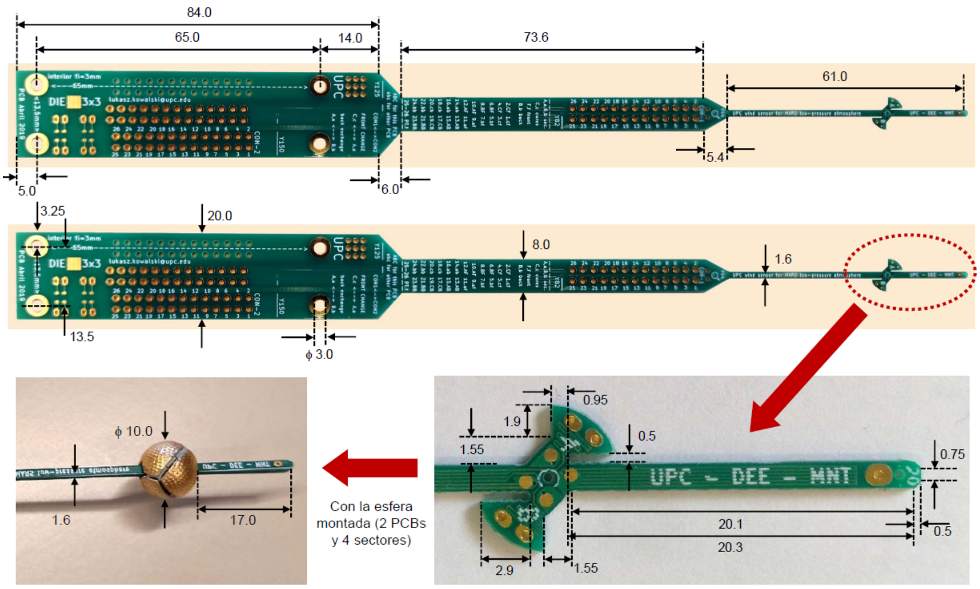

FIGURE C.256: Sensor dimensions [given by the electronics department of the UPC].

C.10.2 Geometric simplifications

For the first case studied certain simplifications will be assumed in order to decrease the difficulty of the geometry of the sensor. The sensor will have just one PCB instead of two and it will have a total thickness of 1.6 mm. The sphere will just be split in two equal sectors, not in four. Figures C.257 and C.258 show the sensor modeled with COMSOL.

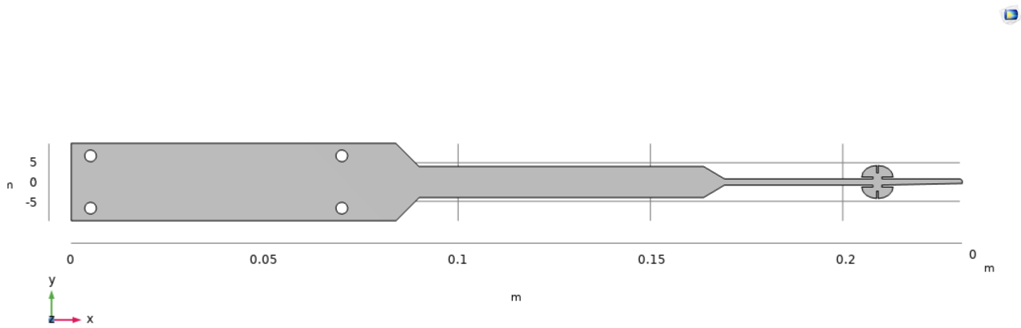

FIGURE C.257: Sensor model using some geometric simplification I [COMSOL].

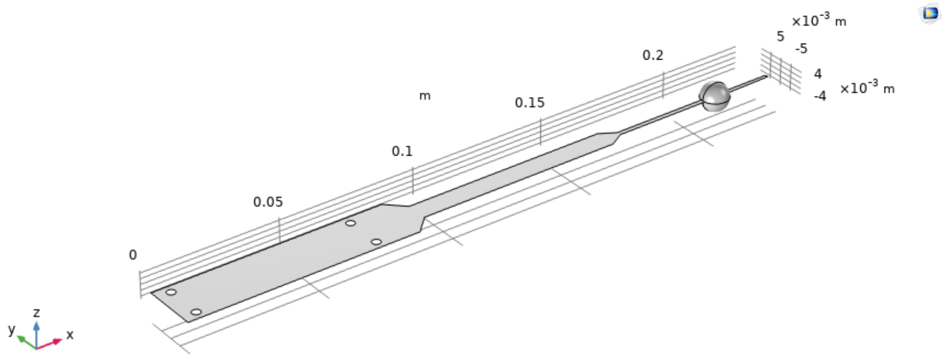

FIGURE C.258: Sensor model using some geometric simplifications II [COMSOL].

C.10.3 Quasi-static Test performed with COMSOL

A first study has been carried on in which a periodic load has been applied on the edges that conform the holes of the structure. The sensor has to pass a test in which an harmonic force will be applied on those edges in order to induce a forced vibration to the whole structure. The acceleration will be of 50g with a frequency of 70Hz. So the equation of the force applied is:

$$F(t) = 50 \cdot g \cdot \sin 2\pi \cdot 70 \cdot t \tag{C.93}$$

Furthermore, figure C.259 shows the location of the harmonic force applied and figure C.260 presents the location of the points that are going to be evaluated.

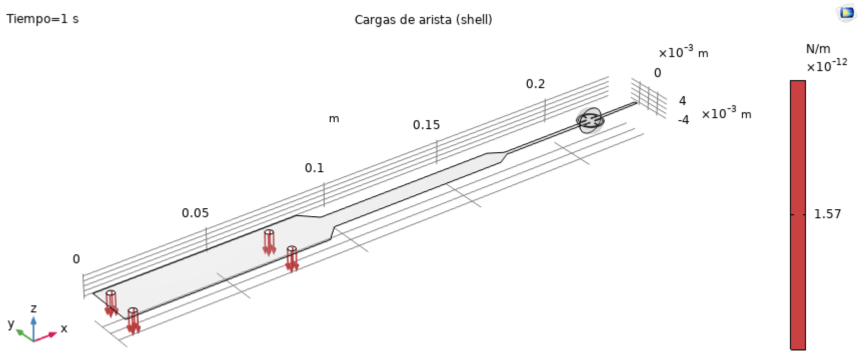

FIGURE C.259: Boundary conditions of the wind sensor [COMSOL].

FIGURE C.260: Location of the evaluated nodes [COMSOL].

Figures C.261 and C.262 shows the displacements evolution during time of the four evaluated nodes and the Von Mises stress distribution respectively. As shown in figure C.261, the point that describes the major displacement is the first one whereas the minor displacement is described by point number three. Moreover, at the beginning of the movement all points seem to be describing a periodical function, however, once being in movement 10 seconds the displacements of the nodes keep increasing.

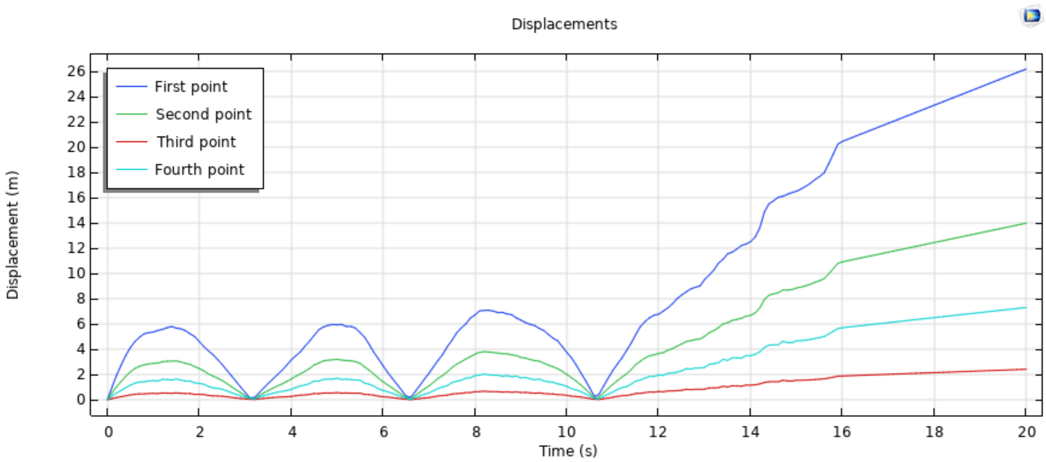

FIGURE C.261: Displacements distribution of the four evaluated nodes of the wind sensor as a function of time [COMSOL].

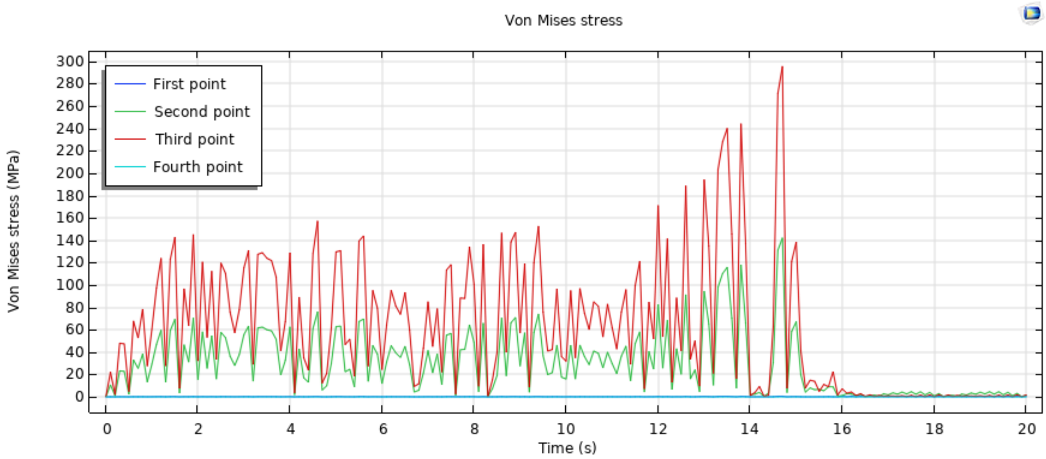

FIGURE C.262: Von Mises stress distribution of the four evaluated nodes of the wind sensor as a function of time [COMSOL].

Moreover, as shown in figure C.262, Von Mises stress distribution over time seems to be quite chaotic. However, it can be seen that the first and the fourth points have a Von Mises stress constant and equal to zero due to the fact that they are located in both free ends. Additionally, Von Mises stress obtained for points two and three begins being arbitrary over time until they get their maximum at 15 seconds approximately and then remain constant and equal to zero.

Polytechnic University of Catalonia
Structural Mechanics
Matlab and Comsol

C.11 Report 11: Third approximation to the wind sensor

The aim of this report is to obtain the displacements and the Von Mises stress distribution along the wind sensor when performing a quasi-static and a random vibration test. In order to do so, the geometry of the sensor has been computed considering just two semi spherical sectors and a linear quadrilateral element mesh. Moreover, not only has the sensor been tested considering its real material properties, but also, the results have been compared to the ones obtained considering that the sensor was only made of PCB. This permit to evaluate the impact that the weight of the sphere had on the displacements and the Von Mises stress distribution.

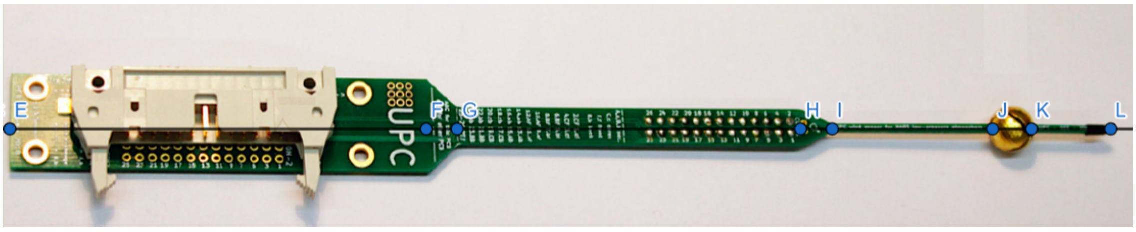

Figure C.263: Overview of the wind sensor [14].

C.11.1 First model definition

The sensor is a 10mm diameter sphere composed of four equally shaped sectors obtained from the projection of a tetrahedron to the spherical surface. The sectors are assembled to two superimposed printed circuit boards (PCBs). Each PCB provides mechanical support and signal routing for two sectors. A customized silicon die, manufactured in UPC White Room, which includes a Pt resistor, is attached to each sector in order to sense temperature and provide heating power. Furthermore, to control the temperature at the core of the sphere where the sectors are assembled, two additional dice are placed on the supporting PCBs. Finally, the sectors are made of silver, a metal with very high thermal conductivity, and kept at the same constant temperature [39].

Material

- Material of the structure: PCB.
  - Young's modulus, E = 22 GPa.
  - Poisson's ratio, $\nu = 0.15$.
  - Mass density, $\rho = 1900\ kg/m^3$.
  - Ultimate tensile strength, $\sigma_{max} =$ 282 MPa.
- Material of the sphere: Silver (Ag).
  - Young's modulus, E = 76 GPa.
  - Poisson's ratio, $\nu = 0.37$.
  - Mass density, $\rho = 10497\ kg/m^3$.
  - Ultimate tensile strength, $\sigma_{max} =$ 140 MPa.

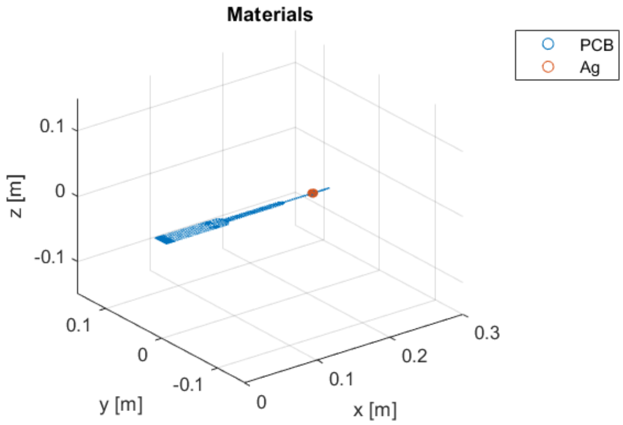

FIGURE C.264: Material distribution along the sensor [MATLAB].

Geometry

Figures C.265 and C.266 show an schematic sketch of the positions of the different sectors as well as the shape of the PCB structure which holds the different sectors. Moreover, figure C.267 defines the sensor dimensions.

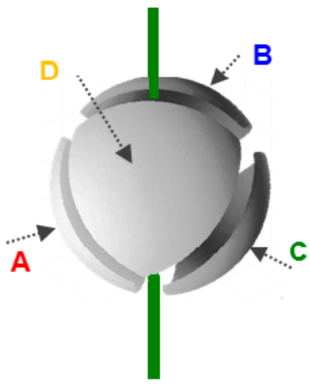

FIGURE C.265: Schematic sketch of the position of each of the four sectors of the wind sensor [14].

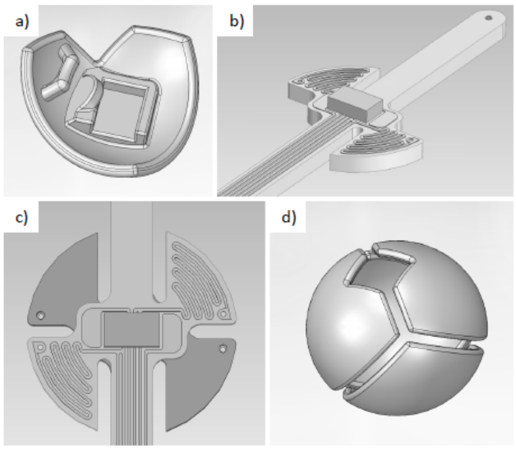

FIGURE C.266: Images of the complex geometry of the wind sensor [15].

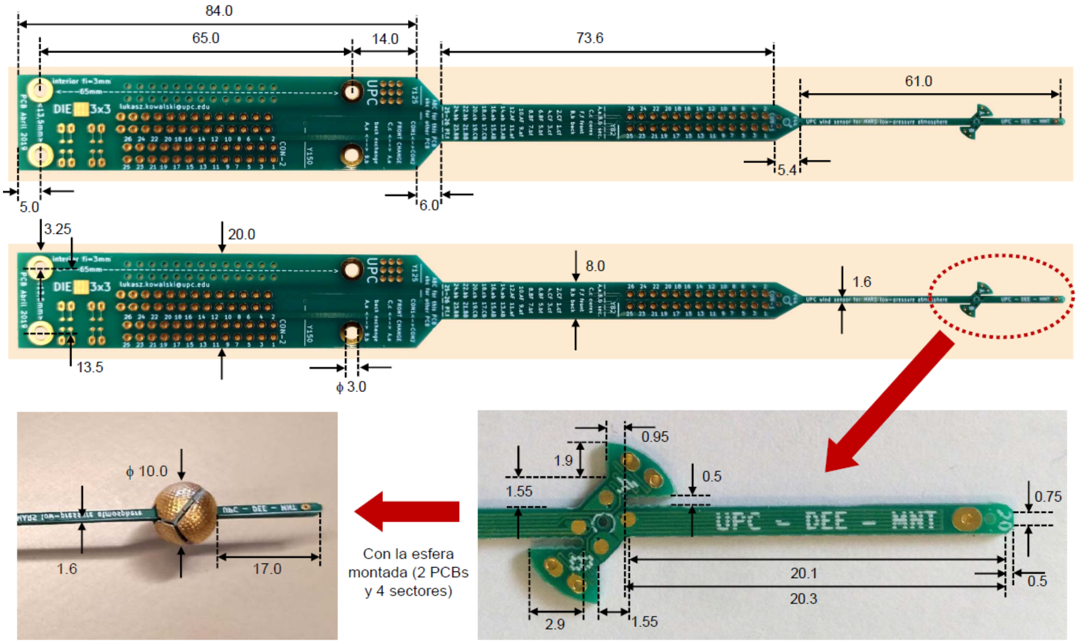

FIGURE C.267: Sensor dimensions [given by the electronics department of the UPC].

Geometric simplification

First, certain simplifications will be assumed in order to decrease the difficulty of the geometry of the sensor. The sensor will have just one PCB instead of two and it will have a total thickness of 1.6 mm. Figure C.268 shows the sensor dimensions with COMSOL. Moreover, the sphere will just be split in two semi-spherical sectors, not in four.

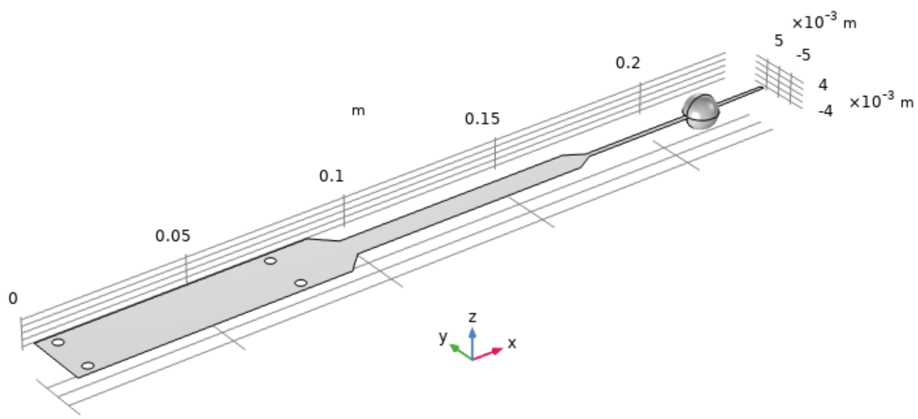

FIGURE C.268: Sensor model using some geometric simplifications [COMSOL].

Mesh

With the use of COMSOL an structured mesh has been configured. Furthermore, the resulting mesh is only composed by quadrilateral elements and a total of 1165 nodes. The mesh created with COMSOL is shown in figure C.269.

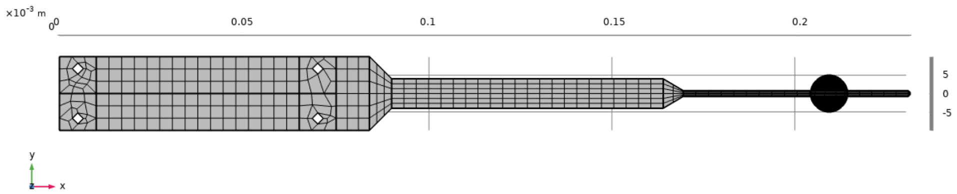

FIGURE C.269: Sensor's structured mesh composed by 1165 nodes [COMSOL].

Evaluated nodes

Moreover, during this report, 5 points have been chosen in order to compute the displacements, rotations and the Von Mises stress on each of them as a function of frequency.

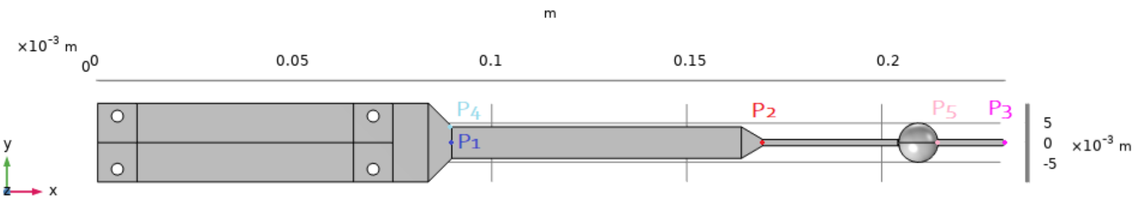

FIGURE C.270: Location of the evaluated nodes along the sensor [COMSOL].

C.11.1.1 Modal Analysis

Then, a modal analysis has been performed in order to identify the first six natural frequencies at which the sensor will experiment resonance. Table C.14 lists the first six eigenvalues obtained considering that there is a prescribed displacement in the z-direction of the nodes located on the holes at which the sensor will be attached during the test. Furthermore, figure C.271 shows the first six vibration modes of the shell.

TABLE C.14: First six natural frequencies [MATLAB].

Mode	Frequency (Hz)
1st	89.4243
2nd	498.404
3rd	1306.67
4th	1779.14
5th	3046.77
6th	3791.81

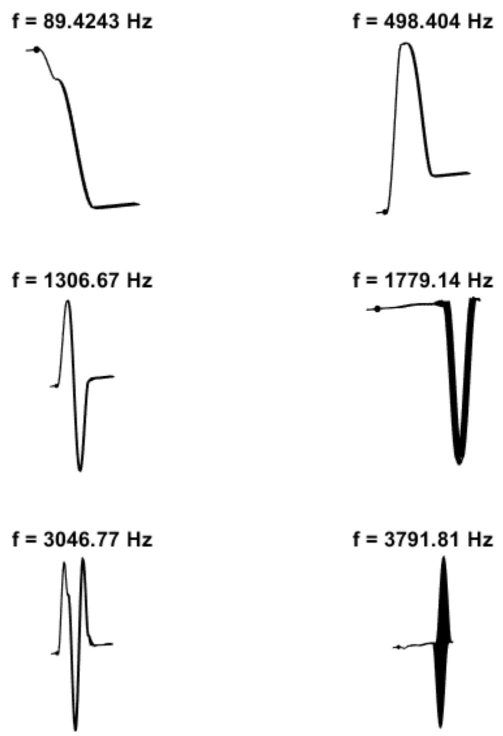

FIGURE C.271: First six modes and natural frequencies [MATLAB].

C.11.1.2 Quasi-Static Test

First, a quasi-static test has been performed to the sensor which consisted in submitting the sensor to an harmonic vibration. The harmonic acceleration has been applied on the nodes that conform the holes of the sensor and the vibration has been induced in the z-direction.

The methodology used to perform the quasi-static vibration test is shown in figure C.272. The harmonic vibration of an amplitude of 50 m/s^2 and a frequency of 70 Hz has been first computed in time domain.

$$s = -50 \cdot \sin(2\pi 70t) \tag{C.94}$$

Then, with the use of the Fourier Transform the acceleration has been transformed from time to frequency domain.

$$S = fft(s) \tag{C.95}$$

The acceleration has been applied on the u_z degree of freedom of the nodes located on the holes of the sensor.

$$\{\mathbf{A}\} = \{\mathbf{A}(DOF, freq)\} \tag{C.96}$$

$$\{\mathbf{A}(I_p, :)\} = S \tag{C.97}$$

Once obtained the acceleration in the frequency domain, the prescribed displacement in the frequency domain $\{\mathbf{U}\}$ can be computed as the following

$$\{\mathbf{U}(I_p, freq)\} = -\frac{\{\mathbf{A}(I_p, freq)\}}{(2\pi freq)^2} \tag{C.98}$$

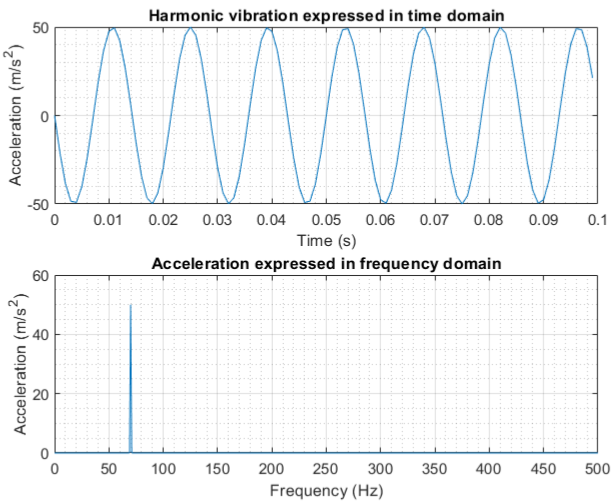

FIGURE C.272: Methodology used to compute the acceleration in the frequency domain [MATLAB].

Figure C.273 shows the displacements distribution versus the frequency for the quasi-static test performed and it can be concluded that the response of an harmonic excitation is sinusoidal as well. In other words, the shape of the displacements in the z-direction and the rotation in both, x and y-direction, agrees with the Fourier Transform of a sinusoidal function. Furthermore, from figure C.273, the frequency at which the maximum displacement takes place is 70 Hz which results to be the same value as the frequency of the harmonic excitation applied.

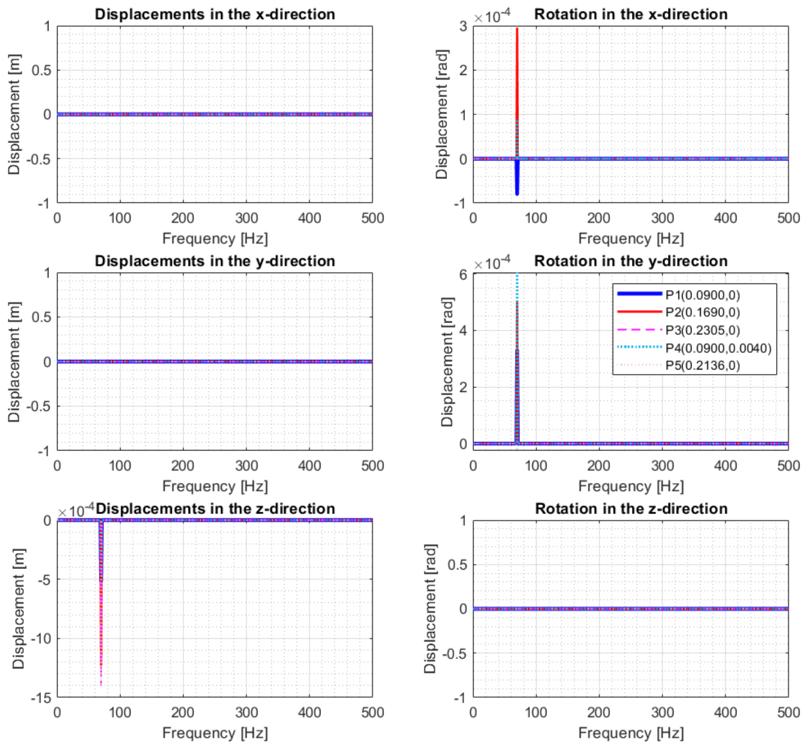

FIGURE C.273: Displacements in the frequency domain obtained for an harmonic acceleration [MATLAB].

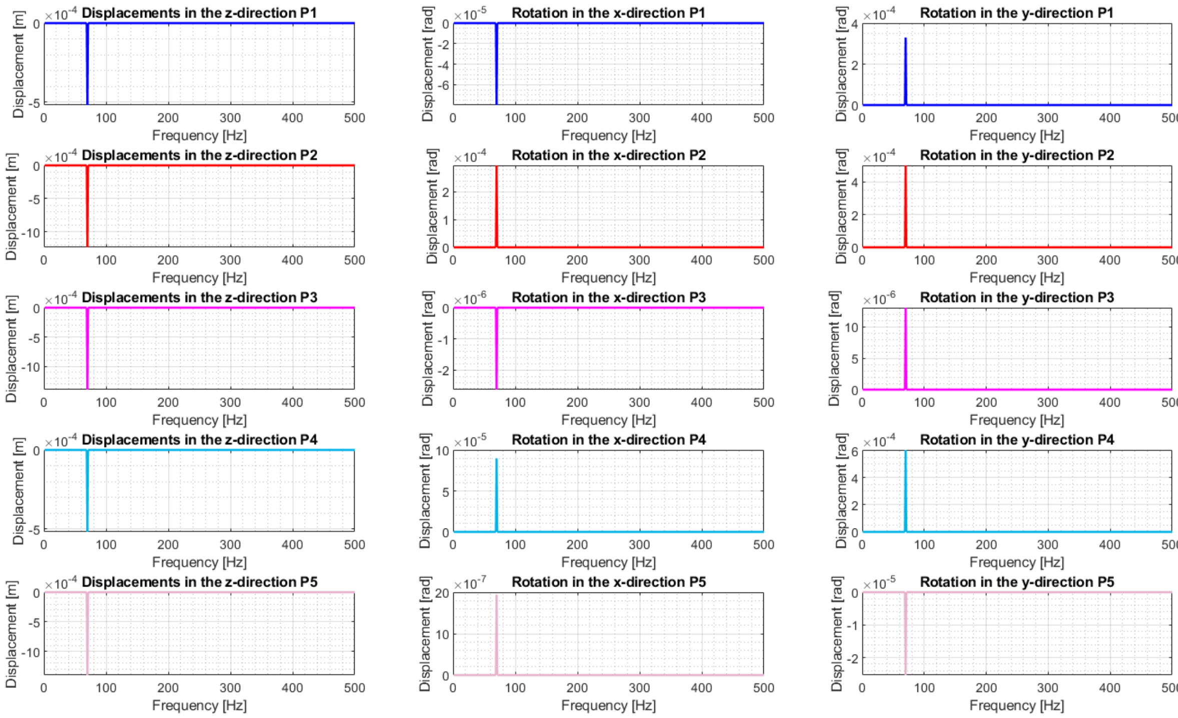

FIGURE C.274: Displacements versus frequency obtained for an harmonic acceleration measured in five points: P1 (0.0900,0), P2(0.1690,0), P3(0.2305,0), P4(0.0900,0.0040) and P5(0.2136,0) [MATLAB].

Moreover, figure C.274 presents the displacements distribution along frequency for the points selected in figure C.270. In this case, P_3 and P_5 result to be the points at which the displacement in the z-direction is maximum. On the other hand, the maximum rotation in both, x and y-direction, appears in point P_2. Figure C.275 shows the Von Mises stress distribution along the frequency domain for the five points previously chosen. From the points selected, P_2 is the one submitted to the highest stress.

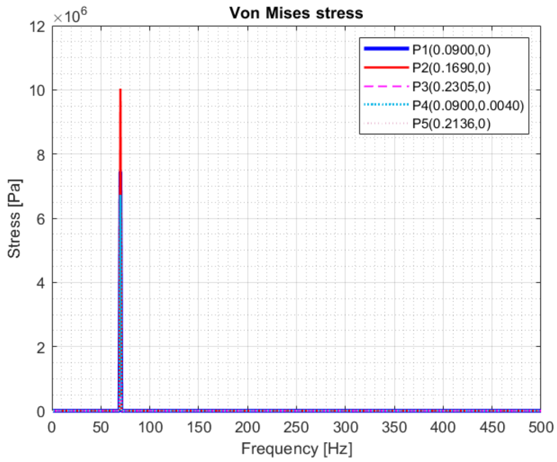

FIGURE C.275: Von Mises stress in the frequency domain obtained for an harmonic acceleration [MATLAB].

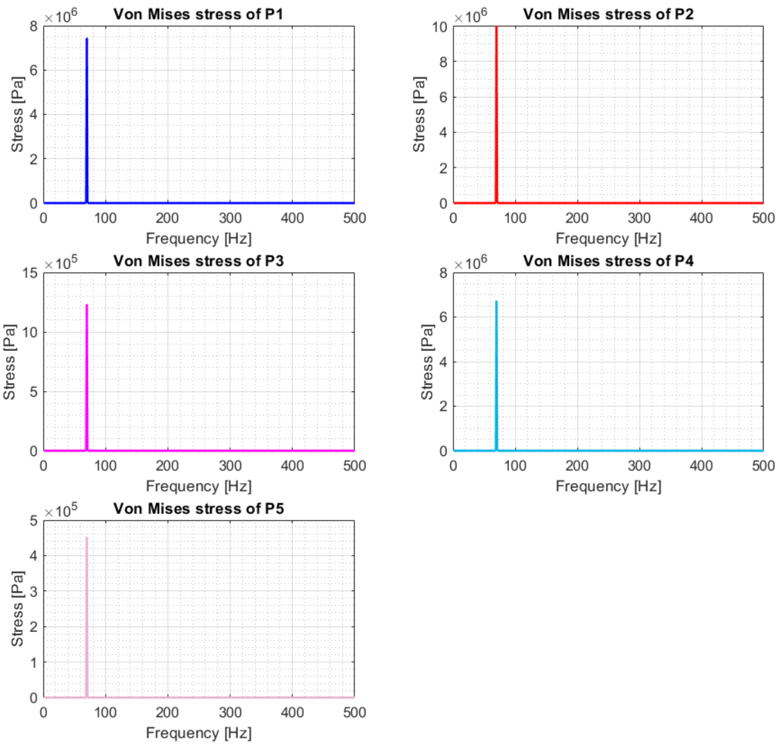

FIGURE C.276: Von Mises stress versus frequency obtained for an harmonic acceleration measured in five points: P1 (0.0900,0), P2(0.1690,0), P3(0.2305,0), P4(0.0900,0.0040) and P5(0.2136,0) [MATLAB].

Figure C.277 shows the displacements distribution in the z-direction along the sensor for the frequency of 70 Hz, frequency at which the maximum displacement takes place. As it can be seen in the figure, the maximum displacement in the z-direction appears at the nodes at which the harmonic acceleration is applied and it has a value of $-2.58 \cdot 10^{-4}$ m. Furthermore, figure C.278 presents the Von Mises stress distribution along the deformed mesh of the sensor for the frequency of 70 Hz. The maximum Von Mises stress is located on the coordinates $(0.2034, 0.0003, 0)$ m and has a value of $3.78 \cdot 10^7$ Pa.

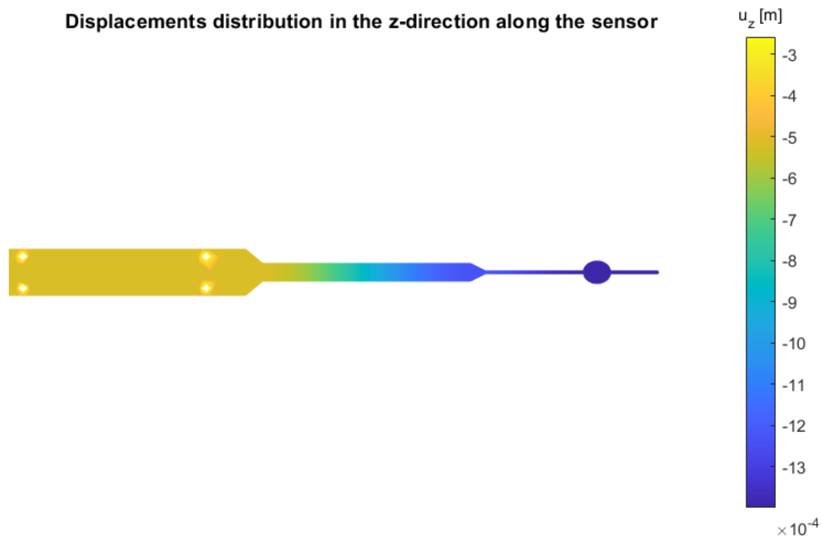

FIGURE C.277: Displacement distribution in the z-direction along the sensor when the frequency is equal to 70 Hz [MATLAB].

FIGURE C.278: Von Mises stress distribution along the sensor when the frequency is equal to 70 Hz [MATLAB].

C.11.1.3 Random Vibration Test

Then, a random vibration test has been performed on the sensor. It consisted in applying a random vibration excitation to the z-direction of the nodes located on the holes of the sensor. First, the Power Spectral Density function that describes the acceleration applied is defined by the following expression

$$PSD = 6 \cdot log_{10}(freq) + 0.04 - 6 \cdot log_{10}(40) \qquad when\ freq < 40\ Hz \tag{C.99}$$

$$PSD = 0.04 \qquad when\ 40\ Hz \leq freq \leq 450\ Hz \tag{C.100}$$

$$PSD = -6 \cdot log_{10}(freq) + 0.04 + 6 \cdot log_{10}(450) \qquad when\ freq > 450\ Hz \tag{C.101}$$

Then, the acceleration has been computed from the PSD input using the equation below:

$$PSD = \frac{S^2}{\Delta freq} \quad \longrightarrow \quad S = \sqrt{PSD \cdot \Delta freq} \tag{C.102}$$

As the acceleration is now expressed in g units, it has been multiplied by 9.81 m/s^2 in order to obtain the acceleration in the international system units. Finally, the acceleration has been applied on the u_z degree of freedom of the nodes located on the holes of the sensor.

$$\{\mathbf{A}\} = \{\mathbf{A}(DOF, freq)\} \tag{C.103}$$

$$\{\mathbf{A}(I_p, :)\} = S \tag{C.104}$$

Once obtained the acceleration in the frequency domain, the displacement in the frequency domain $\{\mathbf{U}\}$ can be computed

$$\{\mathbf{U}(I_p, freq)\} = -\frac{\{\mathbf{A}(I_p, freq)\}}{(2\pi freq)^2} \tag{C.105}$$

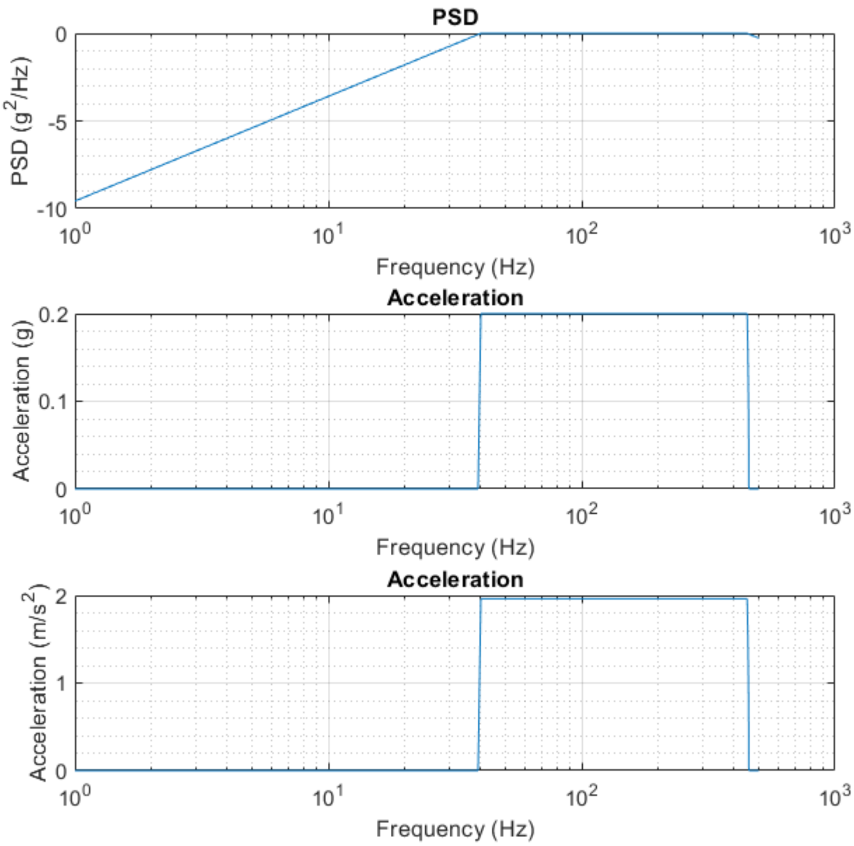

FIGURE C.279: Methodology used to compute the acceleration in the frequency domain considering a $\Delta f = 1$ Hz [MATLAB].

Figure C.280 shows the displacements distribution versus the frequency of the points chosen in figure C.270. In this case, P_3 and P_5 present the maximum displacement in the z-direction; P_2, the maximum rotation in the x-direction; and P_4, the maximum rotation in the y-direction. Nevertheless, all the maximums take place when the frequency is equal to 90 Hz.

Figure C.282 shows the Von Mises stress distribution versus the frequency obtained when performing a random vibration analysis to the sensor. Comparing the results obtained for the different coordinatess, the point at which the Von Mises stress is maximum is P_2 which coincides with the maximum stress when performing the quasi-static analysis as well. This happens due to the fact that the sphere is made of silver which is significantly denser than PCB and, as P_2 is located at a transitioning section of the PCB, it has to support the weight of the sphere so that the PCB doesn't deflect and break in that point.

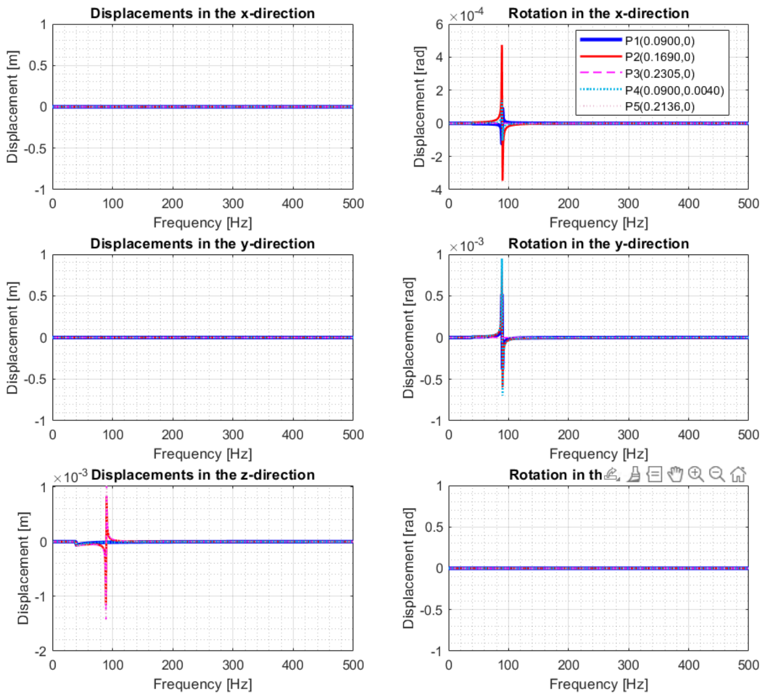

FIGURE C.280: Displacements in the frequency domain obtained for a random vibration considering $\Delta f = 1$ Hz [MATLAB].

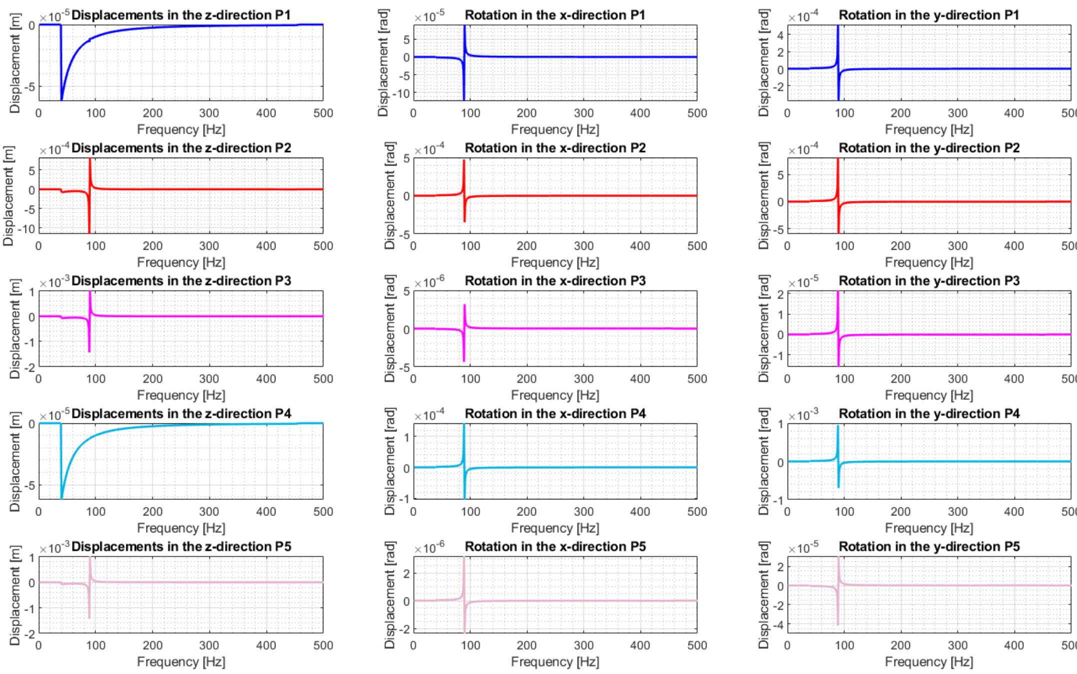

FIGURE C.281: Displacements versus frequency obtained for a random vibration measured in five points: P1 (0.0900,0), P2(0.1690,0), P3(0.2305,0), P4(0.0900,0.0040) and P5(0.2136,0) considering $\Delta f = 1$ Hz [MATLAB].

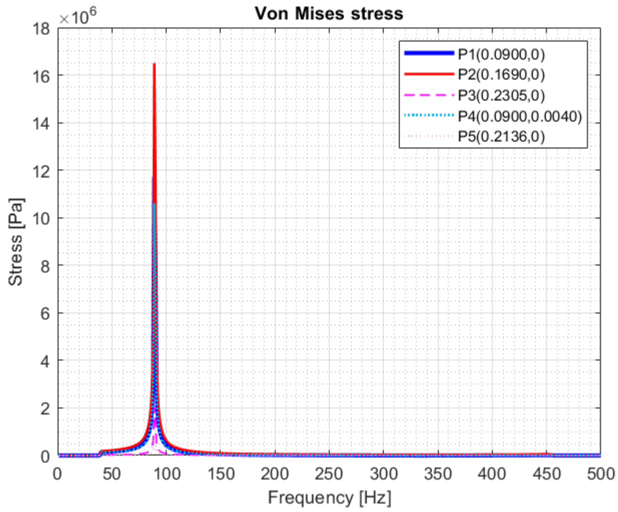

FIGURE C.282: Von Mises stress in the frequency domain obtained for a random vibration considering $\Delta f = 1$ Hz [MATLAB].

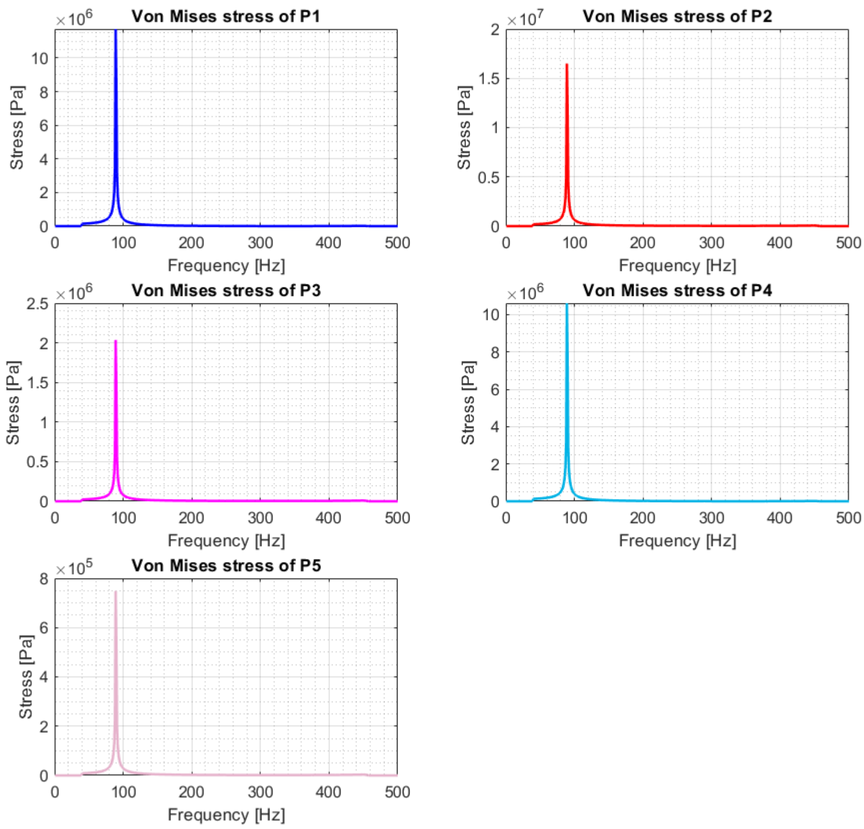

FIGURE C.283: Von Mises stress versus frequency obtained for a random vibration measured in five points: P1 (0.0900,0), P2(0.1690,0), P3(0.2305,0), P4(0.0900,0.0040) and P5(0.2136,0) considering $\Delta f = 1$ Hz [MATLAB].

Figure C.284 shows the displacements distribution in the z-direction along the sensor obtained when the frequency is equal to 90 Hz, when the maximum displacement takes place. In contrast with what happened to the quasi-static test, the maximum displacement is located on $(0.2034, 0.0005, 0)$ m with a value of $1.03 \cdot 10^{-3}$ m. Furthermore, figure C.285 presents the Von Mises stress distribution plotted along the mesh of the sensor. The maximum Von Mises stress is located on the coordinates $(0.2034, 0.0003, 0)$ m with a value of $4.59 \cdot 10^{7}$ Pa.

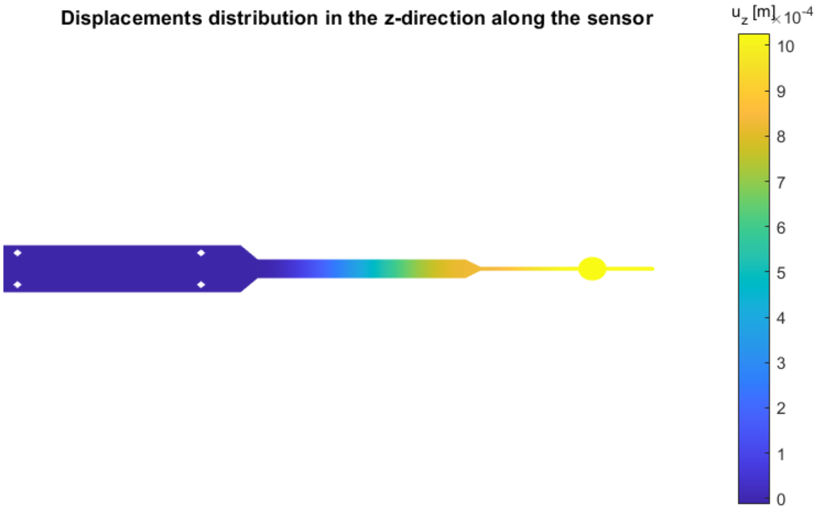

FIGURE C.284: Displacement distribution in the z-direction along the sensor when the frequency is equal to 90 Hz [MATLAB].

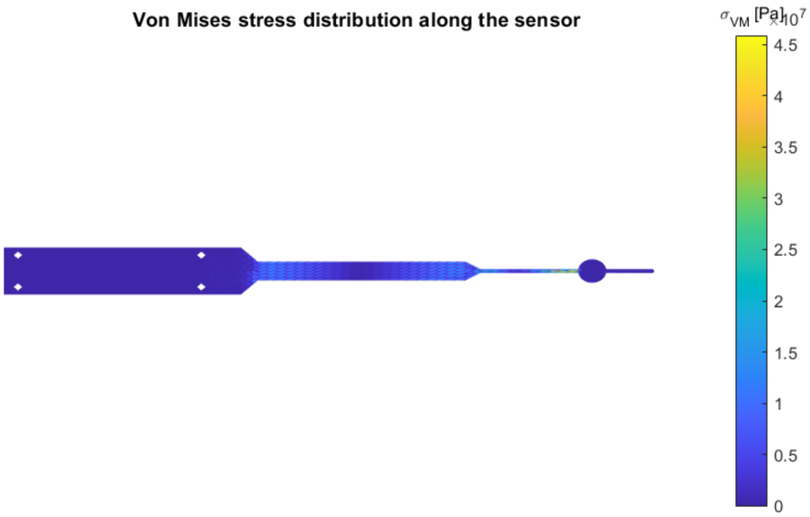

FIGURE C.285: Von Mises stress distribution along the sensor when the frequency is equal to 90 Hz [MATLAB].

C.11.2 Second model definition

In order to verify that the reason why the Von Mises stress is so much higher in P_2 than the rest of the points chosen, there will be performed again the quasi-static and the random vibration test but considering that the sphere is made of PCB as well.

Material

- Material of the structure: PCB.
  - Young's modulus, E = 22 GPa.
  - Poisson's ratio, $\nu = 0.15$.
  - Mass density, $\rho = 1900\ kg/m^3$.
  - Ultimate tensile strength, σ_{max} = 282 MPa.
- Material of the sphere: PCB.
  - Young's modulus, E = 22 GPa.
  - Poisson's ratio, $\nu = 0.15$.
  - Mass density, $\rho = 1900\ kg/m^3$.
  - Ultimate tensile strength, σ_{max} = 282 MPa.

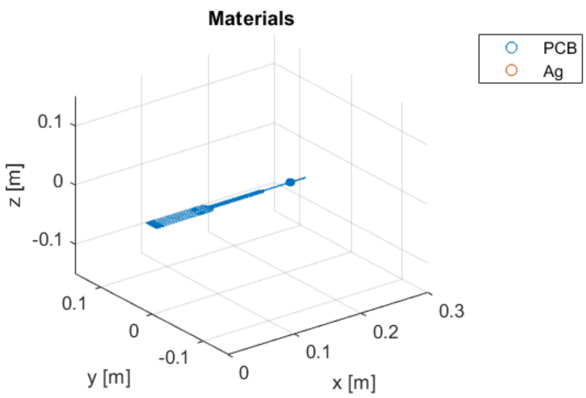

FIGURE C.286: Material distribution along the sensor [MATLAB].

C.11.2.1 Quasi-Static Test

First, the quasi-static test has been performed to the sensor. As what happened to the results obtained for the previous sensor model made of silver and PCB, the new model presents the maximum displacement in the z-direction and rotations in both, x and y-direction, when the frequency is equal to 70 Hz.

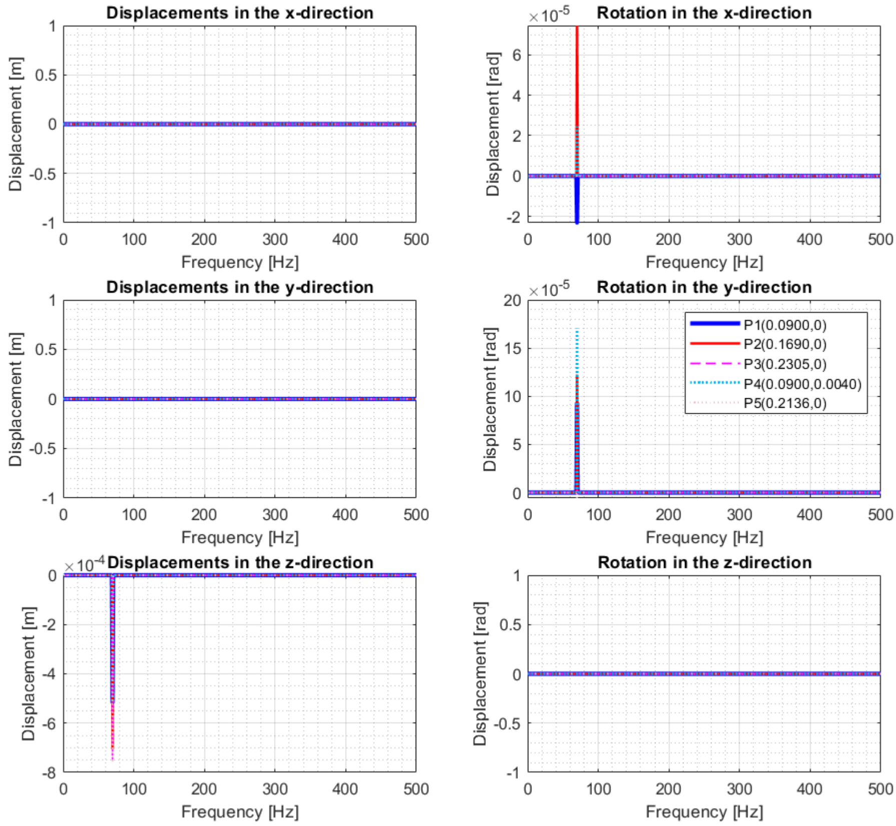

FIGURE C.287: Displacements in the frequency domain obtained for an harmonic acceleration [MATLAB].

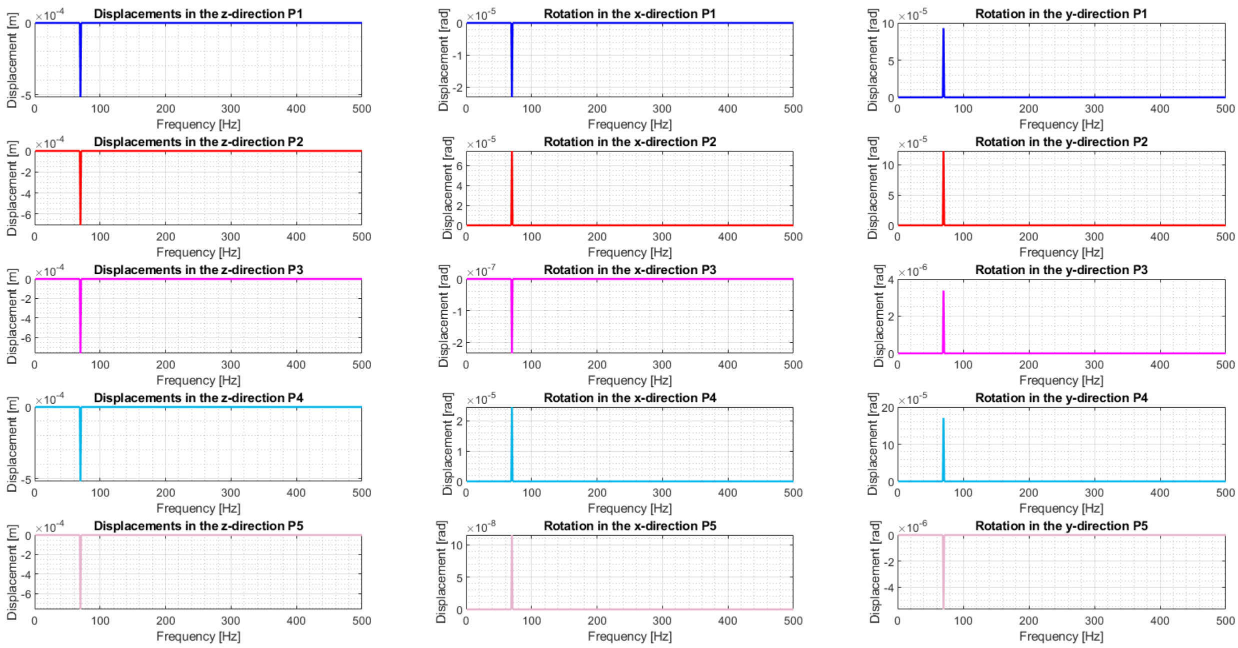

FIGURE C.288: Displacements versus frequency obtained for an harmonic acceleration measured in five points: P1 (0.0900,0), P2(0.1690,0), P3(0.2305,0), P4(0.0900,0.0040) and P5(0.2136,0) [MATLAB].

Figure C.288 shows the displacements distribution obtained for the five points chosen in figure C.270. Furthermore, figure C.289 presents the Von Mises stress distribution versus the frequency obtained when a quasi-static test is performed to the sensor. As expected, the Von Mises stress is maximum when the frequency is equal to 70 Hz and, as what happened to the first model evaluated, P_2 results to be the point at which the stress is maximum in comparison with the rest of the points chosen. However, its magnitude is much lower than the one obtained on the first study.

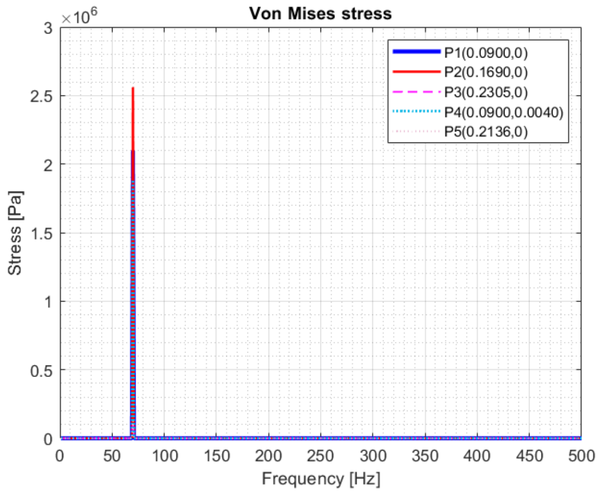

FIGURE C.289: Von Mises stress in the frequency domain obtained for an harmonic acceleration [MATLAB].

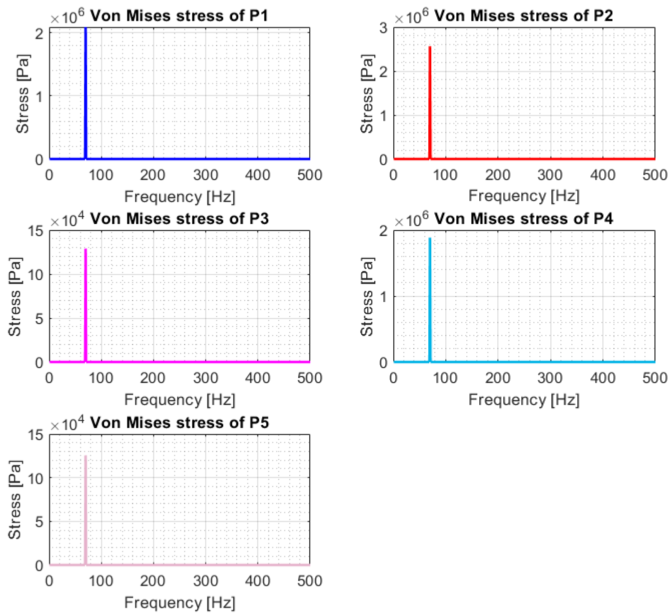

FIGURE C.290: Von Mises stress versus frequency obtained for an harmonic acceleration measured in five points: P1 (0.0900,0), P2(0.1690,0), P3(0.2305,0), P4(0.0900,0.0040) and P5(0.2136,0) [MATLAB].

Figure C.291 shows the displacements distribution in the z-direction along the sensor for the frequency of 70 Hz, frequency at which the maximum displacement takes place. As it can be seen in the figure, the maximum displacement in the z-direction appears at the nodes at which the harmonic acceleration is applied and it has a value of $-2.58 \cdot 10^{-4}$ m. Furthermore, figure C.292 presents the Von Mises stress distribution along the mesh of the sensor for the frequency of 70 Hz. The maximum Von Mises stress is located on the coordinates $(0.2034, 0.0005, 0)$ m and has a value of $4.23 \cdot 10^{6}$ Pa.

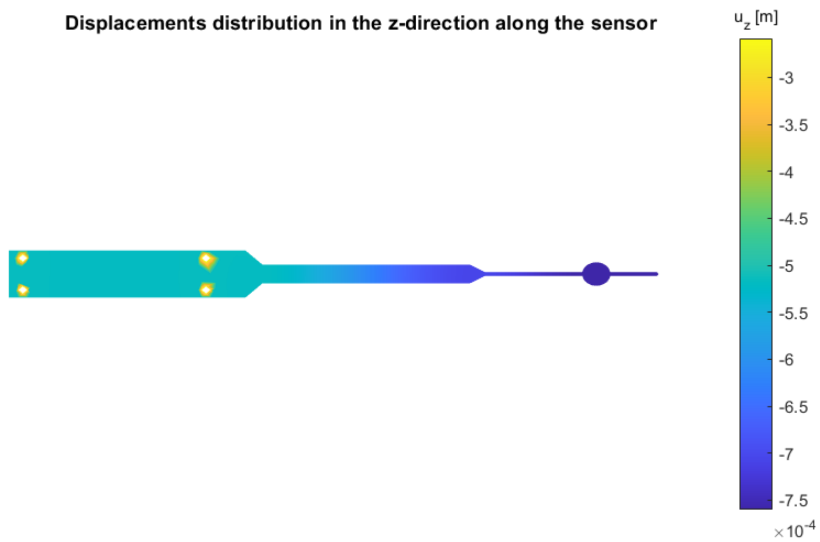

FIGURE C.291: Displacement distribution in the z-direction along the sensor when the frequency is equal to 70 Hz [MATLAB].

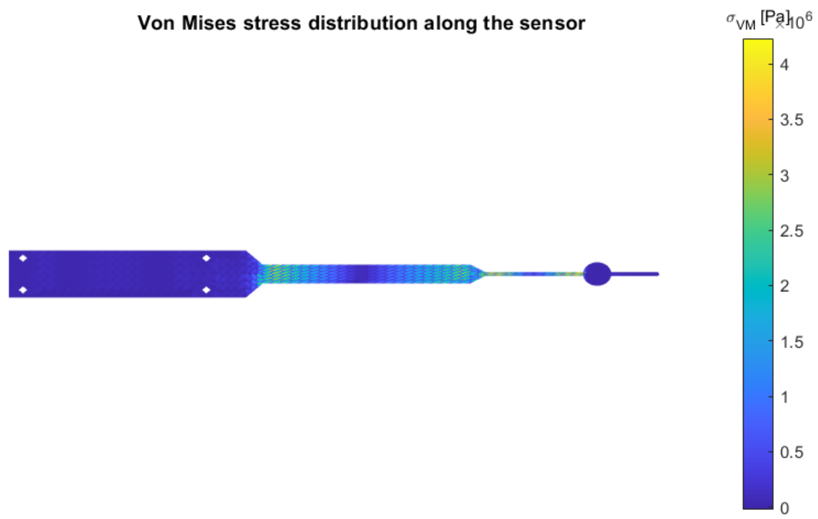

FIGURE C.292: Von Mises stress distribution along the sensor when the frequency is equal to 70 Hz [MATLAB].

C.11.2.2 Random Vibration Test

The next step was to perform the random vibration test to the second model of the sensor which is only made of PCB. Figure C.293 presents the displacements and rotations distributions versus the frequency evaluated on the five points depicted in figure C.270. Furthermore, the frequency at which the maximum displacement in the z-direction and rotations in both, x and y-direction, takes place is when the frequency is equal to 132 Hz.

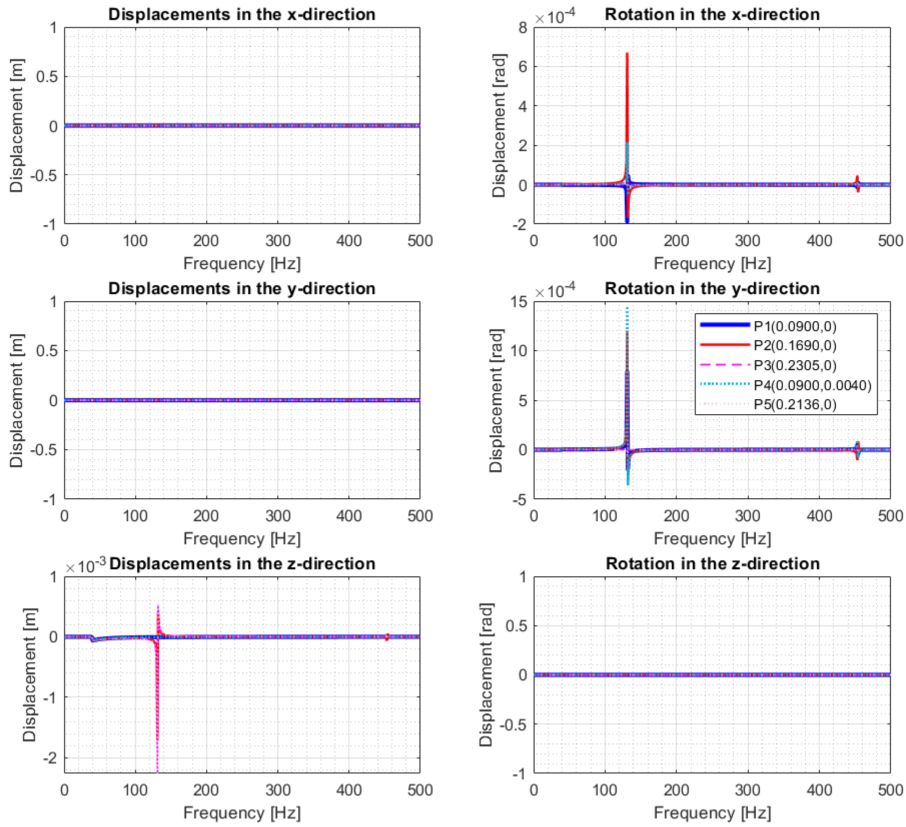

FIGURE C.293: Displacements in the frequency domain obtained for a random vibration considering $\Delta f = 1$ Hz [MATLAB].

Then, the Von Mises stress distribution along the frequency has been plotted in figure C.295 and, as what happened to the displacements distribution, the maximum Von Mises stress appears at the frequency of 132 Hz. Comparing the results obtained for the different chosen points, the maximum Von Mises stress takes place in P_2.

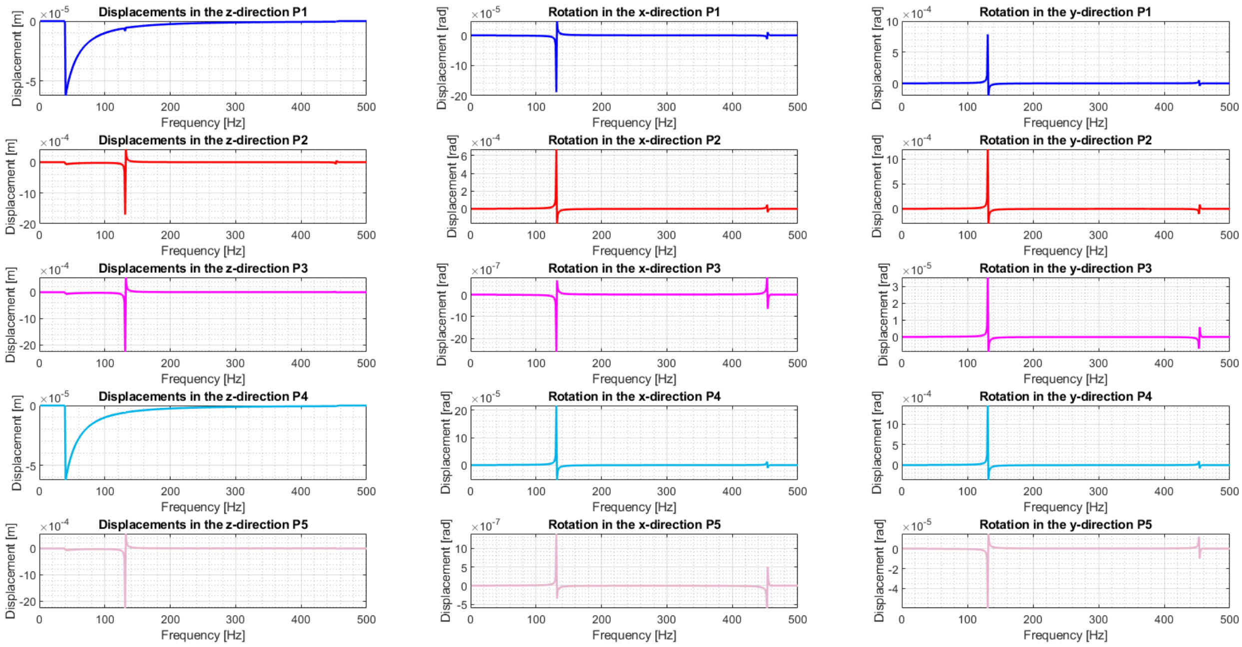

FIGURE C.294: Displacements versus frequency obtained for a random vibration measured in five points: P1 (0.0900,0), P2(0.1690,0), P3(0.2305,0), P4(0.0900,0.0040) and P5(0.2136,0) considering $\Delta f = 1$ Hz [MATLAB].

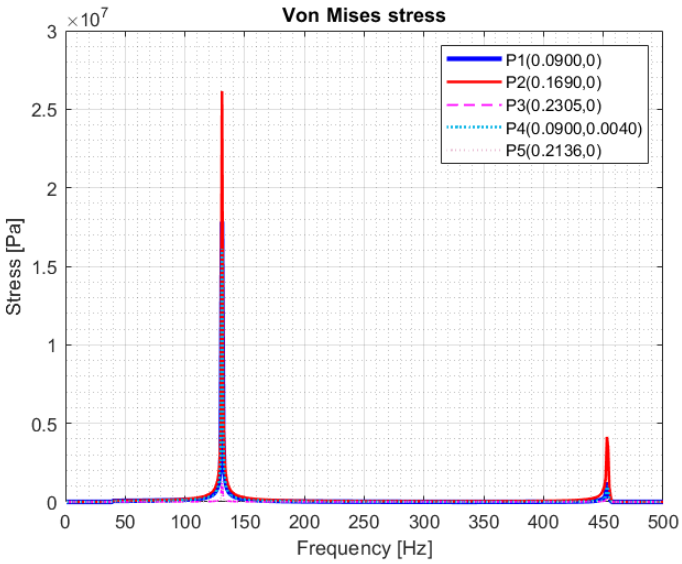

FIGURE C.295: Von Mises stress in the frequency domain obtained for a random vibration considering $\Delta f = 1$ Hz [MATLAB].

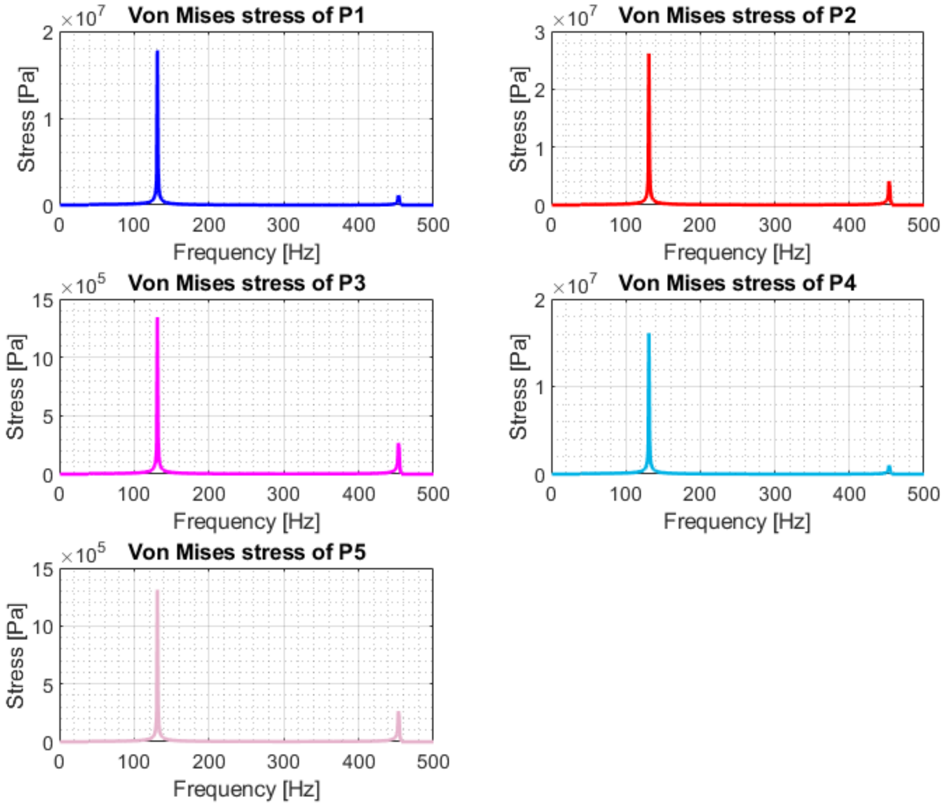

FIGURE C.296: Von Mises stress versus frequency obtained for a random vibration measured in five points: P1 (0.0900,0), P2(0.1690,0), P3(0.2305,0), P4(0.0900,0.0040) and P5(0.2136,0) considering $\Delta f = 1$ Hz [MATLAB].

Figure C.297 shows the displacements distribution in the z-direction along the sensor obtained when the frequency is equal to 132 Hz, when the maximum displacement takes place. In contrast with what happened to the quasi-static test, the maximum displacement is located on $(0.2034, 0.0005, 0)$ m with a value of $5.59 \cdot 10^{-4}$ m. Furthermore, figure C.298 presents the Von Mises stress distribution plotted along the deformed mesh of the sensor. The maximum Von Mises stress is located on the coordinates $(0.2034, 0.0005, 0)$ m with a value of $1.10 \cdot 10^{7}$ Pa.

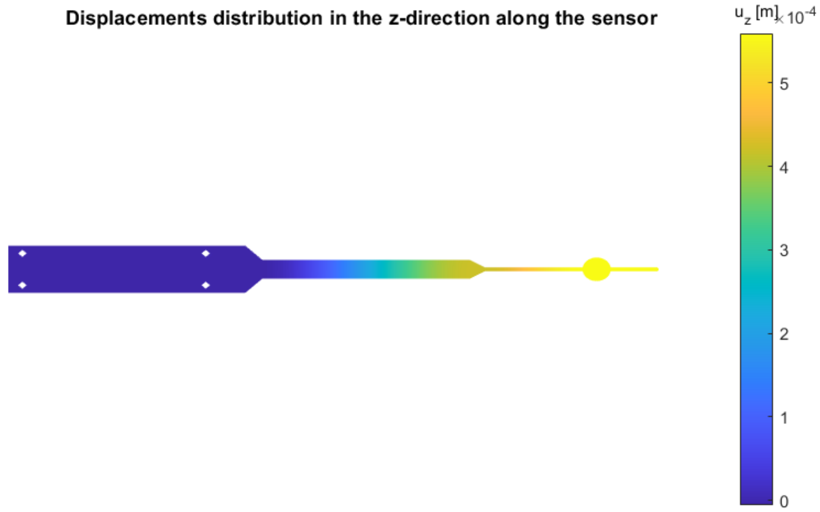

FIGURE C.297: Displacement distribution in the z-direction along the sensor when the frequency is equal to 132 Hz [MATLAB].

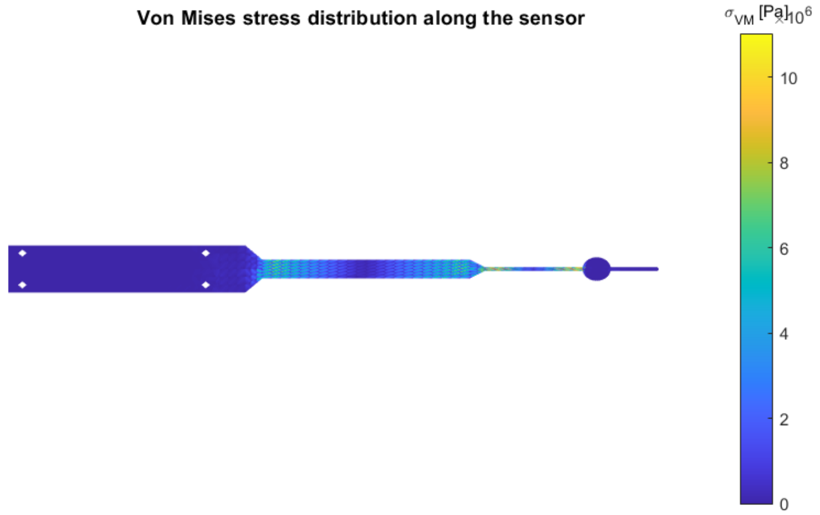

FIGURE C.298: Von Mises stress distribution along the sensor when the frequency is equal to 132 Hz [MATLAB].

C.11.3 Summary of the results obtained

Finally, all the results obtained during the report have been summarised in the following table. It can be concluded that, the stresses at which the sensor is submitted are higher on the first model than on the second one. This happens due to the change on the material of the sphere. In the first case, the sphere was made of silver which is denser than PCB. This fact lead to the nodes of the PCB structure located nearby the sphere to suffer higher stresses. Moreover, the change in the weight of the sphere also lead to a a difference in the magnitude of the z-direction displacement. The denser material used, the more displacement is obtained when performing a vibration test of any type.

Table C.15: Summary of the results obtained for the two models of the sensor.

	Model 1	**Model 2**
Material	PCB and Ag	PCB
Quasi-static Test		
$f_{u_{z\ max}}$ [Hz]	70	70
$X_{u_{z\ max}}$ [m]	Nodes of the holes	Nodes of the holes
$u_{z\ max}$ [m]	$-2.58 \cdot 10^{-4}$	$-2.58 \cdot 10^{-4}$
$X_{\sigma_{max}}$ [m]	$(0.2034, 0.0003, 0)$	$(0.2034, 0.0005, 0)$
σ_{max} [Pa]	$3.78 \cdot 10^{7}$	$4.23 \cdot 10^{6}$
Random Vibration Test		
$f_{u_{z\ max}}$ [Hz]	90	132
$X_{u_{z\ max}}$ [m]	$(0.2034, 0.0005, 0)$	$(0.2034, 0.0005, 0)$
$u_{z\ max}$ [m]	$1.03 \cdot 10^{-3}$	$5.59 \cdot 10^{-4}$
$X_{\sigma_{max}}$ [m]	$(0.2034, 0.0003, 0)$	$(0.2034, 0.0005, 0)$
σ_{max} [Pa]	$4.59 \cdot 10^{7}$	$1.10 \cdot 10^{7}$

C.12 Report 12: Random Test without the sensor

The aim of this report is to calculate the displacements and the Von Mises stress distribution along the sensor when the sphere of the sensor disappears under a random vibration test boundary conditions. In order to do so, the sphere will present a density of $\rho = 1\ kg/m^3$.

C.12.1 Model definition

Boundary Conditions

- An acceleration is applied on the nodes located in the holes of the sensor.
- To be more time-efficient, $u_x = u_y = \theta_z = 0$.

Material

- Material of the structure: PCB.
  - Young's modulus, E = 22 GPa.
  - Poisson's ratio, ν = 0.15.
  - Mass density, $\rho = 1900\ kg/m^3$.
  - Ultimate tensile strength, σ_{max} = 282 MPa.
- Material of the sphere: Silver (Ag). In this report the density of this material will be $\rho = 1\ kg/m^3$ in order to make the sphere disappear.
  - Young's modulus, E = 76 GPa.
  - Poisson's ratio, ν = 0.37.
  - Mass density, $\rho = 1\ kg/m^3$.
  - Ultimate tensile strength, σ_{max} = 140 MPa.

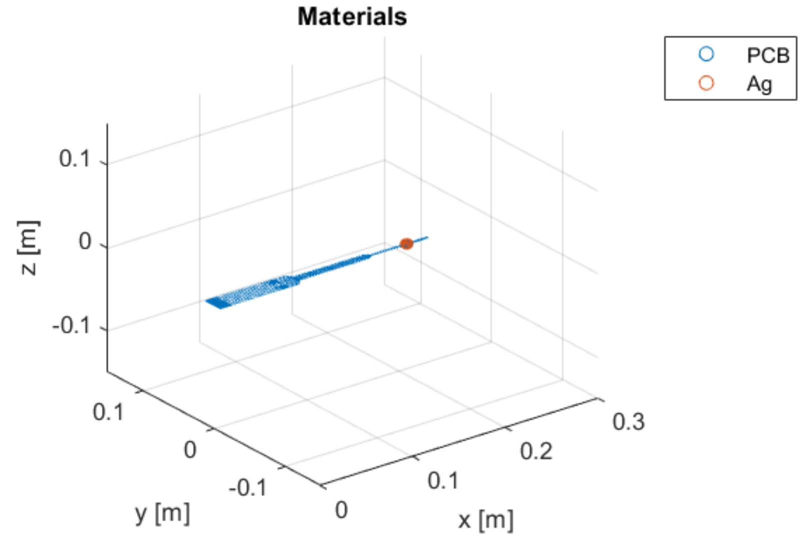

FIGURE C.299: Material distribution along the sensor [MATLAB].

Mesh

The mesh has been created with COMSOL and is depicted in figure C.300. Moreover, the mesh has a maximum length per element of 0.0013 m and it is composed by a total of 3322 4-noded-quadrilateral elements.

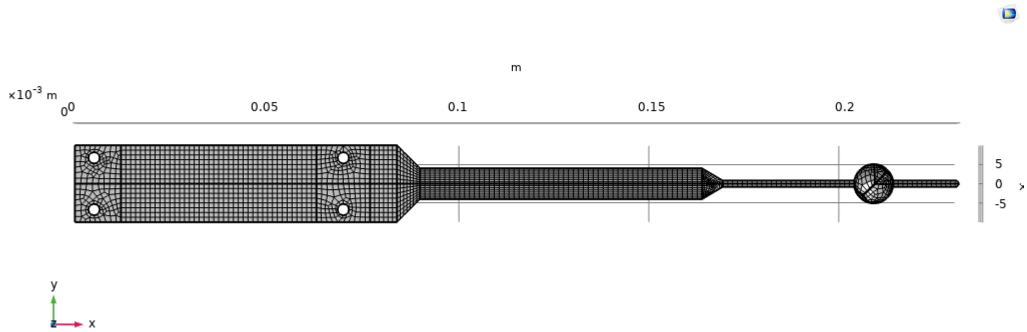

FIGURE C.300: Sensor's structured mesh composed by 3322 quadrilateral elements [COMSOL].

C.12.2 Modal Analysis

First, a modal analysis has been performed to the sensor in order to identify the first six natural frequencies at which the sensor will experiment resonance. Table C.16 lists the first six eigenvalues obtained considering that there is a prescribed displacement in the z-direction of the nodes located in the holes at which the sensor will be attached during the test and that $u_x = u_y = \theta_z = 0$. Furthermore, figure C.301 shows the first six vibration modes of the shell.

Table C.16: First six natural frequencies [MATLAB].

Mode	**Frequency (Hz)**
1st	86.7201
2nd	400.644
3rd	1291.98
4th	2002.65
5th	3113.76
6th	4045.82

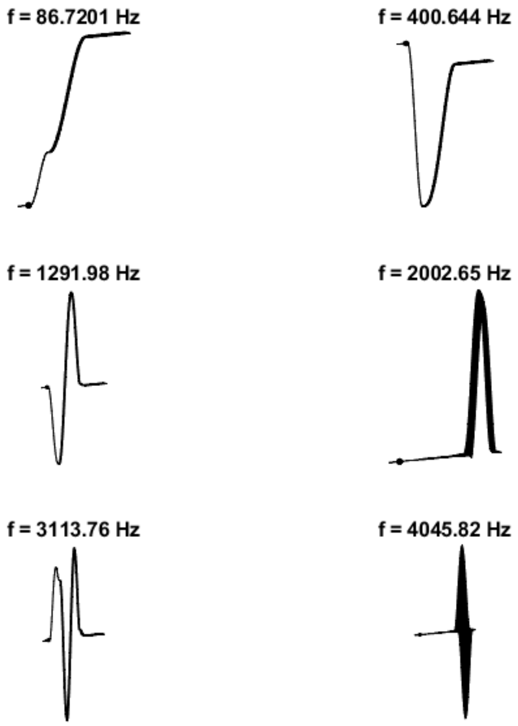

Figure C.301: First six modes and natural frequencies [MATLAB].

C.12.3 Random Vibration Test

Then, a random vibration test has been performed on the sensor. It consisted in applying a random vibration excitation to the z-direction of the nodes located in the holes of the sensor. First, the Power Spectral Density function that describes the acceleration applied is defined by the following expression

$$PSD = 6 \cdot log_{10}(freq) + 0.04 - 6 \cdot log_{10}(40) \qquad when\ freq < 40\ Hz \tag{C.106}$$

$$PSD = 0.04 \qquad when\ 40\ Hz \leq freq \leq 450\ Hz \tag{C.107}$$

$$PSD = -6 \cdot log_{10}(freq) + 0.04 + 6 \cdot log_{10}(450) \qquad when\ freq > 450\ Hz \tag{C.108}$$

Then, the acceleration has been computed from the PSD input using the equation below:

$$PSD = \frac{S^2}{\Delta freq} \quad \longrightarrow \quad S = \sqrt{PSD \cdot \Delta freq} \tag{C.109}$$

As the acceleration is now expressed in g units, it has been multiplied by 9.81 m/s^2 in order to obtain the acceleration in the international system units. Finally, the acceleration has been applied to the u_z degree of freedom of the nodes located in the holes of the sensor.

$$\{\mathbf{A}\} = \{\mathbf{A}(DOF, freq)\} \tag{C.110}$$

$$\{\mathbf{A}(I_p, :)\} = S \tag{C.111}$$

Once obtained the acceleration in the frequency domain, the displacements in the frequency domain $\{\mathbf{U}\}$ can be computed

$$\{\mathbf{U}(I_p, freq)\} = -\frac{\{\mathbf{A}(I_p, freq)\}}{(2\pi freq)^2} \tag{C.112}$$

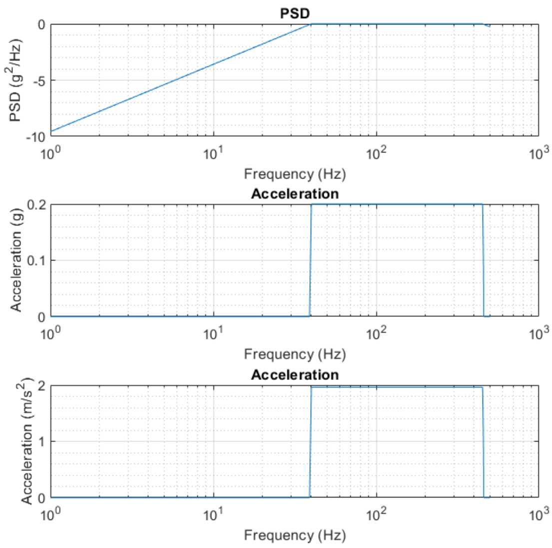

FIGURE C.302: Methodology used to compute the acceleration in the frequency domain considering a $\Delta f = 1$ Hz [MATLAB].

Figures C.303 and C.304 present the displacements and the Von Mises stress distribution along frequency respectively. In this case, when the density of the sphere is equal to $\rho = 1\ kg/m^3$, the maximum displacement takes place at the frequency of 149 Hz. As what happened to the displacements distribution, the maximum Von Mises stress also takes place when the frequency is equal to 149 Hz.

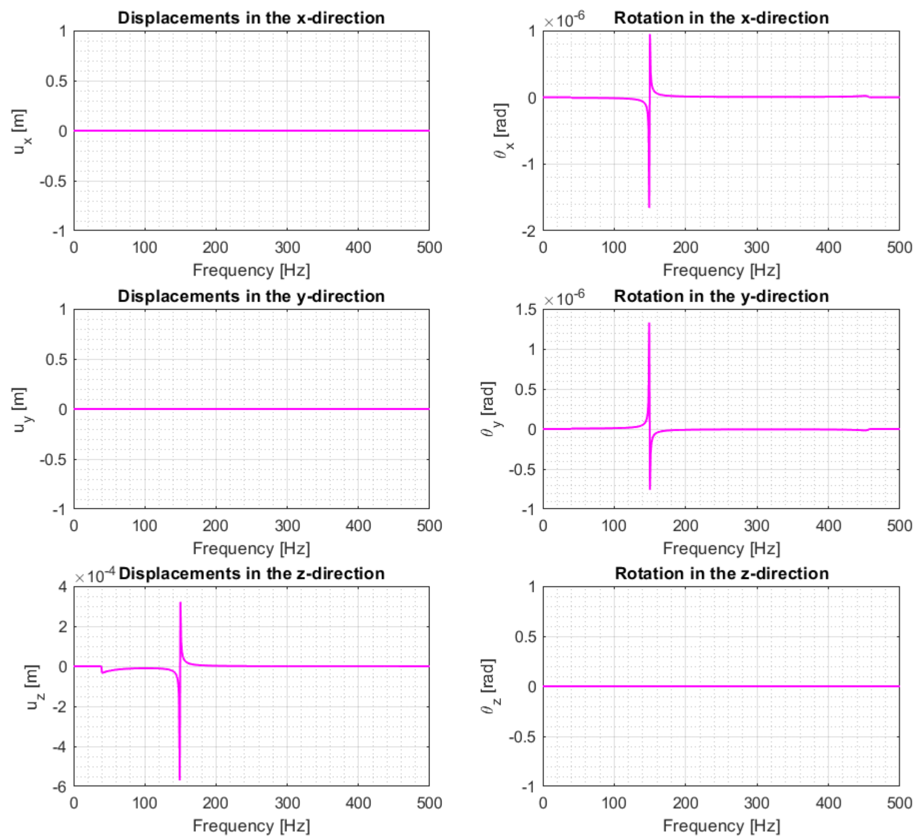

Figure C.303: Displacements in the frequency domain obtained for a random vibration considering $\Delta f = 1$ Hz [MATLAB].

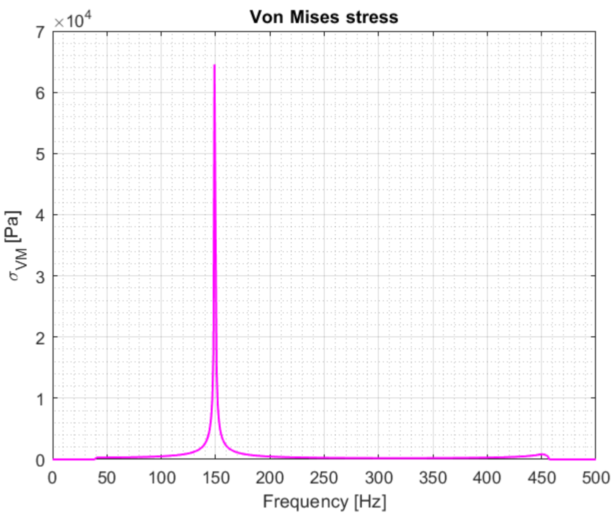

Figure C.304: Von Mises stress in the frequency domain obtained for a random vibration considering $\Delta f = 1$ Hz [MATLAB].

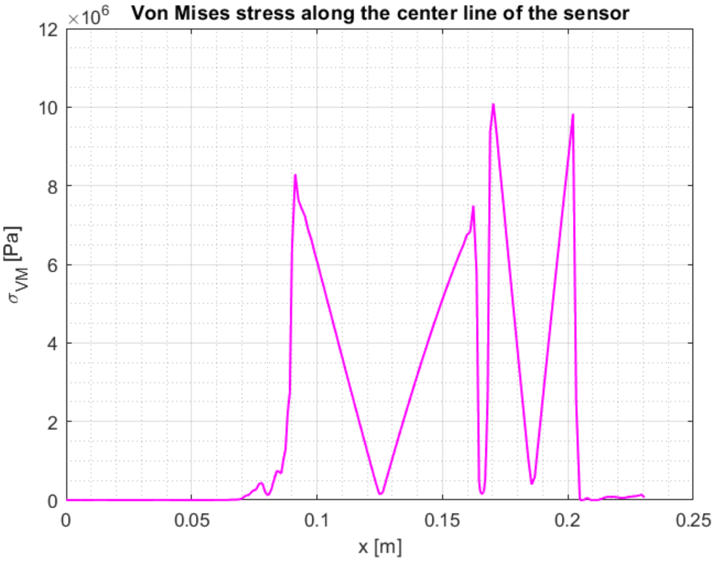

FIGURE C.305: Von Mises stress distribution along the center line of the sensor when the frequency is equal to 149 Hz and considering $\Delta f = 1$ Hz [MATLAB].

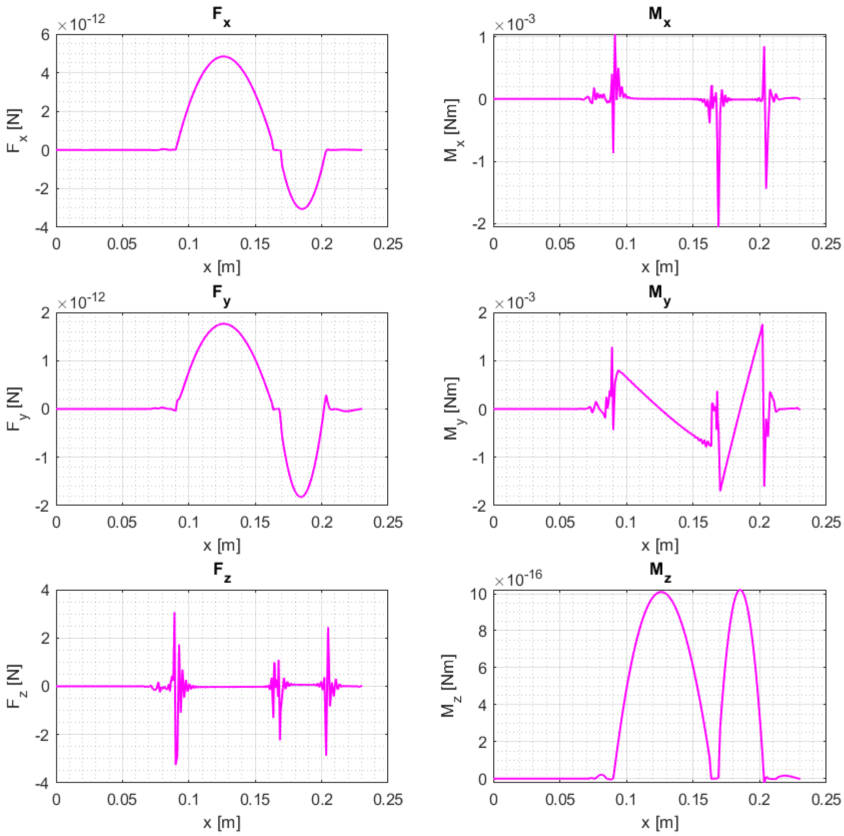

FIGURE C.306: Force and Momentum distribution along the center line of the sensor when the frequency is equal to 149 Hz and considering $\Delta f = 1$ Hz [MATLAB].

Figure C.307 shows the displacements distribution in the z-direction along the sensor obtained when the frequency is equal to 149 Hz, when the maximum displacement takes place. The maximum displacement is located on $(0.2300, -0.0008, 0)$ m with a value of $5.7076 \cdot 10^{-4}$ m. Furthermore, figure C.308 presents the Von Mises stress distribution plotted along the mesh of the sensor. The maximum Von Mises stress is located on the coordinates $(0.1703, 0, 0)$ m with a value of $1.0094 \cdot 10^{7}$ Pa.

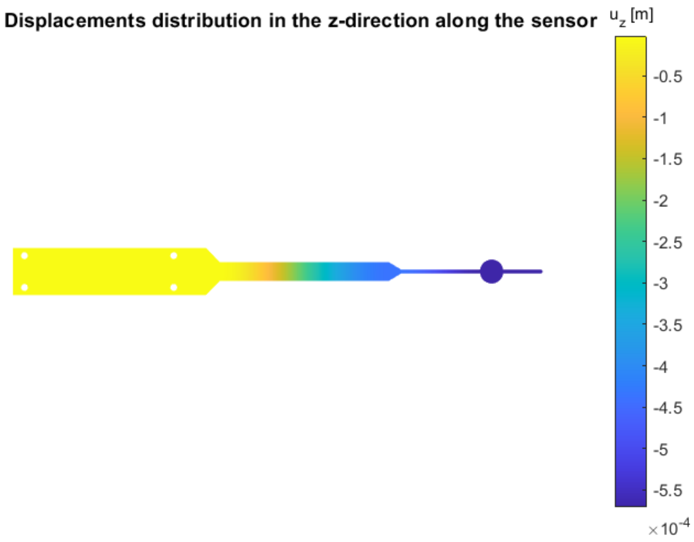

FIGURE C.307: Displacement distribution in the z-direction along the sensor when the frequency is equal to 149 Hz [MATLAB].

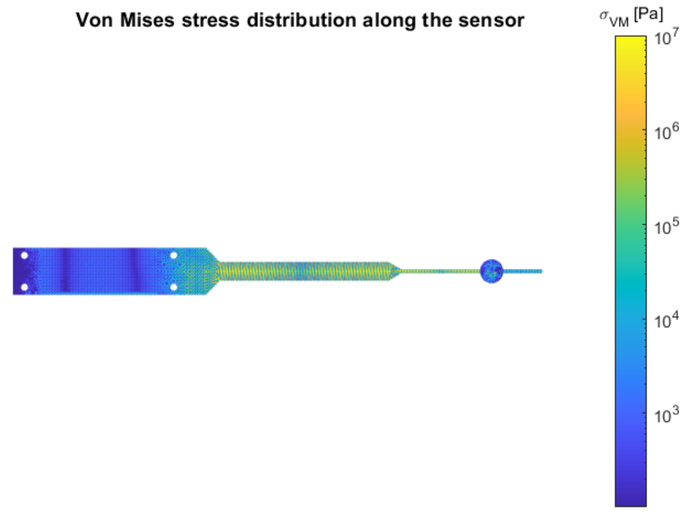

FIGURE C.308: Von Mises stress distribution along the sensor when the frequency is equal to 149 Hz [MATLAB].

Figures C.309 and C.310 present the displacements and the Von Mises stress distribution respectively along the nucleus of the PCB where the different sectors are attached.

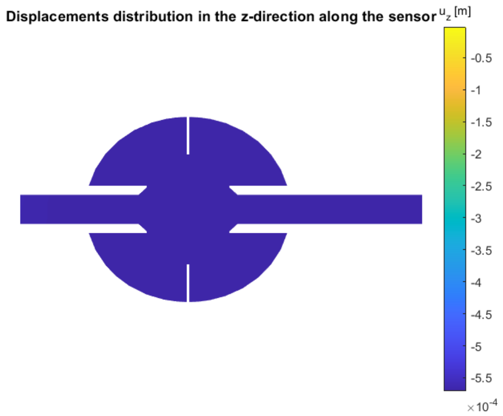

FIGURE C.309: Displacement distribution in the z-direction along the sensor when the frequency is equal to 149 Hz [MATLAB].

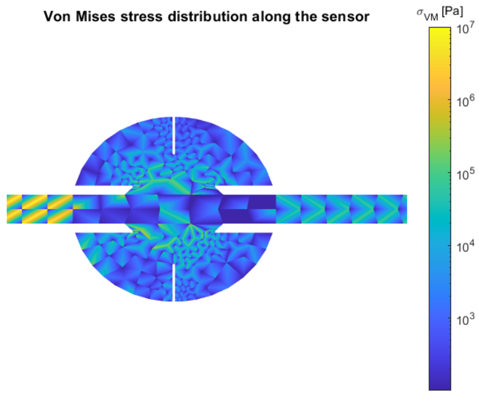

FIGURE C.310: Von Mises stress distribution along the sensor when the frequency is equal to 149 Hz [MATLAB].

Finally, the displacements distribution in the z-direction along the spherical sensor has been also plotted in figure C.311. Moreover, figure C.312 shows the Von Mises stress distribution along the spherical sensor.

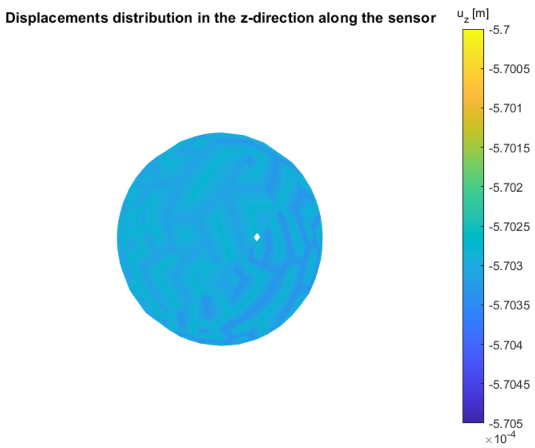

FIGURE C.311: Displacement distribution in the z-direction along the spherical sensor when the frequency is equal to 149 Hz [MATLAB].

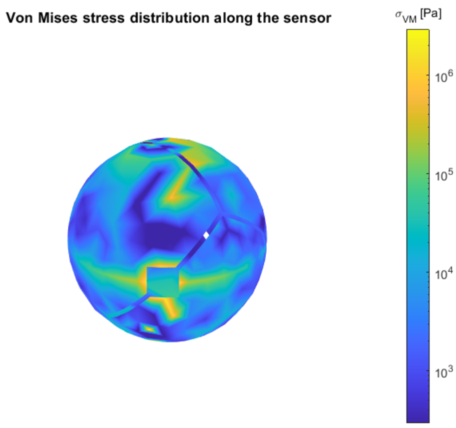

FIGURE C.312: Von Mises stress distribution along the spherical sensor when the frequency is equal to 149 Hz [MATLAB].

Finally, it can be compared the results obtained for the sensor considering the real density of the sphere (section C.11.1.3) with the ones obtained when its density is equal to 1 kg/m^3. The maximum Von Mises stress obtained in section C.11.1.3 is located on the union between the PCB and the spherical sensor and has a magnitude of $4.59 \cdot 10^7$ Pa, whereas the maximum Von Mises stress for the case studied in this report is located on the second PCB's cross section change with a value of $1.0094 \cdot 10^7$ Pa. That means that, due to the high density the sphere presents, the PCB is subjected to higher stresses.

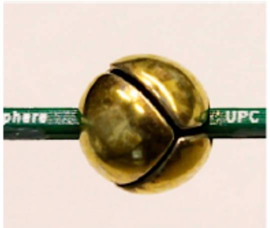

POLYTECHNIC UNIVERSITY OF CATALONIA
Structural Mechanics
Matlab and Comsol

C.13 Report 13: Approximated Quasi-static Test

The aim of this report is to perform an approximated quasi-static test to the wind sensor evaluated. In order to do so, first, a mesh convergence analysis has been carried out followed by the performance of the quasi-static test.

C.13.1 Hypothesis

It is considered to be a first approach of the test due to the fact that some assumptions have been made:

- Although the PCB is composed by a total of two thin plates with an specific silhouette and 0.8 mm thickness each, in this study, the PCB will just be composed by one thin plate. This plate will have the resulting superposed silhouette of the two plates and double thickness, 1.6 mm.
- As the MATLAB code works with really huge matrices and, for the moment, modal projection method is not implemented, it will be considered that the displacements in x and y-direction and the rotation in z-direction will be null. This hypothesis will be corrected in the final simulation presented on the main Report document. However, in the case of x and y-direction displacements, the assumption that will be equal to zero could be close to the final solution as the forces are applied on the normal direction with respect to the neutral plane of the PCB. In contrast, to assume that the rotation in the z-direction will be null can not work due to the non-geometry of the spherical sensor with respect to the xz plane. This can induce easily a torsion momentum. However, as a first approach, it has not been considered.

C.13.2 Model definition

The properties of the materials used are listed bellow. Moreover, figure C.313 depicts the material distribution along the sensor.

- Material of the structure: PCB.
  - Young's modulus, E = 22 GPa.
  - Poisson's ratio, ν = 0.15.
  - Mass density, $\rho = 1900\ kg/m^3$.
  - Ultimate tensile strength, σ_{max} = 282 MPa.
- Material of the sphere: Silver (Ag).
  - Young's modulus, E = 76 GPa.
  - Poisson's ratio, ν = 0.37.
  - Mass density, $\rho = 10497\ kg/m^3$.
  - Ultimate tensile strength, σ_{max} = 140 MPa.

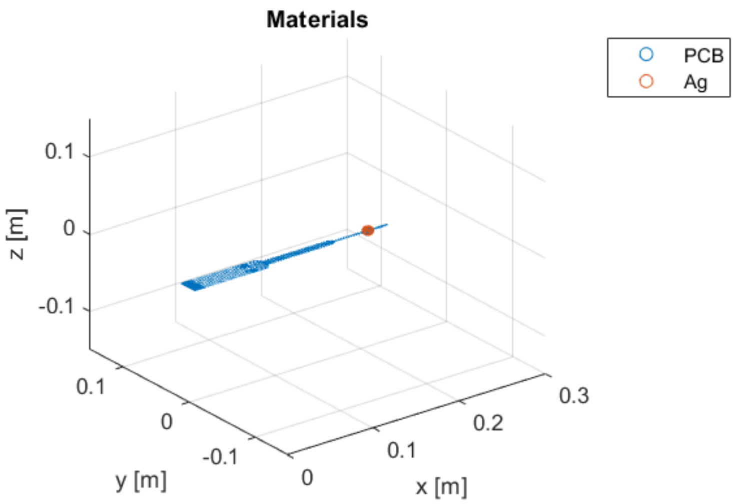

FIGURE C.313: Material distribution along the sensor [MATLAB].

C.13.3 Quasi-Static Test

The quasi-static test consists in submitting the sensor to an harmonic vibration. The harmonic acceleration has been applied on the nodes that conform the holes of the sensor and the vibration has been induced in the z-direction.

The methodology used to perform the quasi-static vibration test is shown in figure C.314. The harmonic vibration of an amplitude of 50 m/s^2 and a frequency of 70 Hz has been first computed in the time domain.

$$s = -50 \cdot \sin(2\pi 70t) \tag{C.113}$$

Then, with the use of the Fourier Transform the acceleration has been transformed from time to frequency domain.

$$S = fft(s) \tag{C.114}$$

The acceleration has been applied to the u_z degree of freedom of the nodes located in the holes of the sensor.

$$\{\ddot{\mathbf{U}}\} = \{\ddot{\mathbf{U}}(NDOF, freq)\} \tag{C.115}$$

$$\{\ddot{\mathbf{U}}(I_p, :)\} = S \tag{C.116}$$

Once obtained the acceleration in the frequency domain, the displacement in the frequency domain $\{\mathbf{U}\}$ can be computed as the following

$$\{\mathbf{U}(I_p, freq)\} = -\frac{\{\ddot{\mathbf{U}}(I_p, freq)\}}{(2\pi freq)^2} \tag{C.117}$$

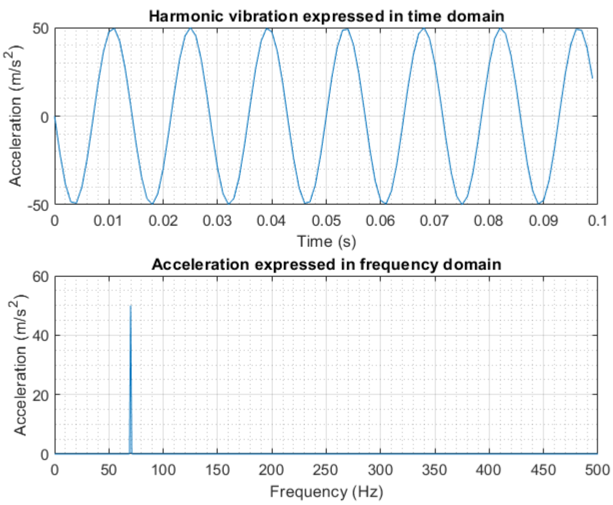

FIGURE C.314: Methodology used to compute the acceleration in the frequency domain [MATLAB].

C.13.4 Mesh Convergence

First, a mesh convergence analysis has taken place.

C.13.4.1 Meshes definition

In order to carry out a mesh convergence study, four meshes have been created.

- **Mesh 1**. Mesh 1 has a maximum length per element of 0.006 m and is composed by a total of 1014 quadrilateral elements.

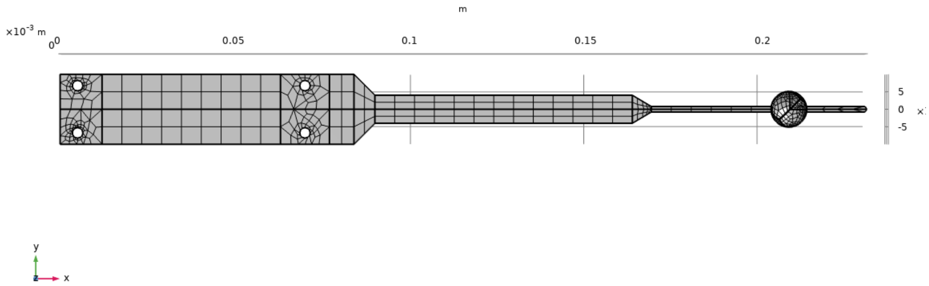

FIGURE C.315: Mesh 1 [COMSOL].

- **Mesh 2**. Mesh 2 has a maximum length per element of 0.003 m and is composed by a total of 1377 quadrilateral elements.

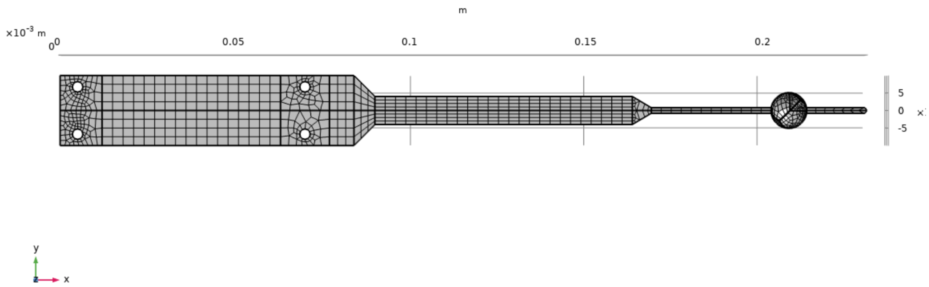

FIGURE C.316: Mesh 2 [COMSOL].

- **Mesh 3**. Mesh 3 has a maximum length per element of 0.0015 m and is composed by a total of 2491 quadrilateral elements.

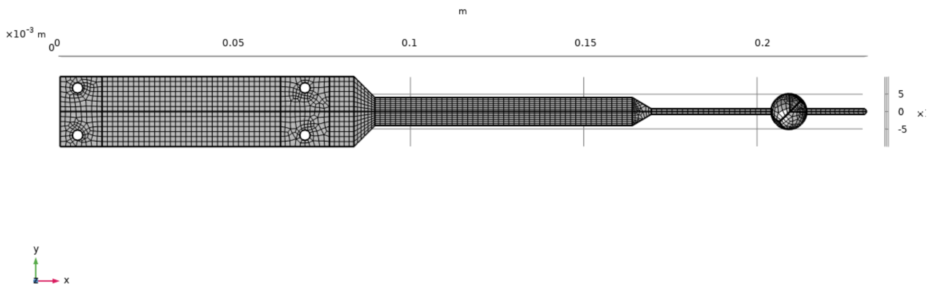

FIGURE C.317: Mesh 3 [COMSOL].

- **Mesh 4**. Mesh 4 has a maximum length per element of 0.0013 m and is composed by a total of 3322 quadrilateral elements.

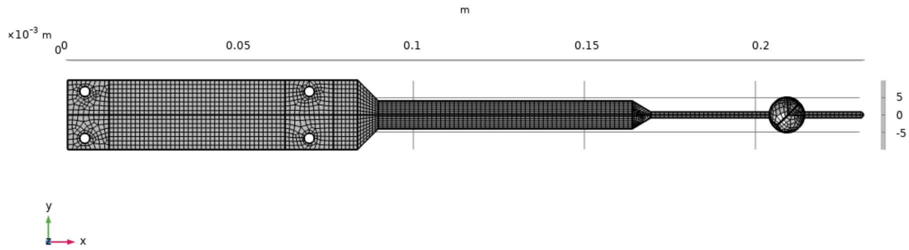

FIGURE C.318: Mesh 4 [COMSOL].

C.13.4.2 Convergence Analysis

Then, with a MATLAB program, the displacements and rotations distributions along the frequency domain for each of the four meshes evaluated have been found and can be seen in figure C.319

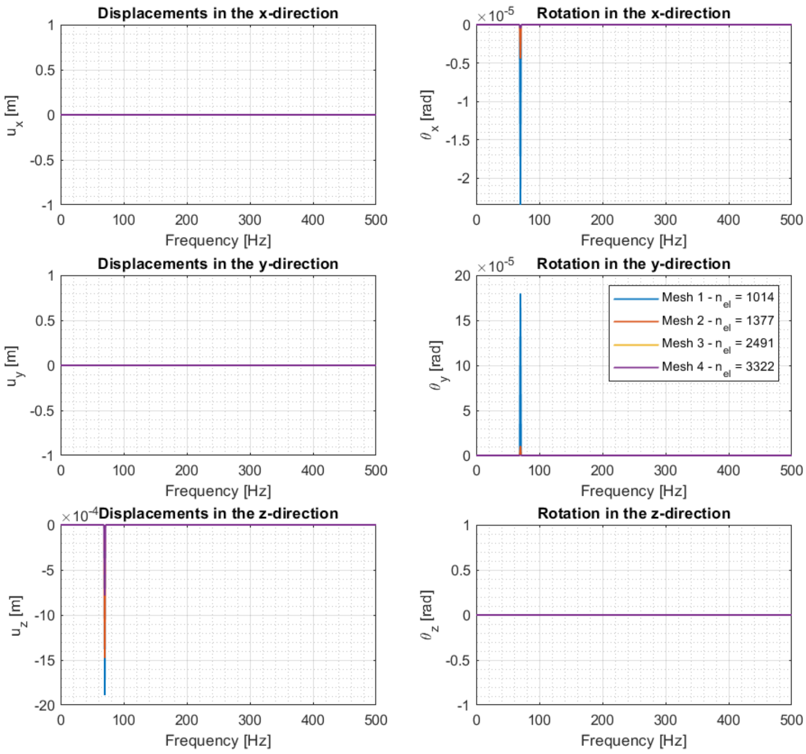

FIGURE C.319: Displacements distribution obtained on the node located in the coordinate (0.231, 0, 0) m of the sensor versus frequency when performing the quasi-static test using three different types of meshes [MATLAB].

Moreover, figure C.320 shows the Von Mises stress distribution along the frequency domain for the four meshes evaluated. As the maximum displacement and Von Mises stress is located at the frequency of 70 Hz, the displacement and the Von Mises stress distribution along the center line of the wind sensor have been also plotted in figures C.321 and C.322 for that specific frequency respectively.

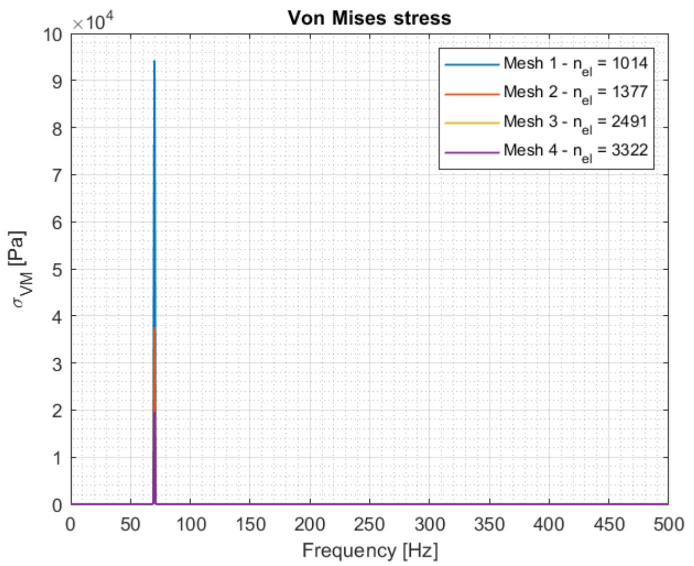

FIGURE C.320: Von Mises stress distribution obtained on the node located in the coordinate (0.231, 0, 0) m of the sensor versus frequency when performing the quasi-static test using three different types of meshes [MATLAB].

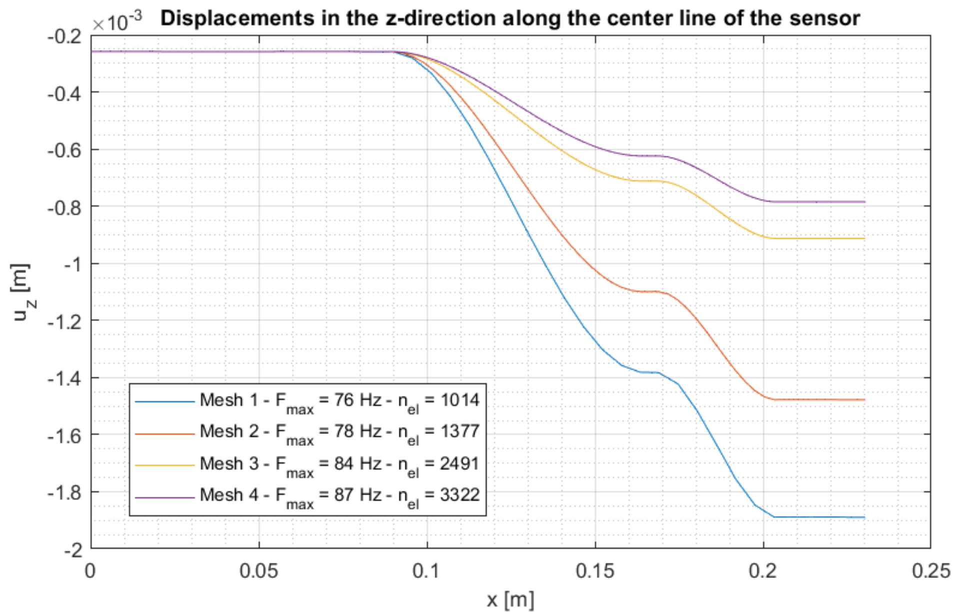

FIGURE C.321: Displacements distribution in the z-direction along the center line of the sensor when performing the quasi-static test using three different meshes [MATLAB].

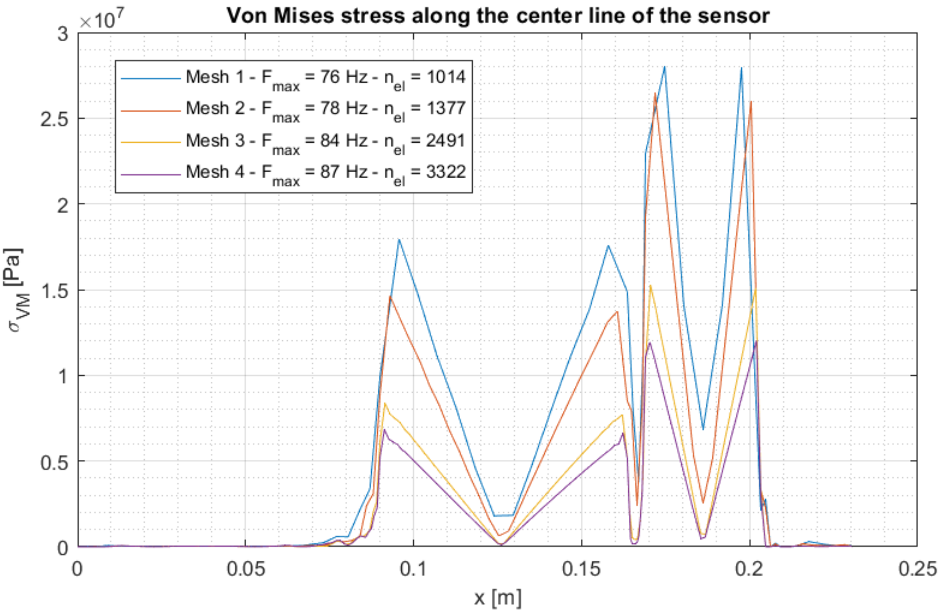

FIGURE C.322: Von Mises stress distribution along the center line of the sensor when performing the quasi-static test using three different meshes [MATLAB].

As depicted in figure C.321, the denser the mesh, the more precision is obtained in the displacements distribution. Moreover, when increasing the number of elements used, the displacement in the z-direction of the last node decreases.

As what happens to the displacements distribution along the center line of the wind sensor, the Von Mises stress distribution along the center line of the sensor depicted in figure C.322 is more accurate when increasing the number of elements used. Also, the different peaks are lower when increasing the mesh discretization.

C.13.5 Results Quasi-static Test

Then, the quasi-static test has been performed on the sensor using mesh 4. Figure C.323 shows the displacements and rotations distribution versus the frequency for the quasi-static test performed. It can be concluded that the response of an harmonic excitation is sinusoidal as well. In other words, the shape of the results obtained coincides with the Fourier Transform of a sinusoidal function. Furthermore, as depicted in figure C.323, the frequency at which the maximum displacement takes place is 70 Hz which results to be the same value as the frequency of the harmonic excitation applied.

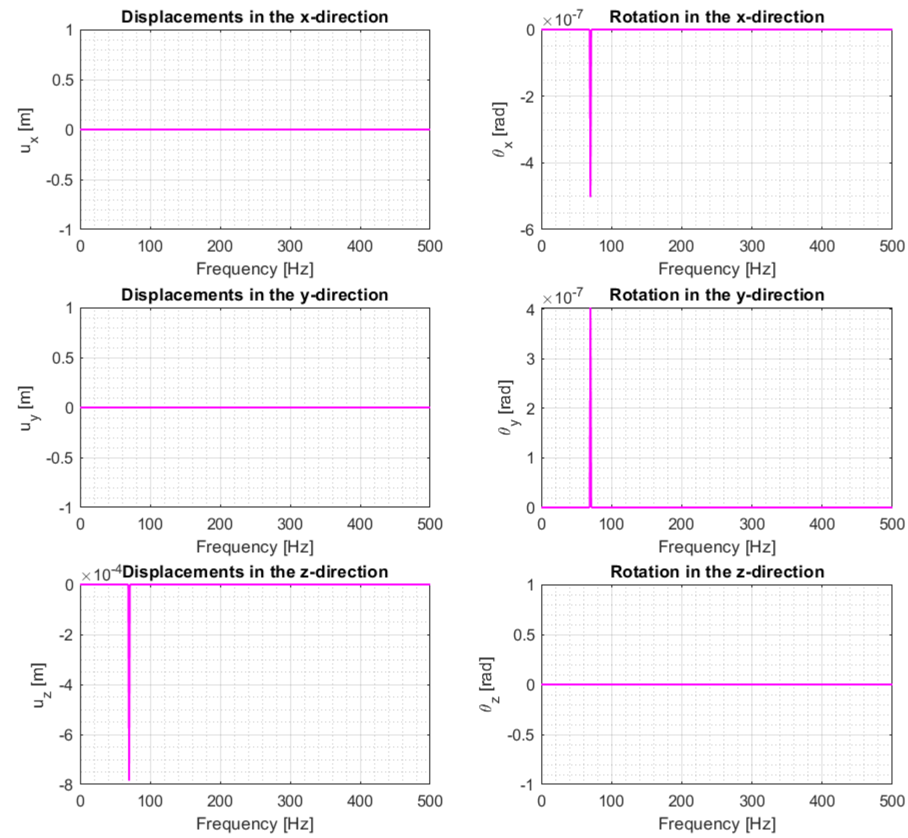

FIGURE C.323: Displacements distribution obtained on the node located in the coordinate (0.231, 0) m of the sensor versus frequency when performing the quasi-static test using Mesh 4 [MATLAB].

Figure C.324 shows the Von Mises stress distribution of the node located in the coordinate (0.231, 0, 0) m of the sensor along the frequency domain when performing the quasi-static test. As what happened to the displacements distribution, it presents a peak where the frequency is equal to 70 Hz. Moreover, figure C.325 presents the Von Mises stress distribution along the center line of the sensor for the frequency of 70 Hz, where the highest displacement and Von Mises stress take place. Considering the results shown in figure C.325, the highest Von Mises stress along the sensor will be located on the region nearby the second transversal section change. Additionally, figure C.326 depicts the forces and momentum distribution along the centre line of the wind sensor. The dominant force is clearly the shear force (F_z) perpendicular to the neutral plane of the sensor.

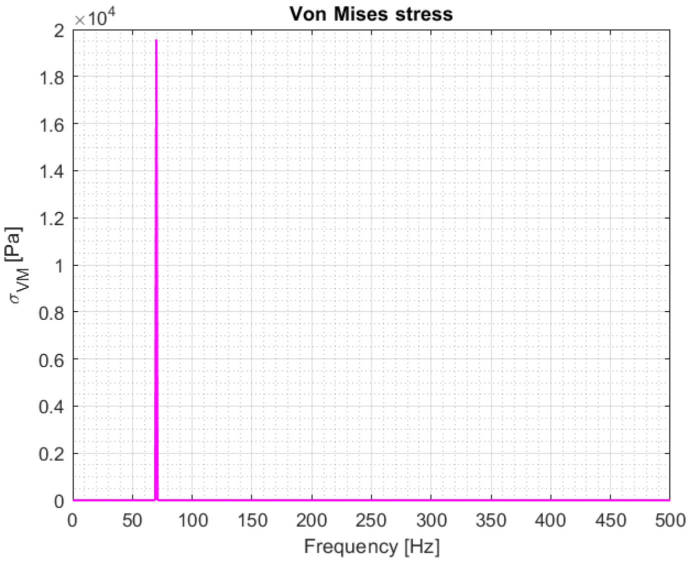

FIGURE C.324: Von Mises distribution obtained on the node located in the coordinate (0.231, 0) m of the sensor versus frequency when performing the quasi-static test using Mesh 4 [MATLAB].

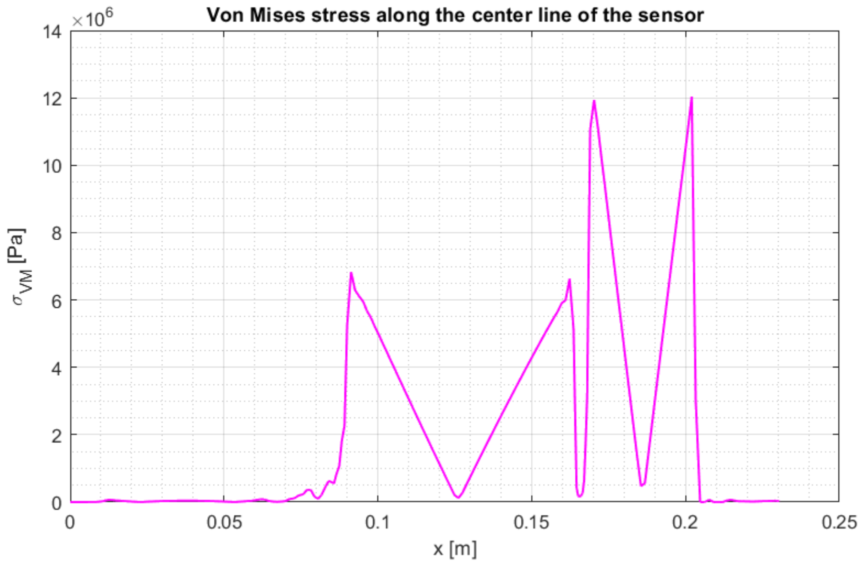

FIGURE C.325: Von Mises stress distribution along the center line of the sensor when performing the quasi-static test using mesh 4 and for the frequency of 70 Hz [MATLAB].

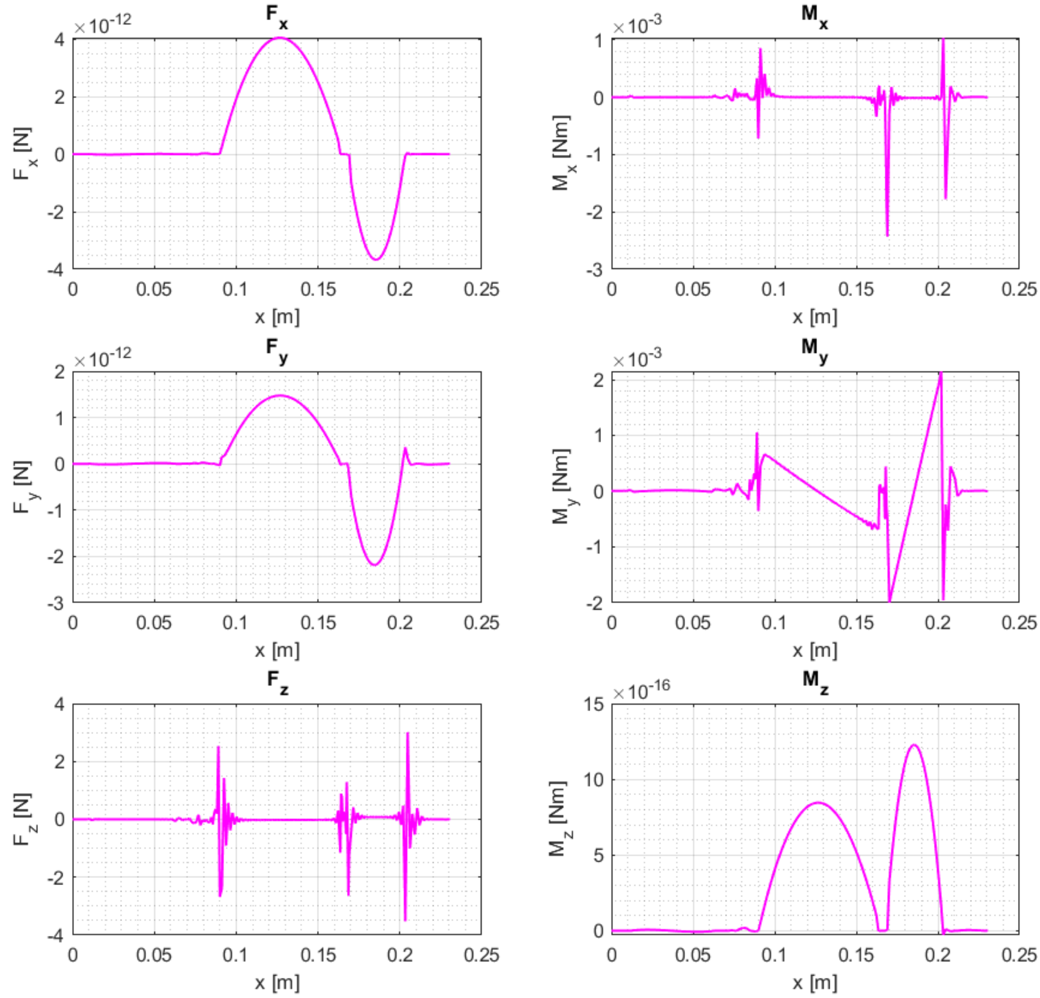

FIGURE C.326: Force and Momentum distribution obtained along the center line of the sensor when performing the quasi-static test using mesh 4 and for the frequency of 70 Hz [MATLAB].

Figure C.327 shows the displacements distribution in the z-direction along the sensor obtained when the frequency is equal to 149 Hz, when the maximum displacement takes place. The maximum displacement is located on $(0.2292, 0, 0)$ m with a value of $-7.8477 \cdot 10^{-4}$ m. Furthermore, figure C.328 presents the Von Mises stress distribution plotted along the mesh of the sensor. The maximum Von Mises stress is located on the coordinates $(0.2020, 0, 0)$ m with a value of $1.2036 \cdot 10^{7}$ Pa.

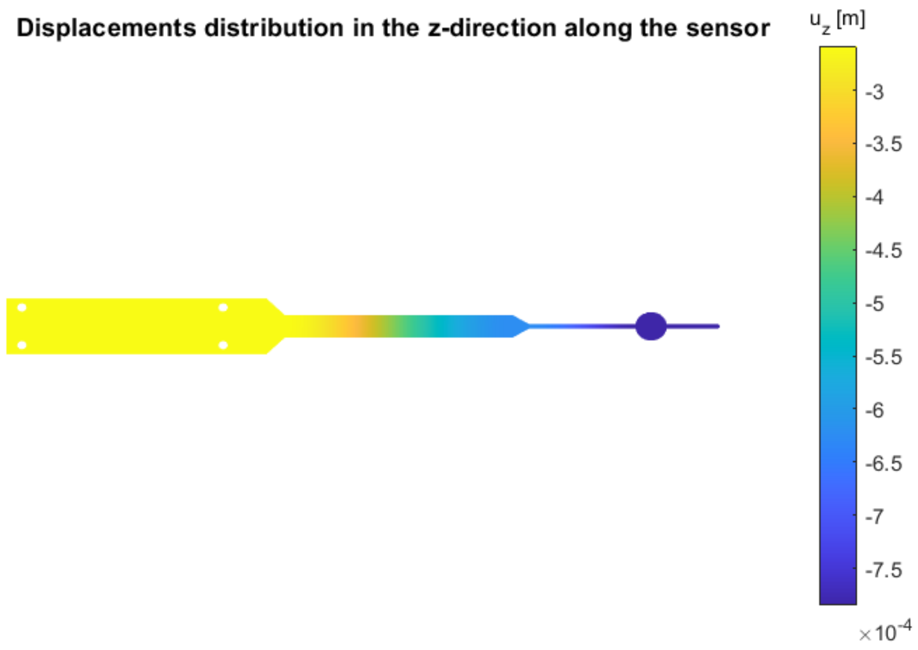

Figure C.327: Displacements distribution in the z-direction along the mesh of the sensor when performing the quasi-static test using Mesh 4 and for the frequency of 70 Hz [MATLAB].

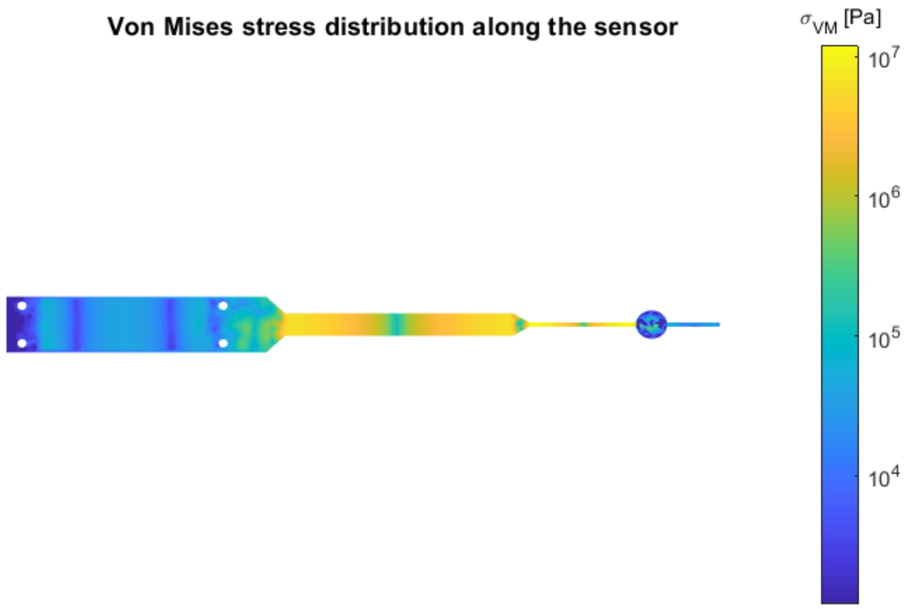

Figure C.328: Von Mises stress distribution along the mesh of the sensor when performing the quasi-static test using Mesh 4 and for the frequency of 70 Hz [MATLAB].

Figures C.329 and C.330 present the displacements and the Von Mises stress distribution respectively along the core of the PCB where the different sectors are attached. Moreover, the displacements distribution in the z-direction along the spherical sensor has been also plotted in figure C.331. Moreover, figure C.332 shows the Von Mises stress distribution along the spherical sensor.

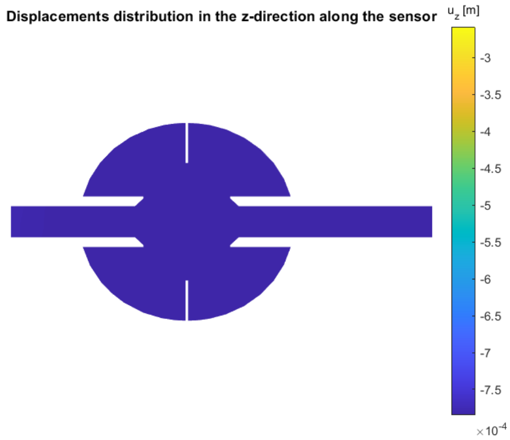

FIGURE C.329: Displacements distribution in the z-direction along the mesh of the PCB when performing the quasi-static test using Mesh 4 and for the frequency of 70 Hz [MATLAB].

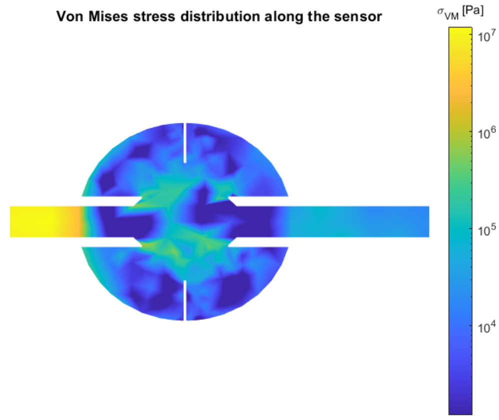

FIGURE C.330: Von Mises stress distribution along the mesh of the PCB when performing the quasi-static test using Mesh 4 and for the frequency of 70 Hz [MATLAB].

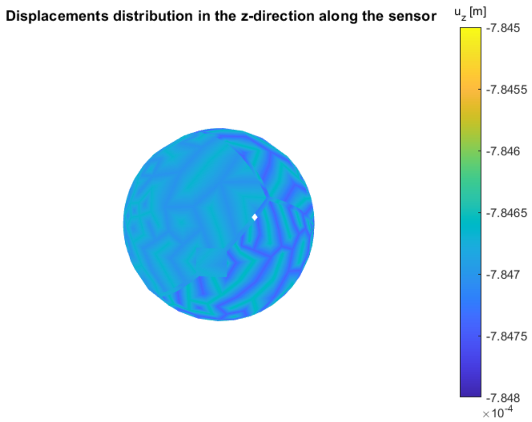

FIGURE C.331: Displacements distribution in the z-direction along the mesh of the spherical sensor when performing the quasi-static test using Mesh 4 and for the frequency of 70 Hz [MATLAB].

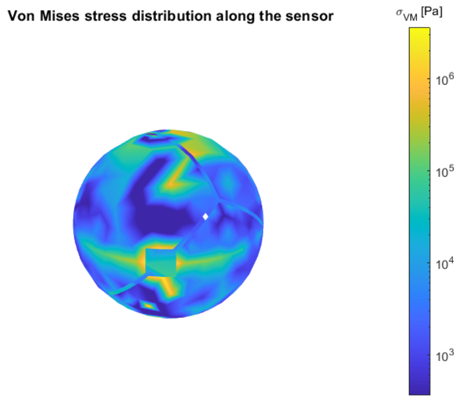

FIGURE C.332: Von Mises stress distribution along the mesh of the spherical sensor when performing the quasi-static test using Mesh 4 and for the frequency of 70 Hz [MATLAB].

C.13.6 Conclusions

Finally, the location and the magnitude of the highest displacement in the z-direction and Von Mises stress have been summarised in table C.17. As the maximum Von Mises stress is located on the PCB structure with a value of $1.2036 \cdot 10^7$ Pa and the ultimate tensile strength of the PCB is $\sigma_{max\ PCB} = 28.2 \cdot 10^7$ Pa, the wind sensor will successfully pass the quasi-static test.

TABLE C.17: Summary of the maximum displacement and Von Mises stress obtained when performing a quasi-static test for the frequency of 70 Hz [MATLAB].

	Location	**Magnitude**
Maximum z-direction displacement	(0.2292, 0, 0) m	$-7.8477 \cdot 10^{-4}$ m
Maximum Von Mises stress	(0.2020, 0, 0) m	$1.2036 \cdot 10^7$ Pa
Second Maximum Von Mises stress	(0.1703, 0, 0) m	$1.1939 \cdot 10^7$ Pa

POLYTECHNIC UNIVERSITY OF CATALONIA
Structural Mechanics
Matlab and Comsol

C.14 Report 14: Approximated Random Vibration Test

The aim of this report is to perform an approximated random vibration test to the wind sensor evaluated. In order to do so, first, a mesh convergence analysis has been carried out followed by the performance of the test.

C.14.1 Hypothesis

It is considered to be a first approach of the test due to the fact that some assumptions have been made:

- Although the PCB is composed by a total of two thin plates with an specific silhouette and 0.8 mm thickness each, in this study, the PCB will just be composed by one thin plate. This plate will have the resulting superposed silhouette of the two plates and double thickness, 1.6 mm.

- As the MATLAB code works with really huge matrices and, for the moment, modal projection method is not implemented, it will be considered that the displacements in x and y-direction and the rotation in z-direction will be null. This hypothesis will be corrected in the final simulation presented on the main Report document. However, in the case of x and y-direction displacements, the assumption that will be equal to zero could be close to the final solution as the forces are applied on the normal direction with respect to the neutral plane of the PCB. In contrast, to assume that the rotation in the z-direction will be null can not work due to the non-geometry of the spherical sensor with respect to the xz plane. This can induce easily a torsion momentum. However, as a first approach, it has not been considered.

C.14.2 Model definition

The properties of the materials used are listed bellow. Moreover, figure C.333 depicts the material distribution along the sensor.

- Material of the structure: PCB.
  - Young's modulus, E = 22 GPa.
  - Poisson's ratio, $\nu = 0.15$.
  - Mass density, $\rho = 1900\ kg/m^3$.
  - Ultimate tensile strength, $\sigma_{max} = 282$ MPa.
- Material of the sphere: Silver (Ag).
  - Young's modulus, E = 76 GPa.
  - Poisson's ratio, $\nu = 0.37$.
  - Mass density, $\rho = 10497\ kg/m^3$.
  - Ultimate tensile strength, $\sigma_{max} = 140$ MPa.

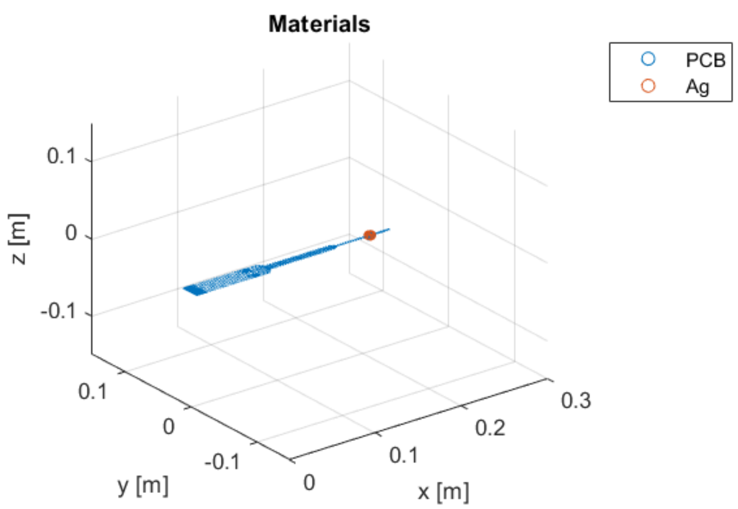

FIGURE C.333: Material distribution along the sensor [MATLAB].

C.14.3 Random Vibration Test

A random vibration test consists in applying a random vibration excitation described by a PSD function to the z-direction of the nodes located in the holes of the sensor. First, the Power Spectral Density function that describes the acceleration applied is defined by the following expression.

$$PSD = 6 \cdot log_{10}(freq) + 0.04 - 6 \cdot log_{10}(40) \qquad when\ freq < 40\ Hz \tag{C.118}$$

$$PSD = 0.04 \qquad when\ 40\ Hz \leq freq \leq 450\ Hz \tag{C.119}$$

$$PSD = -6 \cdot log_{10}(freq) + 0.04 + 6 \cdot log_{10}(450) \qquad when\ freq > 450\ Hz \tag{C.120}$$

Then, the acceleration has been computed from the PSD input using the equation below:

$$PSD = \frac{S^2}{\Delta freq} \quad \longrightarrow \quad S = \sqrt{PSD \cdot \Delta freq} \tag{C.121}$$

As the acceleration is now expressed in g units, it has been multiplied by 9.81 m/s^2 in order to obtain the acceleration in the international system units. Finally, the acceleration has been applied to the u_z degree of freedom of the nodes located in the holes of the sensor.

$$\{\ddot{\mathbf{U}}\} = \{\ddot{\mathbf{U}}(NDOF, freq)\} \tag{C.122}$$

$$\{\ddot{\mathbf{U}}(I_p, :)\} = S \tag{C.123}$$

Once obtained the acceleration in the frequency domain, the displacement in the frequency domain $\{\mathbf{U}\}$ can be computed.

$$\{\mathbf{U}(I_p, freq)\} = -\frac{\{\ddot{\mathbf{U}}(I_p, freq)\}}{(2\pi freq)^2} \tag{C.124}$$

C.14.4 Mesh Convergence

First, a mesh convergence analysis has taken place.

C.14.4.1 Meshes definition

- **Mesh 1**. Mesh 1 has a maximum length per element of 0.006 m and is composed by a total of 1014 quadrilateral elements.

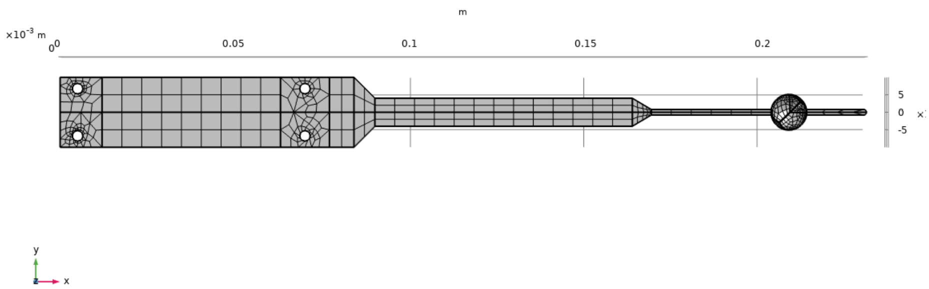

FIGURE C.334: Mesh 1 [COMSOL].

- **Mesh 2**. Mesh 2 has a maximum length per element of 0.003 m and is composed by a total of 1377 quadrilateral elements.

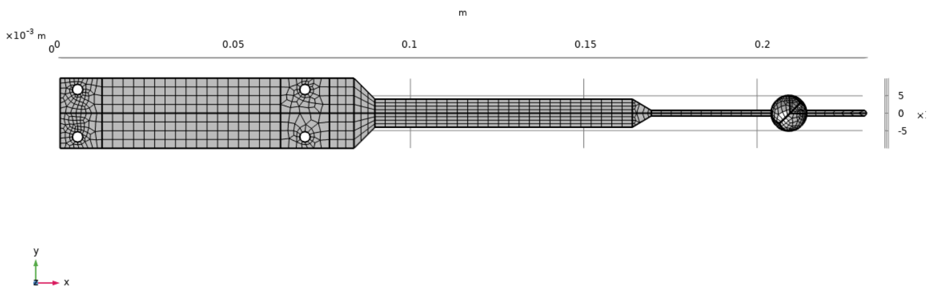

FIGURE C.335: Mesh 2 [COMSOL].

- **Mesh 3**. Mesh 3 has a maximum length per element of 0.0015 m and is composed by a total of 2491 quadrilateral elements.

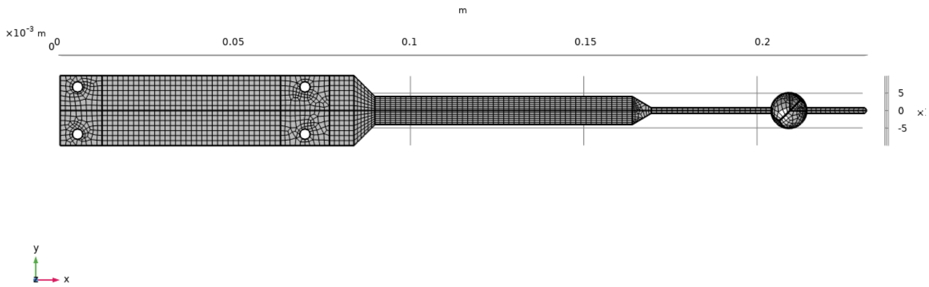

FIGURE C.336: Mesh 3 [COMSOL].

- **Mesh 4**. Mesh 4 has a maximum length per element of 0.0013 m and is composed by a total of 3322 quadrilateral elements.

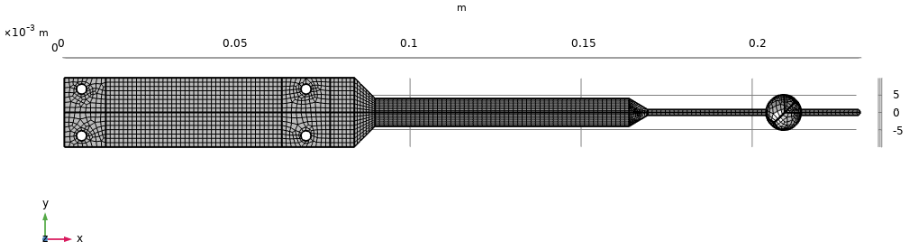

FIGURE C.337: Mesh 4 [COMSOL].

C.14.4.2 Convergence Analysis

Then, with a MATLAB program, the displacements and rotations distributions along the frequency domain for each of the four meshes evaluated have been found and can be seen in figure C.338

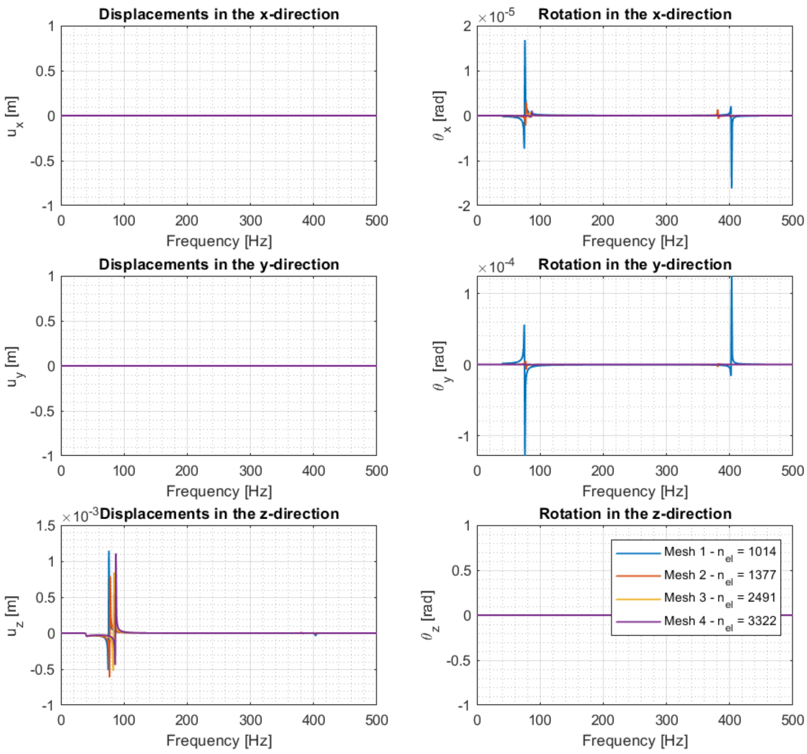

FIGURE C.338: Displacements distribution obtained on the node located in the coordinate (0.231, 0) m of the sensor versus frequency when performing the random vibration test using three different types of meshes [MATLAB].

Moreover, figure C.339 shows the Von Mises stress distribution along the frequency domain for the four meshes evaluated. As the maximum displacement and Von Mises stress varies depending on the mesh used, the displacement and the Von Mises stress distribution along the center line of the wind sensor have been also plotted in figures C.340 and C.341 for the frequency at which each mesh presents its maximum Von Mises stress.

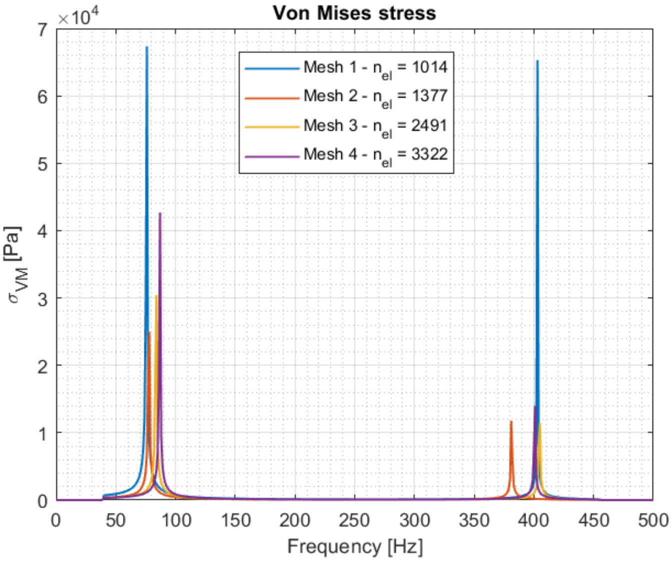

FIGURE C.339: Von Mises stress distribution obtained on the node located in the coordinate (0.231, 0) m of the sensor versus frequency when performing the random vibration test using three different types of meshes [MATLAB].

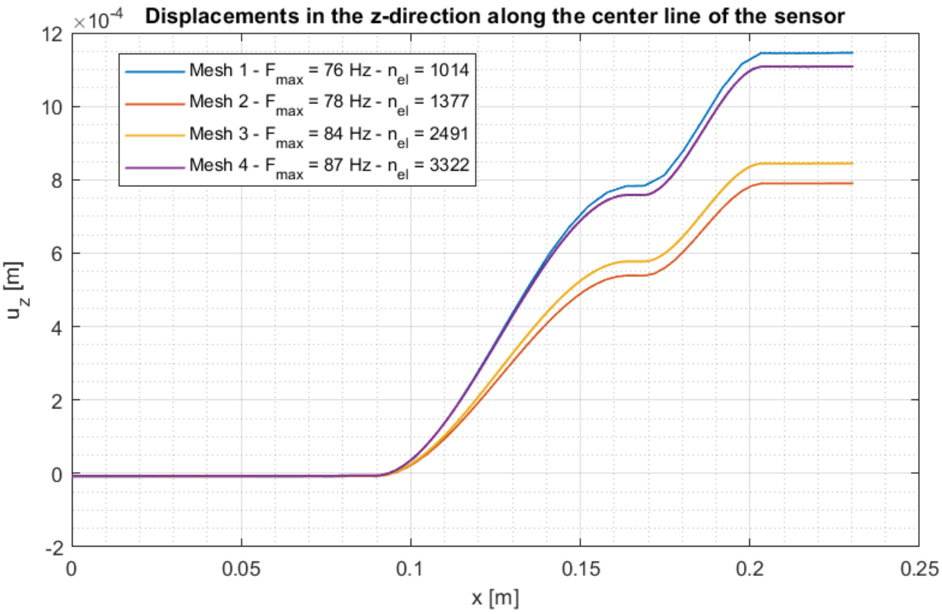

FIGURE C.340: Displacements distribution in the z-direction along the center line of the sensor when performing the random vibration test using three different meshes [MATLAB].

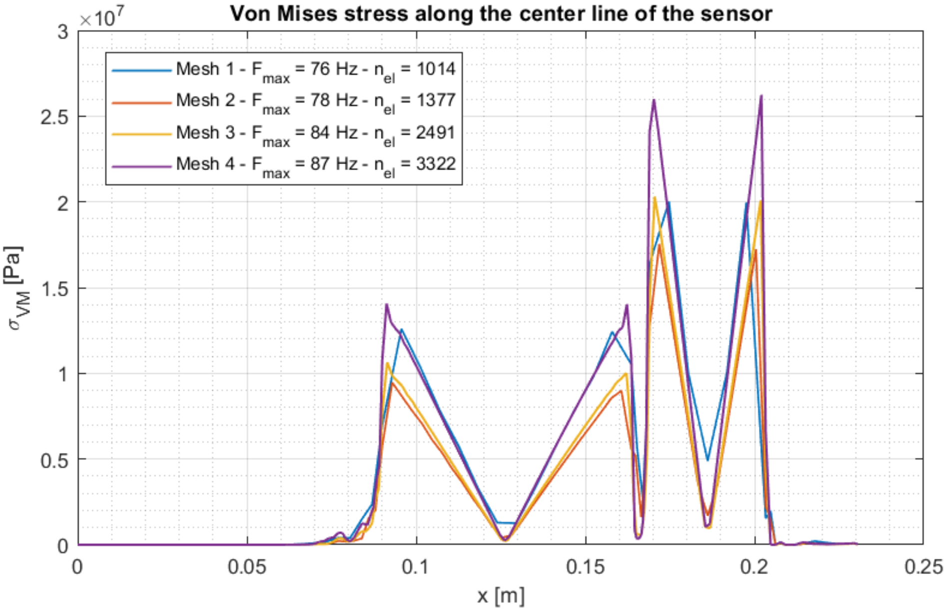

FIGURE C.341: Von Mises stress distribution along the center line of the sensor when performing the random vibration test using three different meshes [MATLAB].

As depicted in figure C.340, the displacements distribution don't presents a mesh convergence. In the case of a Random Vibration test, the results obtained depends not only on the mesh used but also on the frequency step considered.

So it has been concluded that a mesh convergence study should not be carried out with a random vibration test. In contrast, the response of a quasi-static test doesn't depend on the frequency step used and the response always appears at the same frequency. For that reason, the conclusions drawn in the previous report will be also used in this report and the sensor will be evaluated under a random vibration test using mesh 4.

C.14.5 Results Random Vibration Test

The next step is to perform the random vibration test to the wind sensor. Figure C.342 presents the displacements and rotations distribution along the frequency domain when the random vibration test is performed. The picture depicts two relative maximums at the frequencies of 87 and 402 Hz respectively. Moreover, from figure C.342 it can also be concluded that the node located at the end of the PCB is experiencing mostly a vertical displacement in the z-direction.

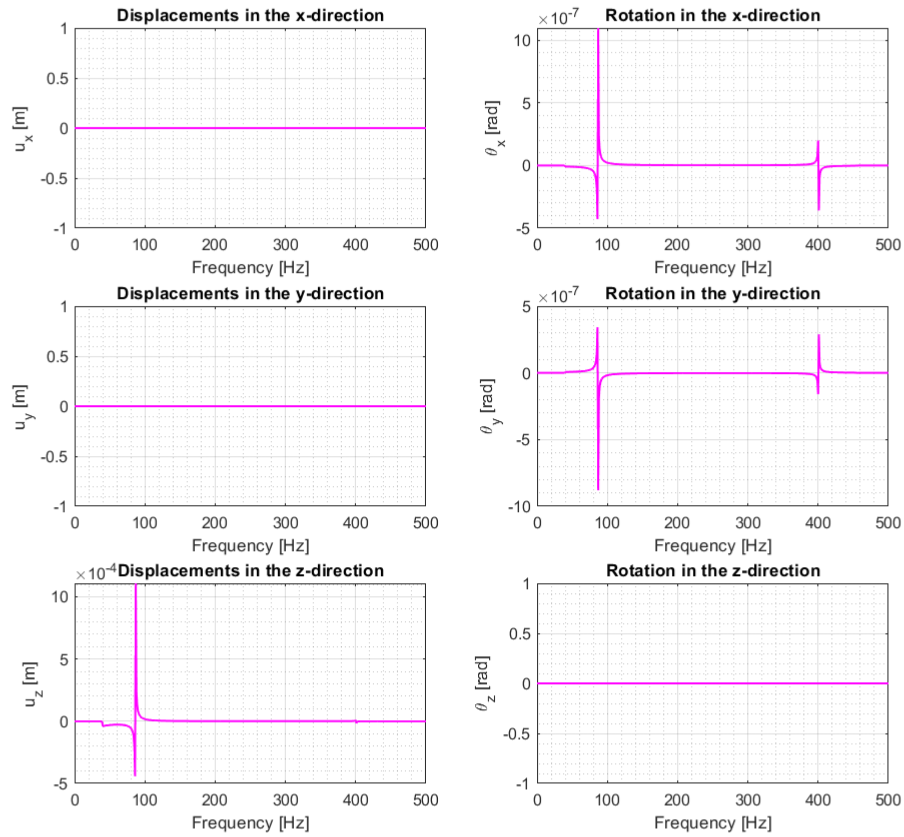

FIGURE C.342: Displacements distribution obtained on the node located in the coordinate (0.231, 0, 0) m of the sensor versus frequency when performing the random vibration test using Mesh 4 [MATLAB].

As what happens with the displacements distribution, the Von Mises stress distribution along the frequency domain also presents two peaks at the same position of the maximum displacements, as shown in figure C.343. However, as the maximum Von Mises stress is located at the frequency of 87 Hz, the displacements and the Von Mises stress distributions will be evaluated for that specific frequency.

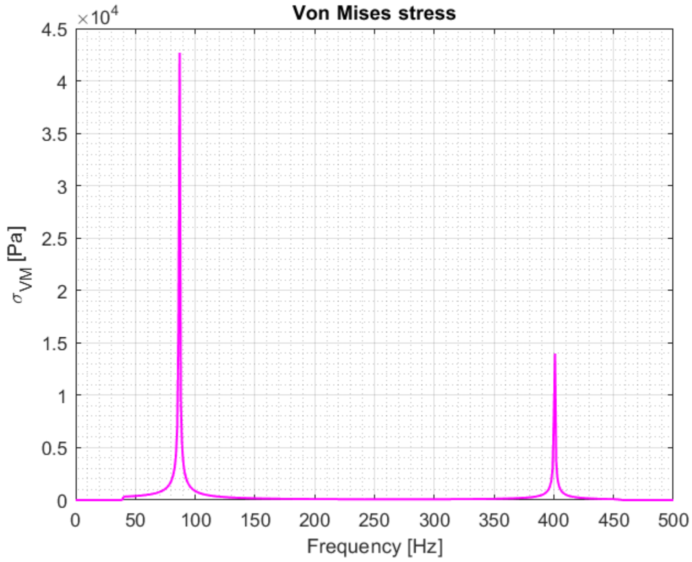

FIGURE C.343: Von Mises distribution obtained on the node located in the coordinate (0.231, 0, 0) m of the sensor versus frequency when performing the random vibration test using Mesh 4 [MATLAB].

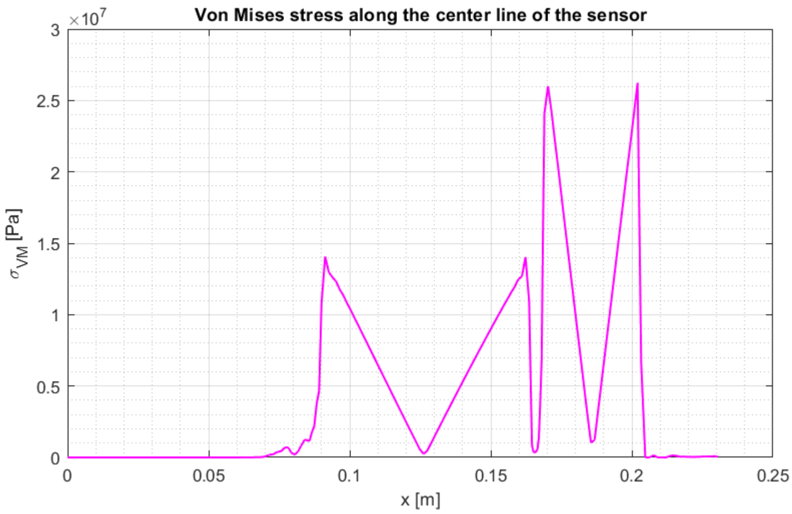

FIGURE C.344: Von Mises stress distribution along the center line of the sensor when performing the quasi-static test using mesh 4 and for the frequency of 87 Hz [MATLAB].

Next, the response at the frequency of 87 Hz will be analysed. Figure C.344 presents the Von Mises stress distribution along the center line of the sensor for the frequency of 87 Hz. Considering the resulting distribution, the maximum Von Mises stress along the sensor is located on the region nearby the second transversal section change.

Moreover, figure C.345 presents the forces and momentum distribution along the centre line of the wind sensor. The dominant force is the shear force (F_z) perpendicular to the neutral plane of the sensor.

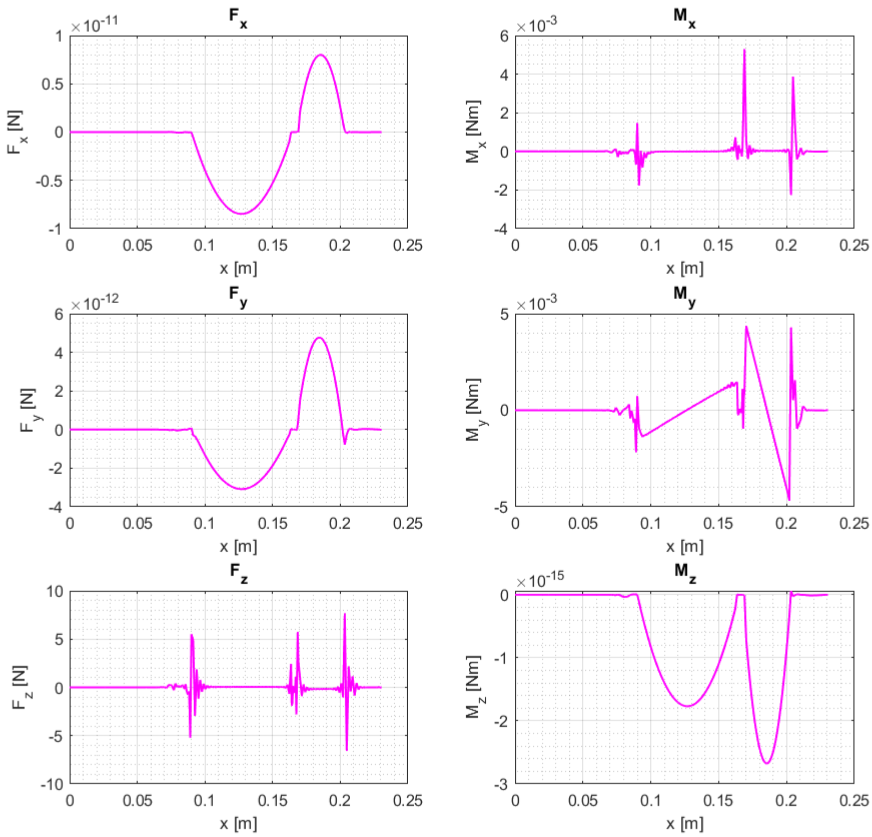

FIGURE C.345: Force and Momentum distribution obtained along the center line of the sensor when performing the quasi-static test using mesh 4 and for the frequency of 87 Hz [MATLAB].

Figure C.346 presents the displacements distribution in the z-direction along the sensor when the frequency is equal to 87 Hz. As shown in this figure, the maximum displacement in the z-direction is located on the coordinates (0.2292, 0, 0) m and has a magnitude of $1.108 \cdot 10^{-3}$ m. Furthermore, figure C.347 shows the Von Mises stress distribution along the sensor for the frequency of 40 Hz. The maximum Von Mises stress is located on the coordinates (0.2020, 0, 0) m with a value of $2.6237 \cdot 10^{7}$ Pa.

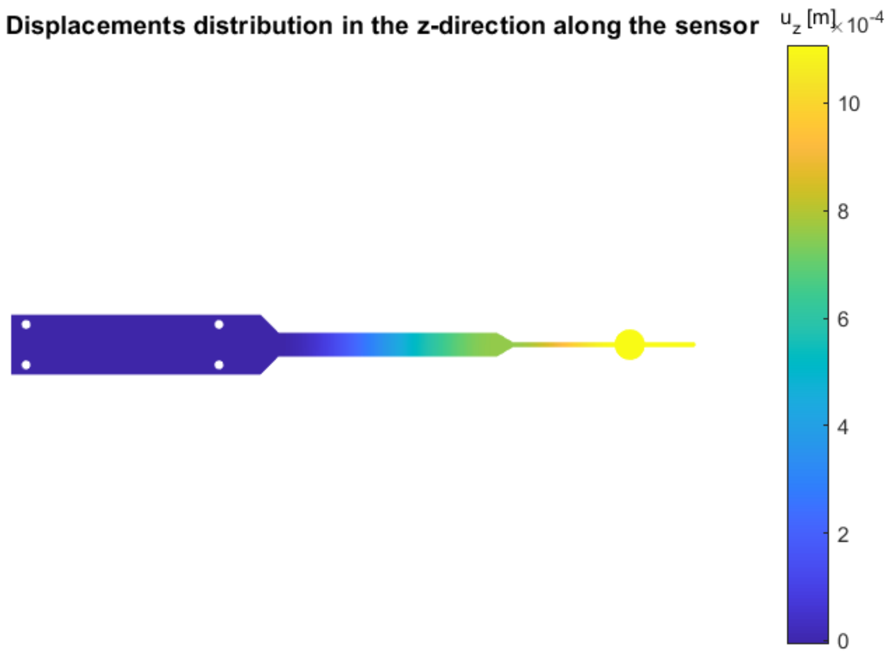

FIGURE C.346: Displacements distribution in the z-direction along the mesh of the sensor when performing the random vibration test using Mesh 4 and for the frequency of 87 Hz [MATLAB].

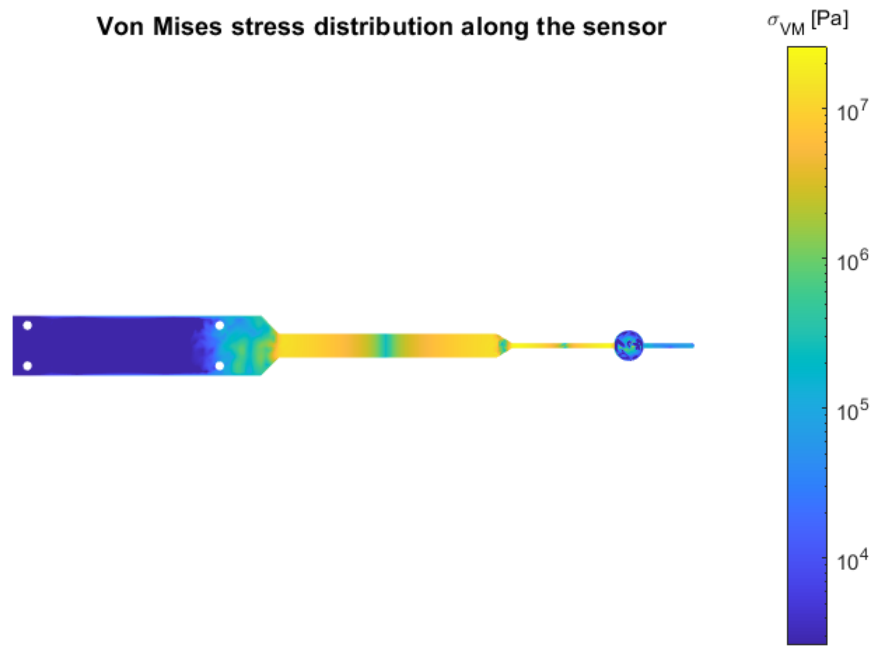

FIGURE C.347: Von Mises stress distribution along the mesh of the sensor when performing the random vibration test using Mesh 4 and for the frequency of 87 Hz [MATLAB].

Figures C.348 and C.349 show the displacement in the z-direction and the Von Mises stress distribution along the core of the PCB structure respectively. Moreover, the displacement in the z-direction and the Von Mises stress distribution along the spherical sensor have been also plotted and can be seen in figures C.350 and C.351.

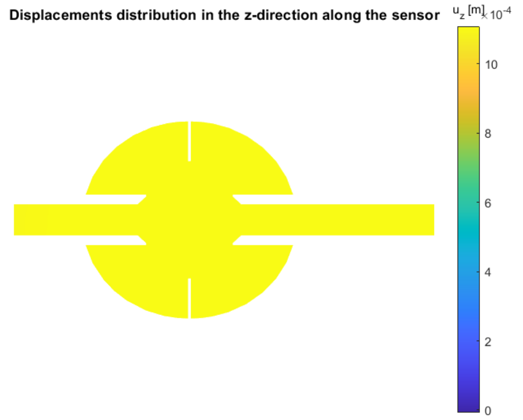

FIGURE C.348: Displacements distribution in the z-direction along the mesh of the PCB when performing the random vibration test using Mesh 4 and for the frequency of 87 Hz [MATLAB].

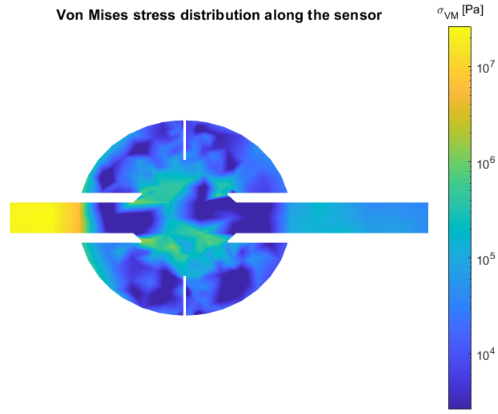

FIGURE C.349: Von Mises stress distribution along the mesh of the PCB when performing the random vibration test using Mesh 4 and for the frequency of 87 Hz [MATLAB].

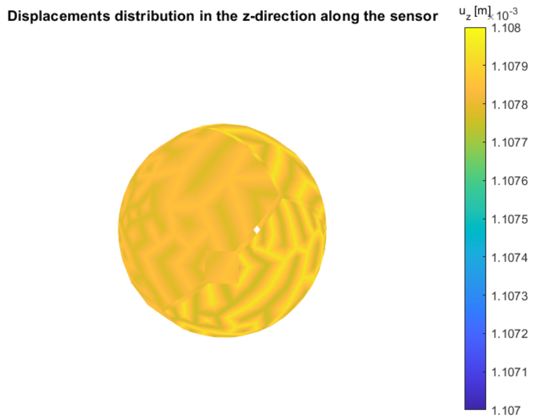

FIGURE C.350: Displacements distribution in the z-direction along the mesh of the spherical sensor when performing the random vibration test using Mesh 4 and for the frequency of 87 Hz [MATLAB].

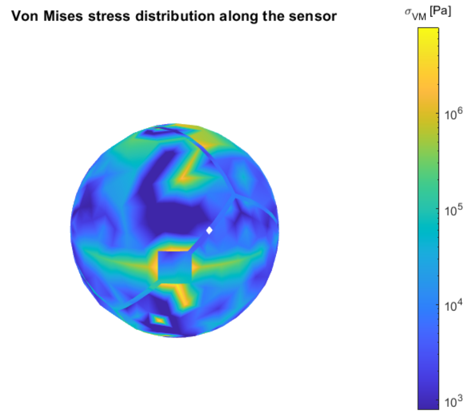

FIGURE C.351: Von Mises stress distribution along the mesh of the spherical sensor when performing the random vibration test using Mesh 4 and for the frequency of 87 Hz [MATLAB].

C.14.6 Conclusions

Then, the location and the magnitude of the highest displacement in the z-direction and Von Mises stress have been summarised in table C.18. As the maximum Von Mises stress is located on the PCB structure with a value of $2.6237 \cdot 10^7$ Pa and the ultimate tensile strength of the PCB is $\sigma_{max\ PCB} = 28.2 \cdot 10^7$ Pa, the wind sensor will successfully pass the random vibration test in this first case scenario of 87 Hz.

TABLE C.18: Summary of the maximum displacement and Von Mises stress obtained when performing the random vibration test for the frequency of 40 Hz [MATLAB].

	Location	**Magnitude**
Maximum z-direction displacement	(0.2292, 0, 0) m	$1.108 \cdot 10^{-3}$ m
Maximum Von Mises stress	(0.2020, 0, 0) m	$2.6237 \cdot 10^7$ Pa
Second Maximum Von Mises stress	(0.1703, 0, 0) m	$2.6007 \cdot 10^7$ Pa

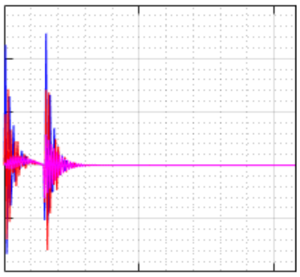

POLYTECHNIC UNIVERSITY OF CATALONIA
Structural Mechanics
Matlab and Comsol

C.15 Report 15: Flat shell pyroshock

The aim of this report is to perform a pyroshock test using MATLAB to a thin plate in order to verify the implemented code so it can be used for more complex geometries. First, some pyroshock parameters will be determined according to the input force and the mesh discretisation. Moreover, a transient study will be carried on in order to obtain, at first, the modal displacement (q), velocity ($\dot{q}$) and acceleration ($\ddot{q}$) distribution along time and, secondly, the displacement (u), velocity ($\dot{u}$) and acceleration ($\ddot{u}$) distribution along time. Finally, the Von Mises stress distribution will also be computed.

C.15.1 Model definition

This report will be analysing a flat squared shell with the following characteristics.

Geometry

- Shell dimensions: 2,00 x 2,00 m
- Shell thickness: 0.05 m

Material

- Young's modulus, E = 69 GPa.
- Poisson's ratio, $\nu = 0.3$.
- Mass density, $\rho = 2700 kg/m^3$.

Boundary conditions

- The shell is totally free.

C.15.2 Mesh

The mesh used in this report will be a really simple one as shown in figure C.352 because the goal of this simulation is to perform a pyroshock test with MATLAB and to verify the code used so it can be implemented for more complex geometries such as the wind sensor.

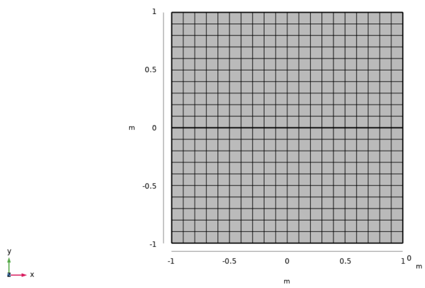

FIGURE C.352: Thin plate mesh discretised in 400 elements [COMSOL].

C.15.3 Pyroshock Test

Pyroshock is a test that consists in a high magnitude shock which takes place in a really small interval of time. Moreover, some parameters are of the uttermost importance when calculating the response of a pyroshock [27] such as:

- The damping ratio ζ of the SDOF dynamic system. Generally, it has a value of 5% which is the equivalent to $Q = 10$.
- The number of SDOF systems for which the maximum response is computed.
- The time frame of the transient period T_{min}. It will be chosen the highest value between $T_{min} \geq \frac{1}{f_{min}}$ and twice the maximum shock time $T_{min} \geq 2t_{shock}$.
- The time step. The increment time step should be less than the 10% of the reciprocal value of the maximum frequency f_{max}.

$$\Delta t \leq \frac{0.1}{f_{max}} \tag{C.125}$$

- The mesh element type and size. The mesh element size and type should be determined according to the maximum frequency of the range at which the structure is evaluated, in this case, 100 kHz. With the highest frequency, the smallest wavelength is computed considering that, in every structure, three types of waves take place: shear, flexural and compression waves.

C.15.4 Input force

Once defined the mesh and the time step that is going to be implemented, the force input has been defined. In this case, the force will be applied on the middle node of the thin plate in the z-direction. The location of the force applied is shown in figure C.353. Moreover, the force will describe a half-sine function with an amplitude of 1000 N and a chock time of 0.3 ms.

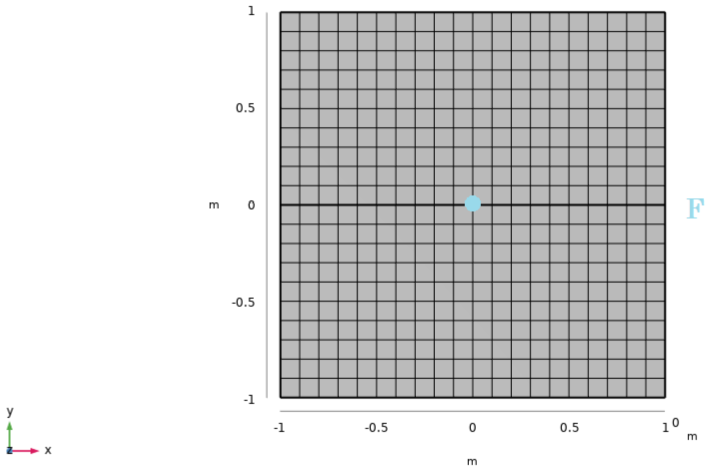

FIGURE C.353: Force application node [COMSOL].

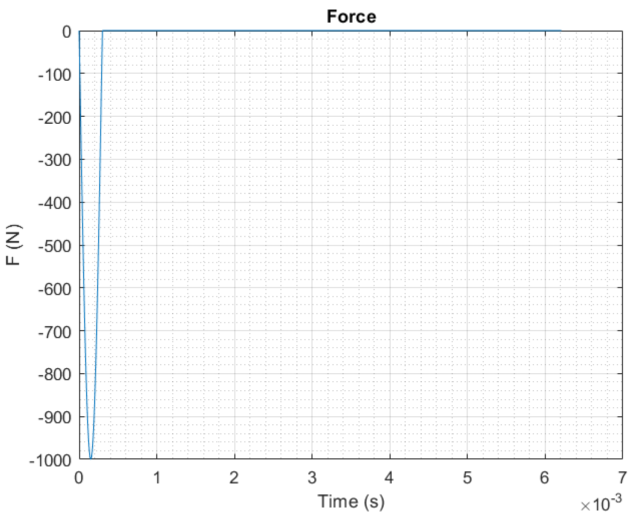

FIGURE C.354: Force distribution as a function of time [MATLAB].

C.15.5 Transient study

Then, the transient study has been performed in order to calculate the modal and real displacement, velocity and acceleration distributions in the z-direction along time for a given points. The evaluated nodes are depicted in picture C.355.

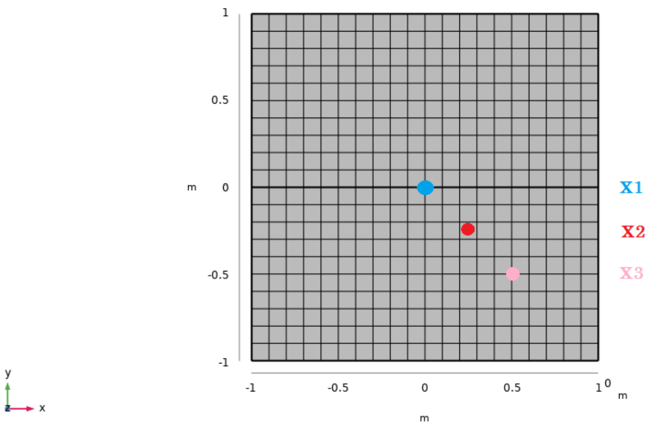

FIGURE C.355: Evaluated nodes [COMSOL].

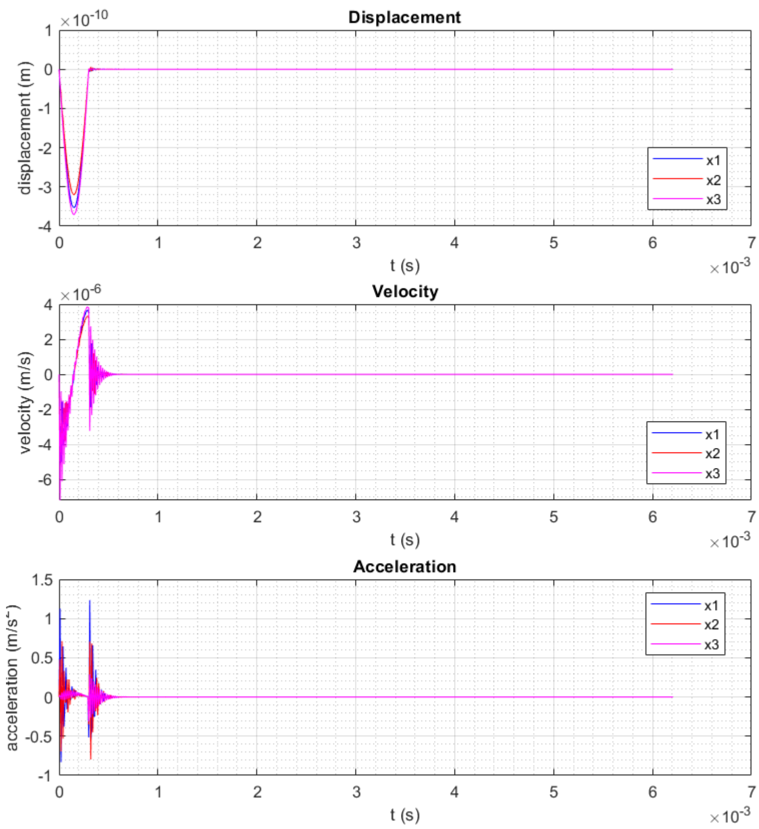

FIGURE C.356: Modal displacement, velocity and acceleration distributions in the z-direction of nodes located at x_1, x_2 and x_3 as a function of time [MATLAB].

Figure C.356 presents the modal displacement, velocity and acceleration distributions in the z-direction of nodes located at x_1, x_2 and x_3 as a function of time. In the modal base, the response is concentrated on the first 0.6 ms and then it stabilises at a value around zero. However, when calculating the real displacement, velocity and acceleration distributions in the z-direction of nodes located at x_1, x_2 and x_3 as a function of time, the response doesn't stabilise after a certain amount of time as can be seen in figure C.357.

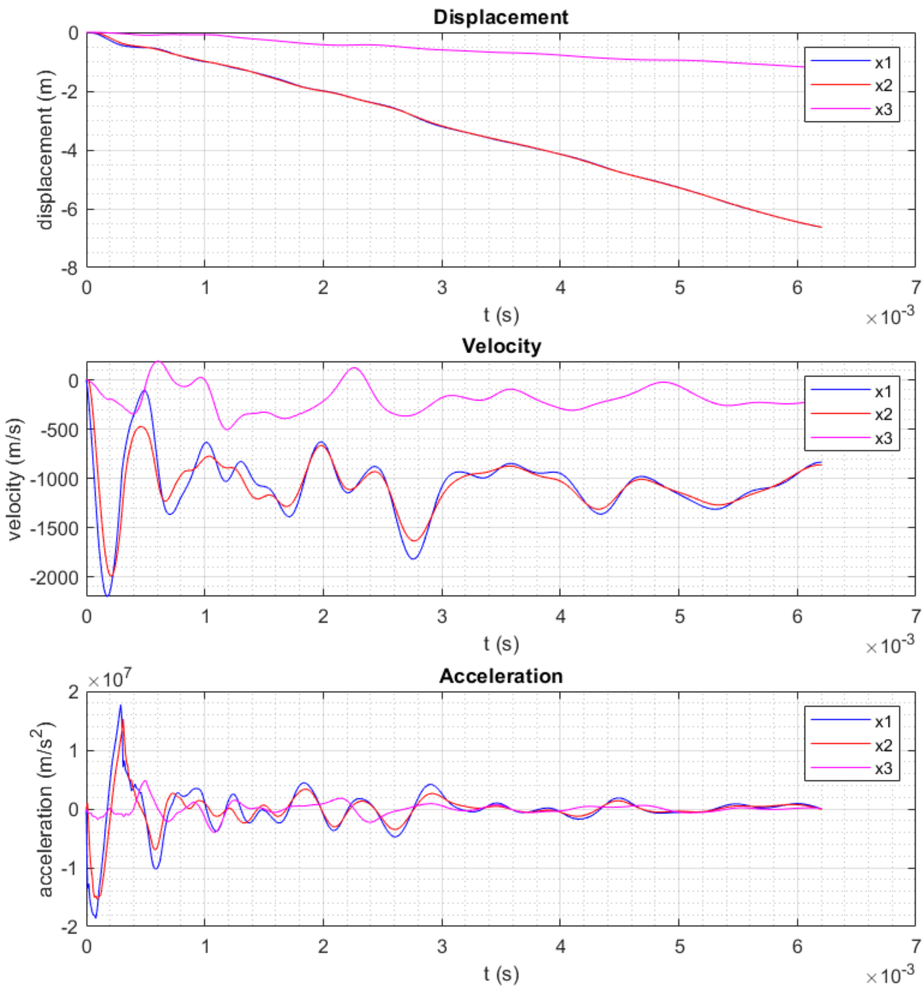

FIGURE C.357: Displacement, velocity and acceleration distributions in the z-direction of nodes located at x_1, x_2 and x_3 as a function of time [MATLAB].

Finally, the Von Mises stress distribution has been computed from the displacements obtained in figure C.356. The Von Mises stress distribution as a function of time is shown in figure C.358.

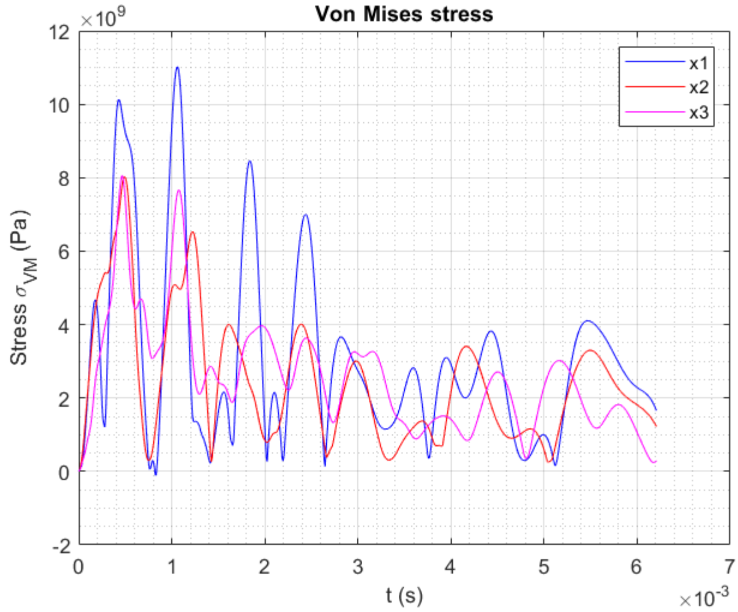

FIGURE C.358: Von Mises stress distribution of nodes located at x_1, x_2 and x_3 as a function of time [MATLAB].

C.15.6 Conclusions

The MATLAB code implemented to solve this problem with this simple geometry of a flat shell will be the foundation used to implement a more efficient code.

C.16 Report 16: Approximated Pyroshock Test

The aim of this report is to perform an approximated pyroshock test to the wind sensor evaluated.

C.16.1 Hypothesis

It is considered to be a first approach of the test due to the fact that some assumptions have been made:

- Although the PCB is composed by a total of two thin plates with an specific silhouette and 0.8 mm thickness each, in this study, the PCB will just be composed by one thin plate. This plate will have the resulting superposed silhouette of the two plates and double thickness, 1.6 mm.
- As the MATLAB code works with really huge matrices and, for the moment, modal projection method is not implemented, it will be considered that the displacements in x and y-direction and the rotation in z-direction will be null. This hypothesis will be corrected in the final simulation presented on the main Report document. However, in the case of x and y-direction displacements, the assumption that will be equal to zero could be close to the final solution as the forces are applied on the normal direction with respect to the neutral plane of the PCB. In contrast, to assume that the rotation in the z-direction will be null can not work due to the non-geometry of the spherical sensor with respect to the xz plane. This can induce easily a torsion momentum. However, as a first approach, it has not been considered.

C.16.2 Model definition

The properties of the materials used are listed bellow. Moreover, figure C.333 depicts the material distribution along the sensor.

- Material of the structure: PCB.
  - Young's modulus, E = 22 GPa.
  - Poisson's ratio, $\nu = 0.15$.
  - Mass density, $\rho = 1900\ kg/m^3$.
  - Ultimate tensile strength, $\sigma_{max} = 282$ MPa.
- Material of the sphere: Silver (Ag).
  - Young's modulus, E = 76 GPa.
  - Poisson's ratio, $\nu = 0.37$.
  - Mass density, $\rho = 10497\ kg/m^3$.
  - Ultimate tensile strength, $\sigma_{max} = 140$ MPa.

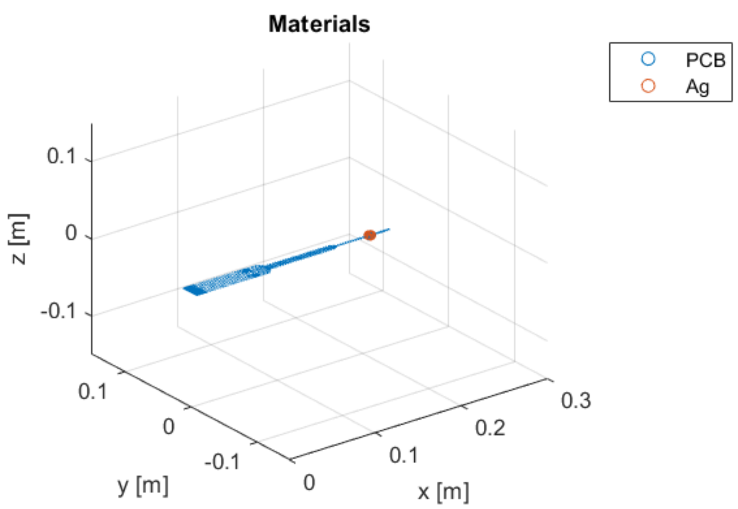

FIGURE C.359: Material distribution along the sensor [MATLAB].

C.16.3 Mesh

- **Mesh 1**. The mesh has a maximum length per element of 0.006 m and is composed by a total of 1014 quadrilateral elements.

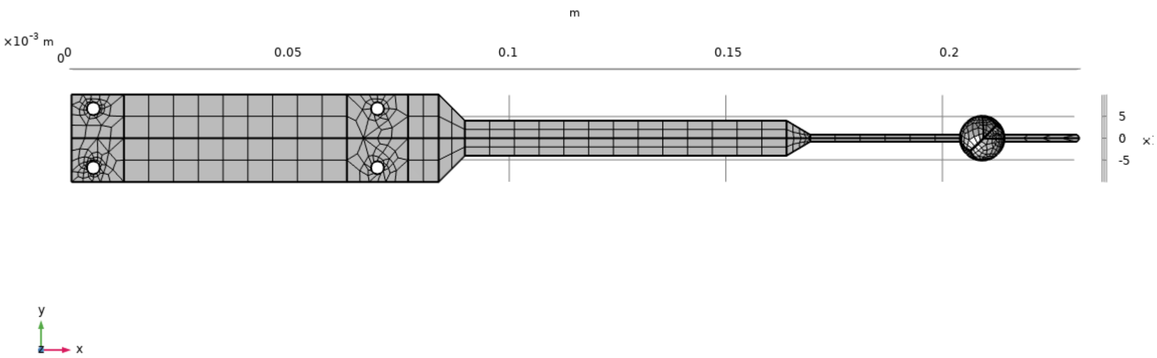

FIGURE C.360: Mesh [COMSOL].

C.16.4 Pyroshock Test

Some parameters are of the uttermost importance when calculating the SRS [27]:

- The damping ratio ζ of the SDOF dynamic system. Generally, it has a value of 5% which is the equivalent to $Q = 10$.
- The number of SDOF systems for which the maximum response is computed.
- The time frame of the transient period T_{min}. It will be chosen the highest value between $T_{min} \geq \frac{1}{f_{min}}$ and twice the maximum shock time $T_{min} \geq 2t_{shock}$.
- The time step. The increment time step should be less than the 10% of the reciprocal value of the maximum frequency f_{max}.

$$\Delta t \leq \frac{0.1}{f_{max}} \tag{C.126}$$

- The mesh element type and size. The mesh element size and type should be determined according to the maximum frequency of the range at which the structure is evaluated, in this case, 100 kHz. With the highest frequency, the smallest wavelength is computed considering that, in every structure, three types of waves take place: shear, flexural and compression waves.

C.16.5 Boundary conditions

This test consists in applying a punctual half-sine pulse force in the z-direction to the sensor (see figure C.361). The half-sine pulse that describes the force can be seen in figure C.362. For the moment, just 1N will be applied on the PCB structure. Moreover, the sensor will be subjected by its holes.

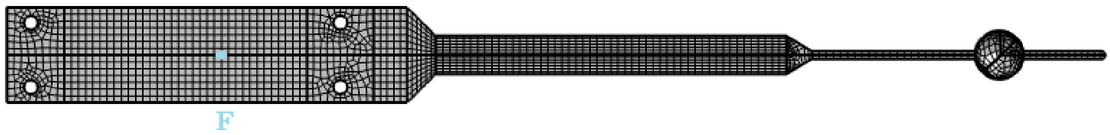

FIGURE C.361: Location of the node at which the force is applied [COMSOL].

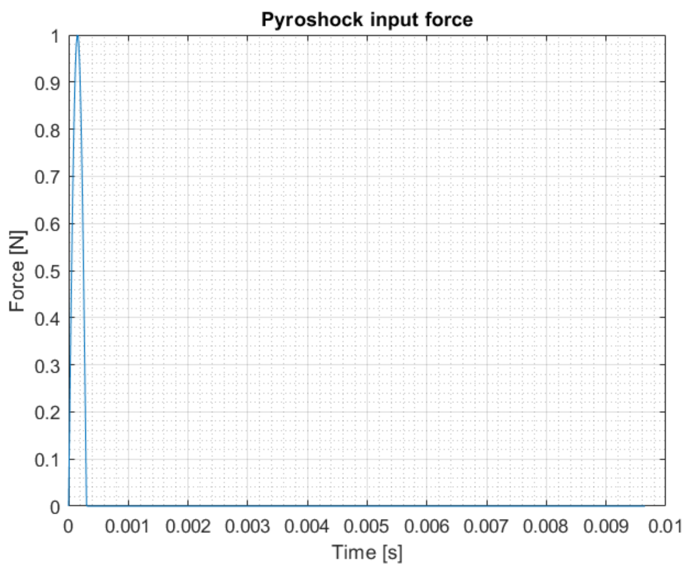

FIGURE C.362: Pyroshock input force as a function of time [MATLAB].

C.16.6 Shock Response Spectrum Study

The shock response spectrum will be computed using the methodology explained in section B.4.3 of the annex. First of all, it will be studied how the time step used impacts on the final solution. Then, it will be plotted the different SRS graphs for different nodes of the PCB structure.

C.16.6.1 Time step dependency

In the first place, the time step dependency has been studied. As figure C.363 shows, the functions tends to move to the right side of the graphic when decreasing the time step used. So, a major drawback when implementing this methodology in a MATLAB code will be deciding which is the time step that bests suits the geometry used and best describes what it is really happening. However, if the pyroshock test parameters previously defined in section C.16.4 are considered, the blue curve will be the one used.

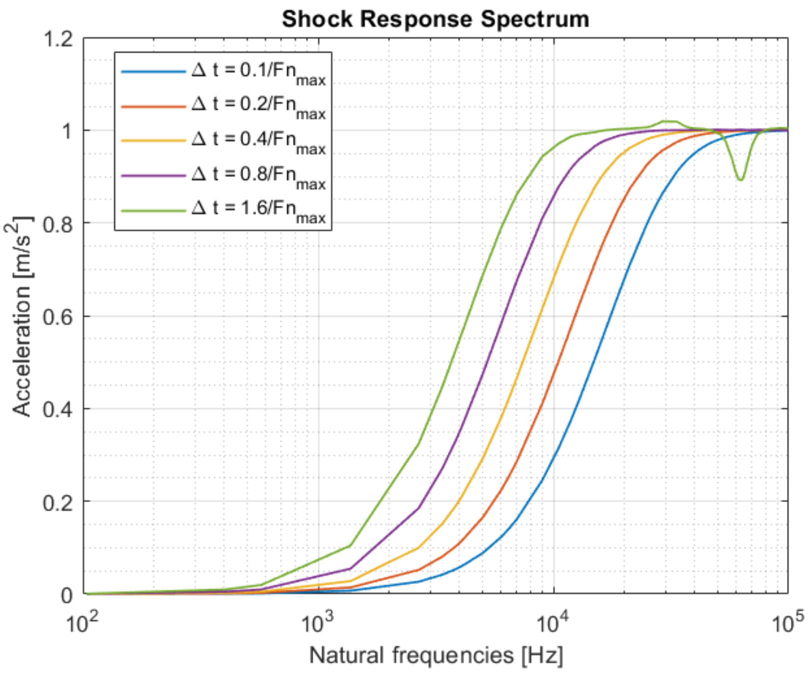

FIGURE C.363: Shock Response Spectrum obtained for the node 1 along the frequency domain considering different time discretizations [MATLAB].

C.16.6.2 SRS graphics

Then, different SRS solutions for three different nodes along the PCB have been depicted in figure C.364. Another major drawback of this methodology is that the SRS information is only contained on the node at which the external force is applied. In other words, as the external force is applied to node 1, when using the SRS methodology explained in section B.4.3 of the annex, the force doesn't impact to another degree of freedom so the SRS can only be computed for node 1.

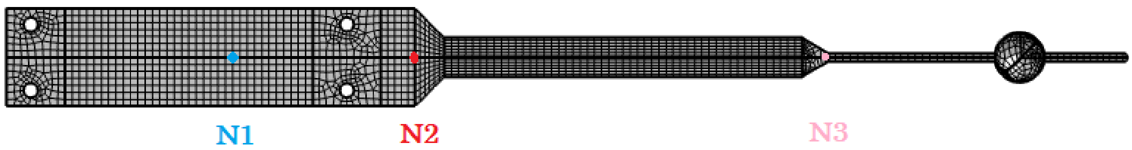

FIGURE C.364: Location of the evaluated nodes [COMSOL].

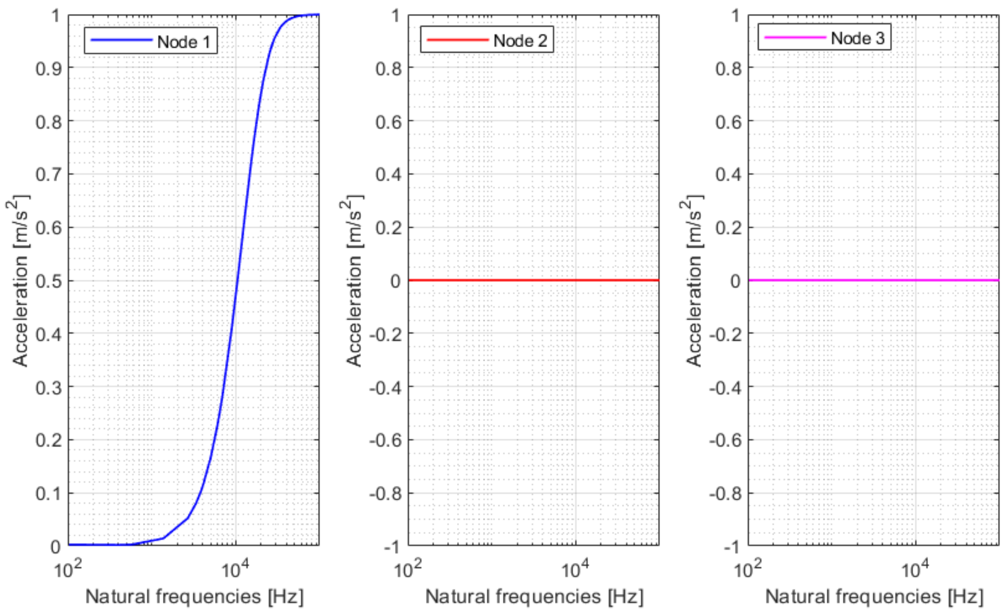

FIGURE C.365: Shock Response Spectrum obtained for nodes 1, 2 and 3 for the time step of $\Delta t = 0.1/Fn_{max}$ [MATLAB].

C.16.7 Transient study

As the Shock Response Spectrum methodology used has not been successful, a transient study will be implemented. This second methodology is further explained in section B.4.4 of the annex. In this case, two different boundary conditions will be studied and the evaluated nodes that will be used to plot the different displacements and Von Mises responses are shown in figure C.366.

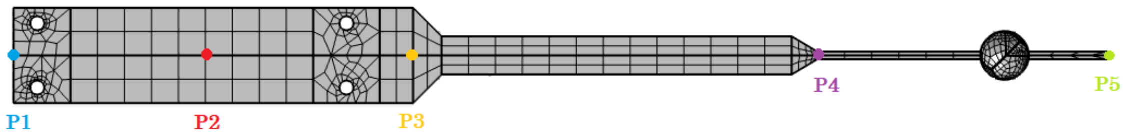

FIGURE C.366: Location of the evaluated nodes [COMSOL].

C.16.7.1 First Boundary Condition

As previously mentioned, the sensor will be evaluated under two boundary conditions. In the first place:

- A half-sine force of an amplitude of 1 N will be applied in the z-direction to the node located at (0.042, 0, 0) m.
- And the sensor will have restricted the displacements in the x and y-direction and the rotation in the z-direction.

Figure C.367 shows the modal displacements and rotations distribution obtained for the different nodes evaluated along time. All the nodes describe a half-sine pulse displacement in the z-direction and rotation in both, x and y-direction. Moreover, the node that describe the maximum modal displacement and rotation is node located at P2 where the force is applied.

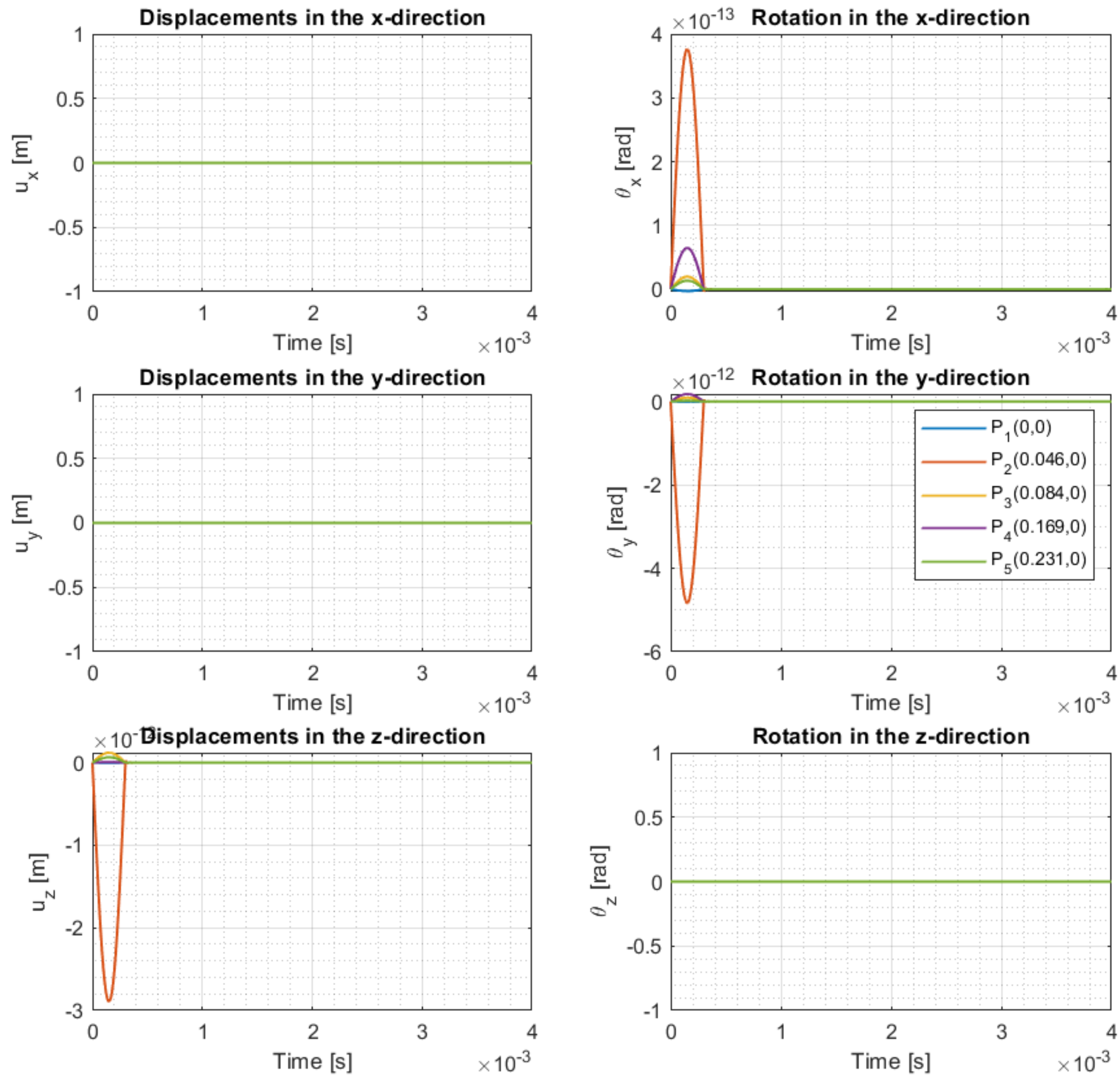

FIGURE C.367: Modal displacements distribution versus time when performing the pyroshock test using Mesh 1 [MATLAB].

Figure C.368 shows the modal linear and angular velocities distribution obtained for the different nodes evaluated along time. All the nodes describe a complete sine pulse velocity in the z-direction and a complete sine pulse angular velocity in both, x and y-direction. Moreover, as what happened to the displacements distribution, the node that describe the maximum modal velocity is the node located at P2 where the force is applied.

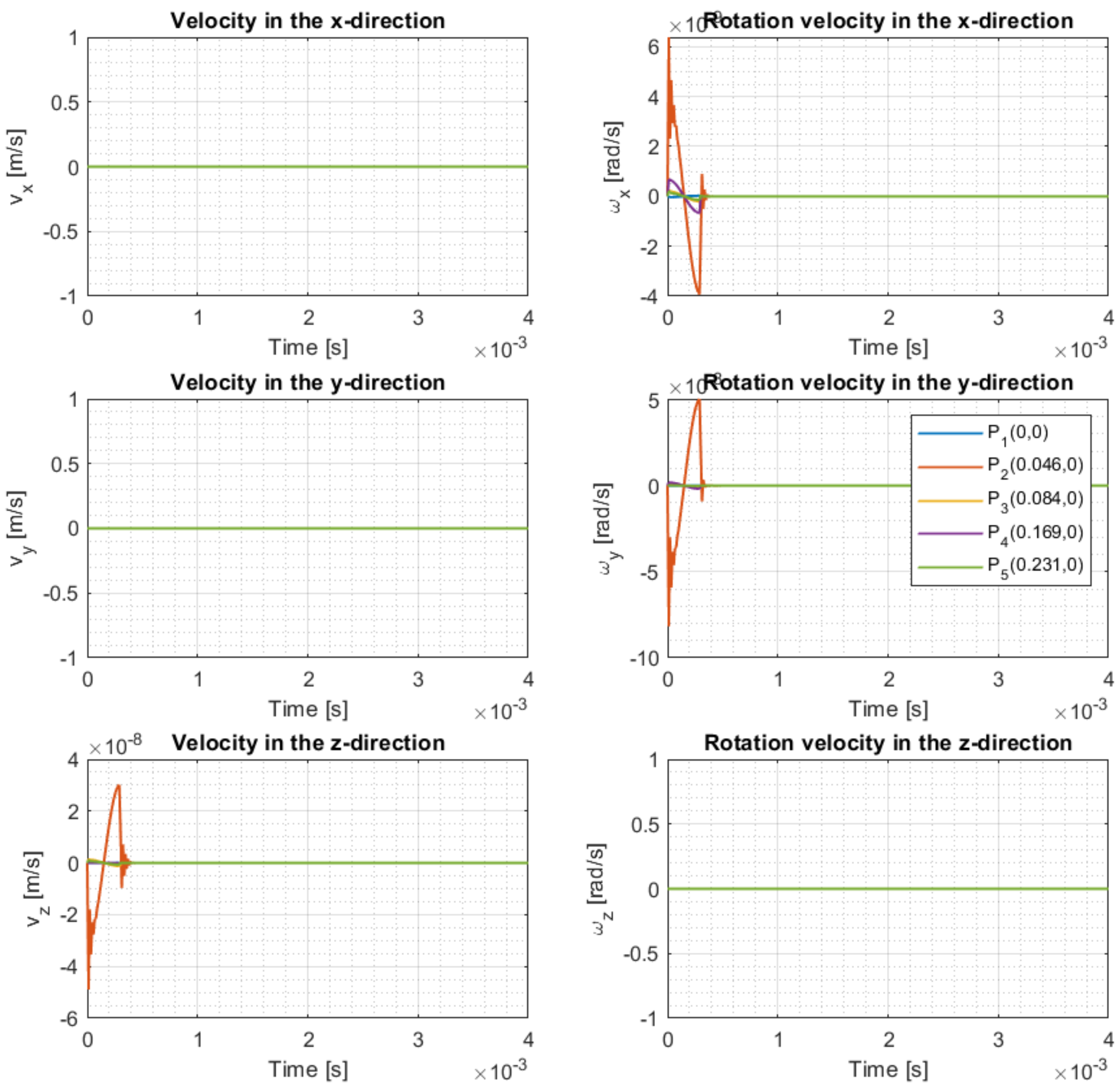

FIGURE C.368: Modal velocity distribution versus time when performing the pyroshock test using Mesh 1 [MATLAB].

Figure C.369 shows the modal linear and angular acceleration distribution obtained for the different nodes evaluated along time. All the nodes describe two peaks, one at t=0s and the other when t=0.3ms. Moreover, as what happened to the displacements and velocities distribution, the node that describe the maximum modal acceleration is the node located at P2 where the force is applied.

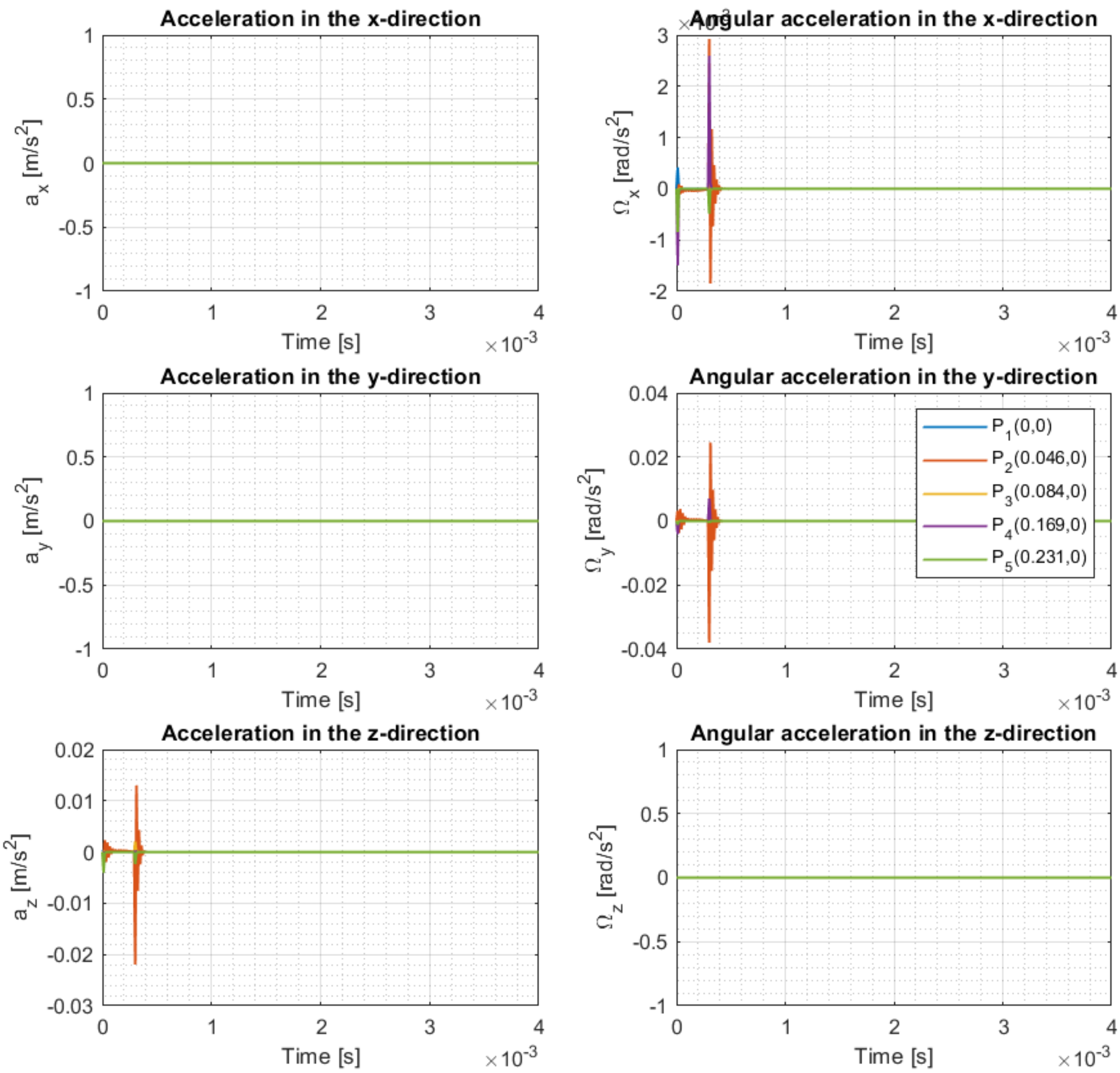

FIGURE C.369: Modal acceleration distribution versus time when performing the pyroshock test using Mesh 1 [MATLAB].

Figure C.370 shows the real displacements and rotations distribution obtained for the different nodes evaluated along time. The nodes tend to describe a sinusoidal displacement in the z-direction and rotation in both, x and y-direction. Moreover, as no displacement in the z-direction has been restricted, it also presents a translation in the negative z-direction.

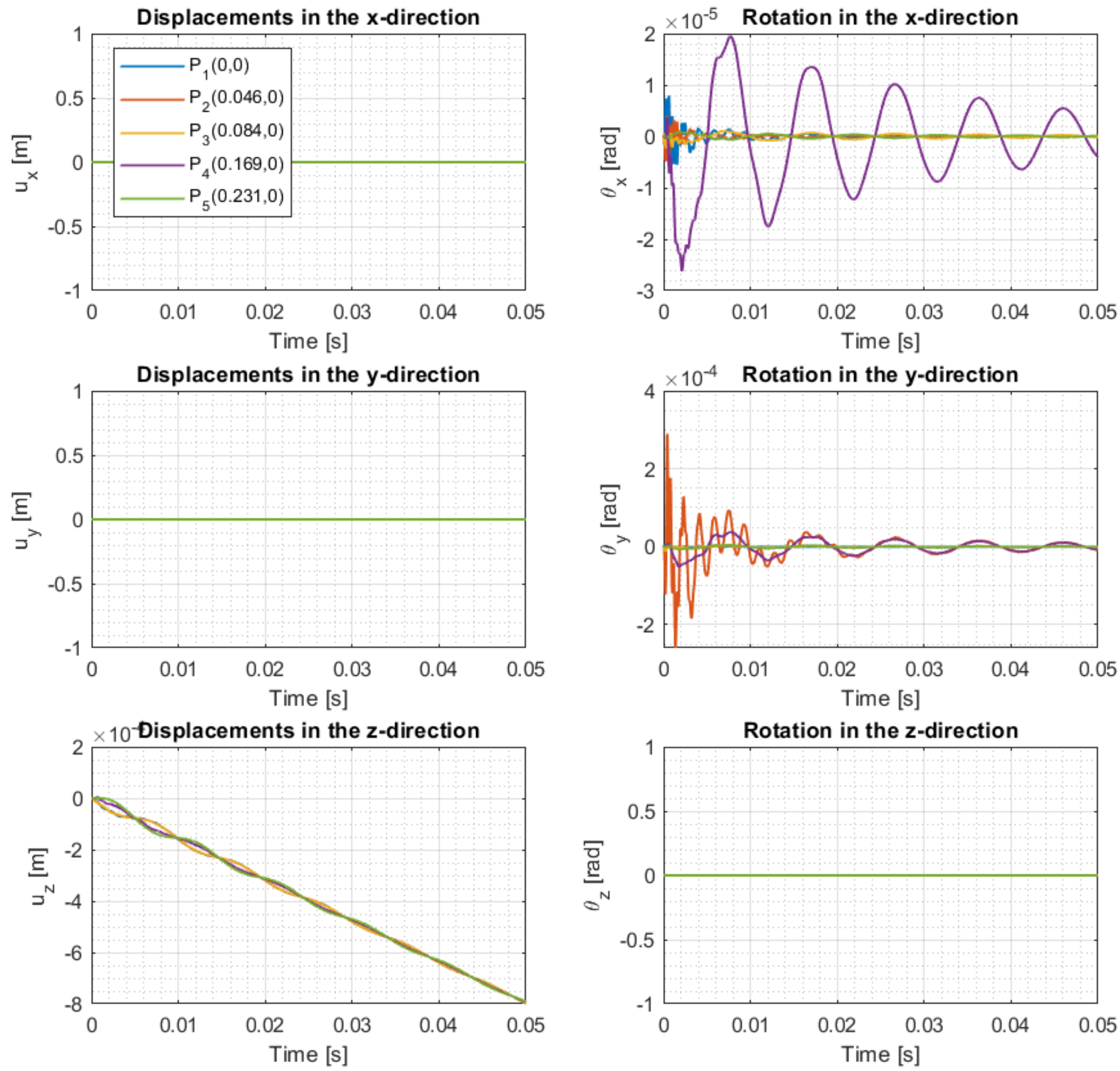

FIGURE C.370: Real displacements distribution versus time when performing the pyroshock test using Mesh 1 [MATLAB].

Figure C.371 shows the real lineal and angular velocities distribution obtained for the different nodes evaluated along time. The nodes tend to describe a sinusoidal velocity profile in the z-direction and rotation in both, x and y-direction. Moreover, the amplitude and the frequency of this sinusoidal responses is not the same along time domain. The amplitude and the frequency are maximum where the shock takes places and this properties fade during time.

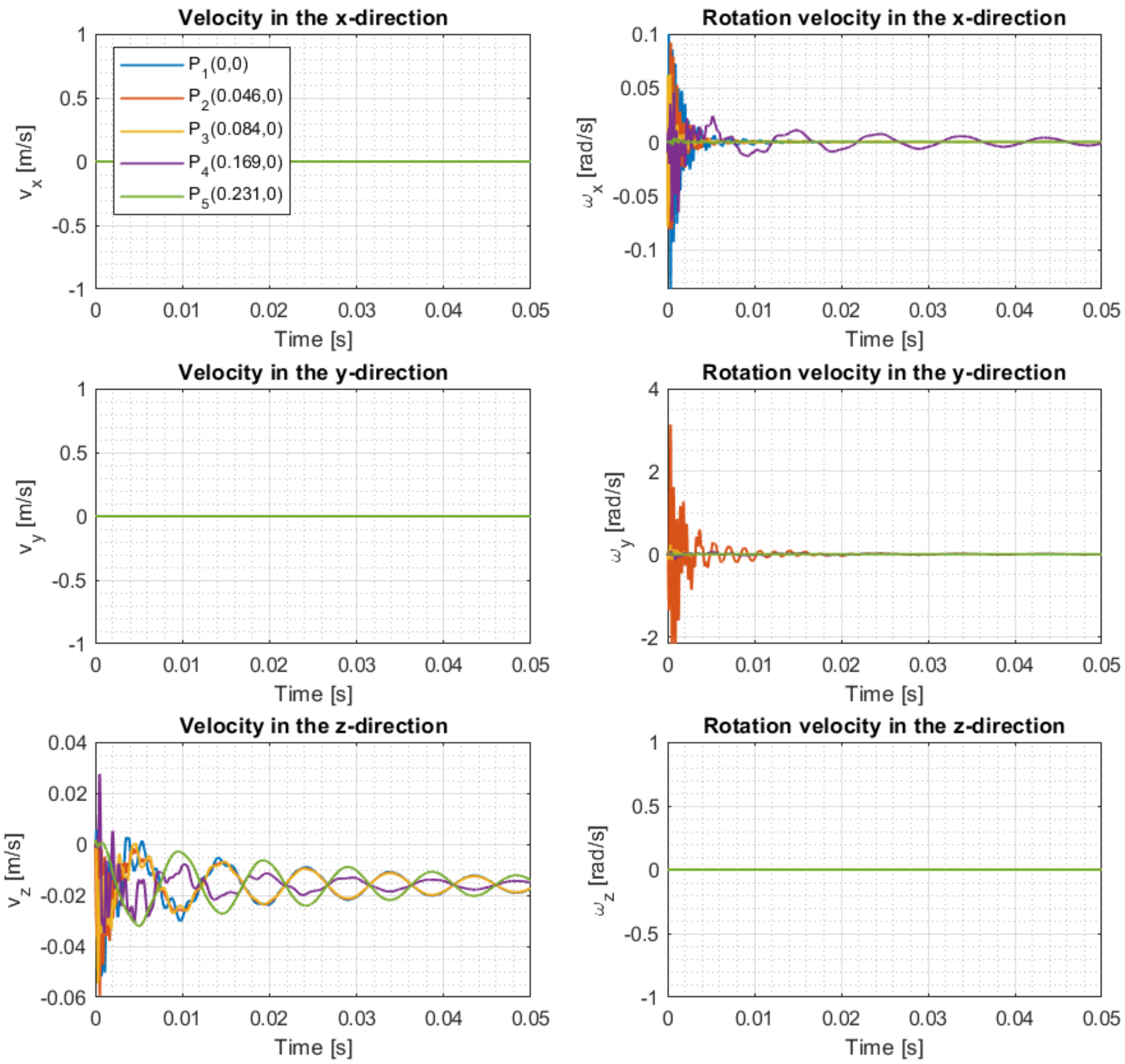

FIGURE C.371: Real velocity distribution versus time when performing the pyroshock test using Mesh 1 [MATLAB].

Figure C.372 shows the real lineal and angular acceleration distribution obtained for the different nodes evaluated along time. The nodes tend to describe a sinusoidal acceleration profile in the z-direction and rotation in both, x and y-direction. However, the amplitude and the frequency of this sinusoidal responses is not the same along time domain. The amplitude and the frequency are maximum where the shock takes places and this properties fade during time.

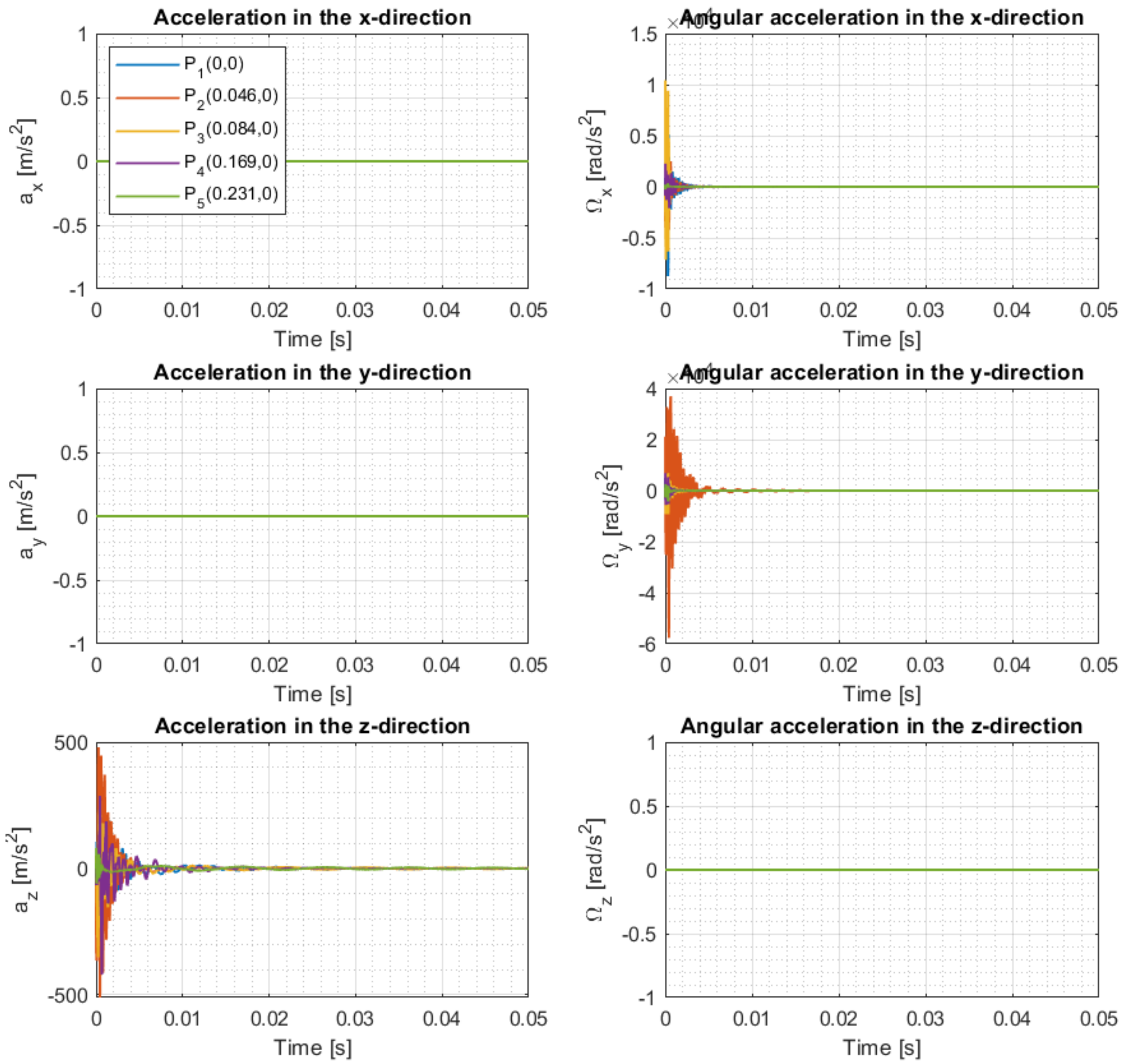

FIGURE C.372: Real acceleration distribution versus time when performing the pyroshock test using Mesh 1 [MATLAB].

Figure C.373 presents the Von Mises stress distribution along time domain for the five nodes evaluated. The nodes tend to describe the absolute value of a sinusoidal function profile. Moreover, the node that presents the maximum stress along time is node located on P4.

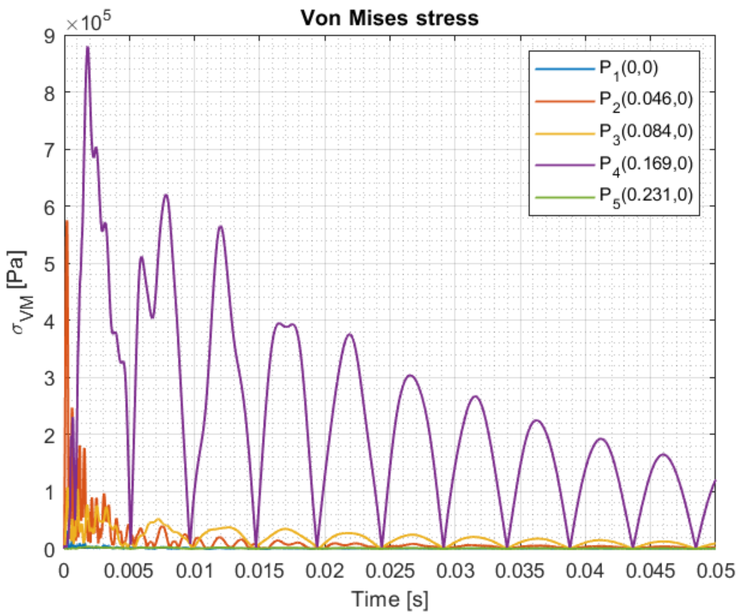

FIGURE C.373: Von Mises stress distribution versus time when performing the pyroshock test using Mesh 1 [MATLAB].

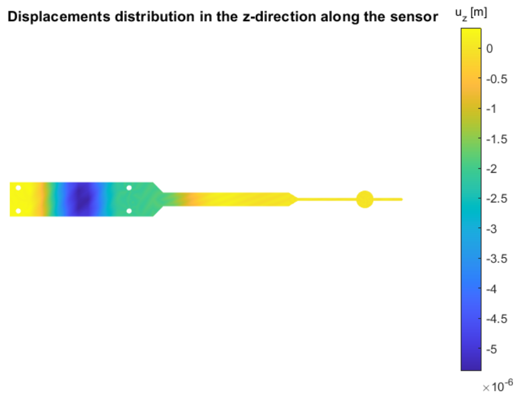

FIGURE C.374: Displacements distribution in the z-direction along the mesh of the sensor when performing the pyroshock test using Mesh 1 and for the initial time [MATLAB].

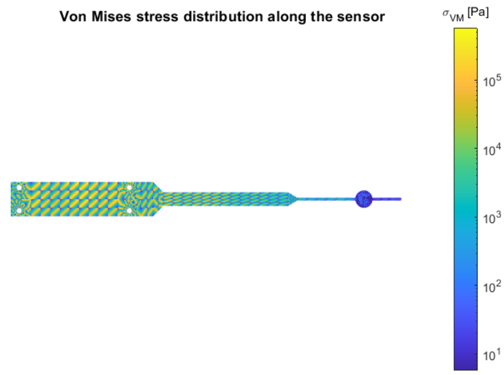

FIGURE C.375: Von Mises stress distribution along the mesh of the sensor when performing the pyroshock test using Mesh 1 and for the initial time [MATLAB].

Figures C.374 and C.375 present the displacement in the z-direction and the Von Mises stress distribution along the sensor for the initial time. Moreover, figures C.376 and C.377 depict the displacement in the z-direction and the Von Mises stress distribution along the spherical sensor respectively.

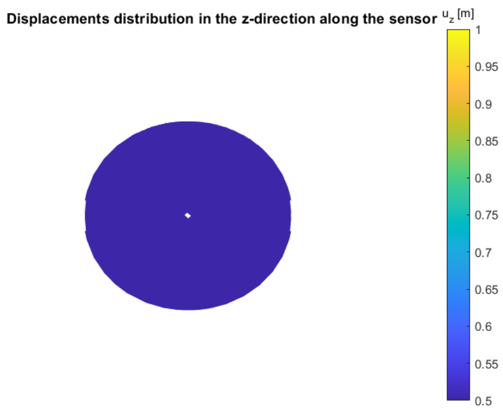

FIGURE C.376: Displacements distribution in the z-direction along the mesh of the spherical sensor when performing the pyroshock test using Mesh 1 and for the initial time [MATLAB].

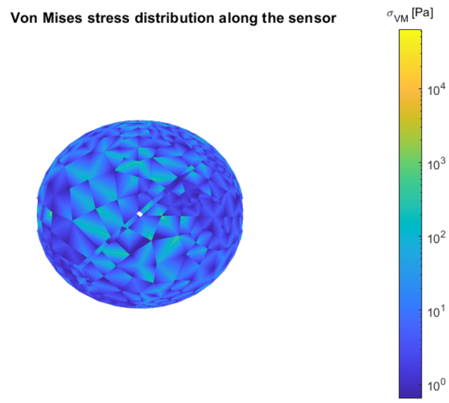

FIGURE C.377: Von Mises stress distribution along the mesh of the spherical sensor when performing the pyroshock test using Mesh 1 and for the initial time [MATLAB].

C.16.7.2 Second Boundary Condition

As previously mentioned, the sensor will be evaluated under two boundary conditions. The second boundary conditions are:

- A half-sine force of an amplitude of 1 N will be applied in the z-direction to the node located at (0.042, 0, 0) m.
- The sensor will have restricted the displacements in the x and y-direction and the rotation in the z-direction.
- The sensor is subjected by its four holes. The restrictions defined on the nodes located in the holes of the sensor are: $u_z = 0$, $\omega_x = 0$ and $\omega_y = 0$.

Figure C.378 shows the modal displacements and rotations distribution obtained for the different nodes evaluated along time. All the nodes describe a half-sine pulse displacement in the z-direction and rotation in both, x and y-direction. Moreover, the node that describe the maximum modal displacement and rotation is node located at P2 where the force is applied.

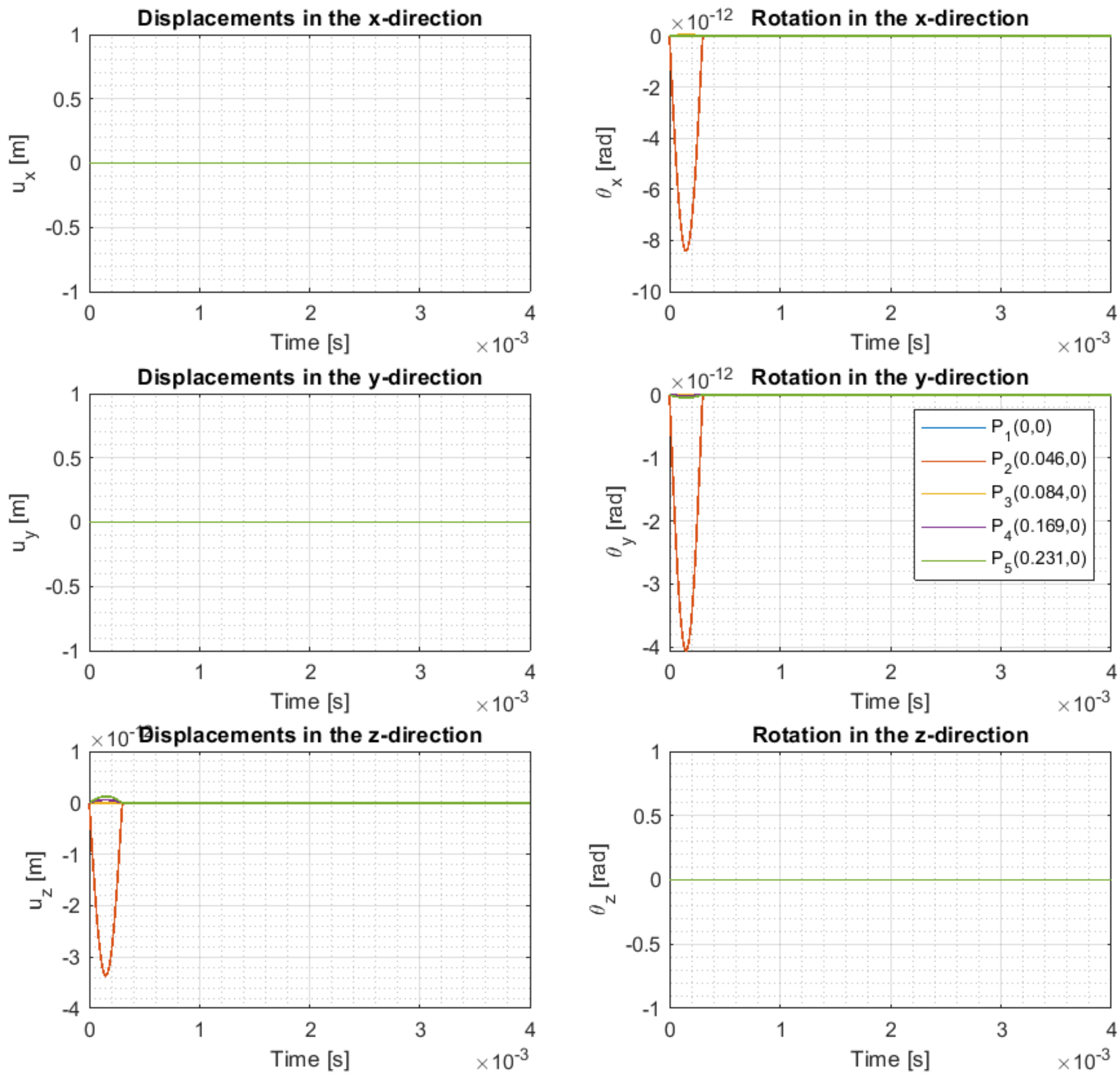

FIGURE C.378: Modal displacements distribution versus time when performing the pyroshock test using Mesh 1 [MATLAB].

Figure C.379 shows the modal linear and angular velocities distribution obtained for the different nodes evaluated along time. All the nodes describe a complete sine pulse velocity in the z-direction and a complete sine pulse angular velocity in both, x and y-direction. Moreover, as what happened to the modal displacements distributions, the node that describe the maximum modal velocity is the node located at P2 where the force is applied.

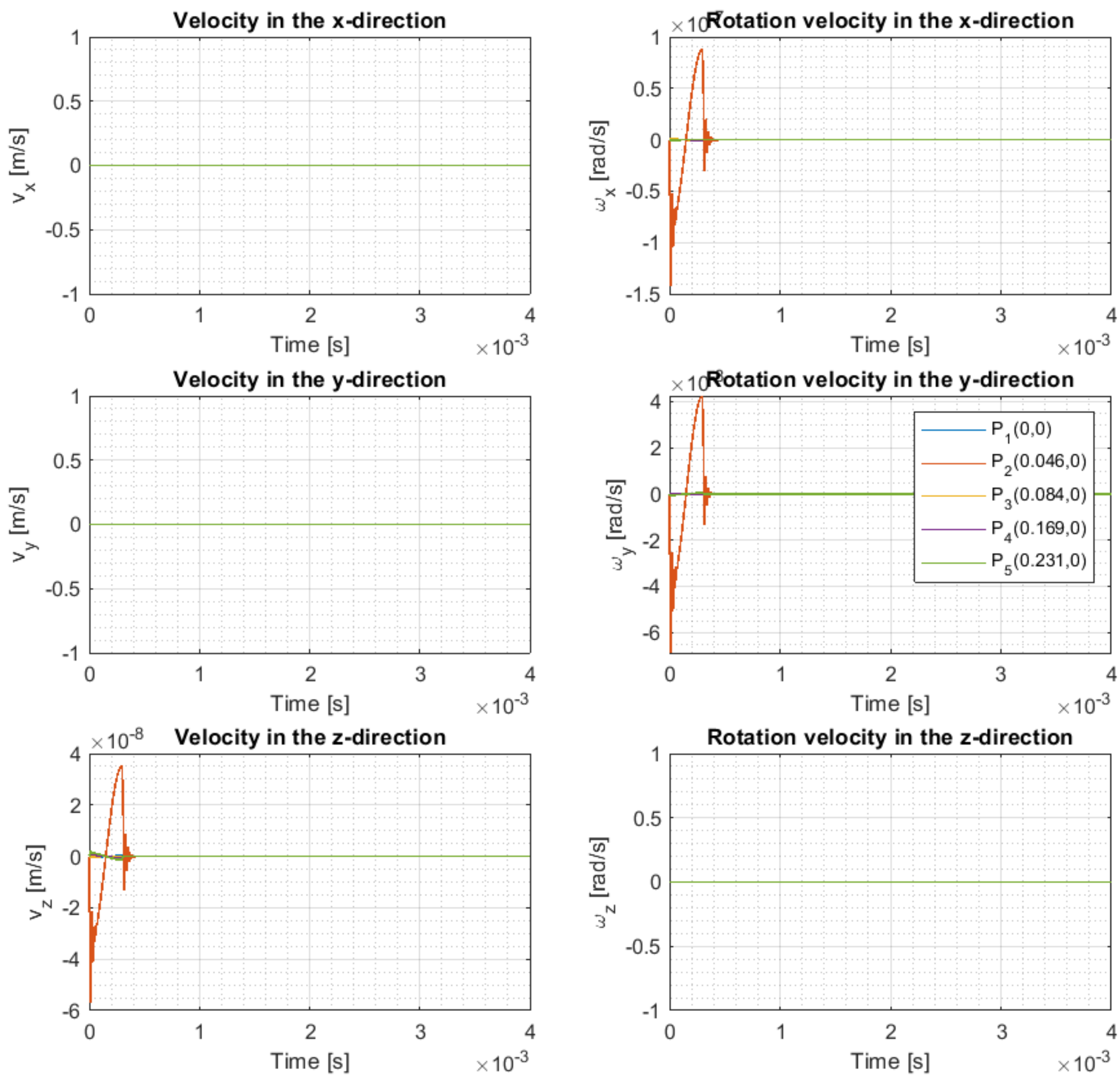

Figure C.379: Modal velocity distribution versus time when performing the pyroshock test using Mesh 1 [MATLAB].

Figure C.380 shows the modal linear and angular acceleration distribution obtained for the different nodes evaluated along time. All the nodes present two peaks, one at t=0s and the other when t=0.3ms. Moreover, as what happened to the modal displacements and velocities distribution, the node that describe the maximum modal acceleration is the node located at P2 where the force is applied.

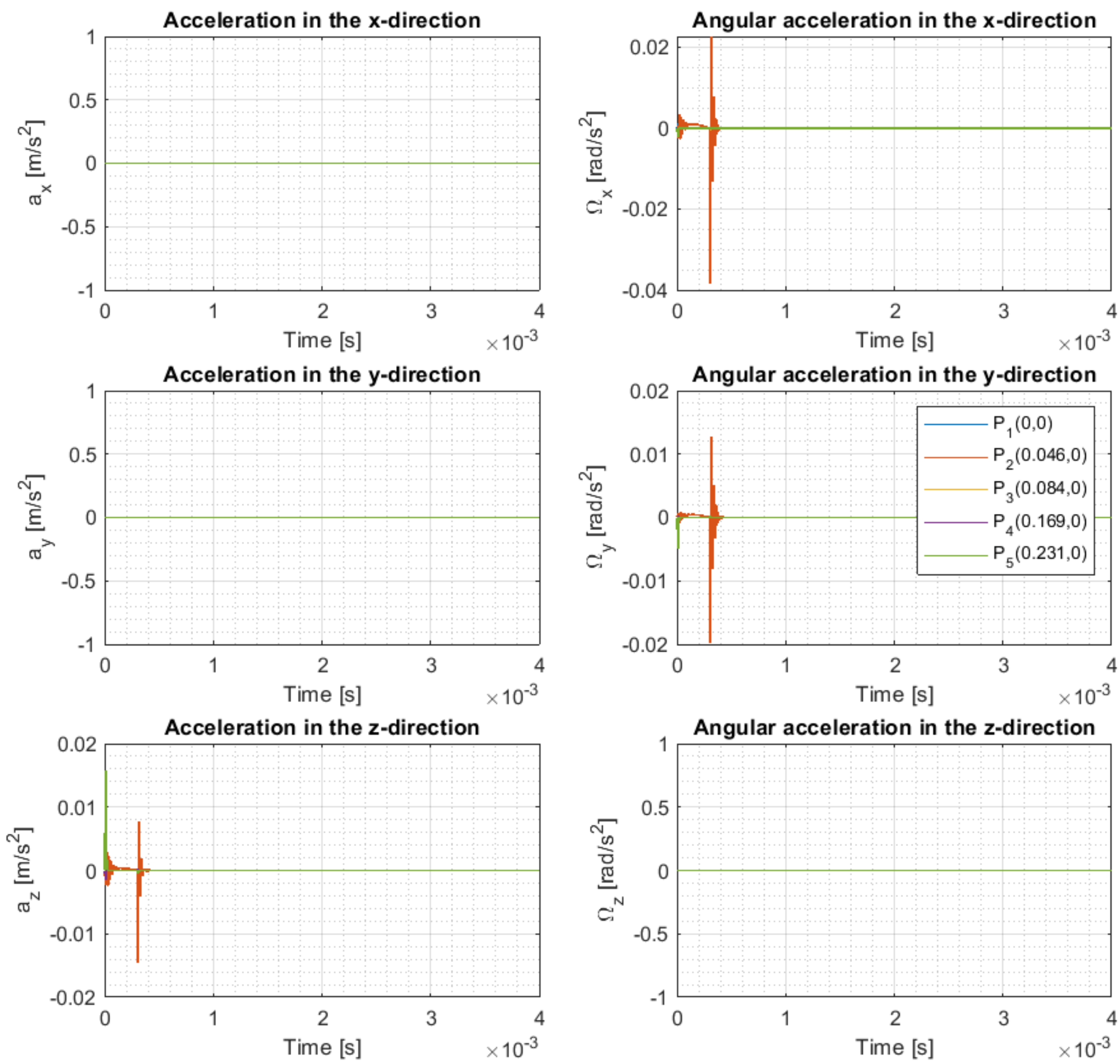

FIGURE C.380: Modal acceleration distribution versus time when performing the pyroshock test using Mesh 1 [MATLAB].

Figure C.381 shows the real displacements and rotations distribution obtained for the different nodes evaluated along time. The nodes tend to describe a sinusoidal displacement in the z-direction and rotation in both, x and y-direction. Moreover, the amplitude of the displacements and rotations fade over time as a result of adding damping to the properties of the structure.

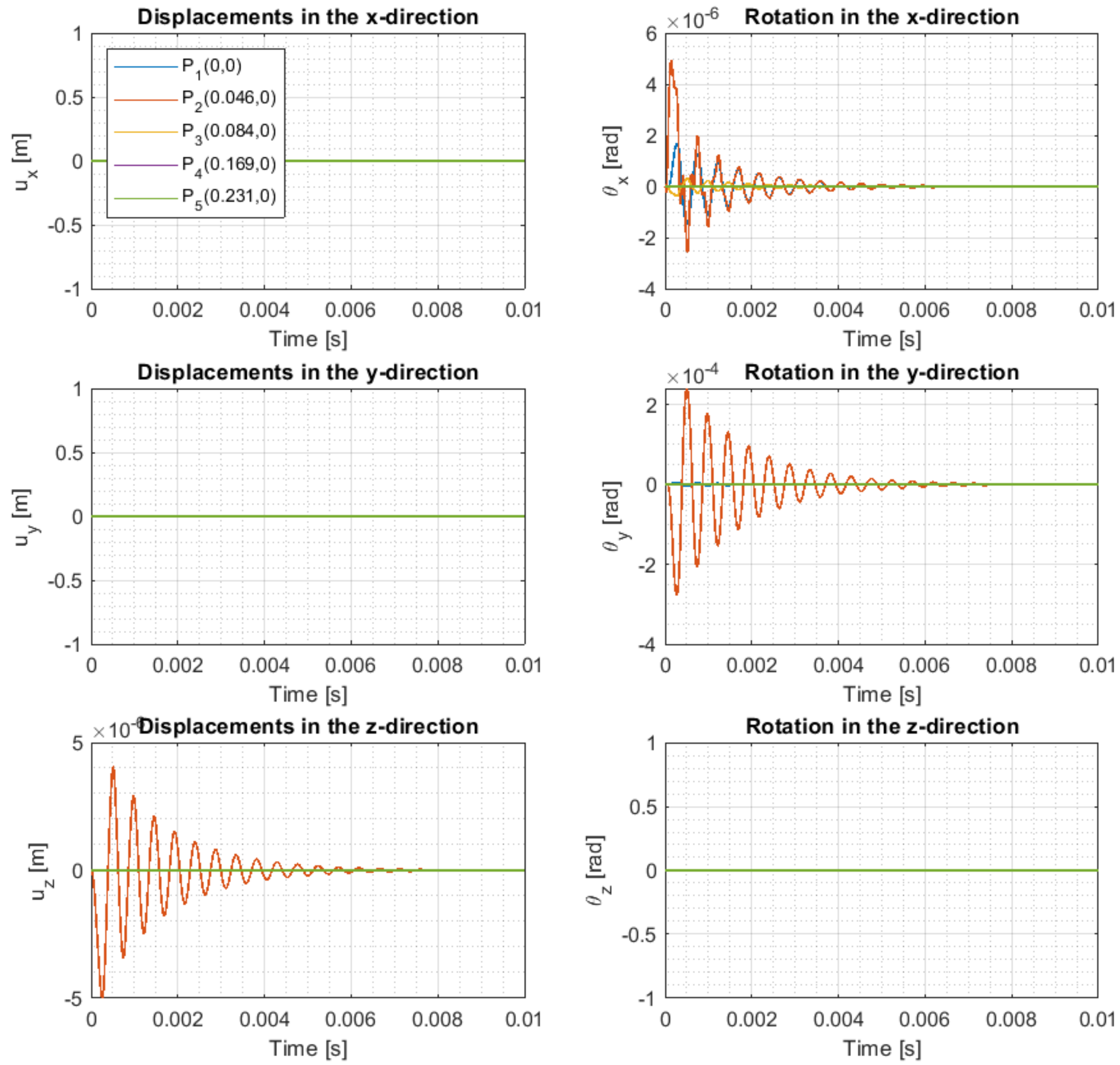

FIGURE C.381: Real displacements distribution versus time when performing the pyroshock test using Mesh 1 [MATLAB].

Figure C.382 shows the real lineal and angular velocities distribution obtained for the different nodes evaluated along time. The nodes tend to describe a sinusoidal velocity profile in the z-direction and rotation in both, x and y-direction. Moreover, the amplitude of this sinusoidal responses is not the same along time domain. The amplitude is maximum where the shock takes places and fades over time.

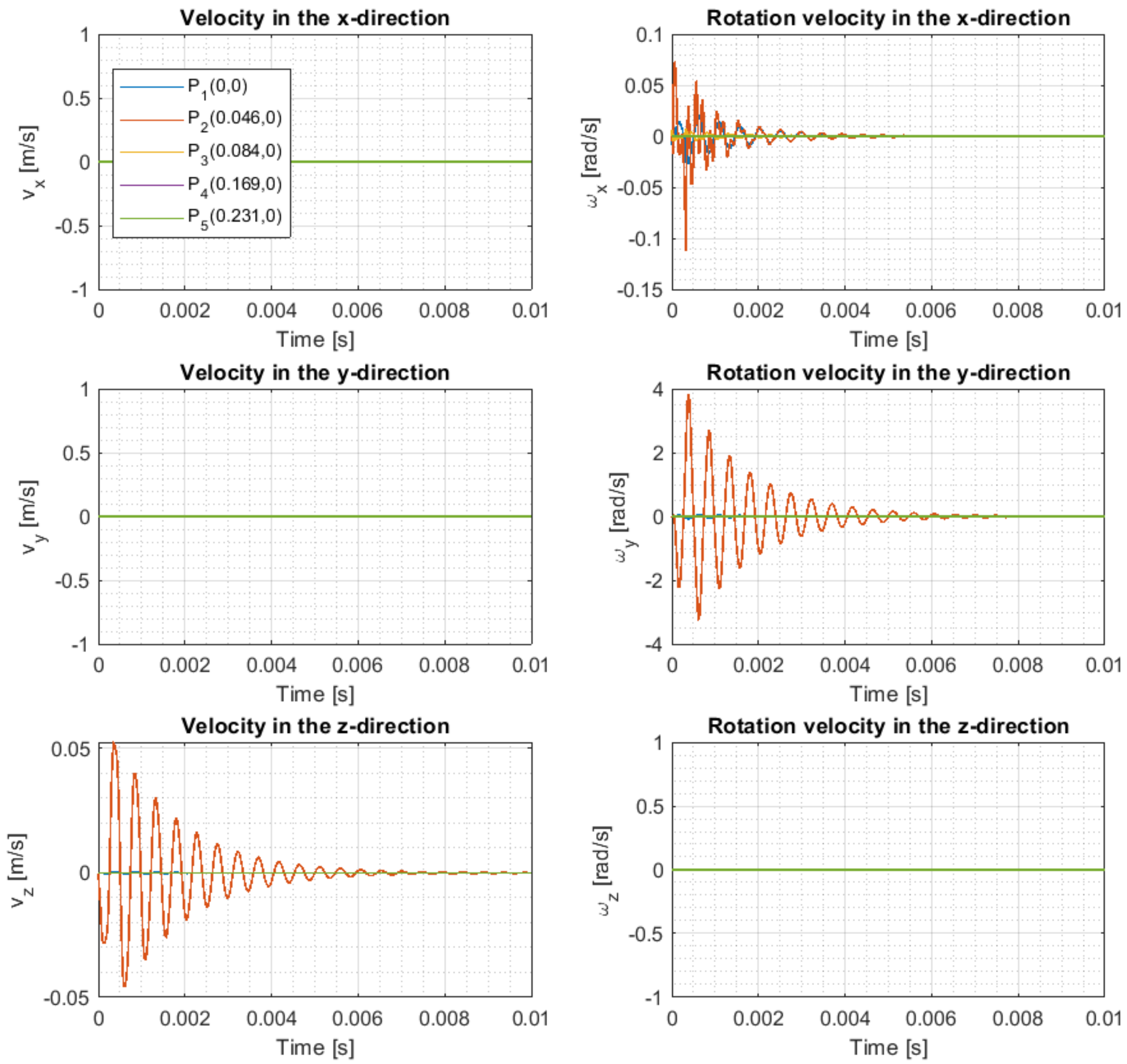

FIGURE C.382: Real velocity distribution versus time when performing the pyroshock test using Mesh 1 [MATLAB].

Figure C.383 shows the real lineal and angular acceleration distribution obtained for the different nodes evaluated along time. The nodes describe a sinusoidal acceleration profile in the z-direction and rotation in both, x and y-direction. Moreover, the amplitude of this sinusoidal responses is not the same along time domain. It is maximum where the shock takes places and fades over time as a result of adding a damping factor to the structure.

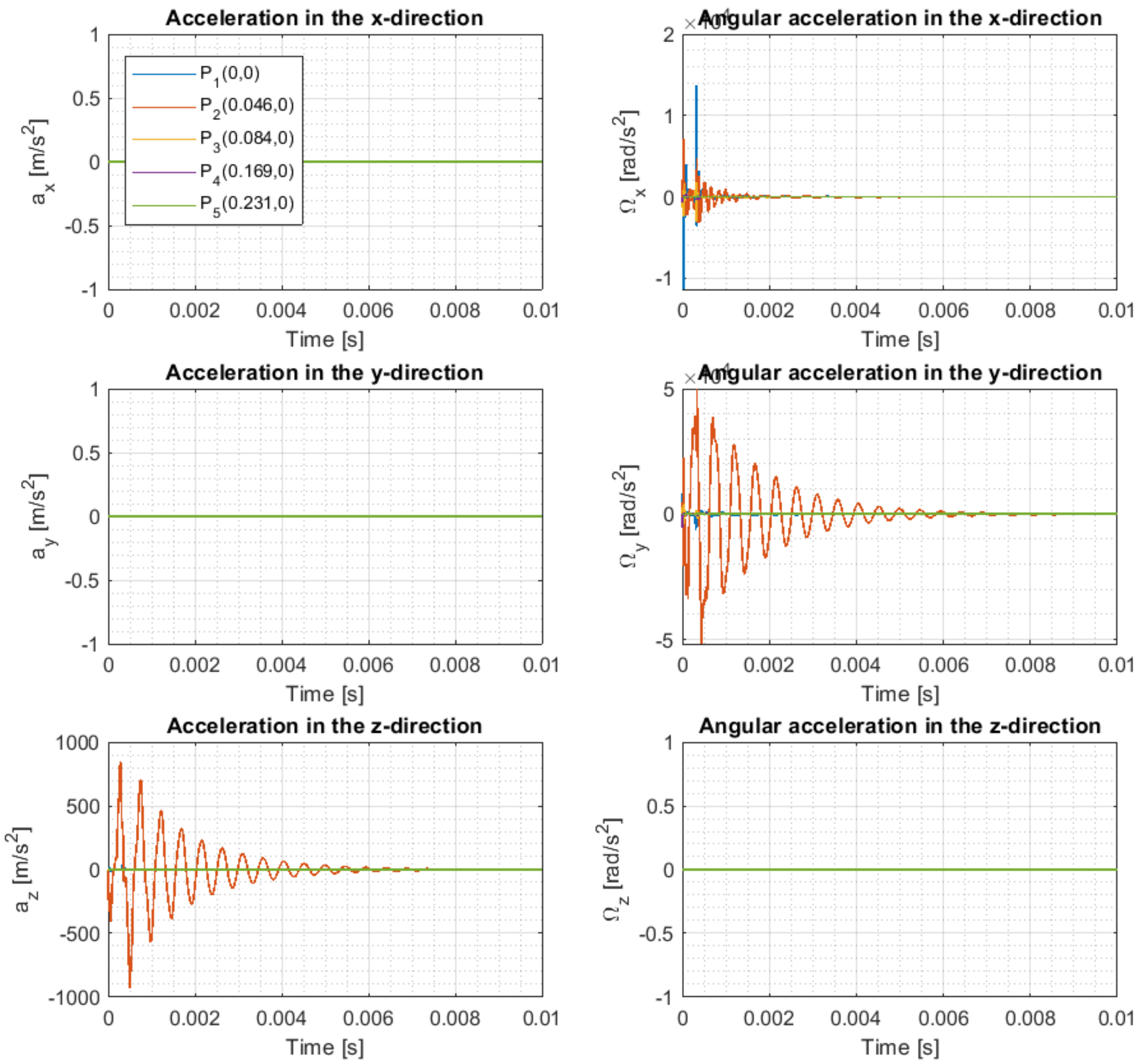

FIGURE C.383: Real acceleration distribution versus time when performing the pyroshock test using Mesh 1 [MATLAB].

Figure C.384 presents the Von Mises stress distribution along time domain for the five nodes evaluated. The nodes tend to describe the absolute value of a sinusoidal function profile that fades over time. Moreover, the node that presents the maximum stress along time is node located on P2, where the force is applied.

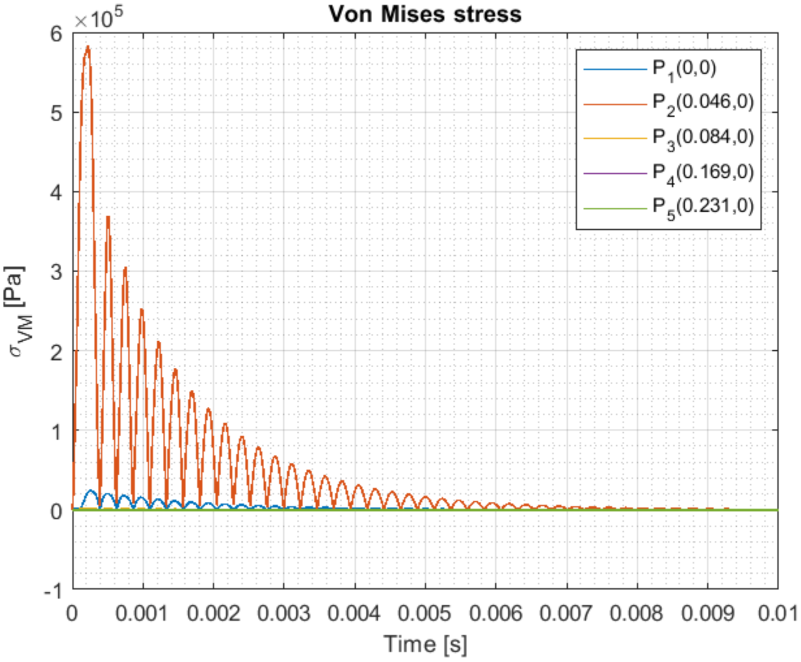

FIGURE C.384: Von Mises stress distribution versus time when performing the pyroshock test using Mesh 1 [MATLAB].

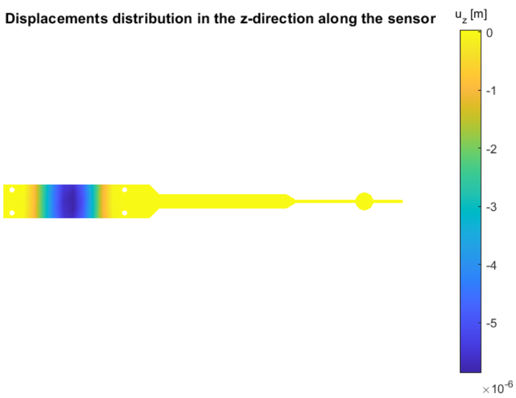

FIGURE C.385: Displacements distribution in the z-direction along the mesh of the sensor when performing the pyroshock test using Mesh 1 and for the initial time [MATLAB].

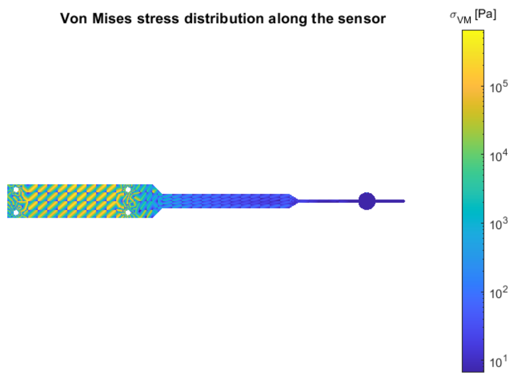

FIGURE C.386: Von Mises stress distribution along the mesh of the sensor when performing the pyroshock test using Mesh 1 and for the initial time [MATLAB].

Figures C.385 and C.386 present the displacement in the z-direction and the Von Mises stress distribution along the sensor for the initial time. Moreover, figures C.387 and C.388 depict the displacement in the z-direction and the Von Mises stress distribution along the spherical sensor respectively.

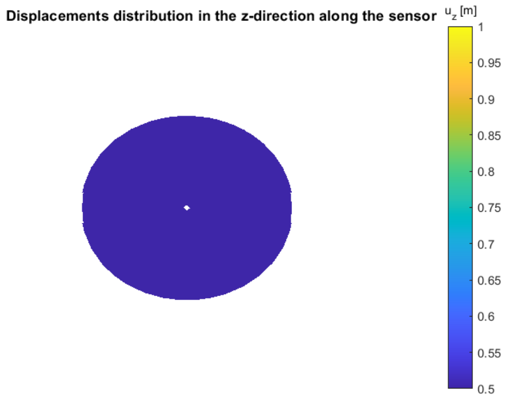

FIGURE C.387: Displacements distribution in the z-direction along the mesh of the spherical sensor when performing the pyroshock test using Mesh 1 and for the initial time [MATLAB].

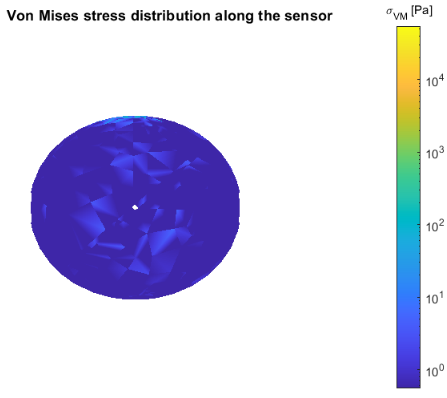

FIGURE C.388: Von Mises stress distribution along the mesh of the spherical sensor when performing the pyroshock test using Mesh 1 and for the initial time [MATLAB].

C.16.8 Conclusions

In conclusion, on the final Report a transient study methodology will be used due to the fact that the force have an impact on different degrees of freedom and one can see what happens to all the nodes that conform the sensor for a certain boundary condition defined.

Bibliography

[1] Siemens, "Spectrum versus autopower." https://community.sw.siemens.com/s/article/spectrum-versus-autopower. (Accessed on the 28th of January of 2022).

[2] Scheidler, P., "Frequency leakage in fourier transforms." https://blog.endaq.com/fourier-transform-leakage. (Accessed on the 1st of February of 2022).

[3] University of Oxford, "Lecture 7 - the discrete fourier transform." https://www.robots.ox.ac.uk/~sjrob/Teaching/SP/l7.pdf. (Accessed on the 1st of February of 2022).

[4] Sarafin T., Doukas P., Demchak L., Browning M. and Wright L., "Vibration Testing of Small Satellites," *Instar Engineering and Consulting, Inc.*, 2018.

[5] Siemens, "The autopower function... demystified!." https://community.sw.siemens.com/s/article/the-autopower-function-demystified. (Accessed on the 30th of January of 2022).

[6] Siemens, "What is a power spectral density (psd)?." https://community.sw.siemens.com/s/article/what-is-a-power-spectral-density-psd. (Accessed on the 30th of January of 2022).

[7] Oñate, E., *Structural analysis with the finite element method. Linear statics: volume 2: beams, plates and shells.* Springer Science & Business Media, 2013.

[8] Cazarola, D. R., "Computational engineering. plate and shell elements," *Univeritat Politècnica de Catalunya*, 2021.

[9] Villamarín, R. A., *Vibracions mecàniques.* Universitat Politècnica de Catalunya, 2020.

[10] Irvine, T., "An introduction to the shock response spectrum," *Rev P, Vibrationdata*, 2002.

[11] Küçükbayram, A. , "Analysis and verification of a pyroshock test system," Master's thesis, Middle East Technical University, 2021.

[12] Massa, J., Giró, J. and Giudici, A., "Capítulo 4. teoría de placas," *Compendio de Cálculo Estructural II*, 2015.

[13] Chen, M.-T. and Ali, A., "An efficient and robust integration technique for applied random vibration analysis," *Computers & Structures*, vol. 66, pp. 785–798, 1998.

[14] Domínguez-Pumar, M., Kowalski, L., Jiménez, V., Rodríguez, I., Soria, M., Bermejo, S., and Pons-Nin, J., "Analyzing the performance of a miniature 3d wind sensor for mars," *IEEE Sensors Journal*, vol. 20, no. 20, p. 5912, 2020.

[15] Kowalski, L., Atienza, M. T., Gorreta, S., Jimenez, V., Dominguez-Pumar, M., Silvestre, S., and Castañer, L. M., "Spherical wind sensor for the atmosphere of mars," *IEEE Sensors Journal*, vol. 16, no. 7, pp. 1887–1897, 2015.

[16] Quispe, B. F., "Estudio de placas: Solución analítica (formulación de timoshenko)." `https://www.inesa-tech.com/blog/estudio-placas-formulacion-timoshenko`, July 2021. (Accessed on the 5th of March of 2022).

[17] COMSOL, "Structural mechanics module. user's guide," *COMSOL*, pp. 587–612, 2017.

[18] Siemens, "What is the fourier transform?." `https://community.sw.siemens.com/s/article/what-is-the-fourier-transform`. (Accessed on the 1st of February of 2022).

[19] Wikipedia, "Fast fourier transform." `https://en.wikipedia.org/wiki/Fast_Fourier_transform`. (Accessed on the 1st of February of 2022).

[20] Bekele, A., "Cooley-tukey fft algorithms." `http://people.scs.carleton.ca/~maheshwa/courses/5703COMP/16Fall/FFT_Report.pdf`. (Accessed on the 2nd of February of 2022).

[21] Yilmaz, F., Haktanir, O. O., and Uygur, A. B., "Quasi-static structural test of satellites," in *2015 7th International Conference on Recent Advances in Space Technologies (RAST)*, pp. 421–424, IEEE, 2015.

[22] Japan Aerospace Exploration Agency, "Centrifugal acceleration test facility." `https://shiken.jaxa.jp/en/facility13_e.html`. (Accessed on the 28th of January of 2022).

[23] Save Load Testing Technologies, "Random vibration testing vs sine vibration: which one best suits your needs?." `https://www.safeloadtesting.com/random-vibration-testing-vs-sine-vibration-which-one-best-suits-your-needs/`. (Accessed on the 28th of January of 2022).

[24] Ontaç, S., "Finite element analysis of a micro satellite structure under vibration induced loads during launch," Master's thesis, Middle East Technical University, 2008.

[25] Simmons, R., "Calulating grms (root-mean-square acceleration)." `https://femci.gsfc.nasa.gov/random/randomgrms.html`. (Accessed on the 2nd of February of 2022).

[26] Cazarola, D. R., "Computational engineering. frequency analysis," *Univeritat Politècnica de Catalunya*, 2021.

[27] Wijker, J. J., *Spacecraft structures.* Springer Science & Business Media, 2008.

[28] Aenlle, M., Juul, M., and Brincker, R., "Modal mass and length of mode shapes in structural dynamics," *Shock and Vibration*, vol. 2020, 2020.

[29] Siam, N., "Development of an efficient analysis method for prediction and structural dimensioning of space structures subjected to shock loading," 2010.

[30] NTS, "Pyrotechnic shock." `https://nts.com/services/testing/shock/pyrotechnic/`. (Accessed on the 11th of December of 2021).

[31] Filippi, E., Attouoman, H., and Conti, C., "Pyroshock simulation using the alcatel etca test facility," in *Launch Vehicle Vibrations. First European Conference. Toulouse: CNES*, Citeseer, 1999.

[32] Lee, J.-R., Chia, C. C., and Kong, C.-W., "Review of pyroshock wave measurement and simulation for space systems," *Measurement*, vol. 45, no. 4, pp. 631–642, 2012.

[33] Eriksson, J., Hansson, M., Lago, M., and AB, S. E. S., "Measuring and analysis of pyrotechnic shock," *Chalmers University of Technology*, 1999.

[34] ISO Technical Committee, *Signal Processing - Part 4: Shock-response spectrum analysis, BS ISO 18431-4:2007.* 2007.

[35] Kelly, R. D. and Richman, G., "Principles and techniques of shock data analysis," tech. rep., Measurement analysis corporation from los Angeles, California, 1969.

[36] Nigam, N. C. and Jennings, P. C., "Digital calculation of response spectra from strong-motion earthquake records," 1968.

[37] Gupta, A. K. and Hall, W., *Response spectrum method: in seismic analysis and design of structures.* Routledge, 2017.

[38] MathWorks, "Ode45: solve nonstiff differential equations — medium order method." `https://www.mathworks.com/help/matlab/ref/ode45.html`. (Accessed on the 23rd of April of 2022).

[39] Domínguez-Pumar, M., Rodríguez-Manfredi, J., Jiménez, V., Bermejo, S., and Pons-Nin, J., "A miniaturized 3d heat flux sensor to characterize heat transfer in regolith of planets and small bodies," *IEEE Sensors Journal*, vol. 20, no. 15, p. 4135, 2020.